A Dalitz Plot Analysis of $p\overline{p}$ Annihilation at Rest into $K_S K^{\pm}\pi^{\mp}$ and a Measurement of the Branching Ratio of $\omega \rightarrow \eta\gamma$. Version 1.1

by

Mark Thomas Lakata

B.S. (California Institute of Technology) 1992
M.A. (University of California at Berkeley) 1995

A dissertation submitted in partial satisfaction of the
requirements for the degree of
Doctor of Philosophy

in

Physics

in the

GRADUATE DIVISION
of the
UNIVERSITY of CALIFORNIA at BERKELEY

Committee in charge:

Professor Ken Crowe, Chair
Professor Marjorie Shapiro
Professor John Rasmussen

Fall 1998

The dissertation of Mark Thomas Lakata is approved:

Chair Date

Date

Date

University of California at Berkeley

Fall 1998

A Dalitz Plot Analysis of $p\overline{p}$ Annihilation at Rest into $K_S K^{\pm}\pi^{\mp}$ and a Measurement of the Branching Ratio of $\omega \rightarrow \eta\gamma$. Version 1.1

by

Mark Thomas Lakata

Abstract

A Dalitz Plot Analysis of $p\overline{p}$ Annihilation at Rest into $K_S K^{\pm}\pi^{\mp}$ and a Measurement of the Branching Ratio of $\omega \rightarrow \eta\gamma$. Version 1.1

by

Mark Thomas Lakata

Doctor of Philosophy in Physics

University of California at Berkeley

Professor Ken Crowe, Chair

We report on an analysis of the reaction $p\overline{p} \rightarrow K_S K^{\pm}\pi^{\pm}$, with data taken by the Crystal Barrel with the kaonic trigger of April 1996. The final dalitz plot contains 60K events, much larger than the combined statistics of all previous experiments. The partial wave analysis uses P and S-wave annihilation. Contributions from $a_0(980)$, $a_0^{\pm}(1450)$, $K_2^*(1430)$ and $\rho(1450, 1700)$ are discussed. If the well-known $K_2^*(1430)$ is included in the fit, it perfectly recreates the $K\bar{K}$ threshold enhancement without an explicit resonance, i.e. the $a_0(980)$ is no longer needed. An $I = 1$ resonance is needed at roughly $m = 1500$ MeV, but the spin is not well determined, so it may be either $\rho(1450)$ or $a_0(1450)$.

We also report on a measurement of the branching ratio of the rare decay, $\omega \rightarrow \eta\gamma$ relative to the well known decay $\omega \rightarrow \pi^0\gamma$. The ω's are produced in $p\overline{p} \rightarrow \eta\omega$ and $p\overline{p} \rightarrow \pi^0\omega$. Eigenstate mixing and interference effects of the ω and ρ^0 are taken into account, as well as coherent interference with the background. The result is BR($\omega \rightarrow \eta\gamma$)= $4.2^{+1.3}_{-1.8} \times 10^{-4}$. We report a first measurement of the non-resonant annihilation channel $BR(p\overline{p} \rightarrow \eta\eta\gamma) = (3.5 \pm 1.3) \times 10^{-5}$. This work supersedes an earlier Crystal Barrel value.

This updated version 1.1 contains corrections to the official thesis filed with the University of California.

Professor Ken Crowe
Dissertation Committee Chair

Contents

List of Figures

List of Tables

Acknowledgements

I thank the American tax payers for their money. Peter Kammel gave me many suggestions and helped guide me through the analyses. Tom Case gave me great stories of him and his dad in Utah, as well as explanations of everything else. Ken Crowe listened to my endless "new" discoveries. My parents kept asking me when I was going to be done. David Bugg, Lucien Montanet and Maurice Benayoun gave me many useful comments on my paper. Marjorie Shapiro and John Rasmussen both read and helped me improve my final draft of the thesis. Crystal Barrel collaborators gave me (without telling me) endless software bugs to fix. The tax payers of Europe supplied me with the antiprotons. KALX radio provided the much needed musical entertainment. Thank you all.

Part I

The Crystal Barrel Detector

Chapter 1

The Crystal Barrel Detector

1.1 Overview

The study of $p\overline{p}$ annihilations began more than thirty years ago with bubble chambers at LBL, CERN and BNL, and has since been pursued at these laboratories together with Serpukhob and KEK. The advent of the low energy antiproton (LEAR) ring at CERN, with its intense and extremely pure $\bar{p}$ beams, enables the quality of the data to be further improved. In addition, the advent of computerized data acquisition and electronic photon detection now makes it possible to collect lots of data on previously inaccessible final states with neutral particles.

The CERN Crystal Barrel detector's main physics program is meson spectroscopy through antiproton-nucleon annihilations. The detector receives cooled antiprotons from the Low Energy Antiproton Ring (LEAR), which annihilate on a fixed target, producing charged and neutral particles which are measured with high precision and nearly full solid angle coverage. Within the volume of the annihilation region, very short lived intermediate state mesons are formed and decay; these are the states in which we are interested. The strength of the Crystal Barrel is the excellent solid angle coverage for photon detector (inspired by the Crystal Ball Experiment). A good review of the Crystal Barrel and important physics results is given by Amsler [1].

The Crystal Barrel Experiment was proposed in 1985 by a collaboration of many institutions. The Berkeley group at LBL was responsible for design and construction of the Jet Drift Chamber. The Barrel took data at CERN from December 1989 until December 1996, at which point it was disassembled. Roughly 10^8 good $p\overline{p}$ annihilations were recorded over this period.

During the lifetime of the experiment, two important upgrades were made. The Jet Drift Chamber (JDC) was redesigned to improve the fields of the inner layers, and a Silicon Vertex (SVX) detector replaced the Proportional Wire Chambers (PWC). Part II of this thesis concerns data taken after both of these upgrades where installed, while Part III of this thesis concerns data taken before the upgrades.

The analyses of the Crystal Barrel consistent usually of two types. The first is a partial wave analysis of a Dalitz plot (or higher dimensional plot) of all the particles resulting from the $p\overline{p}$ annihilation. The purpose of these analyses is true spectroscopy, categorizing the entire energy structure of all intermediate resonances in hopes of finding new structures. The second type of analysis is usually a search for rare decays of specific known particles. This thesis deals with both types of analysis, with Part II a partial wave analysis of $p\overline{p}\rightarrow K_S K^{\pm}\pi^{\mp}$ and Part III a measurement of the rare decay $\omega\rightarrow\eta\gamma$.

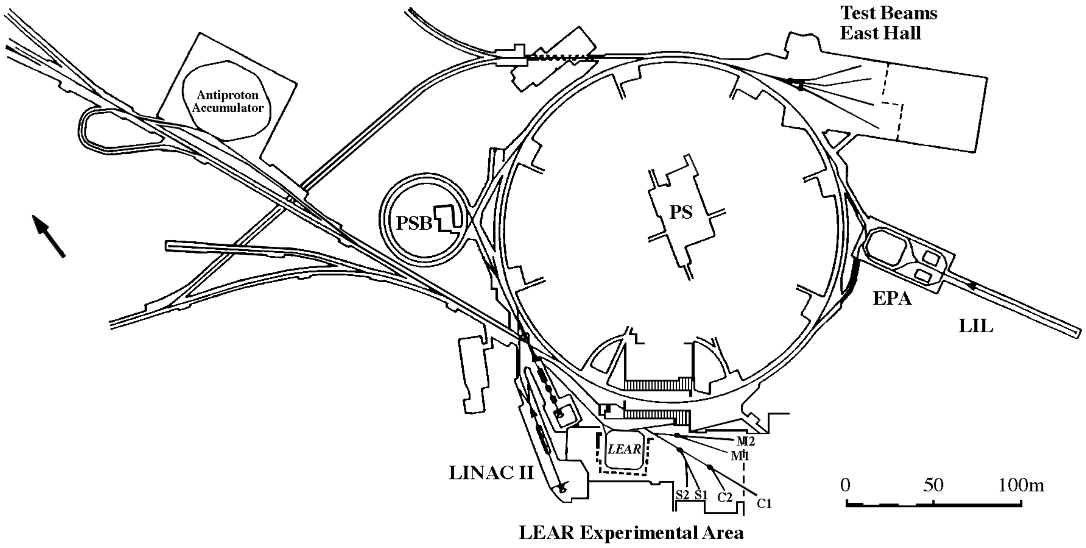

Figure 1.1: The CERN PS complex. Protons produced in the Linac 2 are accelerated to several GeV in the PSB and PS. They impact on a target and a small fraction produces antiprotons, which are accumulated in the AA and then transfered to LEAR. After final cooling, the antiprotons are slowly extracted to the experiments in the switch-yard. The Crystal Barrel sits on beam C2.

1.2 Low Energy Antiproton Ring (LEAR)

The study of $p\overline{p}$ annihilations at rest requires two things, a source of $\bar{p}$ and a way to slow them down. The CERN Proton-Synchrotron Complex contains the system for these two requirements. Protons are initially accelerated to several GeV in the Proton-Synchrotron (see figure 1.1). They are extracted in bunches of 10^{13} and are directed to an iridium target at 3.5 GeV/c. The interaction with the target produces 10^7 antiprotons per batch that are collected and cooled by the Antiproton Accumulator complex. Up to $10^1 2$ antiprotons can be stacked in the Accumulator. When a sufficient number are accumulated, a packet of 10^{10} is decelerated to 600 MeV/c and sent to the Low Energy Antiproton Ring for further cooling.

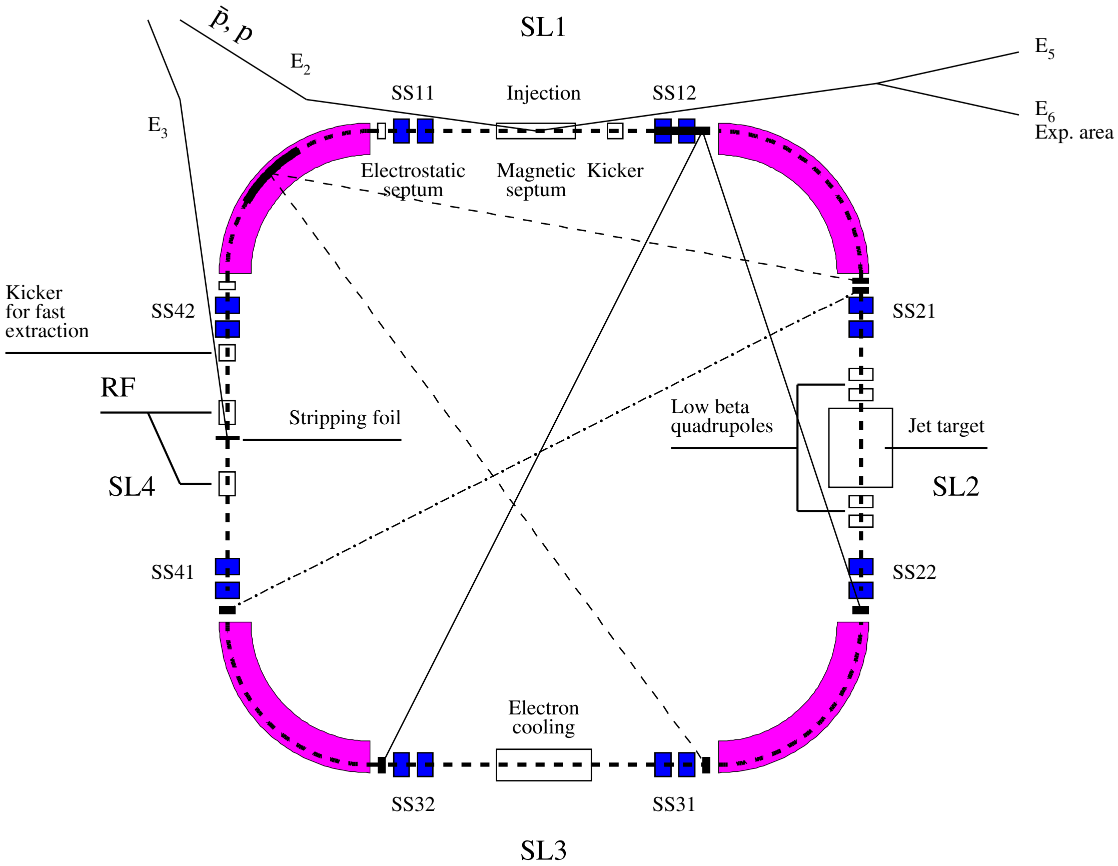

Figure 1.2: The LEAR ring. Antiprotons enter from the upper-left corner. The diagonal criss-crossing lines are the signal wires between pickups and kickers for stochastic beam cooling. The cooled antiprotons exit on E6 on their way to the Crystal Barrel.

LEAR (see figure 1.2) uses decelerators and electron cooling for slowing the antiprotons to 200 MeV/c. This works by injecting a parallel beam of transversely cold electrons into a straight section of the antiproton beam. The electrons absorb the transverse momentum of the antiprotons and then are scattered out of the beam. The antiprotons are then very slowly extracted at a rate of 10-100 kHz by means of an electrostatic foil that slices off the edge of the beam profile. These antiprotons are then sent to the experimental switchyard through beam line E6, and finally switched to line C2 before entering the Crystal Barrel experiment.

The Crystal Barrel nominally receives antiprotons at 12-20 kHz, over a spill run that nominally lasts a half hour. Between spills, the detector is calibrated.

1.3 The Crystal Barrel Experiment

The Crystal Barrel Experiment was designed as a high resolution detector for gamma rays, as well as having charged particle tracking. A full description of the detector is given in Aker *et al*[2]. The antiprotons from the LEAR annihilate on nucleons, protons in the case of a hydrogen target or protons and neutrons in the case of a deuterium target. Because the annihilation spin state is a function of the density, a liquid or gaseous target can be used. However, in this analysis only data taken with the liquid hydrogen target was used. The components of the detector (see figure 1.3), in order of increasing radius from the annihilation point, are

1. Trigger counters

2. Liquid Hydrogen target

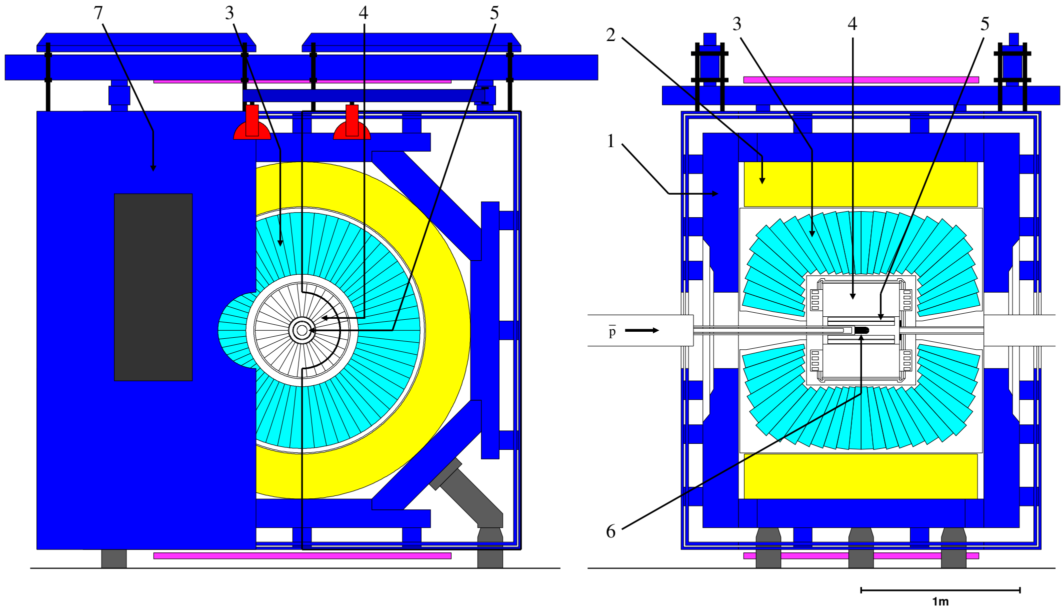

Figure 1.3: Overall layout of the Crystal Barrel detector showing (1) magnet yoke, (2) magnet coils, (3) CsI barrel, (4) jet drift chamber, (5) proportional chamber, (6) liquid hydrogen target, (7) one half of the end-plate. (left) view as seen by incoming antiproton (right) side view.

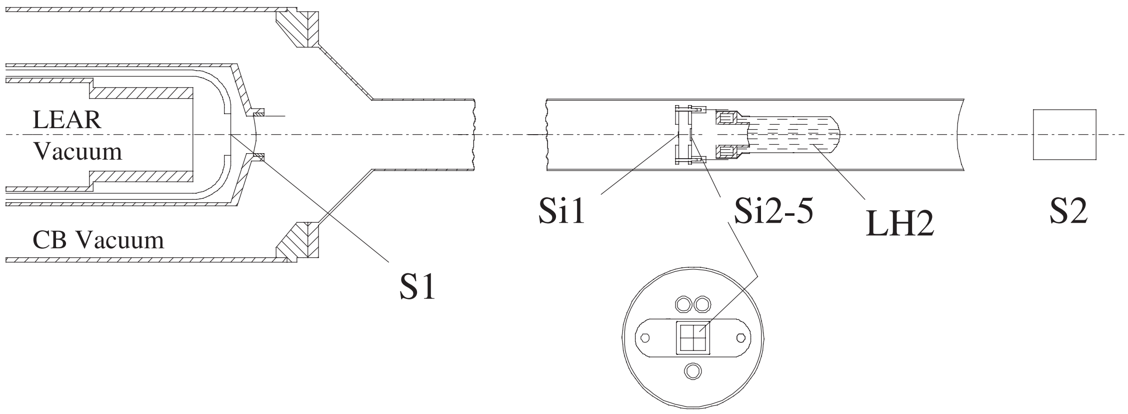

Figure 1.4: The LH_2 target

3. Silicon Vertex Detector (SVX) or Proportional Wire Chamber (PWC), depending on year of experiment

4. Jet Drift Chamber (JDC)

5. Crystal Barrel Calorimeter (CB)

6. 1.5 T magnet and support structure

1.4 Target and counters

Figure 1.4 shows the layout of the LEAR beam pipe, beam counters and target. Antiprotons first leave the LEAR vacuum through a beryllium window at the end of the LEAR beam pipe. They pass through the first entrance wire chamber counter (S1) and then travel about 35 cm through the Crystal Barrel target vacuum. Just before entering the LH_2 chamber, the antiprotons pass through one of 4 Silicon counters (Si2-5), used to help center the beam. Finally, the particles (ideally) enter the liquid hydrogen chamber (LH2), which is a mylar tube. If a particle does not stop in the chamber, it contains through into the downstream scintillator counter (S2). The entrance counter S1 defines the start of an event, while the exit counter S2 vetos the event.

1.5 Proportional Wire Chamber

The Proportional Wire Chamber (PWC) consisted of two coaxial wire chambers situated outside of the target but inside the JDC. For this thesis, the PWC was only used as a veto for events with charged particles. The PWC was replaced by the SVX in 1995.

1.6 Silicon Vertex Detector

The Silicon Vertex detector (SVX) was installed in 1995[3], to replace the PWC. It consists of 15 microstrip detectors arranged in a cylinder. Each detector has 128 front-side strips and 1 global backplane. Each strip forms a diode with the backplane. The diode is reversed biased; when a charged particle passes through the silicon junction and creates additional charge pairs, a small current flows through the diode. Because the current flows through both the strip and the backplane, the backplane acts as a logical OR on all the strips, allowing for a fast determination of the multiplicity of the tracks. The fired strips are readout serially.

For the $K_S K^{\pm}\pi^{\mp}$ analysis, a fast trigger on K_S was desired. A neutral K_S decays into two charged particles over a distance of a few centimeters. By triggering on events that have more tracks at a larger radius than at a smaller radius, K_S events are selected.

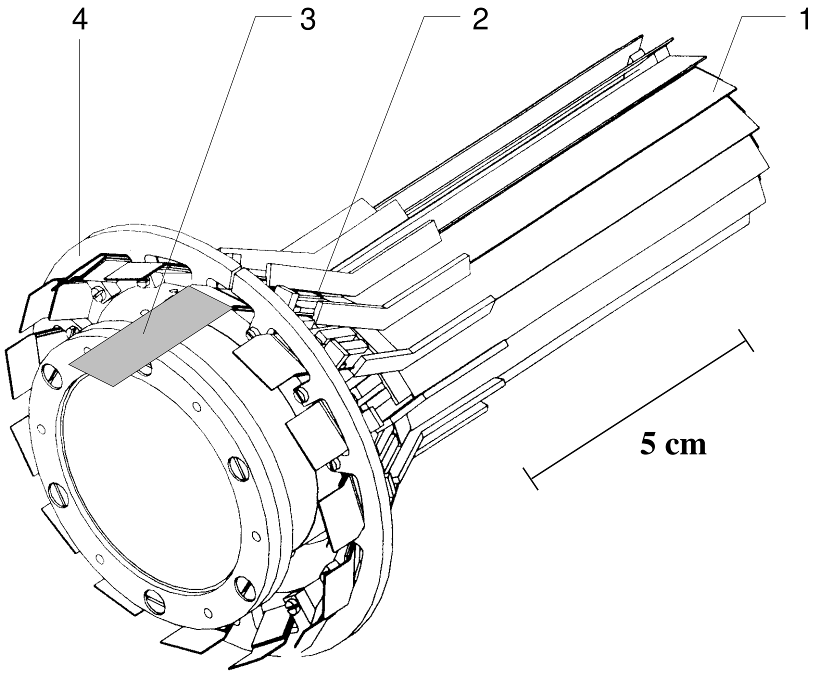

Figure 1.5: The Silicon Vertex detector (SVX). (1) Microstrip detectors (2) hybrids (3) readout electronics (4) cooling ring

The radial decay distribution is an exponential drop-off (convolved with the geometry). By sampling the number of tracks at the smallest possible radius, the greatest efficiency for K_S will be achieved. The advantage of the SVX over the PWC is due to the fact that the SVX is situated at a smaller radius than the PWC, and thus can trigger on roughly 50% of the K_S produced.

1.7 Jet Drift Chamber (JDC)

The Jet Drift Chamber (JDC) was used for the measurement of momenta of charged particles. Charged particles in a strong magnetic field travel along helical paths,

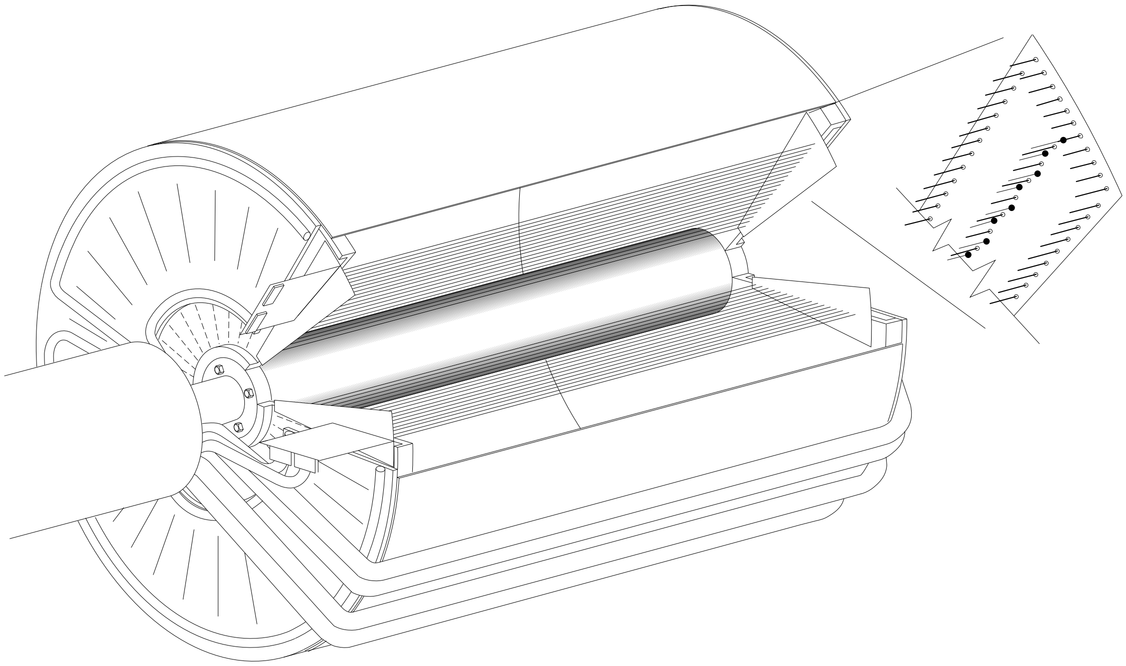

Figure 1.6: The Jet Drift Chamber (JDC). The staggering of the wires is exaggerated.

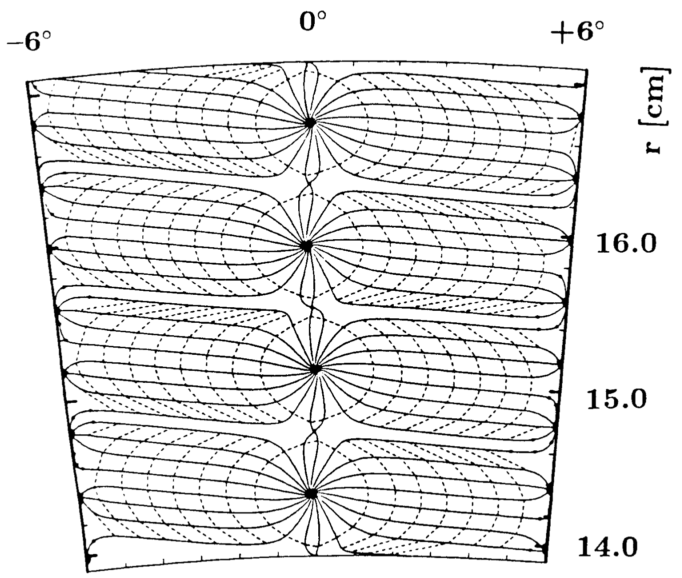

Figure 1.7: The field-map for four layers of one sector of JDC I. The lines of electric force are shown as solid lines, while the isochrone contours are shown as dashed lines. The force lines converge on the sense wires. Between the sense wires and along the edges of the cells lie the high voltage field shaping wires (not shown).

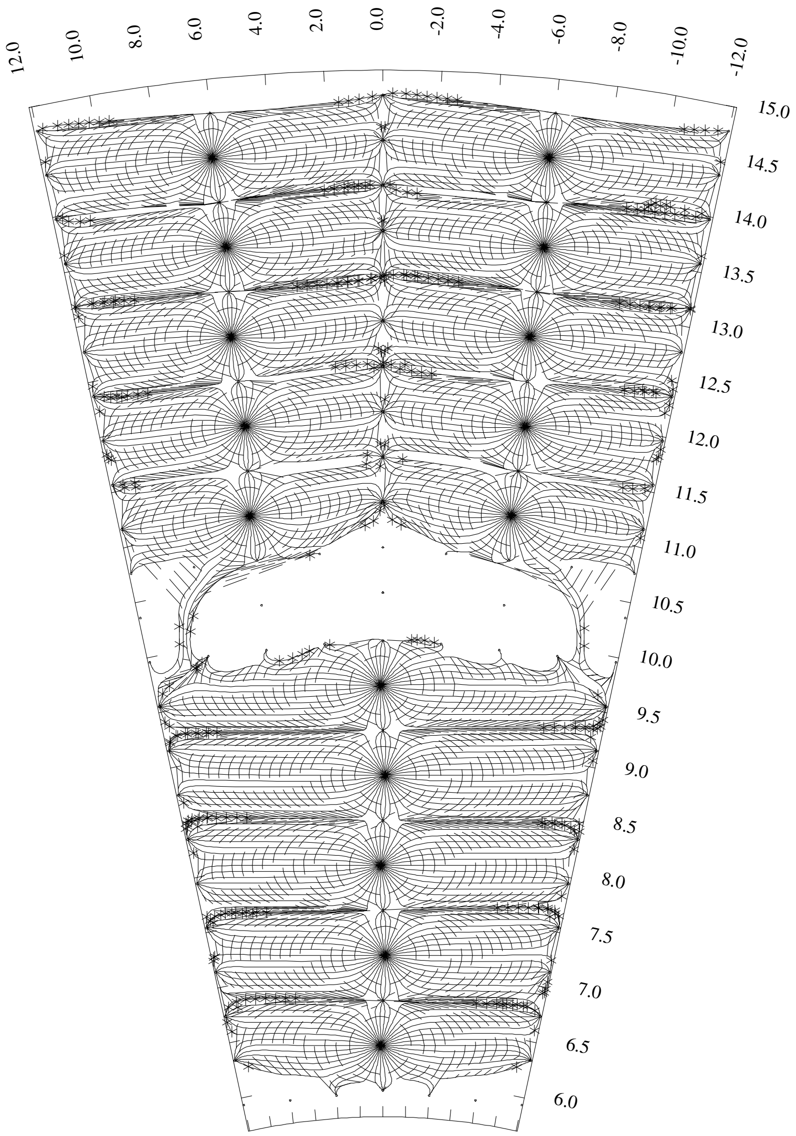

Figure 1.8: The field-map of JDC II, showing the inner 5 layers and the first 5 outer layers. The sense wires of layer 6 were removed. The lines of force are drawn as solid lines , while isochrones are dashed lines.

whose curvatures are inversely proportional to the particles' momenta. The entire Crystal Barrel experiment is situated inside a conventional 2.5 MW magnet, providing a uniform magnetic field of 1.5 Tesla.

The cylindrical JDC is roughly 25cm in radius and 50cm in length, which is divided into cells, with 30 azimuthal sectors by 23 radial layers (See figure 1.6). Each cell contains one sense wire at the center, and several field shaping wires at roughly -2000 V potential. The potentials are chosen to set up a nearly uniform electric field in the azimuthal direction (see figure 1.7). When an ionizing particle passes through the JDC chamber gas (90% CO_2 and 10% Isobutane), the electrons released along the particle's path drift towards the central sense wire, with a roughly constant velocity of 8.4 μm/ns. The collected charge on the sense wire is measured as a short current pulse by fast current meters at each end of the wire. Because the wire is resistive, the ratio of current measured on each end of the wire gives additional information as to the longitudinal position of the electron shower along the wire. Since there is an ambiguity in which direction the electrons come from (left or right), there are two hit entries per wire, a "left" and "right" hit. One of these hits is the true position of the track, while the other is a mirror image, reflected over the sense wire plane. To solve this ambiguity, the sense wires are staggered. This causes the positions of the mirror hits to be staggered (by twice the stagger amount), thereby forcing the circle recognition subroutine to select the true hits because of the better fit. This stagger is shown in exaggerated detail in figure 1.6.

The current is amplified by preamplifier cards attached to each end-plate, and eventually digitized by flash analog to digital converters (ADC's). For triggering purposes, threshold circuitry was attached to 6 of the 23 layers. The sum of fired sectors per trigger layer gave an estimate of the number of tracks passing through that layer. For the K_S trigger, 4 or more sectors were required to fire for the outer layers.

The original JDC (JDC I) suffered from overcrowding in the inner layers. A new JDC II was designed and commissioned in 1994. The difference was that the inner 5 layers had 15 azimuthal sectors rather than 30 sectors. The sense wires at layer 6 were removed because of the discontinuity in field configurations. Figure 1.8 shows the effect of new design.

The energy loss, dE/dx, of tracks is used for K/π identification. It is measured by averaging the integrated charge of all JDC pulses along a track. Slow particles leave behind more ionization energy per unit distance, and thus a larger integrated signal on the sense wires than faster moving particles. This difference allows a K/π separation up to about 450 MeV/c in momentum.

1.8 Track reconstruction

The first task for track reconstruction is to find the time of the start of the current pulses in the digitized signals. This time is converted into a position by a lookup table calculated using the GARFIELD program to calculate the isochrones. This gives the azimuthal position of the hit on the track. The z position [1] is determined using the integrated current pulses $A_\pm$ from either end of the wire,

$$z = z_0 + z_L \frac{A_+ - \alpha A_-}{A_+ + \alpha A_-}.$$

[1] The people responsible for calibration of z_L (typically 24 cm) did not get the correct value for the April 96 run. The data was later corrected by scaling all z measurements by +6%.

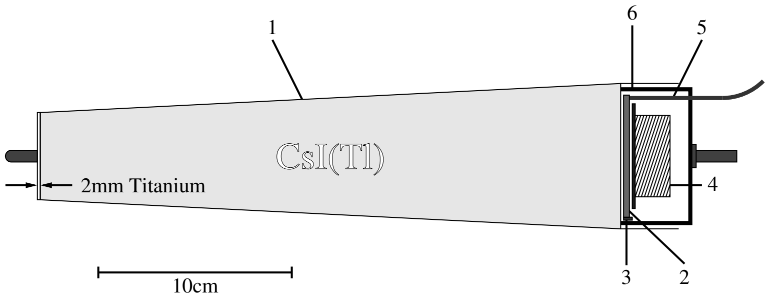

Figure 1.9: A single crystal detector. (1) CsI Crystal in titanium can (2) wavelength shifter (3) photodiode (4) preamplifier (5) calibration light fiber (6) brass cover

The values of z_0, z_L and α (for each wire) are determined through a calibration with 4-track events.

The next task for the reconstruction is to group the hits into tracks. A fast-fuzzy radon transform is used to recognize circles in the hits. This step of the reconstruction is extremely CPU intensive, but offered a higher track reconstruction efficiency than an older "road" method. Once the hits are group, they are first fit to a 3 parameter circle (ignoring the z information). This 3 parameters are then used to seed a 5 parameter helix fit, which uses both the azimuthal and z information of all the hits.

Finally, a vertex fit is performed on the resultant tracks. This vertex fit was developed for the purpose of this thesis, and is described in greater detail in section4.4.

1.9 Crystal Calorimeters

The gamma rays are detected by 1380 Cesium-Iodide crystal scintillators (see figure 1.9), arranged in a projective geometry that covers 95% of the total solid angle (see

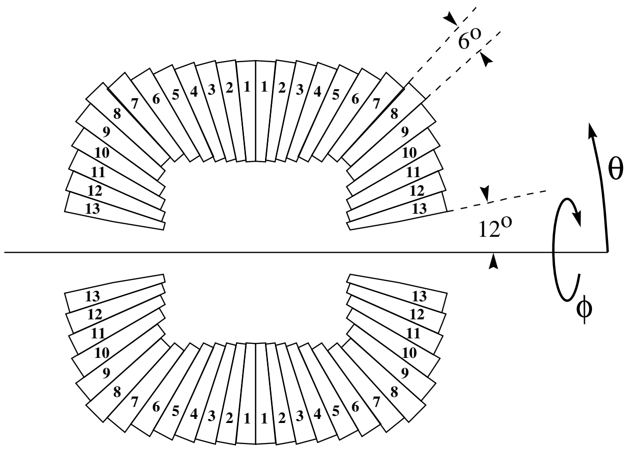

Figure 1.10: The crystal layout

figure 1.10. The crystals are 16 radiation lengths long (30 cm). The scintillation light is read out on the back-end via a wavelength-shifting plastic coupled to a photodiode. The photodiode is digitally sampled with two independent ADC's, the 2282's and the FERA's, to increase the dynamic range, and for internal integrity checks. The crystals are arranged in a $6° \times 6°$ array, and provide an angular resolution of $1.5°$ when the center of gravity of a cluster of crystals is considered. The energy resolution is $2.5\%/\sqrt[4]{E(\mathrm{GeV})}$, resulting in $\sigma(m_{\pi^0}) = 8MeV$ and $\sigma(m_\eta) = 17MeV$.

In between antiproton spills from LEAR, the readout electronics are calibrated with a Xenon flash lamp whose output is channeled to each crystal by a fiber optic. Also, the no-signal pedestals are measured and applied for the next spill.

1.10 Photon Reconstruction Algorithm

All particles can trigger a shower in the crystals. Every localized shower (whether electro-magnetic or hadronic) is called a Particle Energy Deposition (PED). Hadronic showers can not be well measured in the crystals. If the hadron was charged, these PEDs can be removed by connecting them with the appropriate track. Other PEDs are most likely to be the result of γ ray photons. The reconstruction algorithm attempts to accurately identify all of the PEDs in an event, with the goal of making a one to one mapping of "good" PED to photon.

The electro-magnetic shower of a gamma ray interaction covers many contiguous crystals. Thus the reconstruction software first identifies contiguous clusters of crystals. The criteria for starting a cluster is that a seed crystal have an energy above a certain threshold called the cluster crystal threshold. All contiguous neighbor crystals above 1 MeV are added to the cluster. Because the cluster may be the result of more than one photon, secondary local maxima are searched for in the cluster. The energy of the secondary local maxima must be above the secondary-PED crystal threshold.

Finally, one can apply an absolute energy cut on the total reconstructed PED. The previous two thresholds are crystal thresholds rather than PEDs thresholds.

After the γ's are reconstructed, their resolutions can be improved by means of a fit to certain constraints. Because the final strong annihilation occurs at rest, the total four-momentum is known to be (0,0,0; 1876) MeV. This provides four constraints to the fit. Additionally, if the γ's are the result of decays from narrow resonances, such as $\pi^0 \to \gamma\gamma$ or $\eta \to \gamma\gamma$, the invariant masses of these pseudoscalars can be additional constraints to the

γ momenta. For example, in the $\omega \rightarrow \eta\gamma$ decay analysis (part III), the final states are $\eta\eta\gamma$, $\eta\pi^0\gamma$ and $\pi^0\pi^0\gamma$, so the final kinematic fits have six constraints. The results of the fit are two-fold. First, it returns slightly modified momenta of each γ, which more accurately describe the true momenta. Second, it returns a probabilistic confidence level that the given event satisfied the applied decay hypothesis. This can be used to select the desired channels and reject background channels. The fit is described in more detail in appendix A.1.

1.11 Trigger System

The trigger system (see figure 1.11) is arranged in several layers, to minimize losses due to dead-time. Each layer requires a longer time to make a decision, thus rejecting events at an early stage saves the later levels from being saturated. The zeroth level trigger is the π counter, which runs typically at 10000 π/s. For a minimum bias trigger, all events at this level are written to tape. The first hardware level trigger consists of the charge particle multiplicity (CPM) device and the fast cluster encoder (FACE). The CPM counts the number of tracks by counting the number of SVX backplanes, PWC wires or JDC wires at a certain layer which have fired over threshold. The FACE is a special hardware processor that counts the number of crystal clusters in the calorimeter. These devices take about 20 μs to reach a decision, thus limiting the throughput to 500 events/s. The next level is the software trigger, which is a fast version of the gamma reconstruction finder followed by a fast $\gamma\gamma$ invariant mass calculation that checks for a requirement of two or more π^0, η, or η', depending on the configuration desired. Finally, events are built into zebra data banks and written to tape (IBM cartridges pre 1996 and DLT tapes post 1996).

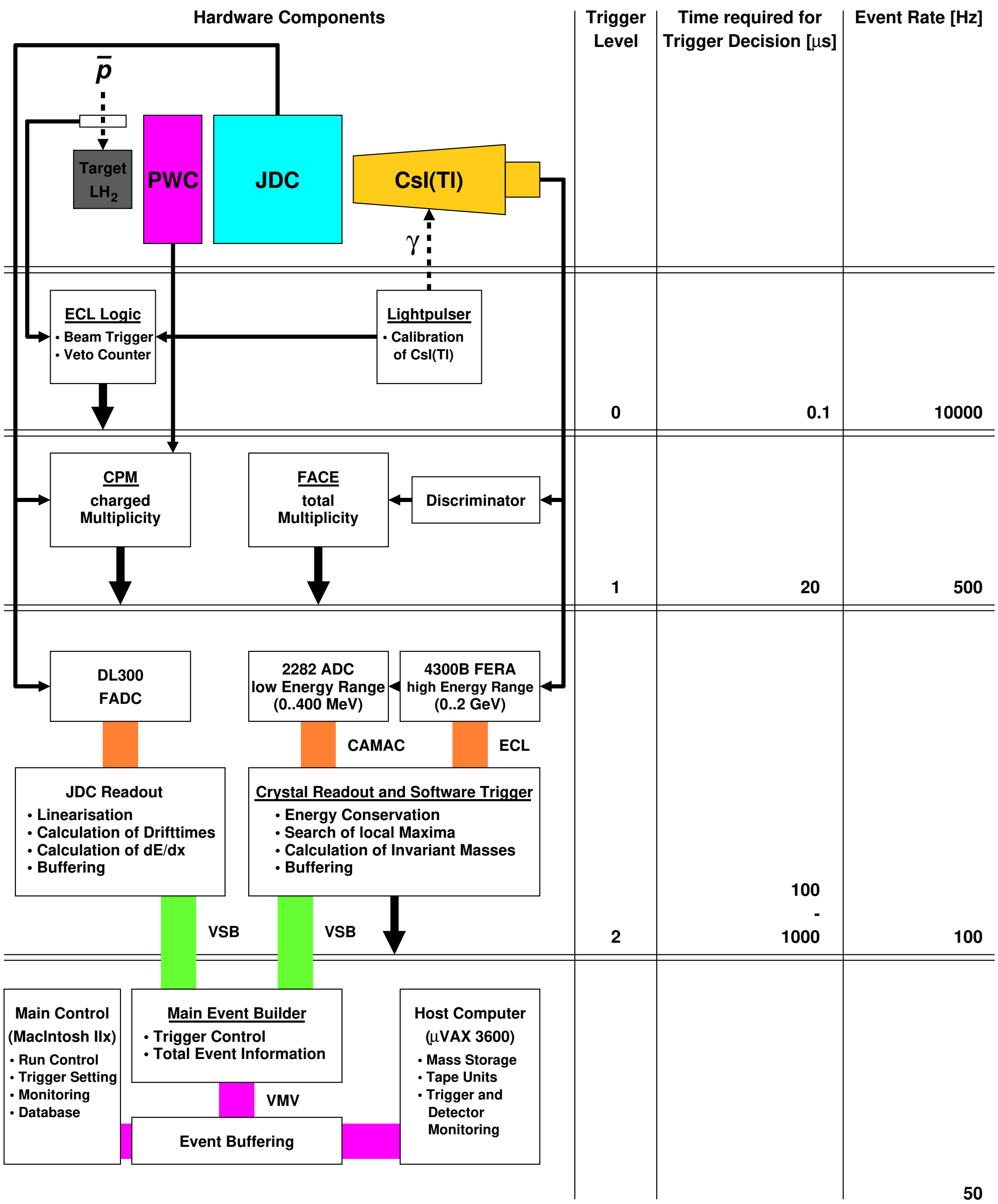

Figure 1.11: The Trigger system

The special trigger used in the April 1996 K_S run period is described in section 5.1.

1.12 Data Acquisition (DAQ) System

A schematic of the data acquisition system is given in figure 1.12. In the electronics hut, there were 6 VME crates: one event builder which orchestrated the data flow from the other crates, two JDC readout crates, one calorimeter readout create, one discriminator/trigger logic crate, and one slow control crate. All crates were controlled by 68040 microprocessors, interfaced together via a VMV bus and local Ethernet. Control over the data acquisition was done via a Macintosh II computer in the control room.

Several quasi-online monitors were used. During spill-breaks, the xenon flash tube was used to calibrate all of the crystals; the data collected for this was analyzed on a μVAX during the next run so that the results could be fed back into the readout electronics. The μVAX also collected statistics on events and presented online histograms of event parameters. A slow control monitor measured environmental parameters, such as magnet current, temperature of critical components, JDC field voltages and gas flow rates. If any parameter deviated outside the allowed range, an alarm would signal.

Once every four hours, one entire run of collected data would be immediately analyzed through the full offline reconstruction code. This was known for historical reasons as the "bicycle" offline program, because in previous years the data tape would be shuttled via a bicycle courier to the computing center. In later years, a fiber optic link replaced the bicycle, and fed the data directly into a DEC workstation. This important test verified the working of the trigger system, as well as the data quality.

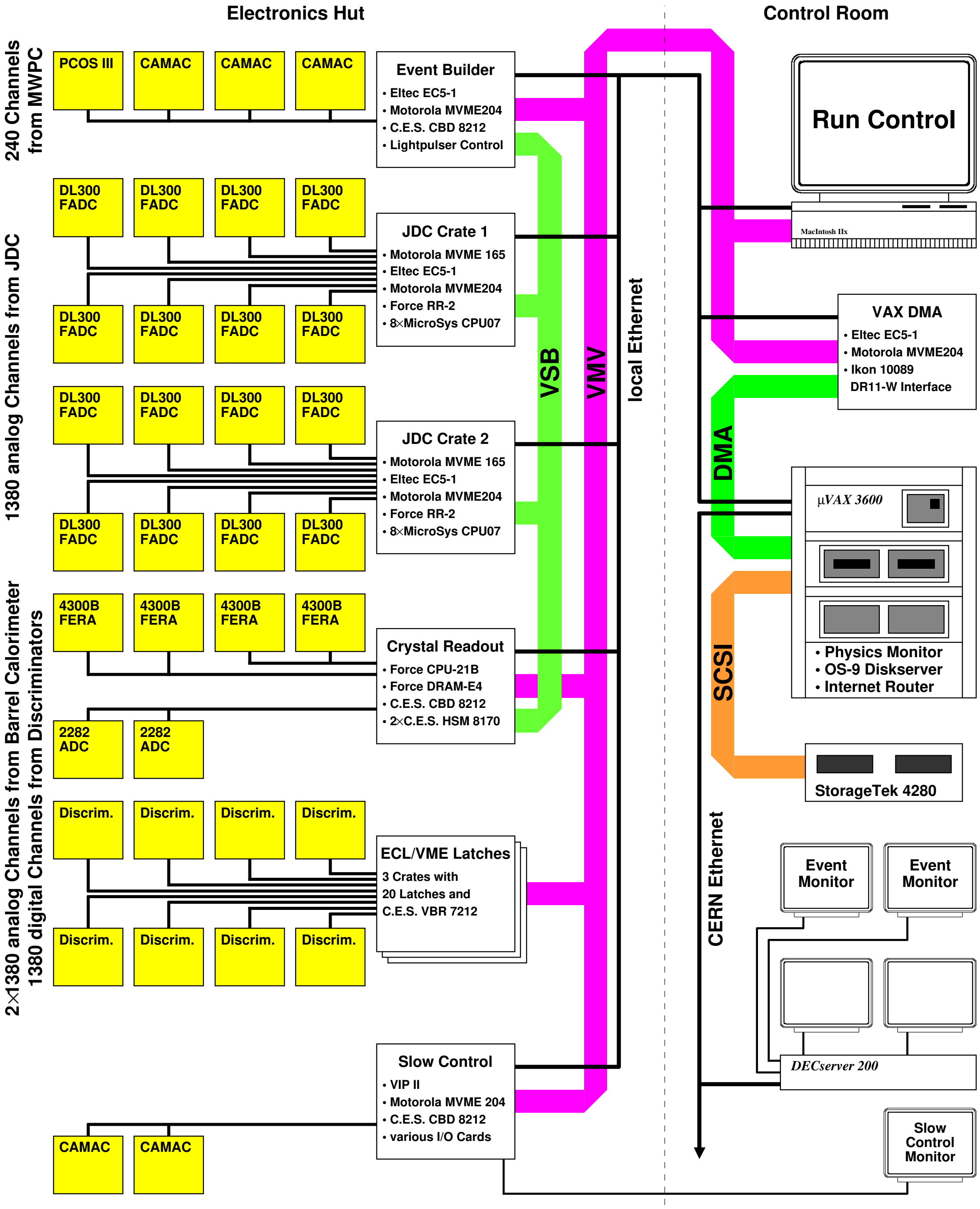

Figure 1.12: The Data Acquisition

1.13 Triggering system

The lowest level of the trigger required a hit in the upstream counter and no corresponding veto hit in the downstream counter, indicating that the incoming antiproton annihilated on the target and did not escape.

The next level of triggering was dependent on the device immediately surrounding the target, either the proportional wire chambers (PWC) pre-1995 or the silicon vertex detector (SVX) post-1995.

For the $p\overline{p}\rightarrow K_S K^{\pm}\pi^{\mp}$ data collection (i.e. Part II of this thesis), the SVX and JDC was used as a second level trigger. Details of the trigger are discussed in section 5.1. Briefly, a long-lived K_S decays outside the SVX, so a change in track multiplicity between the SVX and the JDC was used to tag these events.

For the $\bar{p}\rightarrow 5\gamma$ data collection (i.e. Part III of this thesis), the PWA was used as a second level trigger. This trigger was called the "0-prong" or "all neutral trigger". The 0-prong trigger required no hits in either chamber, thus vetoing events that contain charge particles. A jet drift chamber (JDC) surrounds the PWC, but for this analysis it was not used in its usual momentum measuring mode for there are no charged particles. It was used only as an additional off-line veto.

When the main trigger fires, all crystal calorimeter values are digitized, pedestal subtracted, and zero suppressed. Likewise, the JDC signal wires are digitized too, and all data is eventually gathered into an event, and written to magnetic tape. Over the period 1989 to 1994, over 20 million 0-prong events in liquid hydrogen were collected on tape. During the April 1996 run, more than 9 million K_S triggered events were collected.

Part II

$$p\overline{p} \rightarrow K_S K^{\pm} \pi^{\mp}$$

Chapter 2

Introduction

The study of $p\overline{p}$ annihilations is a useful method for the spectroscopy of low mass mesons in the 1-2 GeV/c^2 mass spectrum. Annihilations into three scalar particles are especially useful, because of the simplicity of describing the complete kinematics with only two variables, which can be nicely plotted in a Dalitz plot. Three body channels involving pions and etas have been well studied and have resulted in many new discoveries of mesons. The true nature of these mesons, however, is still not well understood.

Some of the various $q\overline{q}$ meson nonets are fairly well established, including the pseudoscalars (i.e. π, η, η', K), vectors (i.e. ρ, ω, ϕ and K^*) and tensors (i.e. $a_2(1320)$, $f_2(1270)$, $f_2'(1525)$, $K_2^*(1430)$). The scalar nonet is not well established. In fact, none of the members are assigned without controversy (except perhaps the $K_0^*(1430)$). But the scalar sector is where the lowest mass glueball is predicted. A glueball is a bound state of two or three gluons; the only hard predictions are from the lattice QCD community[4] and [5] who predict the scalar glueball to be in the 1.4-1.8 GeV range.

Two of the new mesons discovered in pionic and eta-mesonic physics are the $f_0(1500)$ and the $a_0(1450)$. The $f_0(1500)$ is believed to be either the glueball alone or a mixed state of glueball and $q\overline{q}$ meson, while the $a_0(1450)$ is rumored to be the $I = 1$ member of the 0^{++} meson nonet[6, 7, 8]. The best evidence for the glueball nature of the $f_0(1500)$ is its decays into channels of different flavor, i.e. up, down and strangeness. Its decays into non-strange channels is well known, but its decays into strange channels is less so. It is crucial to know the coupling into strangeness, because this will aid in determining whether it is a flavor-blind glueball or if it is the $s\overline{s}$ member of the $q\overline{q}$ nonet.

The first measurement of the branching ratio of $f_0(1500)\rightarrow K\bar{K}$ was done in an analysis of $p\overline{p}\rightarrow K_L K_L \pi^0$[9]. In this case, the $f_0(1500)$ was seen decaying into $K_L K_L$. However, the $a_0(1450)$ (if it exists) can also decay this way, and it was seen that it was difficult to separate the contributions of these two scalar mesons. What was needed was a channel where only one of these scalar mesons was allowed, in order to definitively measure their strangeness couplings without interference. Even without a constraint on the $a_0(1450)$ the $s\overline{s}$ coupling of the $f_0(1500)$ was "small", making it low in $s\overline{s}$ content. This means that another meson must be the $s\overline{s}$ meson, e.g. the $f_J(1700)$ or some other undiscovered f_0 meson. A better constraint on the BR($f_0(1500)\rightarrow K\bar{K}$) value requires a precise measurement of BR($a_0(1450)\rightarrow K\bar{K}$) from another channel.

One such channel is $p\overline{p}\rightarrow K^0 K^{\pm}\pi^{\mp}$ where the neutral kaon is either K_S or K_L. The reaction with K_L has been studied in a previous work; however, because the K_L is virtually undetected by our experiment, the resolution of this study was not ideal. The alternative, with K_S decaying in its charged mode, $K_S\rightarrow\pi^+\pi^-$, has higher resolution because the event is fully reconstructed, and also allows a trigger to enrich the data sample. The only drawback is that in order to get high statistics, a K_S trigger requires a secondary vertex outside of the vertex detector. This requirement makes a large effect on the momentum-dependent efficiency, cutting on low momentum kaons that decay inside the vertex detector, thus vetoing the trigger. With proper Monte Carlo simulations, this trigger effect can be corrected.

There were three aims of this analysis.

1. The first goal was to determine which resonances make up the $p\overline{p}\rightarrow K_S K^{\pm}\pi^{\mp}$ annihilation channel. Besides the well known mesons ($K^*(892)$ and $a_2(1320)$ which are visually apparent), there is some confusion over the contributions from $a_0(1450)$, $a_2(1650)$, $\rho(1450)$, and $\rho(1700)$. The $K\bar{K}$ threshold enhancement (typically called the $a_0(980)$ resonance) needs to be better understood.

2. The second goal was to describe the properties of the $a_0(1450)$ (if it exists) including its mass, width and branching ratios from $p\overline{p}$ annihilation. Knowledge of the $a_0(1450)$ will help in determining the $K\bar{K}$ decay mode of the $f_0(1500)$.

3. The third goal was to determine the properties of the $a_0(980)\rightarrow K\bar{K}$ decay with high statistics.

In the process of doing this experiment, several new results were found. First, the contribution from $K_2^*(1430)$ was surprisingly important in the fits. The statistical significance of this channel is much greater than the evidence for the "expected" resonances, such as the $a_0(980)$ or $a_0(1450)$. Second, the unique shape of the $K_2^*(1430)$ mimics the *exact* shape of the $K\bar{K}$ threshold enhancement, and can entirely replace the $a_0(980)$ intensity.

This means that the $a_0(980) \rightarrow K\bar{K}$ branching ratio can be much smaller than previously measured, consistent with zero. The true nature of the $a_0(980)$ has been a mystery since its discovery (see Cahn's "Mystery of the [$a_0(980)$]"[10] for a discussion about how the $a_0(980)$'s branching ratios seem to be dependent on the production), and this discovery may aid in developing a consistent picture of this "particle". Finally, the statistical evidence for the $a_0(1450)$ is not as high as previously thought, and the signal may be instead the $\rho(1450)$.

Chapter 3

Physics background

3.1 $p\overline{p}$ Annihilation at rest

Theoretical understanding of $p\overline{p}$ annihilation is lagging far behind experimental observations, mostly because quantum chromo-dynamics (QCD) is not directly calculable at this energy scale because the color coupling-constant becomes too large for perturbation calculations. The limited theoretical guidance comes from conservation of quantum numbers, including angular momentum, parity, charge parity, isospin and G-parity. Some success has been had by treating the quarks as confined in bags [11] or a harmonic oscillator potential[12, 13, 14].

In $p\overline{p}$ annihilation at rest, the three antiquarks of the $\bar{p}$, the three quarks of the p and all the gluons and other sea-quarks interact with each other. This quark gas of energy 2 GeV evaporates into an average of five pions, and may be thought of as a statistical thermodynamic process. There are similarities between this low energy process and that of the quark-gluon plasma sought in high energy experiments (such as RHIC) [15]. Within this color-rich environment, bound states of gluons, called "glueballs", and other exotic mesons are expected to be formed. An exotic meson is one that is not formed by a simple $q\overline{q}$ pair, but by $q\overline{q}g$ or $qq\overline{q}\overline{q}$.

3.2 Capture and Cascade in Hydrogen

In liquid or gaseous hydrogen, very slow antiprotons (200 MeV/c) eventually come to a stop and are captured by protons in a hydrogen-like atom called protonium. For a complete description of $p\overline{p}$ annihilation at rest, see [16]. The capture states usually have a quantum number of $n \sim 30$ and high angular momentum of $L \sim 30$. Eventually this excited state decays to a low angular momentum state through the emission of x-rays. Typically, annihilation does not occur until $L < 2$, because the orbital wave-functions do not overlap sufficiently.

In rare gaseous hydrogen, the $1P$ $(L = 1)$ state is arrived at first in the cascade, and thus annihilation occurs primarily from the P wave. This contrasts the situation in the liquid where S $(L = 0)$ wave annihilation dominates. Due to the higher density of liquids, the increased collisions with neighboring H_2 atoms cause significant Stark mixing of levels. The Stark effect causes transitions to the S state to occur faster than annihilation in P states. In fact, annihilation in liquid is nearly 90% due to S-wave. The exact ratio of P to S wave annihilation is still not understood because the ratio depends on the final state observed. Historically, P wave annihilation in LH_2 annihilation at rest has been ignored to simplify the partial wave analysis calculations, and this has been successful to a large extent based on the quality of the final fits. However, in this analysis with its high statistics, including P wave annihilation in the fits improves the χ^2 significantly.

Because the cascade process involves interaction with the surrounding medium, the quantum coherence between different states is lost. Essentially the constant bumping of neighboring hydrogen atoms and the emission of real X-rays has "measured" the state of the protonium, and thus collapsed the wave-function before annihilation takes place. Thus channels that proceed from different initial states do not coherently interfere with each other. The initial state is defined by the J^{PC} of the $p\overline{p}$ state, listed in section 3.6.

3.3 Isobar model

In the two-body isobar model[17, 18], $p\overline{p}$ annihilation proceeds primarily through two-meson intermediate states. In a three-body final state, $p\overline{p}$ proceeds through a short-lived resonance, called the *isobar*, and a spectator meson. The isobar then further decays to two mesons.

The dynamics and angular momentum of the isobar dictates the final form of the Dalitz plot. For a particular isobar in a Dalitz plot, one axis of the intensity is described by the dynamical form, usually a Breit-Wigner or K-matrix. The perpendicular axis is described by the spin-parity function, a function of the various angular momenta of the particles, the total angular momentum and Clebsch-Gordan coefficients. Spinless particles have a flat distribution in this perpendicular axis, while vector and tensor particles have variations similar to the shapes of the letter "U" or "W."

This analysis is concerned with analyzing the $KK\pi$ system. In this three body reaction, there are two possible classes of isobars, the non-strange KK isobar and the

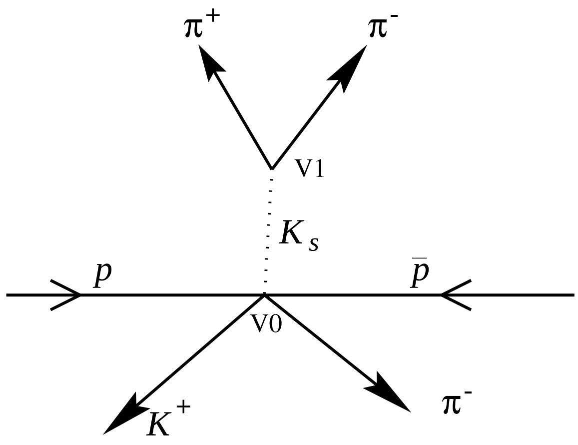

Figure 3.1: The topology for the reaction, starting with $p\overline{p}$ annihilation at vertex V0 into K_S, $K^{\pm}$ and $\pi^{\mp}$, with subsequent $K_S \rightarrow \pi^+\pi^-$at vertex V1.

strange $K\pi$ isobar. The particular choice of $KK\pi$ system determines which isobars are present and which initial states are allowed.

In particular, the reaction

$$p\overline{p} \rightarrow K^0 K^{\pm} \pi^{\mp}$$

is the physical reaction of interest. This channel is unique in that the $K\bar{K}$ system must have isospin $I = 1, I_3 = \pm 1$ because it is recoiling against the $\pi^{\mp}$ which has isospin $I = 1, I_3 = \mp 1$. This rules out contributions from $I = 0$ states such as ϕ, $f_0(980)$, $f_0(1300)$, $f_0(1500)$, and $f_2(1525)$, leaving only $I = 1$ states such as $\rho(1700)$, $a_0(980)$, $a_2(1320)$ and $a_0(1450)$. Also, the strange $K\pi$ states include both charged and neutral combinations of K and π. This makes for interesting interference patterns where the two combinations cross in the Dalitz plot.

3.4 The reaction $K_S K^\pm \pi^\pm$

The K^0 meson is the strong eigenstate, but it is not observed. It is a linear combination of two other states, the K_1 and K_2, which are CP eigenstates and are nearly the observed states. The observed states are actually $K_S \sim K_1$ and $K_L \sim K_2$; the small CP violating differences are not important in this analysis. Because the K^0 is then half K_S and half K_L, the branching ratios that are quoted for states with K^0 are usually double that quoted for states with K_S or K_L.

The specific reaction that is analyzed in detail in this report is

$$p\overline{p} \rightarrow \quad K^\pm \pi^\mp K_S$$
$$\hookrightarrow \pi^+ \pi^-.$$

where annihilation occurs at the primary vertex V0 and the K_S decay occurs at the secondary vertex V1 (see figure 3.1). The displacement of the secondary vertex ($c\tau$ = 2.68 cm) allows a fast experimental trigger (see section 5.1) as well as a clean event tag on the K_S.

The resultant four charged particles can be directly measured via their ionization tracks in the Jet Drift Chamber (JDC). Because the trigger also required long tracks, low energy tracks have lower efficiency because they can curl up. Also, the charged kaon can decay ($K^+ \rightarrow \mu^+ \nu$) within the JDC fiducial volume at low energy. Neglecting these minor losses, the complete event is reconstructed.

3.5 Particles, Quantum Numbers and Selection Rules

In this section, we discuss the properties of the particles involved and the appropriate selection rules for $p\overline{p}$ annihilation.

Particle	I^G	J^{PC}
$\pi^{\pm}$	1^-	0^-
a_0	1	0^+
ρ^0	1	1^-
$K^{\pm}$	$\frac{1}{2}$	0^-
K_S	$\frac{1}{2}$	0^{-+}
$K^*(890)$	$\frac{1}{2}$	1^{--}
$K_0^*(1430)$	$\frac{1}{2}$	0^+
$K_2^*(1430)$	$\frac{1}{2}$	2^+

Table 3.1: The quantum numbers for some mesons. G is not defined for strange mesons and C is not defined for charged particles.

3.5.1 Final-state particles

In this reaction, there 5 distinct final-state mesons,

$$\pi^+, \pi^-, K^+, K^- \text{ and } K_S.$$

These are all pseudoscalar mesons, meaning

$$J^P = 0^-.$$

3.5.2 Intermediate state isobar particles

The isobar decays into pairs of final-state particles. To determine allowed isobars, we shall combine the final pseudoscalar mesons together pairwise with a relative angular momentum $l = 0, 1, 2$. Using $P_l = -1^l$ and the fact that the pseudoscalars have no spin, we see that the intermediates can only be

$$J^P = 0^+, 1^-, 2^+ \ldots.$$

Next, considering isospin I, the pair πK can have isospin $1/2$ or $3/2$. However, if we limit our analysis to intermediates that can be described by the quark model, $I = 3/2$

is eliminated because it can not be constructed with only two quarks (3-quark baryons are eliminated by insufficient energy from $p\overline{p}$ annihilation). In addition, the spin-parity structure is the same for $I = 1/2$ and $I = 3/2$. Thus we limited ourselves to $I = 1/2$ for πK resonances. The allowed quantum numbers for πK resonances are

$$IJ^P = \frac{1}{2}0^+, \frac{1}{2}1^-, \frac{1}{2}2^+.$$

These correspond to the known resonances $K_0^*(1430)$, $K^*(890)$, and $K_2^*(1430)$.

For the pair KK, we can get $I = 0$ or $I = 1$. In the next section, we will show that $I = 0$ is not allowed in this particular annihilation channel. $G = -1^{L+S+I} = -1^{L+1}$ for $S = 0$ and $I = 1$. So the allowed quantum numbers for KK resonances are

$$I^G\ J^P = 1^-\ 0^+, 1^+\ 1^-, 1^-\ 2^+,$$

corresponding to the known states $a_0(980, 1450)$, $\rho(1400, 1700)$ and $a_2(1320)$. Of course, there can be additional energy poles with the same quantum numbers.

3.6 $p\overline{p}$ Initial states

.

The allowed quantum numbers for $p\overline{p}$ annihilation states can be easily enumerated by combining all possible values of $L' = 0, 1$ (the prime is to distinguish this L' from the L used later on) with all possible values of spin. We know that $p\overline{p}$ annihilation at rest proceeds dominantly from $L' = 0$ and somewhat from $L' = 1$. Since the spin of the proton is $\frac{1}{2}$, the total spin of $p\overline{p}$ is either 0 or 1. Then J can take on 0,1 or 2. The parity of a fermion-antifermion pair is calculated using

$$P = -1^{L+1}$$

while the charge-parity is calculated using

$$C = -1^{L+S}.$$

L'	S	$^{2S+1}L_J$	J^{PC}
0	0	$^1S_0$	0^{-+}
0	1	$^3S_1$	1^{--}
1	0	$^1P_1$	1^{+-}
1	1	$^3P_0$	0^{++}
1	1	$^3P_1$	1^{++}
1	1	$^3P_2$	2^{++}

The isospin can be either $|II_3\rangle = |10\rangle$ or $|II_3\rangle = |00\rangle$. Note that the I_3 component must be zero. Assuming annihilation through the two-body model, one of the bodies is a spectator meson and the other is a shorter-lived intermediate resonance. In this analysis, the spectator is one of the mesons $\pi^{\pm}$, $K^{\pm}$, or K_S, or in other words, a 0^{-+} pseudoscalar, with $I^G = 1^-$ or $I = 1/2$. If the spectator is the $\pi^{\pm}$ with $|II_3\rangle = |1 \pm 1\rangle$, the intermediate must have $I_3 = \mp 1$, requiring $I = 1$. This explains why $I = 0$ KK intermediates are not allowed, as mentioned in the preceding section.

To see which states are accessible from $p\overline{p}$, we make all combinations of spectator pseudoscalar and intermediate, in relative spin-states of L. This L is between the isobar and spectator, not to be confused with the L' in the previous table which was between the proton and antiproton.

PS + Inter.	$L = 0$	$L = 1$	$L = 2$
$(0^- + 0^+)_L$	0^-	1^+	2^-
$(0^- + 1^-)_L$	1^+	$0^-, 1^-, 2^-$	$1^+, 2^+, 3^+$
$(0^- + 2^+)_L$	2^-	$1^+, 2^+, 3^+$	$0^-, 1^-, 2^-, 3^-, 4^-$

3.7 Isospin and C-Parity Considerations

Because the initial states are well defined J^{PC} states, the intermediates need to be written in eigenstates of P and C. This process coincidentally puts the intermediates in eigenstates of I, even though the initial $p\overline{p}$ state is not an eigenstate of I. In the notation of $|I\ I_3\rangle$,

$$|p\overline{p}\rangle = |\tfrac{1}{2}\ \tfrac{1}{2}\rangle \oplus -|\tfrac{1}{2}\ -\tfrac{1}{2}\rangle = -\sqrt{\tfrac{1}{2}}\left(|1\ 0\rangle + |0\ 0\rangle\right).$$

The isospin doublets and triplets used in the following discussion are defined as follows. The assignment is true for excited states (e.g. K^*) as well.

$$\begin{pmatrix} \frac{1}{2} \\ -\frac{1}{2} \end{pmatrix} \rightarrow \begin{pmatrix} p \\ n \end{pmatrix}, \begin{pmatrix} \overline{n} \\ -\overline{p} \end{pmatrix}, \begin{pmatrix} K^+ \\ K^0 \end{pmatrix}, \begin{pmatrix} \overline{K}^0 \\ -K^- \end{pmatrix}$$

$$\begin{pmatrix} 1 \\ 0 \\ -1 \end{pmatrix} \rightarrow \begin{pmatrix} \pi^+ \\ \pi^0 \\ \pi^- \end{pmatrix}, \begin{pmatrix} a^+ \\ a^0 \\ a^- \end{pmatrix}, \begin{pmatrix} \rho^+ \\ \rho^0 \\ \rho^- \end{pmatrix}$$

The C-parity operation gives the following:

$$C|a^+\pi^-\rangle = +|a^-\pi^+\rangle$$

$$C|\rho^+\pi^-\rangle = -|\rho^-\pi^+\rangle$$

$$C|K^{*0}\overline{K}^0\rangle = -|K^{*0}\overline{K}^0\rangle$$

$$C|K^{*+}K^-\rangle = -|K^{*-}K^+\rangle.$$

The intermediate states $p\overline{p}\rightarrow a\pi$ and $p\overline{p}\rightarrow\rho\pi$ are mixtures of $I = 0, 1, 2$. The initial states $p\overline{p}\rightarrow K^*K$ are mixtures of $I = 0, 1$. However, the simplest isospin eigenstates of the later are not C-parity eigenstates, so linear combinations must be taken to arrive at C-parity eigenstates. The simple decompositions are

$$|1\ 0\rangle_a = \sqrt{\tfrac{1}{2}}(-|K^{*+}K^-\rangle + |K^{*0}\overline{K^0}\rangle) \tag{3.1}$$

$$|1\ 0\rangle_b = \sqrt{\tfrac{1}{2}}(-|K^{*-}K^+\rangle + |\overline{K^{*0}}K^0\rangle) \tag{3.2}$$

$$|0\ 0\rangle_a = \sqrt{\tfrac{1}{2}}(-|K^{*+}K^-\rangle - |K^{*0}\overline{K^0}\rangle) \tag{3.3}$$

$$|0\ 0\rangle_b = \sqrt{\tfrac{1}{2}}(-|K^{*-}K^+\rangle - |\overline{K^{*0}}K^0\rangle) \tag{3.4}$$

The C-parity linear combination of $|I\ 0\rangle_{a,b}$ is given in table 3.2, as well as the decompositions for $|a\pi\rangle$ and $\rho\pi\rangle$. The quantity L is the relative orbital angular momentum between the isobar and its spectator.

What these wave-functions in table 3.2 tell us are the branching ratio scaling factors to be applied to the measured branching ratios to account for the entire wave-function, observed and unobserved. For instance, in the $I = 0$ decomposition of the $|a\pi\rangle$ state, we see that each of the charge variations ($|a^+\pi^-\rangle$, $|a^0\pi^0\rangle$, $|a^-\pi^+\rangle$) have equal coefficients. Since we only observe $|a^+\pi^-\rangle$ and $|a^-\pi^+\rangle$, the final answer needs a factor of 3/2 to account for the unobserved $|a^0\pi^0\rangle$. For the $I = 1$ decomposition, there is no $|a^0\pi^0\rangle$, so there is no correction factor necessary. For the $|K^*K\rangle$, all charge variations are measured, so there is no correction for unobserved channels, but there is a 3/2 correction because of the way the K^* decomposes, which comes from (3.5). These scaling factors are given in the "BR Factor" column of table 3.2. In addition to these scaling factors, only half of the K^0 decays are seen as K_S, so there is another global factor of 2 applied to all channels. This net scaling factor is given in table 3.3.

Isospin $\vert I\ I_3\rangle$	P	C	BR Factor	Wave-function
$\vert 0\ 0\rangle$	-1^{L+1}	+	3/2	$\sqrt{\frac{1}{3}}\left(\vert a^+\pi^-\rangle + \vert a^-\pi^+\rangle - \vert a^0\pi^0\rangle\right)$
$\vert 1\ 0\rangle$	-1^{L+1}	−	1	$\sqrt{\frac{1}{2}}(\vert a^+\pi^-\rangle - \vert a^-\pi^+\rangle)$
$\vert 2\ 0\rangle$	-1^{L+1}	+	3	$\sqrt{\frac{1}{6}}\left(\vert a^+\pi^-\rangle + \vert a^-\pi^+\rangle + 2\vert a^0\pi^0\rangle\right)$
$\vert 0\ 0\rangle$	-1^{L}	−	3/2	$\sqrt{\frac{1}{3}}\left(\vert \rho^+\pi^-\rangle + \vert \rho^-\pi^+\rangle - \vert \rho^0\pi^0\rangle\right)$
$\vert 1\ 0\rangle$	-1^{L}	+	1	$\sqrt{\frac{1}{2}}(\vert \rho^+\pi^-\rangle - \vert \rho^-\pi^+\rangle)$
$\vert 2\ 0\rangle$	-1^{L}	−	3	$\sqrt{\frac{1}{6}}\left(\vert \rho^+\pi^-\rangle + \vert \rho^-\pi^+\rangle + 2\vert \rho^0\pi^0\rangle\right)$
$\vert I\ 0\rangle$	-1^{L+1}	C	3/2	$-\frac{1}{2}\left[\vert K^{*+}K^-\rangle + (-1)^I\vert K^{*0}\overline{K^0}\rangle\right.$ $\left.+C\left(\vert K^{*-}K^+\rangle + (-1)^I\vert \overline{K^{*0}}K^0\rangle\right)\right]$

Table 3.2: The isospin and C-parity eigenstates. The BR Factor is described in section 3.7

3.8 Kaon decays

The strong decays of excited kaons are as follows. If they decay into a kaon and a pion, then we need to consider $1 \times 1/2$ Clebsch-Gordan coefficients. By conserving strangeness and observing the isospin sign convention for K^-, we get

$$K^{*+} \rightarrow \sqrt{2/3}|\pi^+K^0\rangle - \sqrt{1/3}|\pi^0K^+\rangle \tag{3.5}$$

$$K^{*-} \rightarrow \sqrt{2/3}|\pi^-\overline{K^0}\rangle + \sqrt{1/3}|\pi^0K^-\rangle \tag{3.6}$$

$$K^{*0} \rightarrow -\sqrt{2/3}|\pi^-K^+\rangle + \sqrt{1/3}|\pi^0K^0\rangle \tag{3.7}$$

$$\overline{K^{*0}} \rightarrow -\sqrt{2/3}|\pi^+K^-\rangle - \sqrt{1/3}|\pi^0\overline{K^0}\rangle. \tag{3.8}$$

The strong eigenstates of the neutral kaons, K^0 and $\overline{K^0}$ are not CP eigenstates. When they do decay, they decay into either two pions ($CP = +1$) or three pions ($CP = -1$). These two decays have very different rates because of the phase space involved. Thus it appears that the K^0 and $\overline{K}^0$ have been transformed into two new states, K_S and K_L, which are CP eigenstates. The K_S is the short lived particle, which is seen in this analysis. The

$I^G J^{PC}$	$^{2S+1}L'_J$	$\pi^{\pm}a_0$	$\pi^{\pm}\rho^{\mp}$	$\pi^{\pm}a_2$	$K^{\pm}K^{*}{}_0$	$K^{\pm}K^{*}$	$K^{\pm}K^{*}{}_2$
0^+0^{-+}	$^1S_0$	0 (3)		2 (3)	0 (3)	1 (3)	2 (3)
1^-0^{-+}	$^1S_0$		1 (2)		0 (3)	1 (3)	2 (3)
0^+1^{--}	$^3S_1$		1 (3)			1 (3)	2 (3)
1^-1^{--}	$^3S_1$			2 (2)		1 (3)	2 (3)
0^+1^{+-}	$^1P_1$		0,2 (3)		1 (3)	0,2 (3)	1 (3)
1^-1^{+-}	$^1P_1$	1 (2)		1 (2)	1 (3)	0,2 (3)	1 (3)
0^+0^{++}	$^3P_0$						
1^-0^{++}	$^3P_0$						
0^+1^{++}	$^3P_1$	1 (3)		1 (3)	1 (3)	0,2 (3)	1 (3)
1^-1^{++}	$^3P_1$		0,2 (2)		1 (3)	0,2 (3)	1 (3)
0^+2^{++}	$^3P_2$			1 (3)		2 (3)	1 (3)
1^-2^{++}	$^3P_2$		2 (2)			2 (3)	1 (3)

Table 3.3: Initial $p\overline{p}$ states and allowed two-body final states. The values in the table are given as "L (f)", where L is the allowed spin state(s) between isobar and spectator and f is the branching ratio scaling factor (see section 3.7).

decomposition is as follows:

$$K_S = \sqrt{1/2}(|K^0\rangle + |\overline{K^0}\rangle) \qquad (CP = +1)$$

$$K_L = \sqrt{1/2}(|K^0\rangle - |\overline{K^0}\rangle) \qquad (CP = -1)$$

or transforming to the other basis,

$$K^0 = \sqrt{1/2}(|K_S\rangle + |K_L\rangle) \tag{3.9}$$

$$\overline{K^0} = \sqrt{1/2}(|K_S\rangle - |K_L\rangle) \tag{3.10}$$

3.9 Connecting initial $p\overline{p}$ states with isobar states

The next step is connecting the $p\overline{p}$ initial states with the isobar-spectator intermediate states, by comparing allowed quantum numbers. This is done in table 3.3, using the tables in section 3.6 and table 3.2. Only J^{PC} values are needed for selection criteria. The C-parity is critical in determining the isospin.

One can see that there are many allowed initial and intermediate states, with 45 allowed combinations! In practice, not all combinations are used in the fits. This is true especially for P wave annihilation and $L = 2$ states when a $L = 0$ state is also allowed for the same final state. We also note that there are no allowed states from $^3P_0$.

3.10 A discussion of the states used in the partial wave analysis

In the partial wave analysis, we need to know not only how many resonances to use in the fit, but also if there are symmetry restrictions to the number of amplitudes to use in the fit. If there are identical particles in the final state, the dynamical amplitude must be symmetric under interchange of the particles. However, in practice the measured particles are not the original interaction particles and have undergone decays and flavor mixing (i.e. the K_S). In some channels, there may be symmetries that are not obvious from the list of final-state particles. For instance, in the Dalitz plot analysis of $\pi^0 K_S K_L$, the dynamical amplitude is symmetric under interchange of K_S and K_L.

For this analysis, all final-state particles are different ($\pi^{\pm}$, $K^{\pm}$, and K_S), but there may some hidden symmetry. There is also some freedom to choose which basis to use in describing the isobars. In the past [19], the $\pi K K$ system was written in terms of eigenstates of isospin. This was fine in the distant past when isospin was believed to be a good symmetry, but in the present we know that isospin is broken by the differences in up and down quark masses. This difference is small, but easily measurable, for example in the mass difference of $K^*(892)^\pm$ and $K^*(892)^0$, which is 4.4 ± 0.4 MeV/c^2, or about 0.5%. If one does the analysis in the isospin eigenstate basis (which is suited for isospin invariance), this mass difference needs to be inserted by hand in the formula depending on which axis the dynamical amplitude is being calculated. Since isospin invariance is not true, there is no reason to use the isospin eigenstate basis.

In the following steps, we derive the basis states used to describe the $\pi K K$ system. At first, we work in the isospin eigenstate basis, but then show at the end that we can we write the basis in terms of charged and neutral K^* resonances equivalently. Once written in this manner, the mass difference is easier to include in the fitting algorithm. More importantly, the result of the fit gives the amplitudes in terms of charged and neutral K^* contributions, allowing a direct check of charge invariance in the strong reaction of $p\overline{p}$ annihilation which is believed to be charge-blind.

If we expand the intermediate states in table 3.2 with (3.5), (3.6), (3.7) and (3.8) we get the four states $\phi_{I,C}$ where $I = 0, 1$ and $C = +1, -1$. The order of particles listed in the kets is important; the pion and the first kaon decay from the K^* isobar, while the second kaon is a spectator.

$$\phi_{I,C} = \sqrt{\frac{1}{12}} \left\{ \begin{array}{rr} -|\pi^0 K^+ K^-\rangle & +\sqrt{2}|\pi^+ K^0 K^-\rangle \\ -(-1)^I\sqrt{2}|\pi^- K^+ \overline{K^0}\rangle & +(-1)^I|\pi^0 K^0 \overline{K^0}\rangle \\ +C[-|\pi^0 K^- K^+\rangle & -\sqrt{2}|\pi^- \overline{K^0} K^+\rangle \\ +(-1)^I\sqrt{2}|\pi^+ K^- K^0\rangle & +(-1)^I|\pi^0 \overline{K^0} K^0\rangle] \end{array} \right\} \tag{3.11}$$

We can replace the K^0 and $\overline{K^0}$ particles with K_S and K_L. Since we do not observe the K_L nor the π^0, we can simplify the isospin-C-parity $|I,C\rangle$ state expressions by suppressing all terms that are not observed in this analysis:

$$\phi_{I,C} \sim \left\{ \begin{array}{r} +|\pi^+ K_s K^-\rangle \\ -(-1)^I|\pi^- K^+ K_s\rangle \\ +C(-|\pi^- K_s K^+\rangle \\ +(-1)^I|\pi^+ K^- K_s\rangle) \end{array} \right\} \tag{3.12}$$

We note that each term has the same amplitude up to a sign. For $C = +1$, there are two states $I = 0, 1$ or

$$\phi_{0,+} = |\pi^+ K_s K^-\rangle - |\pi^- K^+ K_s\rangle - |\pi^- K_s K^+\rangle + |\pi^+ K^- K_s\rangle$$

$$\phi_{1,+} = |\pi^+ K_s K^-\rangle + |\pi^- K^+ K_s\rangle - |\pi^- K_s K^+\rangle - |\pi^+ K^- K_s\rangle$$

Because each of these states will have an independent production amplitude in the partial wave analysis, we can take linear combinations of these two states and get the same result. Let us take

$$\psi_+ = \phi_{0,+} + \phi_{1,+} = |\pi^+ K_s K^-\rangle - |\pi^- K_s K^+\rangle \tag{3.13}$$

$$\psi_- = \phi_{0,+} - \phi_{1,+} = |\pi^- K^+ K_s\rangle - |\pi^+ K^- K_s\rangle \tag{3.14}$$

We can see in this basis that the ψ_+ state describes $K^{*\pm} \rightarrow \pi^\pm K_s$, and that ψ_- state describes $K^{*0} \rightarrow \pi^\pm K^\mp$. This shows that the amplitude can be separated into two parts which represent the two axes of the Dalitz plot, i.e. the x axis which is $m^2(\pi^\pm K_S)$ and the y axis which is $m^2(\pi^\pm K^\mp)$. This approach is better than previous analyses which fit using the isospin eigenstates, because

1. The data Dalitz plot is obviously not symmetrical

2. The masses of $K^*(892)$ depend on the axis chosen, so isospin is broken anyways.

3. The amplitudes of the charged and uncharged K^* can be fixed to the same magnitude, but keeping individual phases. This can test the hypothesis that the intensities of the charged and uncharged K^* might be the same.

4. The ratio of charged versus neutral components of the $K\pi$ wave can be directly compared.

3.11 Resonances expected in $K_S K^\pm \pi^\pm$

The first experimental results for $K_S K^\pm \pi^\pm$ were published by the Saclay 81 cm bubble chamber collaboration at the CERN PS in May 1965 [20]. From only 1145 events, they noted strong K^* bands at 890 MeV in the $K\pi$ systems, as well as two other enhancements, the $K\overline{K}$ enhancement at threshold and another $K\overline{K}$ enhancement at 1250 MeV. The two $K\bar{K}$ enhancements are known as the $a_0(980)$ and $a_2(1320)$ respectively. We scanned the original data and binned it into a 30x30 histogram, which is shown in figure 8.14.

A later analysis with more statistics from the same bubble chamber (2000 events) attempted a partial wave analysis[19]. In this analysis, they introduced another broad resonance, the so called $K\pi$ S-wave, which they parameterized with a scattering length amplitude. With these four resonances, they were able to adequately fit the data.

There is an interesting asymmetry in the Dalitz plot. If one divides the plot into four sectors defined by the strong $K^*(890)$ bands, the lower-right sector has many more events than the upper-left sector. In addition, the left-end of the horizontal $K^*(890)$ band has much more intensity than the lower-end of the vertical $K^*(890)$ band.

Until the Crystal Barrel, this was the limit of knowledge of the $K_S K^\pm \pi^\pm$ system. The Crystal Barrel published a paper on $K_L K^\pm \pi^\mp$ with much higher statistics (13K)[21]. The fundamental physics behind this reaction, which substitutes a K_L for the K_S, should be the same as for $K_S K^\pm \pi^\pm$. In addition to the bubble-chamber resonances, two extra resonances were need to describe the data, the $a_0(1450)$ (recently discovered by the Crystal Barrel in decays to $\pi^0\eta$) and the $\rho(1450, 1700)$. The $\rho(1450, 1700)$ was characterized by two poles, although in the past it was characterized by one pole, called the $\rho(1600)$. The $K\pi$ S-wave was also improved by using the characterization from the LASS experiment[22].

Two other resonances which may play a part in this reaction are the $K_2^*(1430)$ and $a_2(1660)$. The $K_2^*(1430)$ is a well known resonance in the $K\pi$ system as measured by LASS [22], but because its mass is slightly above the limit of phase space and its spin is high, was not considered previously. The $a_2(1660)$ was used in an analysis of $\pi^0\pi^0\eta$[23], but its significance was not emphasized. The $K_L K^\pm \pi^\mp$ analysis of [21] did not require this resonance.

We discuss the history of all of these resonances in detail below.

3.11.1 $K^*(892)$ resonance

This resonance appears as the dominant vertical and horizontal bands near 0.8 GeV^2 in the dalitz plot. It is the most visually obvious resonance in the reaction.

This resonance is modelled as a relativistic Breit-Wigner,

$$\frac{m_0\Gamma_0/\rho(m_0)}{m_0^2 - m^2 + i m_0 \Gamma_0}.$$

The mass and width of the neutral K^* is $m_0 = 896.10$ MeV and $\Gamma_0 = 50.5$ MeV, while the mass of the charged K^* is $m_0 = 891.59$ MeV and $\Gamma_0 = 49.8$ MeV. The K^* is a vector meson, so its angular distribution appears as $\cos^2\theta$ in the ${}^1S_0$ state, and $\sin^2\theta$ in the ${}^3S_1$ state. Because the intensities of the two initial states are approximately equal, the bands appear flat because the complementary angular distributions cancel to some degree.

3.11.2 $K-\pi$ S wave

The $K\pi$ S-wave is not well understood on theoretical grounds, but is required empirically in all partial wave analyses to date.

The bubble chamber analyses [19] parameterized the S-wave using a scattering length parameterization which rises slowly with increasing mass.

$$\frac{1}{1 - i a_I p_{K\pi}}$$

$a_{1/2} = +0.3 fm$, $a_{3/2} = -0.3 fm$

Later, the LASS collaboration[22] directly extracted the S-wave component from $K-\pi$ scattering, and parameterized it as a sum of an inelastic Breit-Wigner amplitude and a background term parameterized as an effective range. The same data was refit using the K-matrix formalism, with a pole term due to the $K_0^*(1430)$ resonance, and with a background term which describes the additional $K-\pi$ S-Wave component.

$$\hat{K} = \frac{m_0\Gamma_0/\rho(m_0)}{m_0^2 - m^2} + \frac{am}{2 + abq^2} \tag{3.15}$$

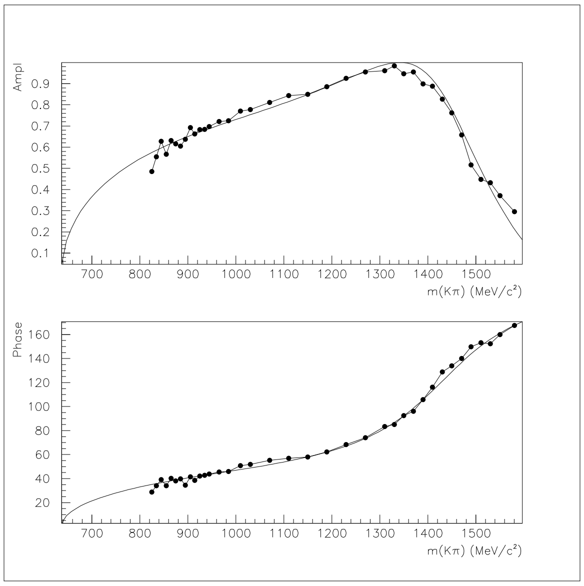

Figure 3.2: The LASS data for $K - \pi$ S-Wave scattering, and the fitted function given by (3.17), (3.16) and (3.15). Shown are magnitude and phase of T.

$m_0 = 1343.0$, $\Gamma_0 = 400.0$, $a = 0.00181$, $b = 0.00258$ (With MeV as units for mass). In the K-matrix formalism, the Lorentz-invariant transition amplitude is given by

$$\hat{T} = (1 - i\hat{K}\rho)^{-1}\hat{K} \tag{3.16}$$

where ρ is the two-body phase space. In the Dalitz plot, the Lorentz-invariant transition amplitude $\hat{T}$ is used rather than the non-relativistic T. The original LASS data and the fitted T function are shown in figure 3.2; in this case, the non-relativistic form T is shown. T is calculated using

$$T = \hat{T}\rho \tag{3.17}$$

and equations (3.15) and (3.16).

In practice, the fit is insensitive to the exact parameterization of the $K\pi$ S-wave because it is so broad; for example, the χ^2 of the fit did not change significantly if the background term was omitted or parameterized as a first-order polynomial with two real coefficients. None of the individual contributions changed much, at least a lot less than the systematic error of the fit, when the background term was removed entirely. For example, the contribution from the $K\pi$ S-wave in $^1S_0$ dropped by only 15%, when the systematic error for this wave is estimated to be somewhere between 25 and 500% (see table 9.1).

3.11.3 $K_2^*(1430)$

The $K_2^*(1403)$ lies significantly outside of the phase space for this annihilation channel. However, because it is a strong resonance, the tails have a significant effect on the Dalitz plot. The LASS experiment has shown that this tensor $K_2^*(1430)$ has roughly twice the intensity of the vector $K^*(892)$ in the $K-\pi$ wave when there is no phase space limitation. See figure 3.3 which shows the large contribution from $K_2^*(1430)$ and the significant Breit-Wigner tail which extends down to at least 1 GeV/c^2. Of course, in the $K_S K^\pm \pi^\pm$ Dalitz plot, there is significant suppression due to phase space and the angular momentum barrier.

The shape of the distribution in the Dalitz plot is somewhat odd, because the central mass lies above the edge of the dalitz plot and because the angular momentum barrier function suppresses the intensity at the edge. The tails that appear in the Dalitz plot do not have the obvious horizontal or vertical ridge that is seen in the $K^*(892)$. Instead, the $^1S_0$ partial wave has diagonal bands caused by the characteristic "W" decay pattern of tensors. Figures 8.4, 8.5 and 8.6 show the unusual resonance patterns of the $K_2^*(1403)$ from different initial states.

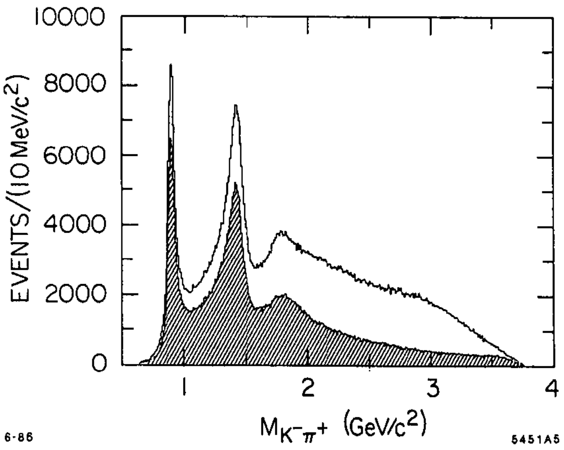

Figure 3.3: The $K^+\pi^-$ invariant mass distribution of events produced from $K\pi$ scattering. The shaded curve represents the effect of removing events from N^* production, which is not important to the discussion here. Figure is reproduced from the LASS experiment[22], Fig. 3.

3.11.4 $a_0(980)$

The $a_0(980)$ is an interesting resonance. It has two primary decay channels,

$$a_0(980) \rightarrow \pi\eta$$

$$a_0(980) \rightarrow K\overline{K}.$$

However, in both channels, the resonance distribution in mass is severely distorted. The distortion in the $K\overline{K}$ channel is due to the fact that the mass of the $a_0(980)$ is at the $K\overline{K}$ threshold, so the decay can not happen at all below the threshold. Due to unitarity and analyticity of the dynamics, the shape of the $K\overline{K}$ amplitude directly influences the shape of the $\pi\eta$ amplitude, giving it a cusp-shape. This phenomenon is explained in the Flatté [24] parameterization of the $a_0(980)$, discussed below. The Flatté shapes are shown in figure 3.4. It is clear that neither the $\pi\eta$ nor $K\overline{K}$ amplitudes can be described by a Breit-Wigner.

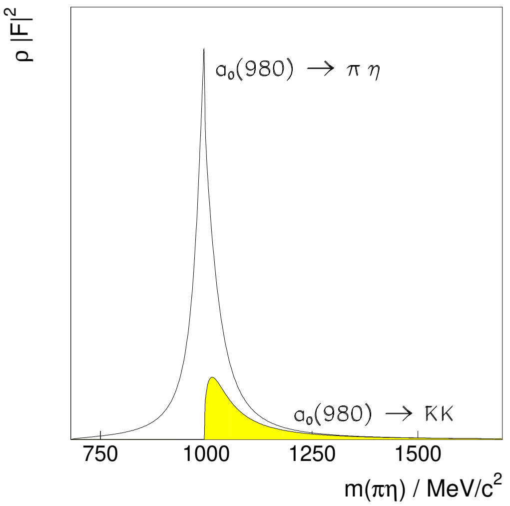

Figure 3.4: Amplitudes $\rho_{\pi\eta}|F_{\pi\eta}|^2$ and $\rho_{K\overline{K}}|F_{K\overline{K}}|^2$ (shared area).

The first bubble chamber analysis[19] parameterized the edge enhancement with a Breit-Wigner with a mass-dependent width

$$\frac{1}{s_{KK} - s_0 + i p_{KK}\gamma}.$$

In the limit of a narrow resonance far from threshold, this width γ may be related to the more classical "constant width" Γ by the relation.

$$\Gamma = p_{KK}\gamma/\sqrt{s_0}$$

This is an approximation to the Flatté distribution, whose width also increases with breakup momentum, p_{KK}.

The actual Flatté distribution is as follows

$$\hat{F}(s) = \frac{g_1}{m_0^2 - m^2 - i(\rho_1 g_1^2 + \rho_2 g_2^2)} \tag{3.18}$$

$$g_1^2 + g_2^2 = m_0\Gamma \tag{3.19}$$

where $g_1 = g_{KK}$ and $g_2 = g_{\eta\pi}$. The details of the Flatté function and the connection to the K-matrix formalism is given in section 8.7.

The phase space terms are

$$\rho_1 = \pm\sqrt{\left(1 - \left(\frac{m_{\pi^\pm} - m_\eta}{m}\right)^2\right)\left(1 - \left(\frac{m_{\pi^\pm} + m_\eta}{m}\right)^2\right)}.$$

$$\rho_2 = \pm\sqrt{\left(1 - \left(\frac{m_{K^\pm} - m_{K^0}}{m}\right)^2\right)\left(1 - \left(\frac{m_{K^\pm} + m_{K^0}}{m}\right)^2\right)}.$$

The phase space signs are taken to be + when calculating the physical resonance, but can take on either sign when calculating on the complex $\sqrt{s}$ plane.

Because of this definition, the total width Γ is about 250 MeV, even though the peak width in the $\pi\eta$ channel is visibly much narrower, about 60 MeV. This has caused lots of confusion in getting a consistent number for the width, as the value is model dependent.

The physical resonance parameters are not the values used in any of the above formulations, but are extracted from the pole positions of the T-matrix of the form

$$E_{pole} = m_0 - i\Gamma/2.$$

Because the Flatté formula involves two phase space quantities (ρ_1 and ρ_2), each which have square-root branch cuts, there are four Riemann sheets in which the poles can be found. The two Breit-Wigner poles are always found on the second and third Riemann sheets (see [25] for a classification of the poles). In the partial wave analysis of this report, we shall cite the relevant pole position to obtain the correct values for the mass and widths

3.11.5 $a_0(1450)$

The assignment of the scalar $q\overline{q}$ nonet to experimentally seen resonances is controversial. Many candidates are available for the $I = 0$ f component, while the historical assignment of the $a_0(980)$ to the $I = 1$ component has been called into question because of evidence that the $a_0(980)$ could be a kaonic molecule or four quark state. Moreover, the mass appears to be lower than expected, assuming that the $K_0^*(1430)$ is the $I = 1/2$ component.

A search for a replacement candidate has yielded some observations in the 1300-1500 range. Boutemeur and Poulet[26] announced at Hadron 89 an isovector scalar meson with mass ~1320 and width 130. In 1994, the Crystal Barrel announced observation[23] of the $a_0(1450)$ with mass $m = (1450 \pm 40)$ MeV and $\Gamma = (270 \pm 40)$ MeV, seen in the $a_0(1450)\to\eta\pi^0$ decay mode in $p\overline{p}\to\pi^0\pi^0\eta$. The reduced χ^2 decreased from 2.1 to 1.3 with $N_{\rm dof} = 1249$. The $a_0(1450)$ is 5% of the Dalitz plot.

A later coupled channel analysis[27] confirmed the $a_0(1450)$ with BR $= (0.29 \pm 0.11) \times 10^{-3}$, $m = 1470 \pm 25$ MeV and $\Gamma = 265 \pm 30$ MeV. A further analysis[28], used $a_0(1450)$ with a 3% contribution and BR$= (0.203 \pm 0.038)^{-3}$, which agrees with the previous coupled analysis. However, the focus of this paper was on the $I = 0$ resonances, not the $a_0(1450)$.

At Hadron 97, the Crystal Barrel announced observation of the $a_0(1450)$'s decay into $K\overline{K}$[21], while the OBELIX collaboration announced observation of an $a_0(1300)$'s decay into $K\overline{K}$[29]. The mass, width and branching ratio parameters of these 2 resonances were *not* compatible. The Crystal Barrel's $a_0(1450)$, with $m = (1480 \pm 30)$ MeV and

$\Gamma = (265 \pm 15)$ MeV, had decay rates into KK that agree with the SU(3) prediction.

In other analyses, inclusion of the $a_0(1450)$ was not incompatible with the data, but not absolutely required. In the $\pi^0\pi^0\eta'$ Dalitz plot[30], the $a_0(1450)$ was needed. However, the contribution could be as small as 1.5 ± 1.2 % and the mass parameters were not well constrained according to the text. In Ehmann's paper, $p\overline{p} \rightarrow \pi^+\pi^-\eta$, and they claim that the $a_0(1450)$ is necessary, but don't give any numbers. In the exotic paper[31], the $a_0(1450)$ was not needed in the fit at all. In truth, the $a_0(1450)$ has only been seen in the $\eta\eta\pi^0$ and $K_L K^\pm \pi^\mp$ Dalitz plots.

Because the parameters of the a_0 are not well determined, we explored the complete parameter space of mass, width and branching ratio for this isovector, scalar resonance, modeling it as a Breit-Wigner resonance. If the mass is indeed above 1300 MeV, the K-matrix formalism is not necessary to describe the distortion from the $a_0(980)$.

3.11.6 $\rho(1450)$ and $\rho(1700)$

The $\rho(1450)$ and $\rho(1700)$ are two "new" resonances which used to be lumped together as the $\rho(1600)$. The $\rho(1700)$ has been seen in its decay into $K\bar{K}$[32], while the $\rho(1450)$ has not[33]. The evidence against the $K\bar{K}$ decay mode of the $\rho(1450)$ is not terribly convincing, because it assumes that the $I = 0$ and $I = 1$ amplitudes are real and positive, which is mostly likely not the case. For example, if the amplitudes were real but relatively negative, there would be evidence for the $K\bar{K}$ decay mode.

The problem with a $\rho(1450)$ is that it has nearly the same mass as the $a_0(1450)$, making it hard to disentangle the two.

3.11.7 $a_2(1660)$

The $a_2(1660)$ was introduced for the first time in a Crystal Barrel analysis on $\pi^0\pi^0\eta$[23]. As stated in the paper,

> We find that the fit ... can be improved by adding a small contribution of a higher mass $\pi^0\eta$ D-wave resonance with a mass of 1600 MeV to 1700 MeV and a width of 180 MeV to 250 MeV. As the contribution of this additional resonance is marginal, (1.0 ± 0.5) %, and localized at the edges of the Dalitz plot where acceptance corrections are relatively more important, we refrain from attaching any physical meaning to this effect.

Recently, the $a_2(1660)$ has aroused more interested in the spectroscopy community, so we attempt to include it in our fits.

3.11.8 $K^*(1410)$

The strange vector $K^*(1410)$ could also be a part of the Dalitz plot, even though its coupling to $K\pi$ is somewhat small. We attempt to include it in our fits.

Chapter 4

Software tools

This chapter discusses the software used in the analysis, including the software written by the author.

4.1 CBLIB - the standard Crystal Barrel Libraries

The standard Crystal Barrel libraries are written in FORTRAN 77 and consist of the following subparts.

1. BCTRAK - Electro-magnetic calorimeter PED reconstruction
2. LOCATER - Jet drift chamber charged track reconstruction
3. GTRACK - "global" tracking, containing results of BCTRAK and LOCATER.
4. CBOFF - The main program containing all the I/O and reconstruction steering.
5. and other minor components.

4.2 CBDISP - The Event Display

The event display for the experiment was originally written by Klaus Peters, but it suffered from numerous bugs and crashes, lack of features and a difficult command line user interface. The FORTRAN part of the code was for the most part rewritten in 1993 to fix bugs and add features[34]. Some of these new features include

1. Mouse driven menu system
2. Arbitrary zoom of detector parts
3. Display of raw JDC wire signals
4. Postscript printing of pictures
5. Correct Geometrical display of crystals
6. Correct Geometrical display of helix tracks and vertex fits
7. Informative displays of reconstructed tracks and photons

In addition to the rewritten FORTRAN engine, a user friendly graphical user interface called `xcbdisp` was written in Tcl/Tk[35]. This is shown in figure 4.1. It allows easy customization of the views, easy access to view presets, easy navigation from event to event, and views of the reconstructed tracks and photon parameters.

The improved event display was installed on the μVAX in the Crystal Barrel control room in 1993, and the Tcl/Tk interface (which ran on a separate DEC work station) was installed in 1995. This greatly aided in online monitoring the data quality.

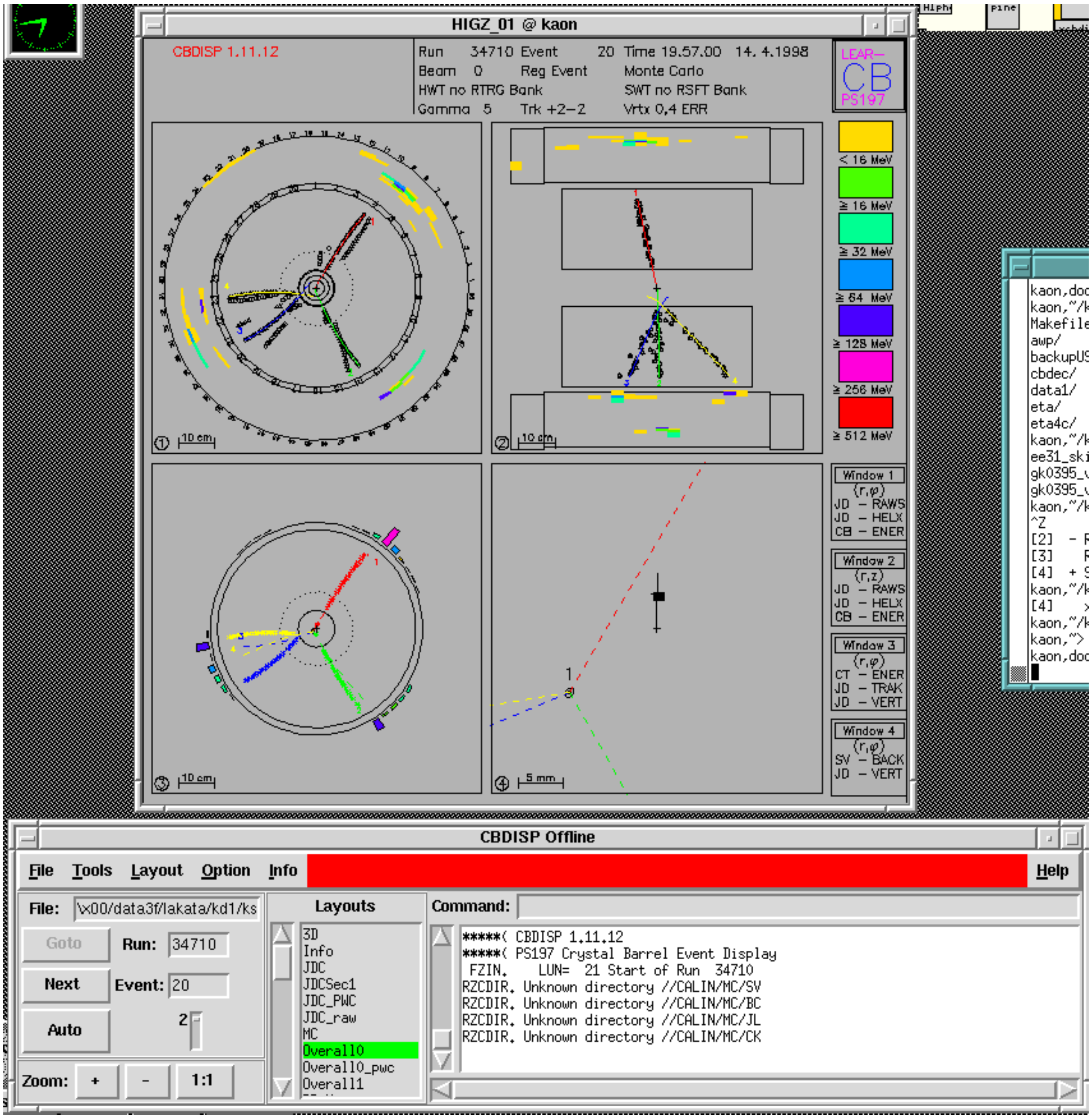

Figure 4.1: The Tcl/Tk interface to the Crystal Barrel Event display (CBDISP).

4.3 `cblbl++`

A C++ class library was written by the Uni-Bochum group to wrap all of the FORTRAN code in a C++ interface. However, with the advent of the CLHEP standard C++ class library for High Energy Physics, much of the code needed to be rewritten to take advantage of the better list handling classes, better interface to HBOOK, as well as improving the data I/O classes. Further more, wrappers for charged data did not exist and needed to be written. This rewritten class is now known as `cblbl++`.

A detailed description of the software is omitted here, because most of it concerns technical details of data management, i.e. pointer juggling or simple 4-vector arithmetic. One of the interesting classes that is part of `cblbl++` is `KinFit`, the general purpose kinematic fitter. This is described below.

4.4 Vertex Fit

The section summarizes the operation of the vertex fit which was specially written for this analysis. The details are given in a technical report[36].

4.4.1 Introduction

There are two components in making a proper multi-vertex fit to an event. First is determining the track-to-vertex topology, and second is constraining the tracks to the measured JDC hits.

The Crystal Barrel was designed primarily for detection of neutral particles, a task that was nearly impossible in the 1960's bubble chamber experiments, especially if there was more than one neutral particle. In most cases, resonances or other intermediates decay via strong or electro-magnetic forces, meaning that the lifetimes are very short ($t << 10^{-15}$ s). The distance such a particle can move in such a short time is only a few nanometers or less, which is entirely undetectable in a drift chamber or vertex detector which have resolutions of 0.1 to 1 mm in the Crystal Barrel. It appears that all charged tracks and nearly all neutral photons originate from the same spot, the $p\overline{p}$ annihilation point.

Thus the old vertex fit algorithm simply assigned all tracks to one vertex. For computational simplicity, the fit did not constrain the tracks to lie on the "hit" positions. It simply took the results from the helix fit, which did constrain the tracks to the hit positions, and adjusted the helix parameters via an iterative algorithm so that they all passed through a common point in space. In practice, this was a reasonable thing to do for 2-track events with long tracks. However, for short tracks in 4-track events, the fit tended to severely rotate tracks around to force a single vertex. These rotated tracks no longer intersected the measured hits; in some cases the rotation was as large as 90 degrees, totally changing the true direction vector of the track. In addition, vertices separated by less than 1 cm would be incorrectly merged into a single vertex if the helix constraints were "soft".

In the unique case of $K_S \rightarrow \pi^+\pi^-$, the K_S travels a few cm before decaying. This distance is easily measurable in the Crystal Barrel, and creates a distinct second vertex. A new vertex fit algorithm was thus needed for two reasons. First, this analysis required a vertex fit that can determine two (or more) simultaneous vertices, which became the "`TCVER3`" routine. Second, because the distance between vertices can be small (down to 1.2 cm), the vertex fit had to be constrained by the original JDC hits, not just the reconstructed

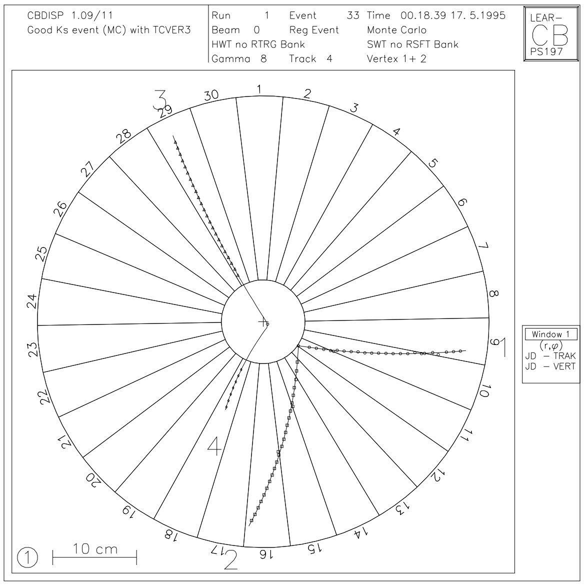

Figure 4.2: An example of a good (2,2) fit to Monte Carlo data

helices. This routine was called "`TCVRHX`". If not, the vertex fit could force true disjoint vertices into a single incorrect vertex. An example of a good fit is shown in figur4.2.

4.4.2 TCVRHX

The new vertex fit code `TCVRHX` implemented a new track-to-hit fitting algorithm, based on the helix fitting code. The geometry of the detector is a cylinder on the $\hat{z}$ axis, with $+z$ the direction of momentum of the incoming $\bar{p}$ beam. The 1.5T magnetic field points in the $-z$ direction (something that wasn't discovered until the second year of running). The tracks bend in the (x, y) plane, which is defined with $+y$ as vertically up (opposing gravity) and $+x$ is defined through the right-hand rule. In the helix fitting code, each set of hits was fit to a parametric curve of 5 parameters: curvature ($\alpha \sim 1/P_{\perp}$), center of circle in cylindrical coordinates (r_0,ψ_0) , pitch ($\tan\lambda$), and offset in beam direction z_0. This resulted

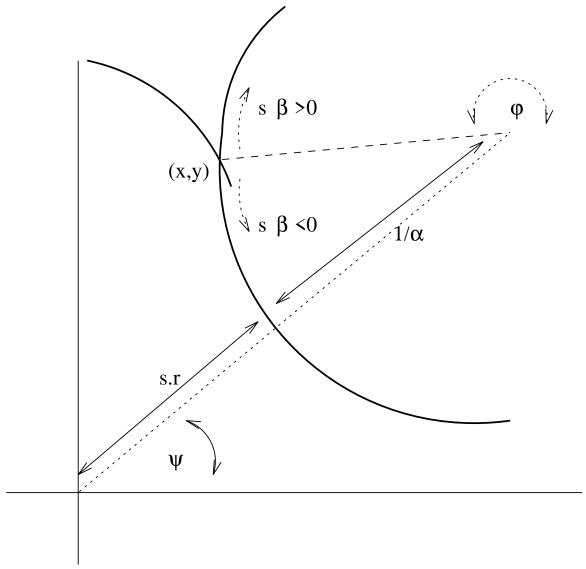

Figure 4.3: The parameterization of the TCVRHX vertex fit.

in 20 parameters for a 4-track event. In the TCVRHX fitter, tracks were parameterized as coming from a vertex in space (x, y, z) and then moving with a curvature, azimuth (ϕ_0) and pitch $(\tan\lambda)$ (see figure 4.3). Because tracks share vertices, this results in 18 parameters for an event with two vertices with two tracks each, or 15 parameters for a single vertex with four tracks. This method of finding the vertex is superior in finding the true position of the vertex, especially when used with the fine precision of a vertex detector which highly constrain the path of the helices. It is better in distinguishing closely spaced vertices, and the momentum resolution is comparable to the old vertex fit routine.

4.4.3 TCVER3

As a companion to the actually fitting code, a new topology generator and selector was written (TCVER3). This routine generates all vertex topologies that are possible from all the tracks of an event. Topologies are written in the following notation:

$$(n_1, n_2, \ldots n_m)$$

where m is the number of vertices and n_i is the track multiplicity of the i^{th} vertex. The n_i are sorted in decreasing order. A track that appears to come from "nowhere" is assigned a vertex multiplicity of 1 and the vertex position is the closest approach to the z-axis. For two-track events, there are only 2 topologies: either the tracks come from a common vertex (2) or they don't $(1, 1)$. For three-tracks, there are 3 topologies $(1, 1, 1)$, $3 \times (2, 1)$ or (3), where there are 3 permutations of the $(2, 1)$ topology. For four tracks, there are $(1, 1, 1, 1)$, $6 \times (2, 1, 1)$, $3 \times (2, 2)$ $4 \times (3, 1)$ and (4). See figure 4.4 for a schematic of common topologies for 4 tracks.

The algorithm for finding the "best" topology was designed to be robust and independent on the original order of the tracks. The routine starts by assigning each track to a null vertex. It then forces pairwise sets of vertices together and calls the track fitter. The best pairwise combination of all pairwise combinations is kept, if the χ^2 is below a threshold. This process is continued until no vertices can be compared together than would result in a χ^2 below the threshold. The result of this algorithm is to return the topology with the smallest number of vertices. In order to eliminate some combinations, the user can require that 2-track vertices have zero net charge.

The vertex fit uses the reduced χ^2/N_{df} to determine whether a fit is good or not. Using data with 4 golden long tracks, it was determined that a cut off of $\chi^2/N_{df} < 1.8$ was a good discriminator between the (4) and (2,2) topologies. For $N_{df} \approx 40$, this cut should accept more than 99% of good events. This value was varied to see its effect on the

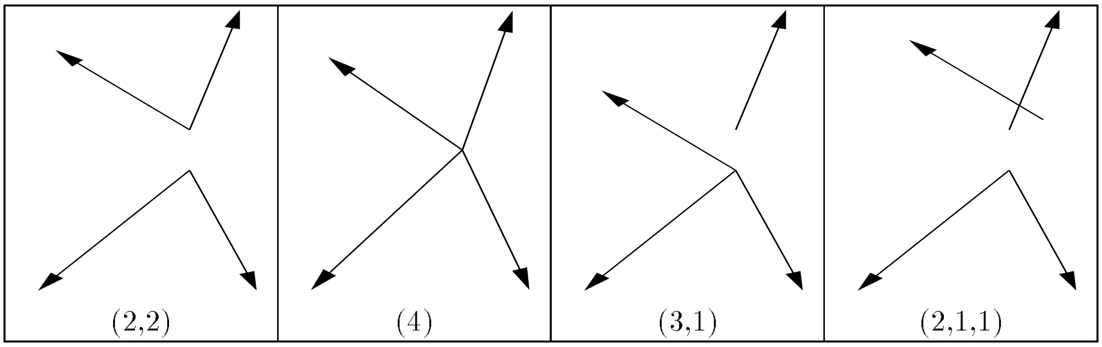

Figure 4.4: Common event topologies. See text for notation

$K_S K^{\pm}\pi^{\pm}$ MC. A higher cut off of 3.0 increased the number of accepted (22) events by 5%. This small increase in statistics was not deemed significant enough to merit using 3.0 as the cut off instead of 1.8, since the vertex fit quality of the additionally accepted events was worse.

Additional "outlier" rejection is applied to hits in the vertex fit. In earlier processing, outliers are tagged by assigning an enormous error to it, thereby "effectively" removing the influence of the hit from the fit. However, leaving these outliers in the fit makes the χ^2/N calculation incorrect because N remains the same but χ^2 decreases. Thus these hits are discarded in `TCVRHX`. If the number of "good" hits drops below 10, then the entire track is discarded. This can cause an event with 4-long tracks on input to have only 3 (or less) tracks on output of the vertex fit.

4.4.4 Hit Error Scaling

The vertex fit used the χ^2 value to determine the goodness of fit. A χ^2 calculation depends directly on the estimated errors of the measured values. In this case, the estimated errors are the measurement errors of the JDC hits, measured in two dimensions: the azimuthal ϕ position which is a direct function of the drift time, and the z position which is a function of the charge division measurement. The third position measurement, the radial position of the hit, is a function of the fixed geometry of the JDC fields, and thus does not have significant error compared to the other two measurements. In addition to the small error, because the tracks are mostly radially, the additional constraint on the helical track due to a radial position measurement is minimal. Thus the χ^2 is due only to the ϕ and z errors and not the ρ errors.

The fast Monte Carlo simulation does not simulate the true physics of the ionization due to the track, for example tracking delta electrons, but simply assigns a drift time and z position to the hit. These values are then smeared additionally by a Gaussian to mimic the true data.

Even with this additional smearing, the Monte Carlo is still "too good" compared to the data. To get consistent results, the error estimates of the hits need to be scaled differently so that the final χ^2 distributions take the proper mean. The error scalings S which scale the errors as

$$\sigma_x' = S\sigma_x$$

are given in table 4.1, and the resultant pulls

$$p = \frac{x - \overline{x}}{\sqrt{\sigma^2(x) - \sigma^2(\overline{x})}}$$

are shown in figures 4.5 and 4.6. The pulls as a function of layer number (or equivalently radius) are fairly constant except for the first and last layers. The gap at the 6th layer is due to a missing layer in the JDC.

The pull distributions for Monte Carlo and data are shown in figures 4.5 and 4.6.

Data Type	$S(\sigma_\phi)$	$S(\sigma_z)$
Monte Carlo	0.720	0.840
Real Data	0.952	0.936

Table 4.1: The error scalings applied to the hit errors of real data and Monte Carlo

The pulls are reasonably Gaussian, with no significant mean shift. The ϕ pull distribution deviates from Gaussian slightly, but is satisfactory for this analysis. The width of the z pull distribution is consistent with unity, while the width of the ϕ pull distribution is a little two narrow, and the resultant confidence level distributions are likewise peaked towards high confidence levels. To smooth out this effect which is a result of experimental errors being estimated too large, the experiment errors of the ϕ position are scaled. This results in a flat confidence level for the χ^2 of the individual hits (with 2 degrees of freedom). The scalings for Monte Carlo and data are given in table 4.1. The global scaling is applied to all other scalings.

The reconstruction accuracy is shown in figure 4.8 where the vertices V0 and V1 of Monte Carlo generated events are plotted. The differences to the reconstructed vertices are shown as short line segments. The majority of vertices are correctly reconstructed. The errors are well described by the statistical fitting errors and a the variation induced by multiple scattering between the JDC and the target. The pulls for the kinematic fit, which depends on the 3×3 error matrix of the momentum for each track, are shown in figure 5.14.

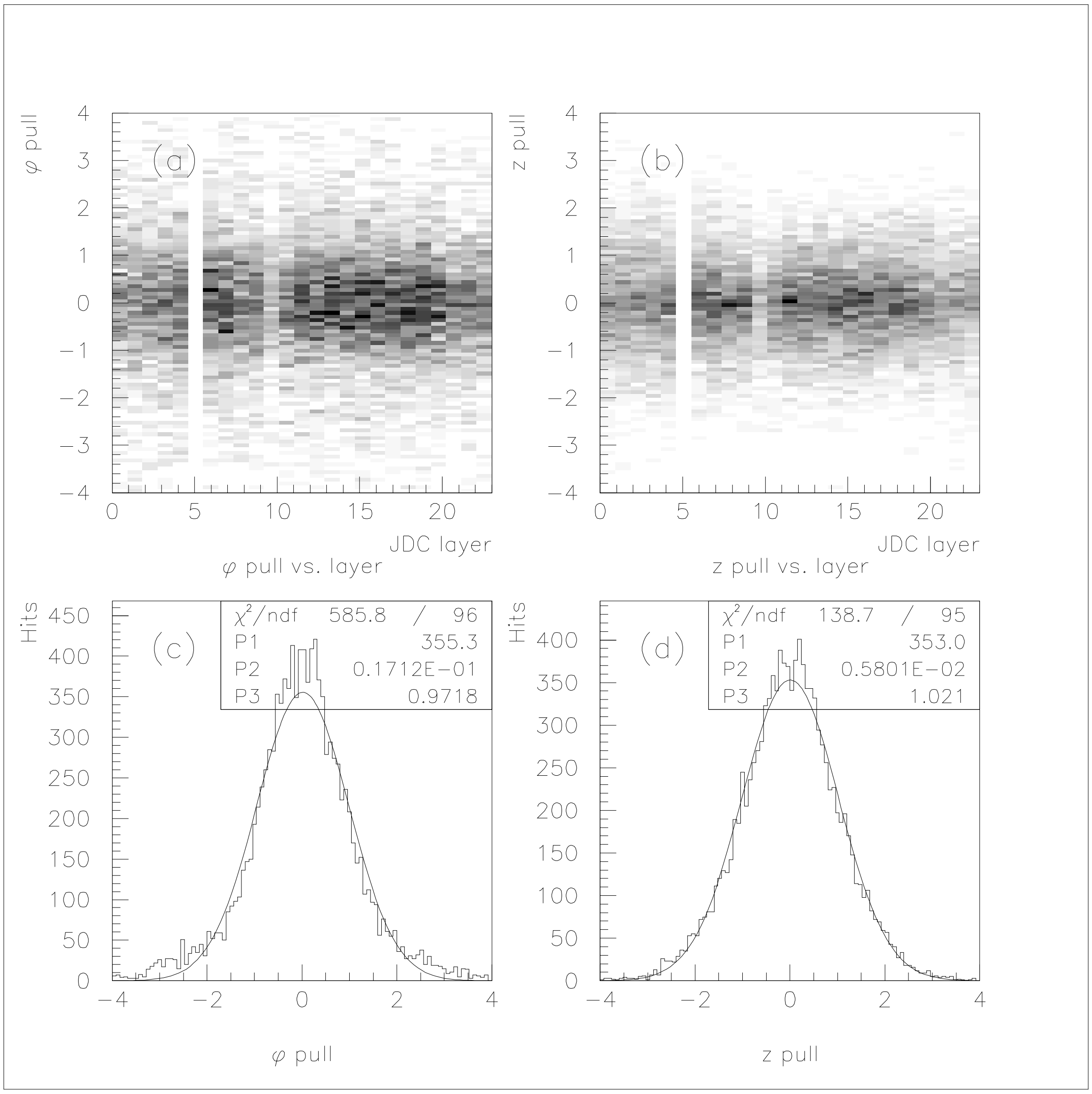

Figure 4.5: Vertex fit pulls for MC. (a) The ϕ pull versus layer number, (b) The z pull versus layer number, (c) The ϕ pull with superimposed Gaussian fit, (d) The z pull with superimposed Gaussian fit

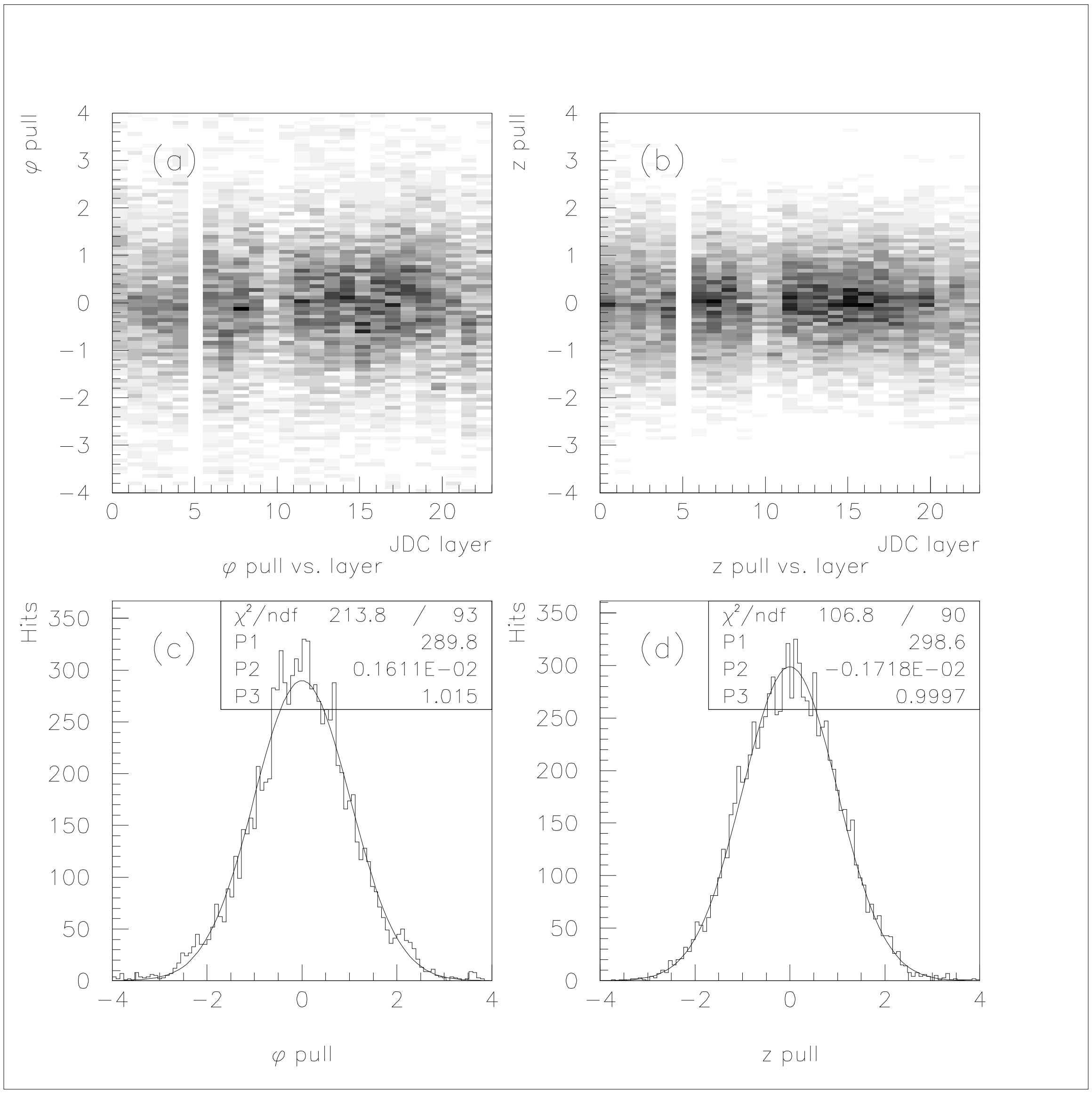

Figure 4.6: Vertex fit pulls for real data. (a) The ϕ pull versus layer number, (b) The z pull versus layer number, (c) The ϕ pull with superimposed Gaussian fit, (d) The z pull with superimposed Gaussian fit

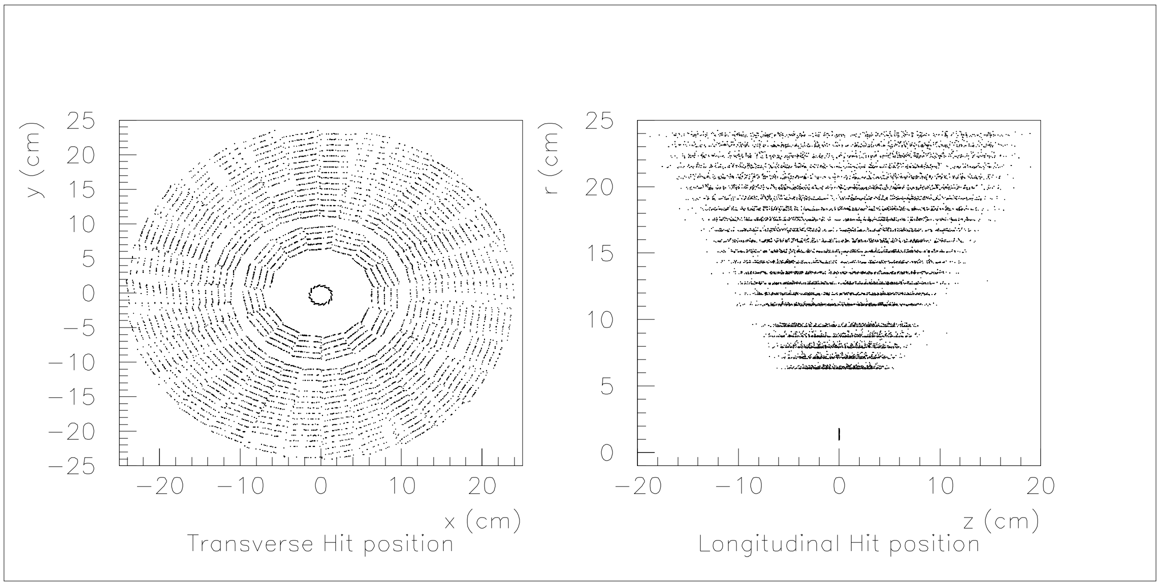

Figure 4.7: The position of the hits used in the vertex fit. (a) the $\phi - \rho$ projection. The gap at $\rho = 10$ cm is due to the missing 6th layer in the JDC, while the small ring at the center is due to the SVX. (b) the $z - \rho$ projection. The vertical line at the bottom is due to the SVX which has no z resolution.

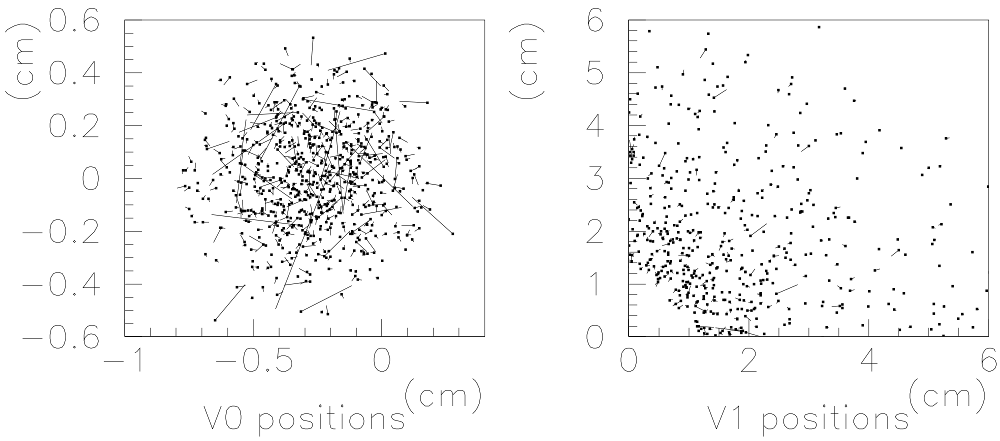

Figure 4.8: The reconstruction accuracy of the vertex fit. The Monte Carlo generated vertices as small squares and connecting line is drawn to the reconstructed vertex position. Note the difference in scale for the two plots of the V0 and V1 vertices, and that only one quadrant of the detector is shown for V1.

4.5 `KinFit` - General Kinematic Fitter

One of the new classes of `cblbl++` is `KinFit` which is a general kinematic fitting algorithm. A kinematic fit is a technique where the measured particle 4-momenta are improved by applying constraints to ensembles of the momenta and varying the momenta slightly to satisfy these constraints. Typical constraints include

1. the total energy of an ensemble of particles
2. the total momentum of an ensemble of particles, either in magnitude or in each spatial component.
3. invariant mass of an ensemble of particles

There are two other uses of the kinematic fit besides improving momenta. The first is to do $\pi^{\pm}/K^{\pm}$ particle ID on an unidentified charged track. Because the $\pi^{\pm}$ and the $K^{\pm}$ have different masses, the total energy of a set of tracks depends on the identification of the track as a $\pi^{\pm}$ or $K^{\pm}$. By testing both hypotheses in a kinematic fit and looking for the lower χ^2 or higher confidence level, the identity of the tracks can be determined usually, unless the momenta of the two tracks are the same. We do not use the kinematic fit for the actual particle identification (this is done by dE/dx), but for particle identification validation.

The second use of a kinematic fit is to test the hypothesis of one or more missing particles. For example, a soft $\pi^0 \to \gamma\gamma$ could escape the detector through the end gaps. A kinematic fit of an event with a lost particle will typically be much worse than of an event with all particles seen.

For $p\overline{p}$ annihilations at rest, the total energy and momentum components are known. They are $E = 1876$ MeV and $\vec{p} = 0$. Typical invariant mass constraints are applied to gamma-gamma pairs to constrain the mass to the π^0 mass (139 MeV) or η mass (547 MeV). Another mass constraint is applied to $\pi^+\pi^-$ or $\pi^0\pi^0$ pairs to the K_S mass (497 MeV). In the case of the later pair, where the $\pi^0 \rightarrow \gamma\gamma$, two levels of mass constraints can be imposed.

In `KinFit`, one constructs a hypothesis using the `Particle` class. The annihilation ensemble is assigned to a pseudo-root particle called "pbarp" with mass of 1876.54 MeV. This root particle then decays into two or more daughter `Particle`s, which can further decay if necessary. Then, each data event is constrained to this hypothesis, with a χ^2 calculated based on the following constraint equations f:

$$\Sigma_\alpha p_i^\alpha - p_i^{tot} = f_i = 0 \tag{4.1}$$

$$\frac{m_\beta^2 - m_{0\beta}^2}{2m_{0\beta}} = f_\beta = 0 \tag{4.2}$$

where α runs over all final-state particles (the leaves at the end of the decay tree), i is x, y or z, β runs over the mass constraints of intermediate particles, m_β and $m_{0\beta}$ are the measured and correct invariant masses, respectively, of the β intermediate particle. In this analysis, there are four measured tracks, so four terms in the momentum sum. Also, there is one mass constraint on the $K_S \rightarrow \pi^+\pi^-$ decay, where $m_{0\beta} = 497$ MeV$/c^2$ for the $\pi^+\pi^-$ pair.

The details of the fit algorithm are given in appendix A.1.

4.6 `awp` - Partial Wave Analysis

The software for the partial wave analysis was called `awp` (a reversal of the acronym for what it does). It originally began as a program written in FORTRAN, and then translated by hand into C++. Unfortunately, the translation was impenetrable gibberish, and did not take into any of the features of object oriented programming. In an effort to understand all of the details of the partial wave analysis, the entire program was rewritten from scratch using C++ objects.

The theoretical physics details are given in the partial wave analysis, chapter 8. Here we describe the software interface. The input file outlines the structure of the partial waves for each Dalitz plot. The form is given here abstractly:

```
PWA {
  ResonanceDefinition
  ResonanceDefinition
  ResonanceDefinition
  ...

  DalitzPlot {
    InitialState {
      FinalState {
        ResonanceProduction
        ResonanceProduction
        ...
      }
      FinalState
      ...
    }
    InitialState
    ...
  }
  DalitzPlot
  ...
}
```

The program first reads all external histograms into memory, and then calculates the spin-parity functions for each bin for each initial state and final state. These values are cached. Then control is given to MINUIT[37], which calls `awp` to numerically calculate the second derivative matrix of the log-likelihood, and then varies the parameters in order to minimize the negative log-likelihood. The source code is attached in the enclosed CDROM.

Some of the features are

1. Free or constrain an overall fudge function of arbitrary polynomial order. This feature is used to take care of any discrepancies between the Monte Carlo and real data.

2. Ability to set two or more production amplitudes to the same value. This is used to constrain the two $K\pi$ axes to the same production strength.

3. Ability to constrain the percentage of each of the different initial states, for example constraining P-wave annihilation to 10% of the total Dalitz plot.

The textual output of the program is in the same format as the input, so the output can be slightly edited and then resubmitted to the program. The histograms are outputted in a private format, and printed using a custom program that generates the postscript directly, to avoid using any of the CERNLIB libraries.

Chapter 5

Overview of Data Selection

This chapter reports on the steps taken in the data collection and data reduction. We discuss the online trigger, the event reconstruction, and the four stages of processing from the raw data to the final Dalitz plot. Table 5.1 gives the event statistics at the end of each stage.

Stage	Description	Events	rel. fraction
0	Trigger	9,448,575	–
1	K_S skim	2,300,360	24 %
2	Energy/Momentum	287,400	12 %
3	Vertex reconstruction	118,372	42 %
4	Particle ID and Kinematic Fit	57,099	48 %

Table 5.1: An overview of the statistics at each processing stage

5.1 K_S Trigger

The general trigger system is discussed in the detector chapter. Here we give a description of the specific K_S trigger.

A K_S decays into $\pi^+\pi^-$ with a branching ratio of 69%. In this reaction, $K_S K^{\pm}\pi^{\mp}$, the $K^{\pm}\pi^{\mp}$ tracks originate from the original annihilation point, forming a 2-prong vertex there. The $K_S \rightarrow \pi^+\pi^-$ forms a second vertex at a typical radius given by $c\tau = 2.6762$ cm. The momentum-dependent mean path length of a decaying particle is given as

$$d = \tau \frac{p}{m}$$

where τ is the particle's rest frame lifetime, p is the particle's momentum and m is the particle's mass. This formula takes into account the effects of velocity ($\beta = p/E$) and the relativistic time-dilation ($\gamma = E/m$). Because the detector is in a cylindrical configuration, the crucial distribution is in $r_{\perp}$, which is shown in figure 5.1. This is not a pure exponential decay distribution, because the proper time (lifetime in the K_S rest frame) is momentum dependent. However, a plot of the proper time would also not be a pure exponential, because of the radial cut imposed by the SVX.

The Silicon Vertex Detector (SVX) was used as the main tool for determining the K_S vertex, because of its close proximity to the annihilation point. It sits at radius 1.2 cm, which is just slightly larger than the liquid hydrogen target. A K_S that decays outside of the SVX will leave no signal, while other tracks originating from the annihilation vertex will leave a hit in the SVX with high probability.

The trigger was run with two independent configurations. If the criteria of either configuration were met, the event was written to tape. The first configuration was designed

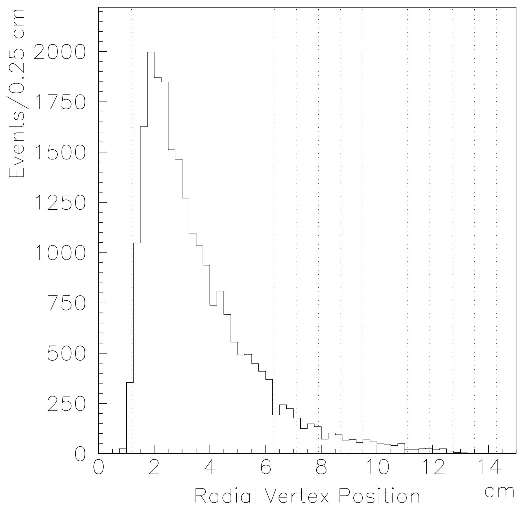

Figure 5.1: The distribution of radial ($r = \sqrt{x^2 + y^2}$) positions of the K_S decay vertex. The vertical lines indicate the radial positions of the SVX and the first 10 layers of the JDC.

to trigger on events with one or more K_S's outside of the SVX and no other tracks, and was named "0→2" meaning 0 charged tracks inside the SVX and 2 (or more) charged tracks outside the SVX. The 0→2 trigger would select events of the type

$$\begin{array}{ll} p\overline{p}\rightarrow K_S K_L \pi^0 & p\overline{p}\rightarrow K_S {K_S}^n \pi^0 \\ p\overline{p}\rightarrow K_S K_L \pi^0\pi^0 & p\overline{p}\rightarrow K_S {K_S}^n \pi^0\pi^0 \end{array}$$

where ${K_S}^n$ indicates the K_S in its neutral decay mode, $K_S\rightarrow\pi^0\pi^0$.

The second configuration was designed to trigger on events with one or more K_S's outside of the SVX and either 1 or 2 tracks inside the SVX, and was named "2→4" meaning 2 (or one) charged tracks inside the SVX and 4 (or more) charged tracks outside the SVX. The 2→4 trigger would select events of the type

$$\begin{array}{ll} p\overline{p}\rightarrow K_S K^\pm \pi^\mp & p\overline{p}\rightarrow K_S K_S \pi^0 \\ p\overline{p}\rightarrow K_S K^\pm \pi^\mp \pi^0 & p\overline{p}\rightarrow K_S K_S \pi^0\pi^0 \\ p\overline{p}\rightarrow K_S K_L \pi^\pm\pi^\mp & p\overline{p}\rightarrow K_S {K_S}^n \pi^\pm\pi^\mp \end{array}$$

The reaction of this thesis is the first one listed in the later configuration.

The hardware trigger consists of a set of discriminators hooked to the signal outputs of the SVX and JDC. The SVX has a fine-grained front side, with 128 wires spaced a few hundred microns apart. However, the readout is too slow for a fast trigger, so instead the back side of the SVX is used for triggering. The backside is simply the common current drain, so it acts as a logical OR of all 128 front-side wires. The JDC sense wires are readout by flash ADC's whose analogue output is discriminated by the trigger system.

The hardware trigger consists of a system of programmable logic units (PLU's) connected to multiplicity counters. The multiplicity counters work by analogue summing of the discriminated signal of all 30 JDC sectors of a particular layer. The sum is digitized and converted to a integral value for the PLU's. The PLU's output goes high when the integer count on its input lie between two predefined values.

The specific trigger condition for the 0→2 trigger was exactly 0 hits in the backplanes of the SVX, and 2 or 3 hits in each of JDC layers 19 and 20. The specific trigger condition for the 2→4 trigger was exactly 1 or 2 hits in the backplanes of the SVX, and 3 or 4 hits in each of JDC layers 9 and 10, and exactly 4 hits in each of JDC layers 19 and 20. These two conditions were part of trigger `ksh44_v2`.

During the run, it was decided to modify `ksh44_v2` slightly by adding a third condition. The SVX backplanes overlap significantly in order to make up for the fact that the pitch of the planes opens gaps between them. However if a particle moves purely radially, it can travel through two backplanes in the overlap region, and this would cause an increase in backplane multiplicity. To recover these events that would otherwise be rejected by the 2→4 trigger, a third condition allowed three backplane hits, as long as there was also a signal in the front-plane in the overlap region, which was about 13 wires wide. This revised trigger was named `ksh44_v3`.

Data taking occurred during the April 1996 run period at the LEAR ring at CERN, from April 13 to May 6. In addition to the `ksh44_v2` and `ksh44_v3` triggers, 4-prong and minimum bias triggers were also taken, for absolute rate calculations and efficiency corrections. This data was recorded on 26 Digital Linear Tapes (DLT's) with 10 GB of data on each. These were copied and brought to Berkeley for further processing.

5.2 Reconstruction and Skimming Stage

The first stage of processing is reconstruction, followed by cuts to reject events that probably do not contain useful information, resulting in a summary data set of good K_S candidates. Reconstruction is the process of decoding the raw data and extracting the momenta of the measured particles, which is described in the detector chapter 1.13. This data processing stage is the most CPU intensive because it involves the full data set and the charged tracking algorithm (Fast Fuzzy Radon) requires a lot of calculations. The cuts used to remove poor events are described below.

5.2.1 Reconstruction Performance

Some distributions of important event parameters, including the number of reconstructed tracks (all tracks, just long tracks and the charges of the tracks), the total energy and momentum of the event, and the momenta of all charged particles and of all photons, are given in figure 5.2. The sharp peaks in the track multiplicities are at four, which is exactly what was expected coming from the trigger. Most of the events contain two positive and two negative tracks. Most of the tracks are fully contained by the detector as evidenced by the peak in the momentum vs energy plot (see figure 5.2 (d)) which peaks at near zero momentum and around 1900 MeV energy, exactly that expected from $p\overline{p}$ annihilation. The charged track momenta peak at 200 MeV, while photon energy peaks at the lower reconstruction threshold. This is to be expected because by selecting 4 charged tracks, there is little phase space left for any neutral particles.

The invariant mass and opening angle of pairs of $\pi^+\pi^-$ are shown in figure 5.3. A peak is clearly seen at the K_S mass of 497 MeV (figure 5.3 (a)). There is also are large broad combinatorial background, as well as a large spike at $2m_\pi$. This spike is correlated to the spike in the angular distribution (figure 5.3 (b)) at $\cos(\theta) = 1$. These events are gamma conversions, $\gamma \rightarrow e^+e^-$, that occur on the JDC field and sense wires or on the inner wall. This background is easily removed at a later stage.

The stability of the data is good over the 3 week period that the data was taken, as seen in the many faces of figure 5.4. Figure (a) shows the number of $2 \rightarrow 4$ triggered events per run; the large step near run 35800 is a result of the trigger definition change. The gaps are simply runs that were not taken with the trigger.

In Figures (b),(c),(e), and (f), one can see a slight hiccup in trend (up for energy and momentum (b,c), down for efficiencies (e,f)) which is most likely due to variations in the barometric pressure at the experiment. Because the JDC is very fragile, the Isobutane/CO_2 gas within is held at atmospheric pressure. Most of this variation is corrected by the reconstruction software, which takes into account the pressure. The momentum accuracy

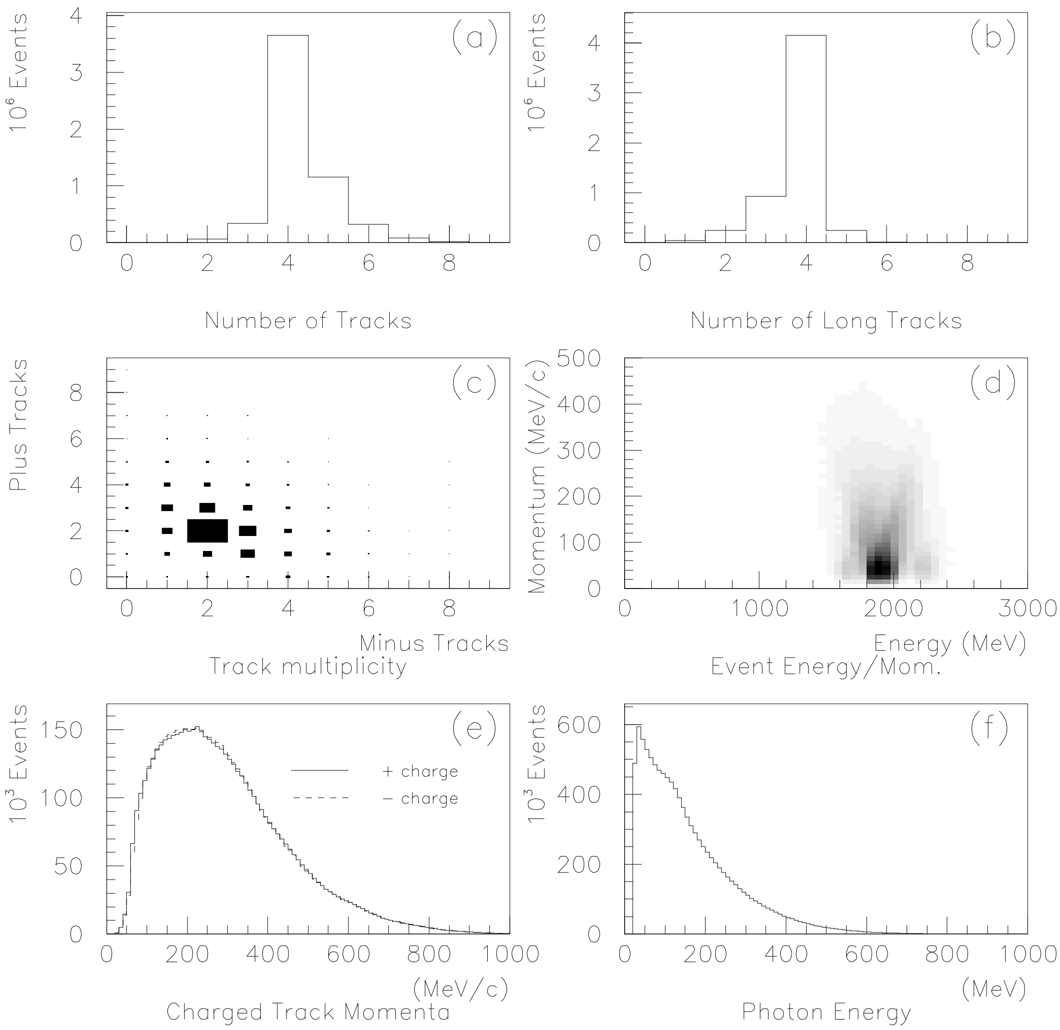

Figure 5.2: Various distributions of important event parameters of the triggered data

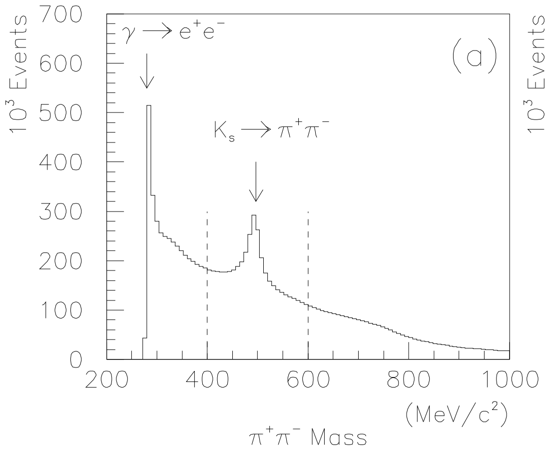

Figure 5.3: (a) The invariant mass of all $\pi^+\pi^-$ pairs. (b) The opening angle of all $\pi^+\pi^-$ pairs.

is corrected to greater degree than the absolute acceptance.

In figures (d,e,f), the relative efficiencies of the first selection criteria are shown. The change in efficiency in (d) is due to the change of trigger, which shows that the data was positively enriched by the change, which was intended.

In figures (g,i), one can see a spike near Run 35450 in the number of hits per track and the dE/dx values. We determined that this spike was caused by a faulty gas flow meter or pressure gauge. At the time of the spike, the ratio of CO_2 to isobutane dramatically increased. The problem was resolved during the periodic inspection during data taking, but it took much longer for the gas mixture to readjust to the proper ratio. When the CO_2 level increases, the gain of the JDC increases, resulting in bigger signals (leading to bigger measured dE/dx values) and more hits being seen. The dE/dx values were corrected later on, described in section 5.5.

In figures (j,k,m,n), the first and last layer of hits of a track are seen, and these are in good condition. There is a small gap in the "first layer" histogram (fig k), which is caused by a slight misalignment between in the inner and outer sections of the JDC, but this is not a major problem. Note that fig (j) shows the *average* first layer of all tracks in a run; the average is higher than "1" as can be seen in (k). For the purpose of stability checks, figures (j,m) are nicely stable. In figures (l,o), the number of low momentum and high momentum tracks per event are stable.

5.2.2 Skimming cuts

1. **2→4 selection.** Because the data contains two triggers (0→2 and 2→4), the first step is to extract the desired trigger (2→4) and only process those events. This is to save some reconstruction time since 33% of the data is the 0→2 trigger.

2. **Exactly 4 Long tracks.** This cut requires exactly long tracks (with at least 10 hits) and exactly no short tracks (with no more than 9 hits).

   From previous experience with reconstructed charged tracks, tracks need at least 10 hits to have a reasonable reconstruction accuracy, even though the helix fit only requires 5 hits. Requiring long tracks of untriggered data typically reduces the solid angle acceptance, since polar-directed tracks can not hit many layers before exiting the JDC. However, the long track condition was already part of the trigger specification, so this cut does not reduce the statistics greatly.

   Many events have "splash-back" tracks which typically originate from interactions of hadrons with the crystals. These junk tracks are not part of the desired physics and

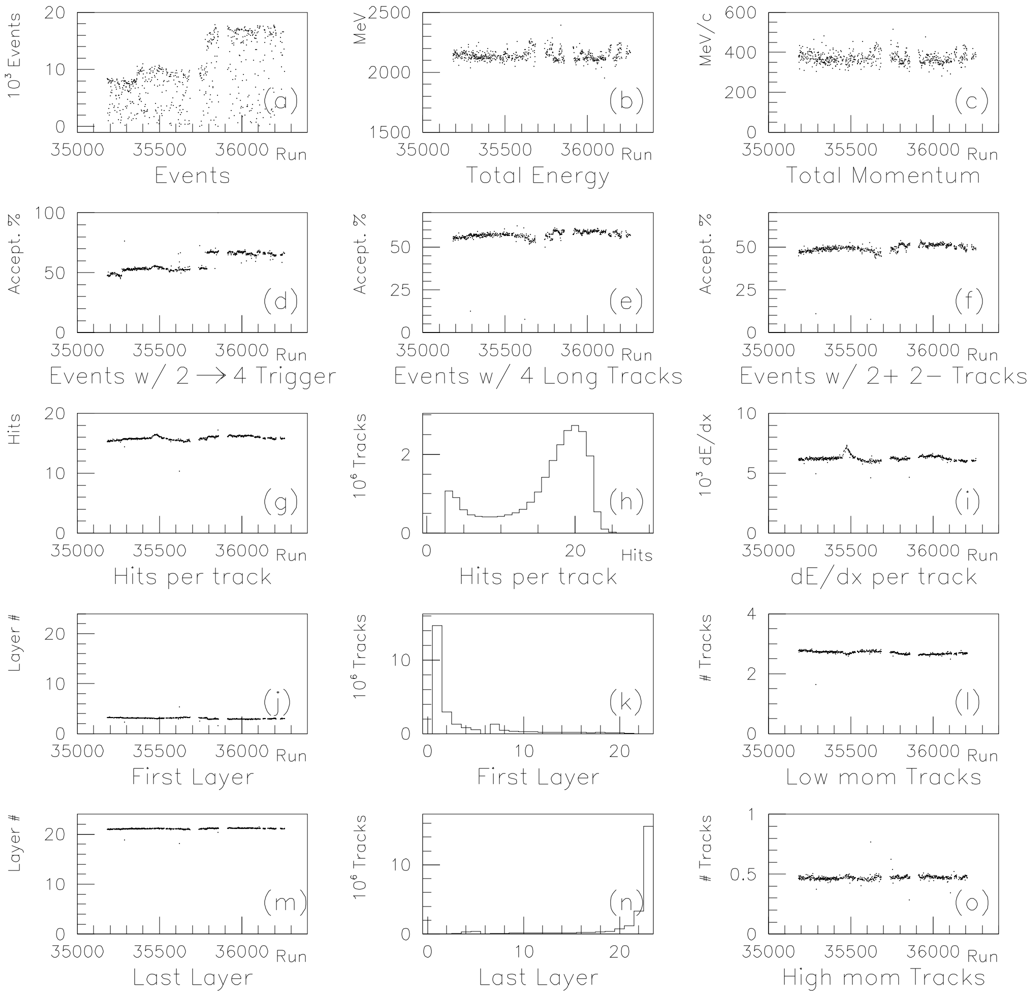

Figure 5.4: Stability checks versus run number.

in principal could be ignored. For two reasons, however, they are not ignorable. First, the junk tracks tend to mess up the reconstruction of the other "good tracks". Second, if one accepts events with extra unidentified tracks, one is opening up the probability of increasing background. Using Monte Carlo simulation (see chapter 6), we found that allowing one short track (that was ignored) increased the signal statistics at the skimming level by 10%. We felt that this small gain was not significant when compared to possible problems with extra background and later data reconstruction.

This cut rejects 43% of all the events of the data, and 22% of the signal as calculated via Monte Carlo.

3. **2 positively-charged and 2 negatively-charged long tracks.** Because the $p\overline{p}$ has zero net charge, this cut is natural. The events that are rejected could come from 3 sources:

   (a) $p\overline{p}\rightarrow 6$ tracks, where 2 positive or 2 negative tracks were lost down the polar directions,

   (b) pile-up events, where two annihilation events occur so near in time that drift electrons from the previous event linger into the next event causing spurious readings, and

   (c) reconstruction errors which assign the wrong curvature to a track.

   This cut rejects 14% of the data, and 6% of the signal as calculated via Monte Carlo.

4. K_S mass cut. This last cut was chosen for a technical reason rather than for physics reasons: It was desired to fit the entire skimmed data on one 20GB tape. Without

this cut (which rejects 14% of the data), the result would not fit on one tape.

The mass of the K_S is 497 MeV, and thus the invariant mass of the decay products ($\pi^+\pi^-$) should be 497 MeV. However, because the vertex of the decay products was not known at this stage in the data processing (the vertex fit was not completed), the correct invariant mass could not be calculated. So an approximation was made by assuming that the vertex position was at the annihilation point. This approximation is worst for true decay vertices that are far away, but only affects the angle between the two pions and not the momenta. Because of the approximation, the mass window was chosen to be much larger than the true experimental width of the K_S.

This cut required at least one pair of $\pi^+\pi^-$ (4 possibilities) to have a mass between 400 and 600 MeV/c^2. This only rejects 1% of Monte Carlo events, while rejecting 14% of data events, which was sufficient to have the output data fit on one tape. The larger rejection fraction is due to much more background in the data, for example from gamma conversion ($\gamma \rightarrow \eta^+ e^-$).

5.3 Energy and momentum selection

The first pass on the data described in section 5.2 was intended to be a general "good event" selection, but did not specifically select the channel $K_S K^\pm \pi^\pm$.

The channel $K_S K^\pm \pi^\pm$ consists pure of 4 charged tracks and no photons. Because of this, we could ignore the crystal calorimeter (except much later when it is used as for an anti π^0 cut). The momenta of the charged tracks is well defined (by the curvature and pitch of the helix), but the energy ($E = \sqrt{m^2 + p^2}$) is not because the particles have not been identified as pions or kaons and thus the mass is unknown. For high energy particles, the energy asymptotically approaches the magnitude of the momentum, but in the case of $p\overline{p}$ annihilation, the mass is important.

To select good $K_S K^{\pm}\pi^{\pm}$ events, the magnitude of the total momentum

$$|\vec{p}_{\text{tot}}| = |\sum_{i=1,4} \vec{p}_i| < 180\text{MeV}/c^2$$

was required to be less than 180 MeV/c, in concordance with at rest annihilation. By assuming that all particles are pions, a fake energy E' quantity can be calculated as

$$E'_{\text{tot}} = \sum_{i=1,4} E'_i$$

$$E'_i = \sqrt{\vec{p}_i^2 + m_\pi^2}.$$

Through Monte Carlo simulation, the minimum value of E'_{tot} for $K_S K^{\pm}\pi^{\pm}$ is 1400 MeV, where the shift in energy from $2m_p = 1876$ MeV is due to one particle being misidentified as a pion rather than kaon. Thus all events were required to have an E' greater than 1400 MeV. Figure 5.5 shows the energy and momentum, and the cut limits.

In figure 5.5.a, there are five features of note. The desired signal lies at **A**, which shows full conservation of energy and momentum. At feature **B** are events of the type $\pi^+\pi^+\pi^-\pi^-$, for example from $K_S K_S$. These lie at the true energy and momentum conservation spot because no tracks are kaons misidentified as pions. At feature **C**, are events of the type $K_S K^{\pm}\pi^{\pm}\pi^0$, where the neutrally decaying π^0 appears as missing momentum. The narrow diagonal blob of **C** can be extrapolated to feature **A** by following the slope. This implies that the in both **A** and **C**, one of the tracks is truly a kaon and not a pion. Feature **D** are due the events with one massive lost particle (not a pion) and perhaps other lost neutral particles. If the event truly contains a K_S seen by the trigger, then the lost massive particle is most likely K_L. for example $K_L K_S \pi^+ \pi^-$. Extrapolating this blob to 0 momentum does not intersect **A**. Because feature **E** does not have an axis pointing diagonally down, it is due to more than one lost or neutral particle, for example $K_S K^\pm \pi^\pm \pi^0 \pi^0$.

5.3.1 Statistics

13.9 Gigabytes of skimmed data were read and 1.75 GB (12.6%) of data with proper energy and momentum were written to Exabyte. The number of runs used was 709.

Cut	Events	Net %
Event Read	2300360	100.0
Momentum Cut	449653	19.5
Energy Cut	287400	12.5

A few runs after this step were removed because either (a) they were the wrong trigger type, (b) the antiproton beam conditions appeared to be bad based on gross asymmetries in the crystal hits, or (c) the SVX did not appear to be working. This accounted for a removal of only 318 events out of 287400.

5.4 Vertex fitting

The third data selection operation was vertex fitting and selection. This involves running the specially written multi-vertex fitter, fine tuning the fit parameters(see section 4.4), and selecting the desired topology.

The vertex fit takes the results of the helix fit and combines tracks pairwise to see if they come from a common vertex. An overview of the special vertex fit and a description of the topology notation is given in section 4.4.

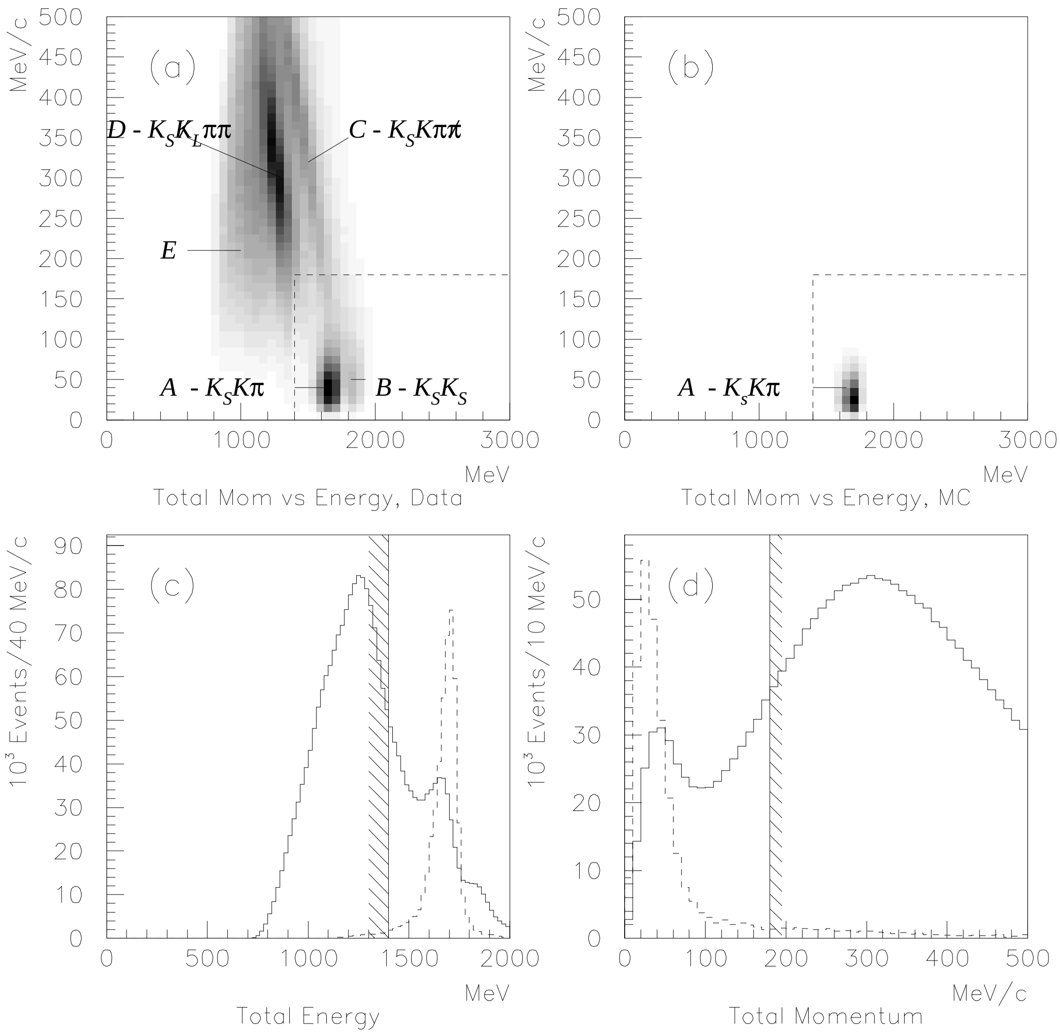

Figure 5.5: Cuts on total energy and momentum. (a) The total energy vs total momentum plot for data. (b) The total energy vs total momentum plot for Monte Carlo of $K_S K^{\pm}\pi^{\pm}$. (c) The total energy with data drawn as a solid line, the MC drawn as a dashed line, and the cut limit. (d) The total momentum, with same definition as (c).

The desired event topology is an inner vertex due to the charged kaon and the charged pion, and an outer vertex due to the decay of the K_S into two charged pions. Thus we select events with a topology equal to (2,2). See figure 4.4 for a schematic of common topologies. At this point, the two remaining vertices are sorted by their radial distance to the origin. The inner vertex is labeled V0 and the outer vertex is labeled V1.

The third cut requires that the vertices open in the correct direction relative to the annihilation vertex. Because the K_S is moving away from the annihilation vertex, the momentum of V1 must point away from the annihilation vertex. However, sometimes there is rare condition where the tracks are accidentally paired to a fake set of vertices which are pointing the wrong way, see figure 5.6. The cut is calculated as follows. First the mean position of V0 and V1 is calculated as

$$\vec{x_{\text{center}}} = \frac{1}{2}(\vec{x_0} + \vec{x_1}).$$

Actually, any point lying on the line connecting the two vertex positions would work for this cut, since we are just interested in the unit direction vectors from this point to each vertex. For each vertex $i = 0, 1$, a direction vector is then defined

$$\vec{d_i} = \vec{x_i} - \vec{x_{\text{center}}}$$

and the cosine of the angle between this direction vector and the momentum of the vertex,

$$\vec{p_i} = \vec{p_i^{\pi^+}} + \vec{p_i^{\pi^-}},$$

is required to be greater than zero,

$$\vec{p_i} \cdot \vec{d_i} > 0.$$

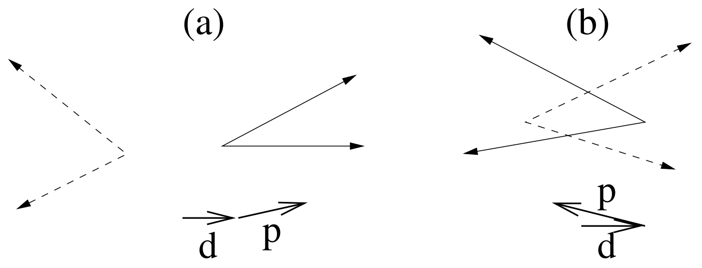

Figure 5.6: (a) A properly reconstructed vertex configuration. $\vec{p}\cdot\vec{d} > 0$. (b) A improperly reconstructed vertex configuration. $\vec{p}\cdot\vec{d} < 0$.

The next cut required that all SVX hits be assigned to the reconstructed tracks. The efficiency of the SVX is higher than the efficiency of the JDC, so it possible for short tracks to be seen in the SVX but not reconstructed properly because some of the JDC hits were below threshold.

The next pair of cuts required the inner vertex, V0, to lie within 0.5 cm of the axis of the LH_2 target, which was centered at (-0.31864, -0.01232, 0), and required the outer vertex V1 to lie outside of the SVX cylinder boundary, with a transverse radius of 1.2 cm.

5.4.1 Statistics

The event counts for the real data and the Monte Carlo of $K_S K^{\pm}\pi^{\pm}$ are given in table 5.2. The most important cut is cut # 2 which requires exactly two distinct vertices. Most of the reject real data events are of the topology (4), which means that the event was most likely a $p\overline{p}\rightarrow\pi^+\pi^+\pi^-\pi^-$ event that leaked passed the SVX at the trigger level. The reason that the "Real data" column does not follow the "$K_S K^{\pm}\pi^{\pm}$ MC" column is that there are still background events in the real data, which are not removed until after the kinematic fit.

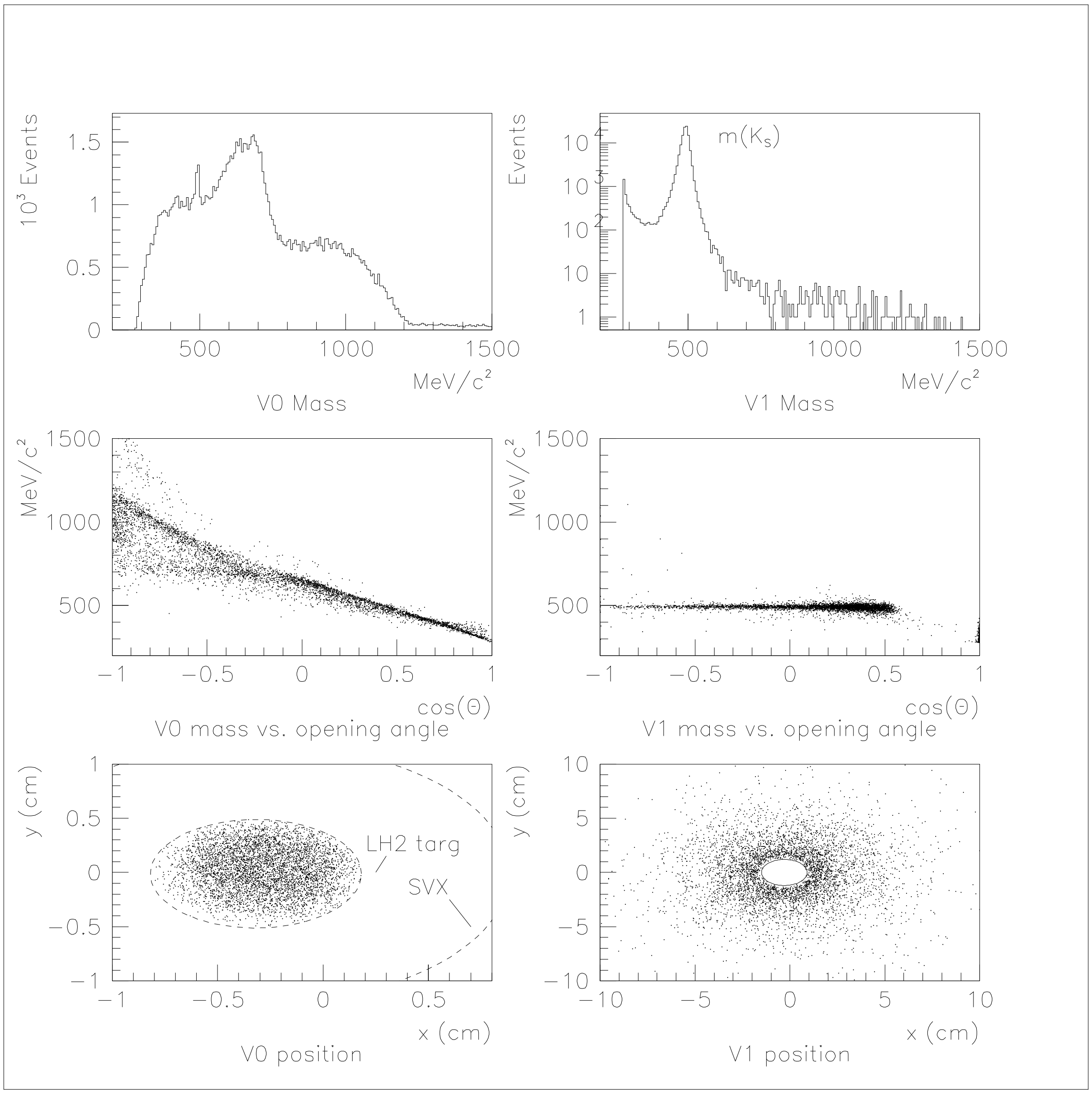

Figure 5.7: The reconstructed vertices. The left column is for the inner vertex, V0, and the right column is for the outer vertex, V1. (a,b) The invariant mass of the $\pi^+\pi^-$ pair at the vertex. The large peak in (b) is due to the K_S. (c,d) The invariant mass vs. the cosine of the angle between the $\pi^+\pi^-$. (e,f) The (x, y) position of the vertex, with the target and SVX boundaries drawn.

NB: An updated JDC calibration database was used at this step of the real data processing. Because the tracks were reconstructed again with the new calibration, some new tracks were found and some old tracks were lost. This explains the > 4 track statistics in table 5.2, which account for less than 0.5% of all events. The < 4 track statistics are due to 2 reasons. The first is due to the new database. The second is that some tracks are rejected in the vertex fit if there are too many "outlier" hits.

5.5 Particle identification using Energy Loss (dE/dx)

At this stage of the analysis, there are exactly four reconstructed charged particles, with two originating from the annihilation vertex and two originating from a displaced vertex outside of the target region. The only possible long-lived, charged particles allowed in this energy range ($E_{\mathrm{tot}} < 1876$ MeV) are pions, kaons and electrons.

Direct $p\overline{p}$ annihilation into electrons is highly unlikely; the strong color force dominates annihilation processes. The branching ratio BR($p\overline{p}\rightarrow e^+e^-$) = 3.2×10^{-7}[15] is several orders of magnitude less than the reactions of interest, for example BR($p\overline{p}\rightarrow K^0\overline{K^{0*}}$) = 1.6×10^{-3} [15]. Electrons are formed however through photon conversion on the JDC sense or field wires. The process creates a displaced vertex, but because of the zero mass of the photon, these vertices ($\gamma\rightarrow\eta^+e^-$) have a $\theta = 0$ opening angle, and are kinematically easily separated from $K_S\rightarrow\pi^+\pi^-$.

The remaining track identification problem is between kaons and pions. At this energy scale, the outer V1 vertex can only be due to the decay of a K_S or a photon conversion, so the tracks originating from V1 are not kaons. By strangeness conservation,

#	Cut	Real data Events	%	$K_S K^{\pm} \pi^{\pm}$ MC Events	%
1	Event in	287092	100	33692	100.0
2	type (2,2)	153908	53.6	27389	81.3
3	$\vec{d} \cdot \vec{p} > 0$	141567	49.3	26515	78.7
4	all SVX hits matched	131359	45.8	26306	78.1
5	V0 inside target	121941	42.5	23680	70.3
6	V1 outside SVX	118861	41.4	23277	69.1
	Topology	Events	%	Events	%
4 track		279671	97.4	33629	99.8
	(4)	75377	26.3	1037	3.1
	(2,2)	153908	53.6	27389	81.3
	(3,1)	14582	5.1	539	1.6
	(2,1,1)	31342	10.9	4443	13.2
	(1,1,1,1)	4462	1.6	221	0.7
<4 track		6186	2.1500	63	0.187
	(1)	1	0.0003	0	–
	(2)	87	0.0303	0	–
	(3)	1688	0.5880	6	0.018
	(1,1)	64	0.0223	0	–
	(2,1)	3541	1.2300	51	0.151
	(1,1,1)	805	0.2800	6	0.018
>4 track		1235	0.4300	0	–
	(5)	26	0.0090	0	–
	(3,2)	52	0.0180	0	–
	(4,1)	258	0.1080	0	–
	(2,2,1)	456	0.1590	0	–
	(3,1,1)	141	0.0490	0	–
	(3,2,1)	1	0.0003	0	–
	(4,1,1)	1	0.0003	0	–
	(2,1,1,1)	229	0.8000	0	–
	(2,2,1,1)	2	0.0006	0	–
	(3,1,1,1)	1	0.0003	0	–
	(1,1,1,1,1)	68	0.0230	0	–

Table 5.2: The statistics for the vertex fitting.

there must be an even number of kaons. There is no phase space for $p\overline{p}\rightarrow 4K$, so events are limited to only 2 kaons with 0 or more pions. The tagged K_S is one of these kaons. The other kaon could be $K^{\pm}$, K_S, K_L. Thus the inner vertex V0 could be $\pi^{\pm}\pi^{\mp}$ with a missing kaon (and zero or more missing pions), or $K^{\pm}\pi^{\mp}$ with zero or more missing pions.

5.5.1 K_S K_L X^0

The background channel with $X^0\rightarrow\pi^+\pi^-$

$$p\overline{p}\rightarrow K_S K_L \pi^+\pi^-$$

would give two tracks at the inner vertex. However, the missing mass of the K_L makes it very unlikely to pass the kinematic fit. Events with additional neutral particles are suppressed even more by the kinematic fit.

5.5.2 K_S K_S X^0

In this reaction, the second K_S decays quickly inside the target region into $\pi^+\pi^-$. From figure 5.7, a small narrow peak (about 500 events) at m($\pi^+\pi^-$) = 497 MeV can be seen in the V0 Mass plot. Background events of the type

$$p\overline{p}\rightarrow K_S K_S \pi^0$$

have the highest probability of being mistaken for the desired channel, $K_S K^{\pm}\pi^{\pm}$, since the missing energy of the π^0 could incorrectly assigned to one of the inner pions, giving it a higher probability to be identified as a kaon. However, as we shall see, this background does not appear significantly in the final data sample. Background events of the type

$$p\overline{p}\rightarrow K_S K_S$$

do not pass the kinematic fit because it is nearly impossible for a $\pi^{\pm}$ to fake a $K^{\pm}$.

5.5.3 $K_S\ K^{\pm}\ X^{\mp}$

Assuming one of the tracks from V0 is $K^{\pm}$, then the other track ($X^{\mp}$) is $\pi^{\mp}$. The events with missing particles in addition to $X^{\mp}$ should be suppressed by the kinematic fit.

Because there is virtually no background from the first two channels, the particle identification must only distinguish $K^{\pm}\pi^{\mp}$ from $K^{\mp}\pi^{\pm}$. In this case, only one particle must be positively identified; the other is identified by process of elimination. This greater simplifies the particle identification process.

5.5.4 dE/dx Theory

As charged particles travel through matter and ionize the surrounding medium, they lose energy. In the limit of particles that are not ultra-relativistic, i.e. $2\gamma m_e << M$, where m_e is the mass of the electron and M is the mass of the charged particle doing the traveling, the equation for the rate of energy loss is given by the Bethe-Bloch equation ([38] Equation 23.1).

$$-\frac{dE}{dx} = Kz^2\frac{Z}{A}\frac{1}{\beta^2}\left[\ln\frac{2m_ec^2\beta^2\gamma^2}{I} - \beta^2 - \frac{\delta}{2}\right]$$

The variables K (overall constant), Z (atomic number of medium), A (atomic mass of medium), I (mean excitation energy of medium) and δ (density effect correction) are a function of the medium. The variable z is the charge of the incident particle, which is ± 1 in the case of pions and kaons. We do not care about the actual value of these parameters, because we fit the dE/dx curves with a simpler function in (5.1). We measure the dE/dx

in the JDC, so the medium is a Isobutane/CO2 gas mixture. The remaining variable is β, the velocity of the particle. The velocity of a particle is given by

$$\beta = \frac{p}{E} = \frac{p}{\sqrt{p^2 + m^2}}.$$

Because a pion and kaon differ in mass, for a particular momentum they will have different velocities, and thus different values of dE/dx. This fact allows identification of particles with the same momentum. Because the dependence on mass m becomes less significant at higher momentum (i.e. $\beta \rightarrow 1$ for both particles as $p \rightarrow \infty$), the identification is good for π/K momenta up to about 500 MeV/c. Beyond that, the identification is not unique.

The ionization energy is measured by integrating the collected charge on each JDC sense wire. The analog-to-digital converters (flash ADC's) on each wire measure the current versus time for each wire at each end, and this data is written to tape with the entire event. Offline, each signal is linearized, integrated and corrected for non-linearities in the electronics and scaled by a calibrated factor for that wire. This is the raw value for the dE/dx measurement.

At the same time, the Monte Carlo simulation simply applies the Bethe-Bloch equation to the particle and gas and calculates a value for dE/dx. Because neither the Monte Carlo nor the data is properly absolutely calibrated, there is no need to use most of the parameters given above. Instead, we can fit the data and Monte Carlo with a simplified 3-parameter equation, and make adjustments to each if necessary. The equation is thus

$$-\frac{dE}{dx} = \frac{M}{\beta^2}\left[\ln\frac{N\beta^2}{1-\beta^2} - \beta^2 - \delta/2\right] \tag{5.1}$$

where $M = -2.8 \times 10^{-7}$ MeV/cm, $N = -0.668$ and $\delta = 20055$. Since the the dE/dx of the JDC was never properly calibrated in absolute terms, the units of M is arbitrary, although

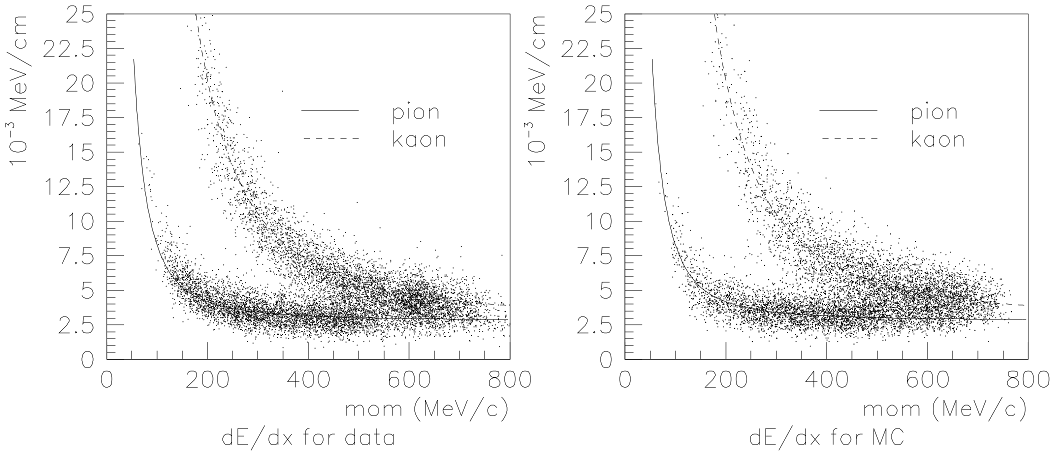

Figure 5.8: The dE/dx profiles for (corrected) data and (corrected) MC. The simplified Bethe-Bloch curves are described in the text.

they are stated to be "MeV/cm" in the literature. The fit to the data and MC is shown in figure 5.8.

5.5.5 Corrections applied to data

A comparison between the raw data dE/dx values and the values in the Monte Carlo calculated theoretically with the Bethe-Bloch equation showed a marked discrepancy. This appears to be due to the fact that there was an unsubtracted positive DC bias to all JDC signals in the real data. It appears that the calibration committee did a quick and dirty job calibrating the dE/dx values for the data using only minimum ionizing particles, thus only at one momentum. As can be seen in figure 5.9, the minimum ionizing point lies more or less on the unity line relating the data to the Monte Carlo. However, everything above that point is incorrect. For each slice of momentum, the mean data value for dE/dx

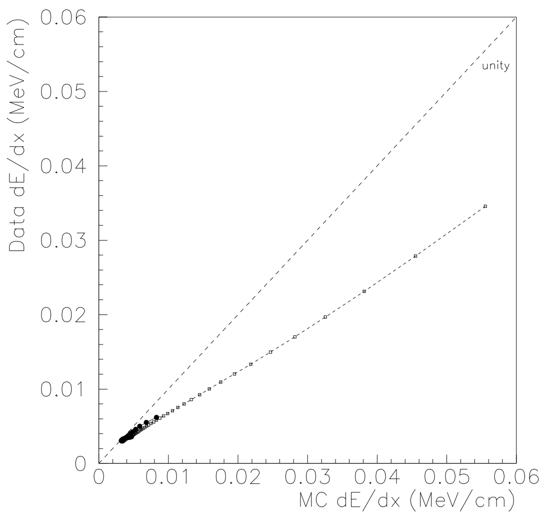

Figure 5.9: The calibration curve for data dE/dx values versus Monte Carlo (Bethe-Bloch) values. The diagonal line indicates what the proper relationship should be.

was plotted versus the Monte Carlo value for dE/dx (see figure 5.9), and a line was fit giving the following

$$y = 0.00118 \text{ MeV/cm} + 0.564x.$$

This equation was then inverted and applied to the data, and the resulting curves for Monte Carlo and data became sufficiently similar (see figure 5.8).

5.5.6 Corrections applied to Monte Carlo

We found that the dE/dx values arrived at through CBGEANT did not have the same statistical variation that the data did. As was to be expected, the default Monte Carlo values were too "clean". The default Gaussian smearing added to the dE/dx values was not enough. To correct for this, additional Gaussian smearing was added to the Monte Carlo values, using the following formula, where gauss() generates a random value from a normal distribution with mean 0.0 and width 1.0,

$$\frac{dE}{dx}_{\text{MC-smear}} += (4.0 \times 10^{-4}\text{MeV/cm}) \cdot \text{gauss}() + (0.15 \cdot \frac{dE}{dx}_{\text{MC}}) \cdot \text{gauss}().$$

The resultant width of the dE/dx distribution is about 20-30% of the mean value, depending on momentum. A comparison between data and Monte Carlo with the preceding smearing is given in figure 5.10. The overlap in the critical region above 450 MeV/c appears to be well described by the Monte Carlo.

5.5.7 Curves used for Particle Identification

As long as the data and Monte Carlo are virtually indistinguishable, one can make graphical cuts on the distributions. We choose to make two curves; one curve gives the upper limit of dE/dx for pions and the other gives the lower limit of dE/dx for kaons. Above 400 MeV/c, there can be an ambiguity as the two curves cross. Thus all tracks are classified into one of four disjoint regions:

1. "π" - must be a pion
2. "K - must be a kaon
3. "ambig" - could be either (ambiguous)
4. "nil" - is neither.

See figure 5.11 to see the positions of the curves.

To generate these curves, we fit each arm with the simplified curve given above in subsection 5.5.4 and shown in figure 5.8. The curves are then shifted in momentum by 50

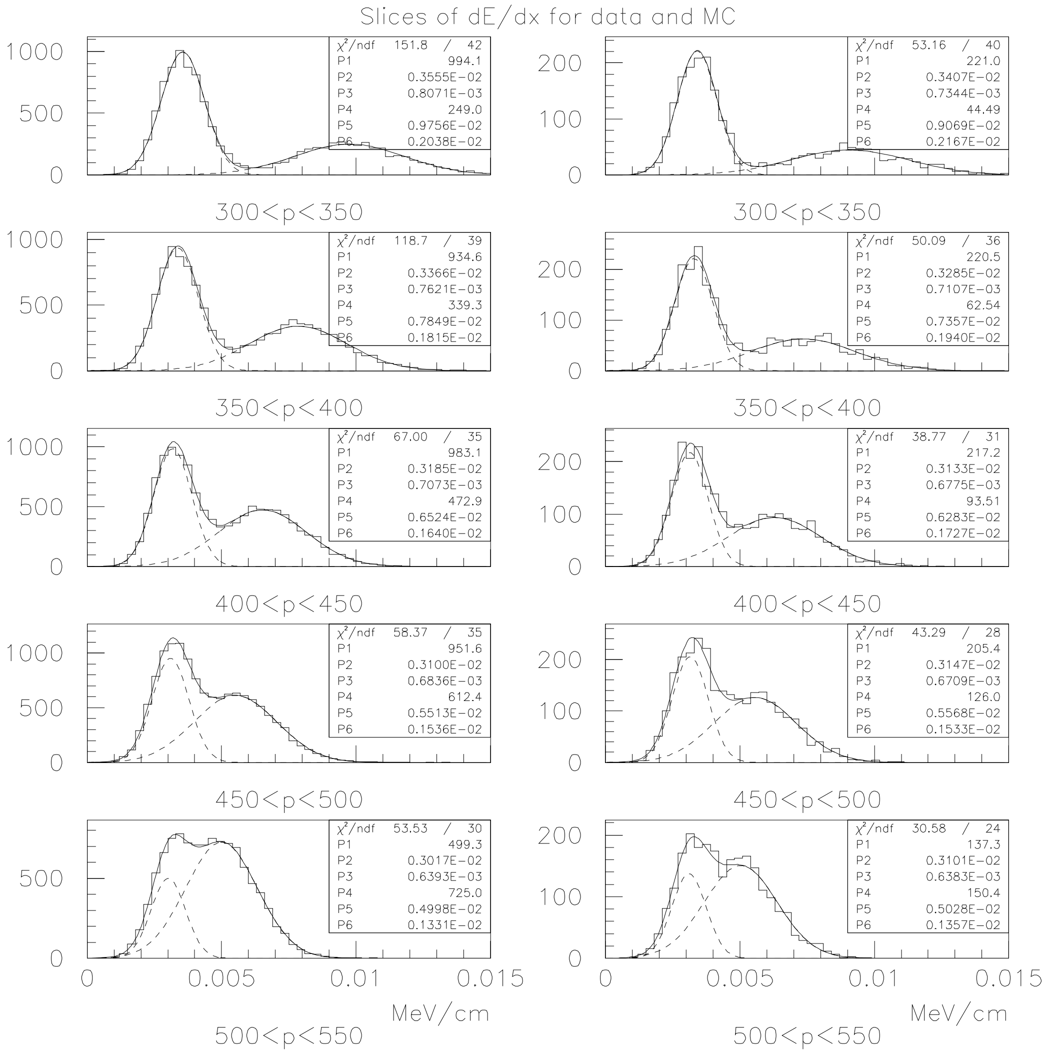

Figure 5.10: The dE/dx distributions in slices of momentum. Each plot shows a double peak, with the left peak due to pions and the right peak due to kaons. The left column is real data, right right column is MC. The agreement between data and MC after corrections and additional MC smearing is good.

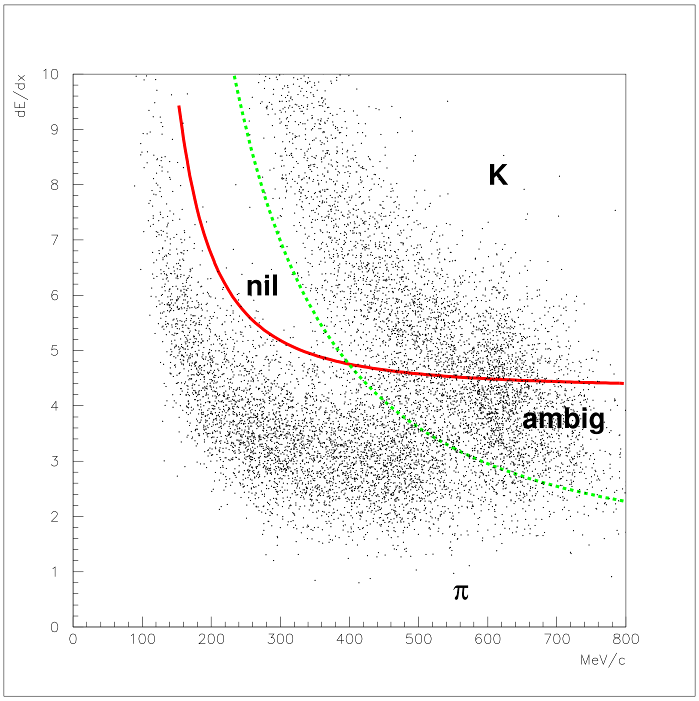

Figure 5.11: The graphical particle identification cuts. There are four labeled regions, "nil", "K", "π" and "ambig".

MeV/c (x axis) and shifted in dE/dx by 0.0015 MeV/cm (y axis). The pion curve is shifted up and right, while the kaon curve is shifted down and left (figure 5.11).

5.5.8 Particle Identification Logic

Events are rejected if both tracks are "ambiguous," meaning that the dE/dx points lie in the ambiguous region: either track could be a pion or kaon. Events are also rejected if either track is "nil" meaning that it lies in the "nil" region. The remaining events have at least one track that is uniquely identified. Because of the arguments given at the beginning of this section, the other particle is also identified: it is a π if the first particle is a K and vice versa.

In the Monte Carlo events, a few events are misidentified. In the $K_S K^+ \pi^-$ MC events, 28 events out of 15K are misidentified as $K_S K^- \pi^+$, while in $K_S K^- \pi^+$ MC Events, 56 events out of 15K are misidentified as $K_S K^+ \pi^-$. This is a total of 84 events out of 30K, or only 0.3 % of data points in the Dalitz plot.

5.6 Corrections

5.6.1 Run by run momentum scaling

The drift-velocity of ionized electrons in the JDC is inversely proportional to the pressure of the JDC gas. Because the Crystal Barrel JDC operates at atmospheric pressure which changes with the ambient weather conditions, the atmospheric pressure is measured concurrently with the data and corrections are applied offline. Also, the JDC gas mixture (isobutane/CO_2) ratio affects the signal pulse height on the wires and to a lesser extent the measured drift-velocity.

During the April 1996 run period, one of the gas flow valves became stuck and the JDC gas mixture became too CO_2 rich. The regulator was fixed shortly thereafter, but it took a significant number of runs for the ratio to reach the desired 1:10 ratio. The impact on the data can be seen in 5.4 where the dE/dx measurement spikes up.

To correct for both of these effects, the measured momenta of each event was scaled by a factor for each run. A run typically lasts on the order of 30 minutes, over which time scale the weather and beam conditions are relatively stable. The scale factor was determined by averaging the invariant mass of the vertex V1 over each run and comparing to $m_K = 497.672$ MeV/c^2. The run-by-run scale factors are plotted in figure 5.12. The

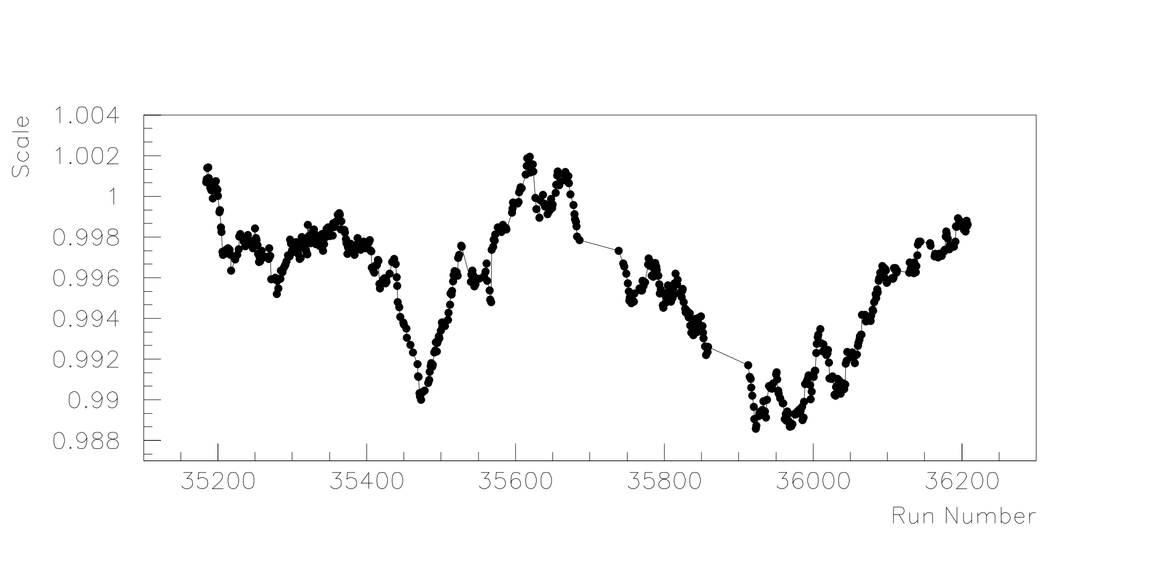

Figure 5.12: The momentum scale factor as a function of run number

sharp dip near run 35450 is due to the gas mixture problem; the valve stopped working near run 35430 and was fixed near run 35470. The broad dip around run 36000 was caused by weather conditions.

5.6.2 Error scaling

Just as the errors of the JDC hits used in the vertex fit needed some tuning, the error estimates of the reconstructed momenta needs some tuning in order that the probabilities returned by the kinematic fit make sense. For accurate measurements with Gaussian errors of the proper channel, the probability distribution (also known as the confidence level) is uniform from 0 to 1.0. The probability is the probability that subsequent events will have a better fit to the hypothesis.

	MC	Data
Momentum x, y Scaling	0.9985	1.0055
Momentum z Scaling	1.0035	1.0709
Momentum Error Scaling	1.25	1.55
$\pi^{\pm}$ correction parameters for energy loss		
α_1	-1.3566	
α_2	-2.283×10^{-2}	
α_3	6.728×10^{-3}	
α_4	-9.316×10^{-6}	
$K^{\pm}$ correction parameters for energy loss		
α_1	0.8719	
α_2	-1.966×10^{-2}	
α_3	1.533×10^{-2}	
α_4	-2.033×10^{-5}	

Table 5.3: The correction parameters for momentum scaling due to JDC geometrical distortion, energy loss and error scaling.

5.6.3 Energy loss Correction

Charged particles experience an energy loss due to ionization in material before entering the JDC, especially at low momenta. This energy loss results in the measured momentum to be systematically too low. This effect increases at slower velocity, so low momentum kaons are affected the greatest. Figure 5.13 shows the correction fractions as a function of momentum for $K^{\pm}$ and $\pi^{\pm}$.

The following phenomenological correction function was applied to all tracks, based on their particle identity:

$$f_{\mathrm{ms}} = 1 + e^{\alpha_1 + \alpha_2 * p} + \alpha_3 + \alpha_4 p$$

where p is the particle's measured momentum and α_i are the parameters given in table 5.3. The functions are plotted in figure5.13.

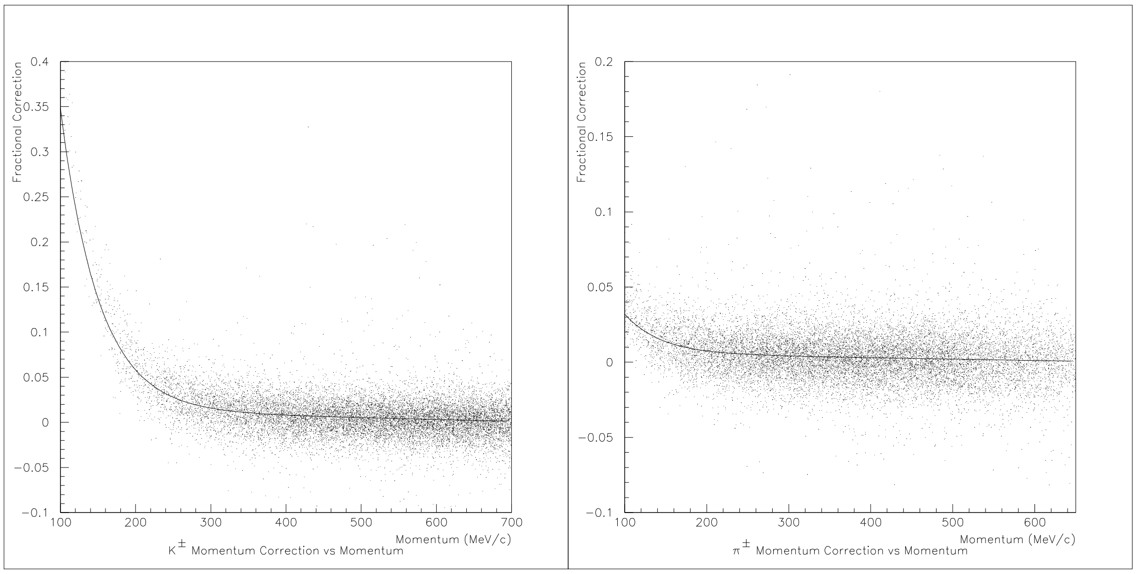

Figure 5.13: The fractional momentum correction vs momentum for $K^{\pm}$ and $\pi^{\pm}$ as derived from Monte Carlo.

5.6.4 JDC geometrical distortion

The z-dimension of the JDC was discovered to be incorrectly calculated in the reconstruction by a significant amount. This was discovered independently by two groups. We found that the invariant mass of the V1 $\pi^+\pi^-$ pair was dependent on the orientation of the decay. If one takes the normal to the K_S decay plane

$$\hat{n} = \vec{p}_{\pi^+} \times \vec{p}_{\pi^-} \tag{5.2}$$

and then looks at the invariant mass of the pair as a function of

$$\cos\theta = \hat{n}_z/|\hat{n}|, \tag{5.3}$$

one could see a significant drop in mass as $\cos\theta \rightarrow 1$. This is because for $\cos\theta = 0$, the z dimension has no affect on the opening angle calculation, but as $\cos\theta \rightarrow 1$ the z dimension becomes important. If the z dimension is compressed, the angle becomes smaller too, and

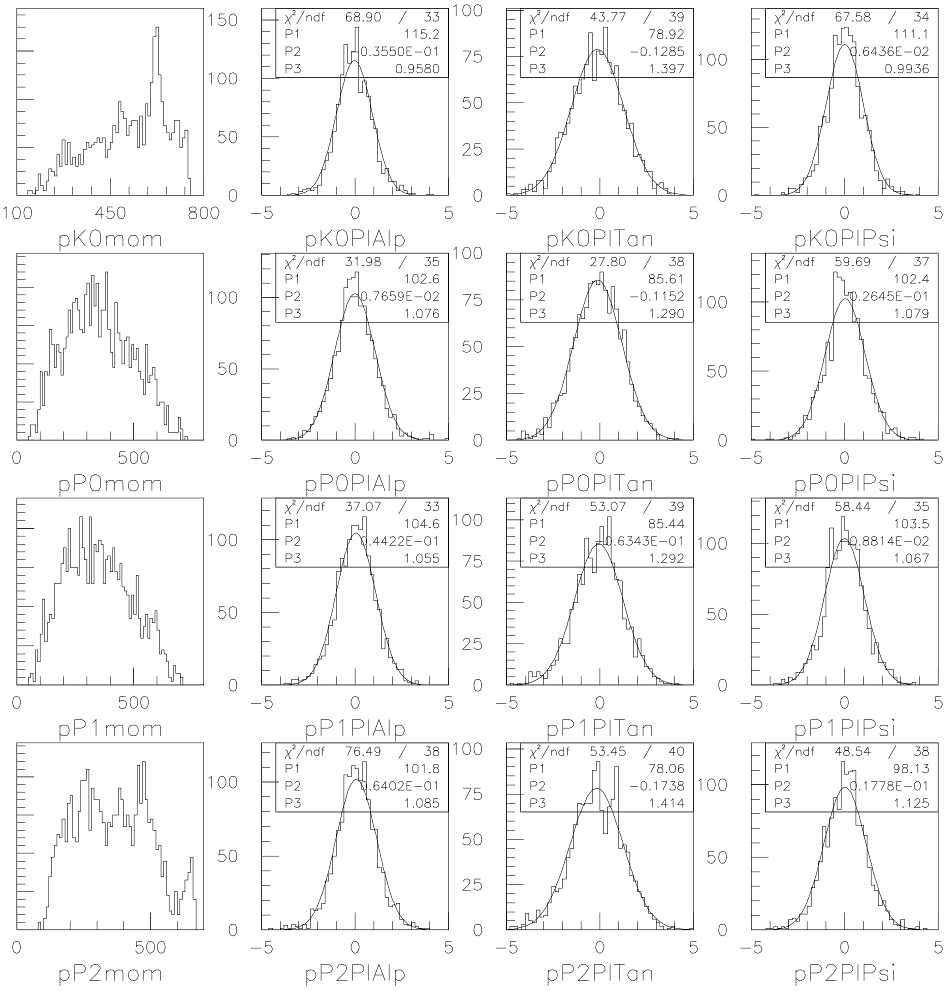

Figure 5.14: The statistical pulls of each particle's momentum component as seen in the real data. Each row represents one particle, in the following order: (from V0) $K^{\pm}$and $\pi^{\pm}$, (from V1) π^{+} and π^{-}. The first column is the particle's total momentum, the second column is the pull in α (curvature), the third column is the pull in $\tan\lambda$ (pitch), the fourth column is the pull in ψ (azimuth).

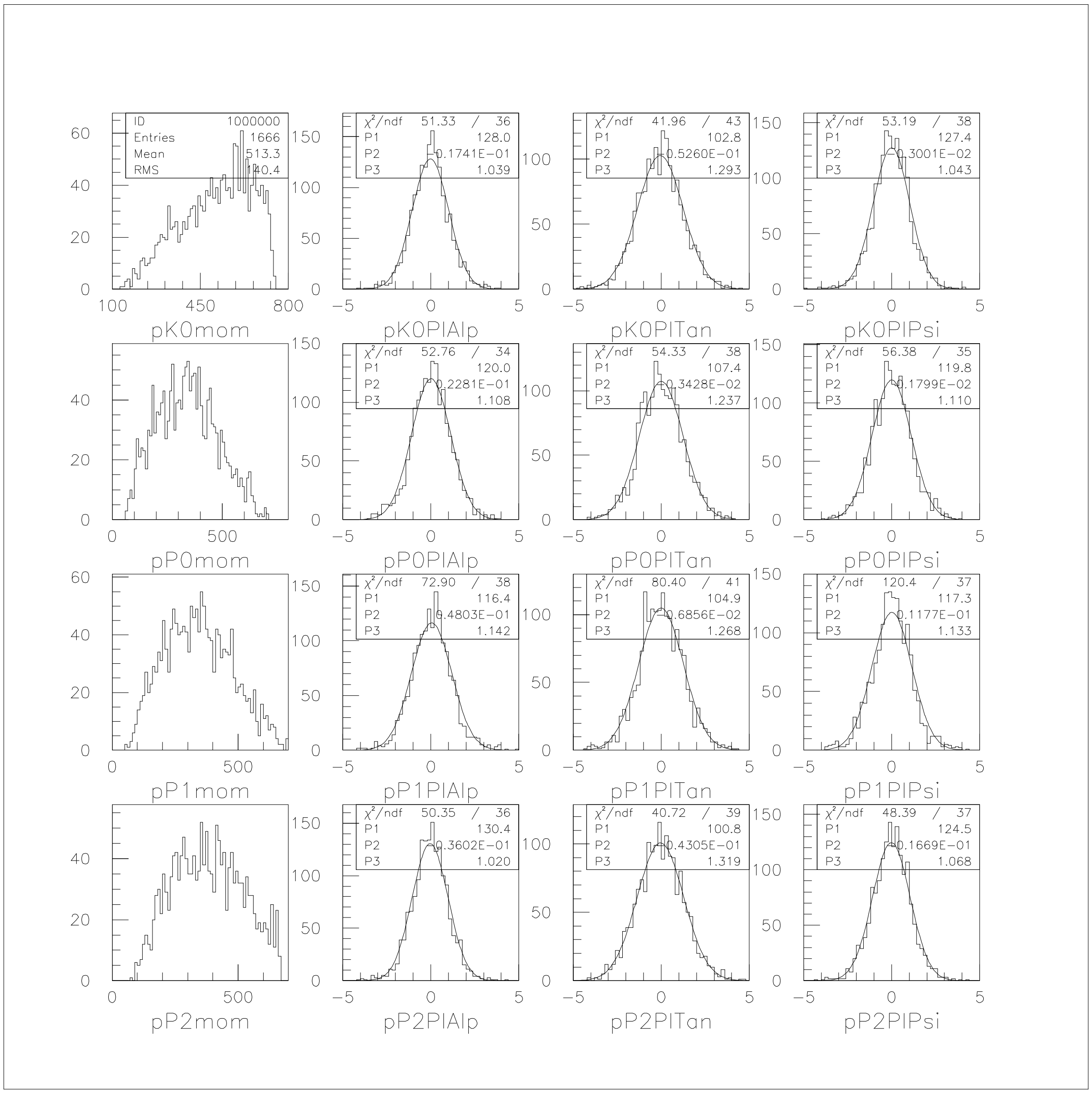

Figure 5.15: The statistical pulls of each particle's momentum component as seen in the Monte Carlo. See figure 5.14 for a description of the plots.

the invariant mass falls. This is shown in figure 5.16.

To determine the correct JDC z dimension, the z dimension was scaled by a parameter until the invariant mass was no longer dependent on the polar angle of $\hat{n}$. The scaling factor of 1.0709 ± 0.005 was determined to satisfy this condition.

A second group in the collaboration discovered that the track-to-PED alignment was significantly off, with the JDC z dimension about 6% too small. This agrees well with the determination made using the $m(K_S)$ vs $\hat{n}$ method. Figure 5.16 shows that the V1 mass is now constant with respect to decay plane angle.

5.7 Kinematic Fit

5.7.1 Introduction

The measurement accuracy and precision can be improved if there are additional constraints imposed on the data beyond the direct measurements of the apparatus. For example, if the total momentum of the event is known to be zero even though the measured values do not sum to zero, the measured values can be slightly adjusted (within the estimated errors or error matrix) by a minimization procedure until they do sum to zero. This typically improves the accuracy of the measurements and always improves the precision. For "good" events, the kinematic fit will return a probability that lies uniformly between 0.0 and 1.0.

At the same time, a kinematic fit can perform two other useful tasks. First, it can help distinguish between charged kaons and pions, because the total energy is a function of the mass of the constituent particles. The correct assignment will have a higher probability. Second, it can reject events that have "missing"particles (such as a K_L or other neutral

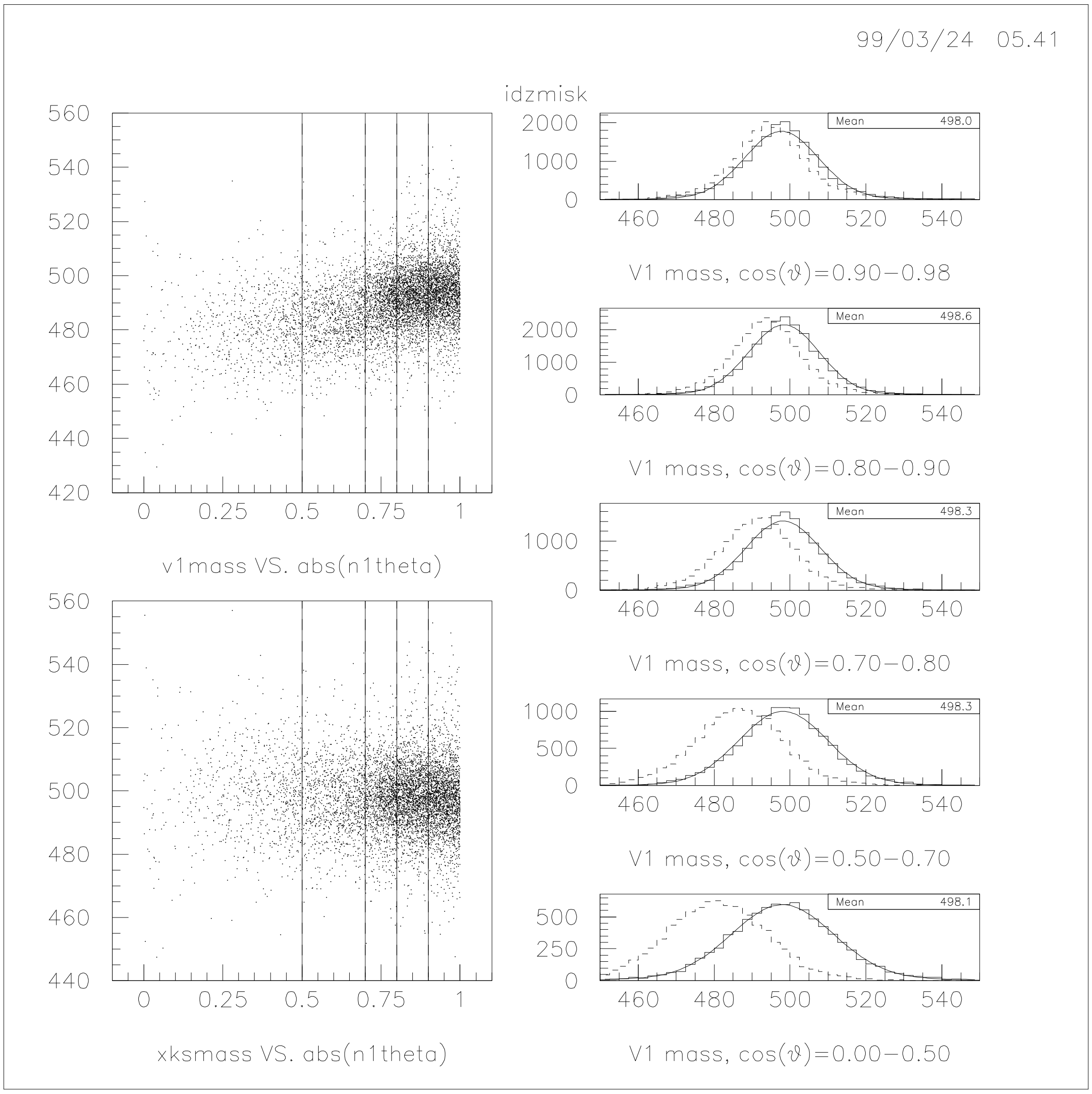

Figure 5.16: V1 invariant mass, before and after z-dimension rescaling. In (a) is shown the invariant mass of V1 versus the decay plane angle (see equation 5.3). In (b) the same is plotted, except after the rescaling of the z dimension. The right column shows the slices of the scatter plots. The solid line is the corrected data, and the dashed line is the uncorrected data.

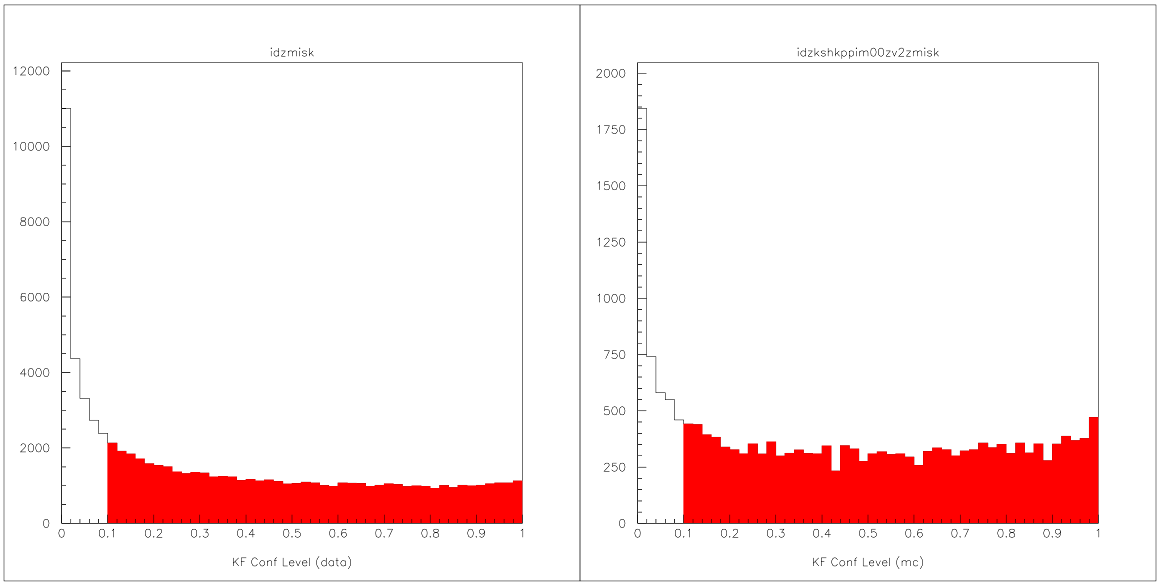

Figure 5.17: The Confidence Level or Probability of the 5C kinematic fit. The shaded region are the accepted events at 10% confidence. (a) real data (b) Monte Carlo

particle) or are otherwise bad, because these events will have a low probability, typically less than 1%. The algorithm of kinematic fitting is given in chapter A.1.

The channel of interest in this analysis has five additional constraints that may be imposed on the measured momenta.

1. Total momentum is 0 (three constraints).

2. Total energy is twice the proton mass (one constraint).

3. Invariant mass of V1 vertex is K_S mass.

At this point in the analysis, all particles have been identified already, so the kinematic fit is used to reject bad events as well as improve the accuracy of the good events.

The kinematic fit depends directly on the estimated errors of the measured momenta. The errors are determined by the vertex fit based on the fit itself plus corrections for multiple-scattering. The errors are diagonal in the vertex-fit basis (α (curvature), $\tan\lambda$ (pitch), and ϕ (azimuth)) but in the Cartesian (p_x, p_y, p_z) basis, the errors are described by a symmetric 3×3 matrix. These errors need to be adjusted slightly in order that the final probability calculated by the kinematic fit makes sense. This procedure is described below.

The events are first subjected to a phase space 4-constraint kinematic fit, meaning that the K_S mass constraint is not imposed, i.e.

$$p\overline{p} \rightarrow K^{\pm}\pi^{\mp}\pi^{+}\pi^{-}.$$

If the fit converges with a reduced $\chi^2/4 < 20.0$ (a very loose constraint), then the events are submitted to the 5-constraint kinematic fit which includes the constraint that the pions from the outer vertex have the K_S mass,

$$\begin{array}{ll} p\overline{p} \rightarrow & K^{\pm}\pi^{\mp}K_S \\ & \qquad\quad \hookrightarrow \pi^{+}\pi^{-}. \end{array}$$

The confidence level for this hypothesis is required to be greater than 0.10, as seen in figure 5.17.

The cleanliness of the signal after the kinematic fit can be seen in figure 5.18. The background level from non-K_S events is negligible.

5.7.2 Reconstruction Accuracy

The invariant mass of the V1 $\pi^+\pi^-$ pair and total energy of the event, after all the corrections, is histogrammed in figure 5.19.

The momenta of physical interest are the momenta at "$t = 0$", i.e. the momenta at the interaction point(s) rather than the momenta as tracked in the JDC. Ideally, the mo-

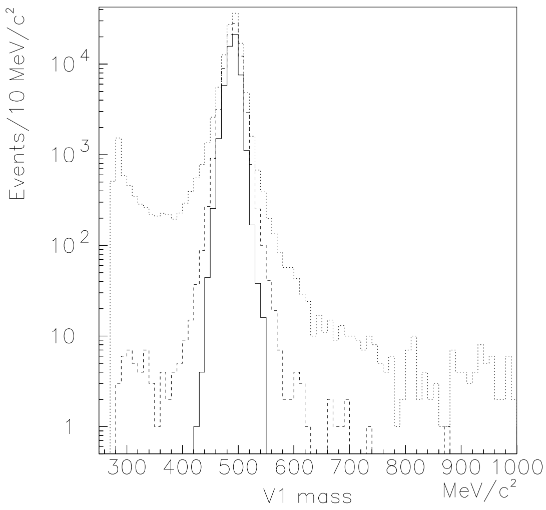

Figure 5.18: The V1 invariant mass distribution, before the kinematic fit (dotted), after 4C phase space fit (dashed) and after full 5C kinematic fit (solid).

menta measured in the JDC can be corrected for multiple-scattering and then kinematically fitted to obtain the physical $t = 0$ values.

A check of this reconstruction accuracy can be done by comparing the $t = 0$ values generated by the Monte Carlo (the "physical" values) with the reconstructed values. To make a meaningful plot of the comparison, the Dalitz plot coordinates $\vec{X} = (x, y)$ for each event are calculated twice, once using the MC generated values $\vec{X}^{\mathrm{mc}}$ and once using the kinematically fitted reconstructed values $\vec{X}^{\mathrm{kf}}$. Ideally, these two values are the same but in practice each event is slightly off. All the events are binned according to the $\vec{X}^{\mathrm{mc}}$ value, with a 2-dimensional vector weighting equal to

$$\vec{\Delta}_i = \vec{X}_i^{\mathrm{kf}} - \vec{X}_i^{\mathrm{mc}}$$

where i runs over the entries for a particular bin. Once all events are binned, a mean

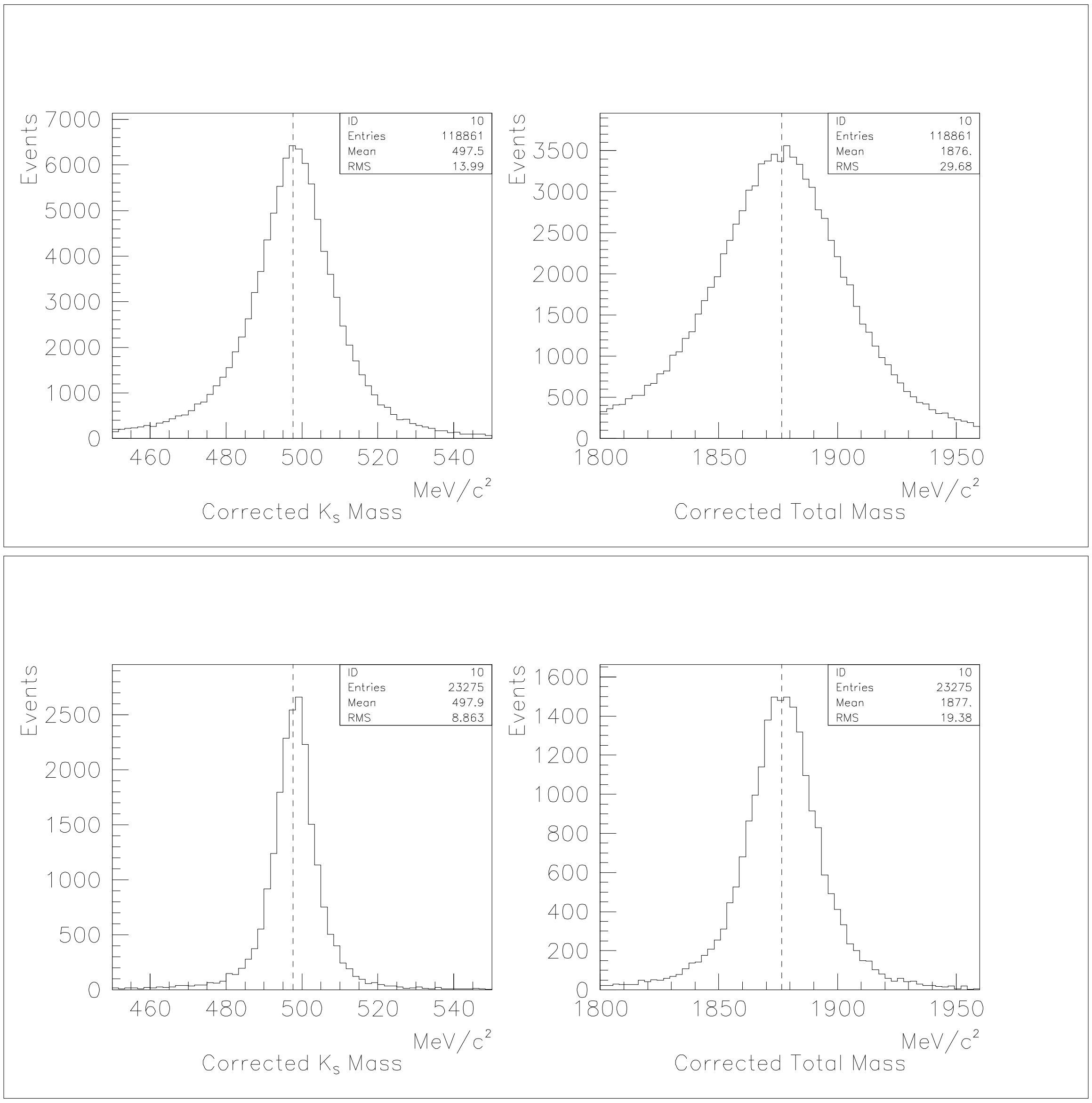

Figure 5.19: The V1 $\pi^+\pi^-$ invariant mass and total energy for data and Monte Carlo

deviation and RMS deviation are calculated,

$$\overline{\vec{\Delta}} = \frac{1}{N} \sum_i \vec{\Delta}_i$$

$$\overline{\Delta}\vec{\mathrm{rms}} = \sqrt{\frac{1}{N-1} \sum_i \left(\vec{\Delta^2}_i - \overline{\vec{\Delta}}^2 \right)}$$

where

$$\vec{\Delta^2} = (\Delta_x^2, \Delta_y^2).$$

Figure 5.20 shows the results of these calculations. As can be seen, the mean shifts are randomly oriented, with large deviations only coming from edge bins with low MC statistics. The shifts are all much smaller than the bin size. Likewise, the RMS spread of the shifts (figure c) are also smaller than the bin size, approximately half the bin size, showing that this bin size is a good choice. Figure (d) shows the fractional reconstruction error for all events in the Dalitz plot variables

$$f_x = \frac{\Delta x}{\overline{x}} = 2\frac{x^{\mathrm{kf}} - x^{\mathrm{mc}}}{x^{\mathrm{kf}} + x^{\mathrm{mc}}}$$

$$f_y = \frac{\Delta y}{\overline{y}} = 2\frac{y^{\mathrm{kf}} - y^{\mathrm{mc}}}{y^{\mathrm{kf}} + y^{\mathrm{mc}}}.$$

There is a small systematic shift of about -0.06 % and the RMS error is about 0.8 %, both of which are excellent for this analysis and independent of axis.

5.7.3 π^0 Suppression

This analysis has only looked at charged data so far. This is because the electromagnetic calorimeter is plagued by hadronic split-offs from the charged particles. Many of the "PEDs" turn out to be not be from physical photons, but caused by dislodged neutrons

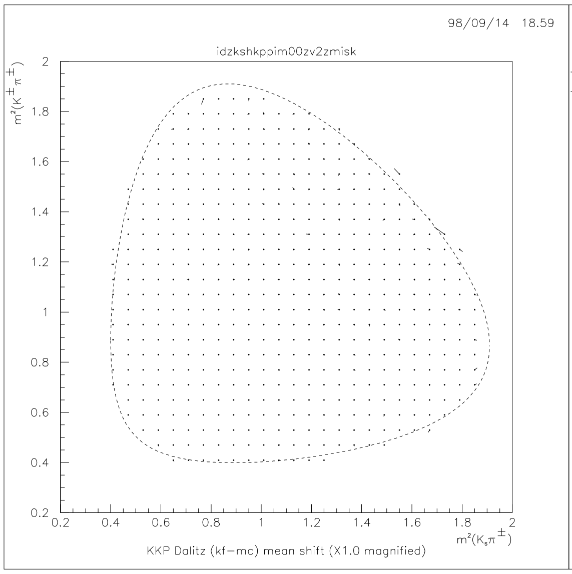

(a)

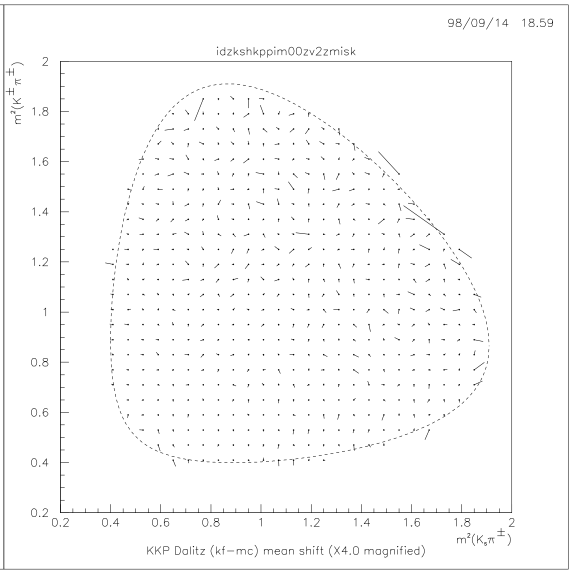

(b)

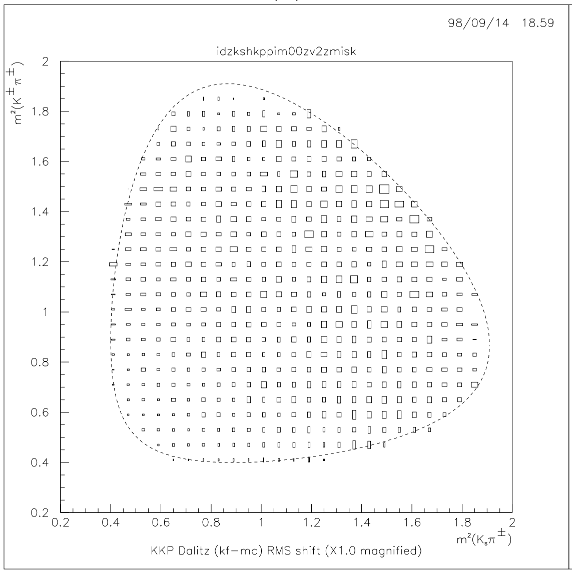

(c)

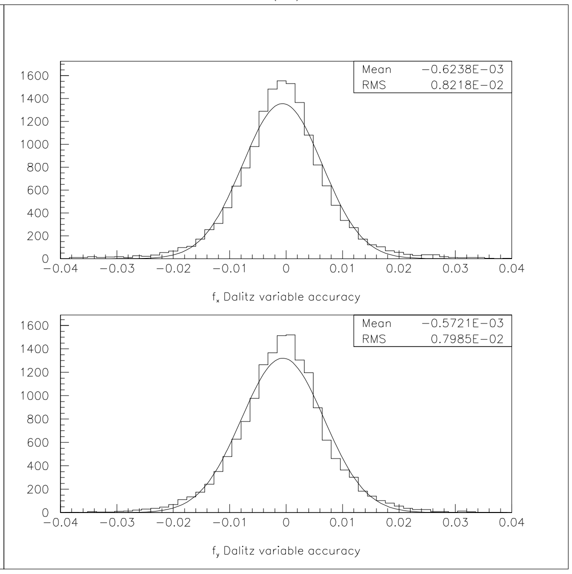

(d)

Figure 5.20: A comparison between the reconstructed and MC generated Dalitz plot variables. Figures (a) and (b) show the average mean deviation for each bin. The short line segment in each bin has one vertex at the center of the bin; the other vertex is the mean of the deviation, $\overline{\vec{\Delta}}$, as described in the text. Figure (a) shows the unscaled deviation vector, while figure (b) shows the deviation vector scaled by a factor of 4 to make the deviations easier to see. Figure (c) shows the RMS deviation, with each box dimension ($l \times w$) equal to twice the RMS deviation in that direction. (d) Shows the accuracy of all events, f_x and f_y (see text).

and other uninteresting hadronic debris (caused by the collision of the desired pions and kaons hitting the crystals) flying from one half of the detector to the other side. These PEDs are not part of the interesting physics and just cause additional random background to the photon signal. Luckily, in this analysis we are not looking for photons, so this background doesn't matter.

However, the PEDs can still be used to check to see if events with a $\pi^0 \rightarrow \gamma\gamma$ (for example $p\overline{p} \rightarrow K_S K^{\pm} \pi^{\mp} \pi^0$) are surviving the preceding cuts and kinematic fit. Happily, the answer is no, as seen in figure5.21. The invariant mass of all pairs of PEDs before the kinematic fit cuts is plotted first. While most PEDs are junk and therefore form just a smooth combinatorial background that decreases with energy, a significant π^0 peak can be seen above the background. This peak totally vanishes for events that pass the kinematic fit, shown as the second dashed histogram. No $\eta \rightarrow \gamma\gamma$ peak was seen before or after the kinematic fit.

5.8 Charge symmetry

The two reactions

$$p\overline{p} \rightarrow K_S K^+ \pi^-$$

$$p\overline{p} \rightarrow K_S K^- \pi^+$$

should have identical Dalitz plots if the strong force is charge independent. The experimental Dalitz plot may have some charge dependence, however, for two reasons.

First, the JDC is inherently chiral. The external magnetic field causes the drift lines to rotate about each sense wire by 7.2°[2], the Lorentz angle. Tracks which curve in

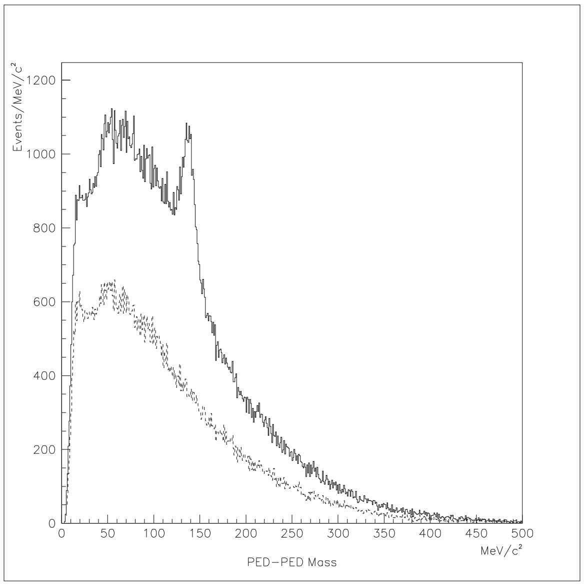

Figure 5.21: The PED-PED invariant mass for events before (solid line) and after (dashed line) the kinematic fit cut.

opposite directions will not see the mirror symmetric fields, and this could cause a small asymmetry between measured tracks of opposite sign.

Second, hadronic interactions with the detector are charge dependent. For example, the biggest asymmetry is between K^+ and K^- which interact differently with protons. For kaons between 0.1 and 1.0 GeV/c, the K^-p cross section is roughly 5 to 10 times that of K^+p [38]. This increased interaction probability can cause more interactions in the JDC and the Barrel, raising the probability that splash-back particles can re-enter the JDC and cause an event to be rejected.

The ratio of charge configurations accepted in the final Dalitz plot are

$$\frac{N(K_S K^+ \pi^-)}{N(K_S K^- \pi^+)} = \frac{26994}{26736} = 1.0097 \pm 0.0086$$

which very nearly consistent with unity. The projections of the Dalitz plot for each charge configuration is given in figure 5.22. There is a slight enhancement of $K_S K^+ \pi^-$ events below 1 GeV$^2/c^4$ but it is probably not significant in the fit. The χ^2 comparison between the two Dalitz plots (shown in figure 5.23)

$$\chi^2 = \sum_{i\,\mathrm{bins}} \frac{[N_i(K_S K^+ \pi^-) - N_i(K_S K^- \pi^+)]^2}{N_i(K_S K^+ \pi^-) + N_i(K_S K^- \pi^+)}$$

gives $\chi^2/N_{df} = 457/505 = 0.91$, showing good compatibility.

For the Monte Carlo, 1 million events of each charge configuration were generated. The ratio of accepted events was

$$\frac{N(K_S K^+ \pi^-)}{N(K_S K^- \pi^+)} = \frac{15087}{14964} = 1.0082 \pm 0.012$$

which is also in agreement with unity and even better agreement with the observed ratio. Thus the small ($< 1\%$) charge asymmetry in the data is due to the detector and reconstruction and not interesting physics. Since the effect is only 1σ from unity and the asymmetry is consistent with the Monte Carlo, it will not be considered further.

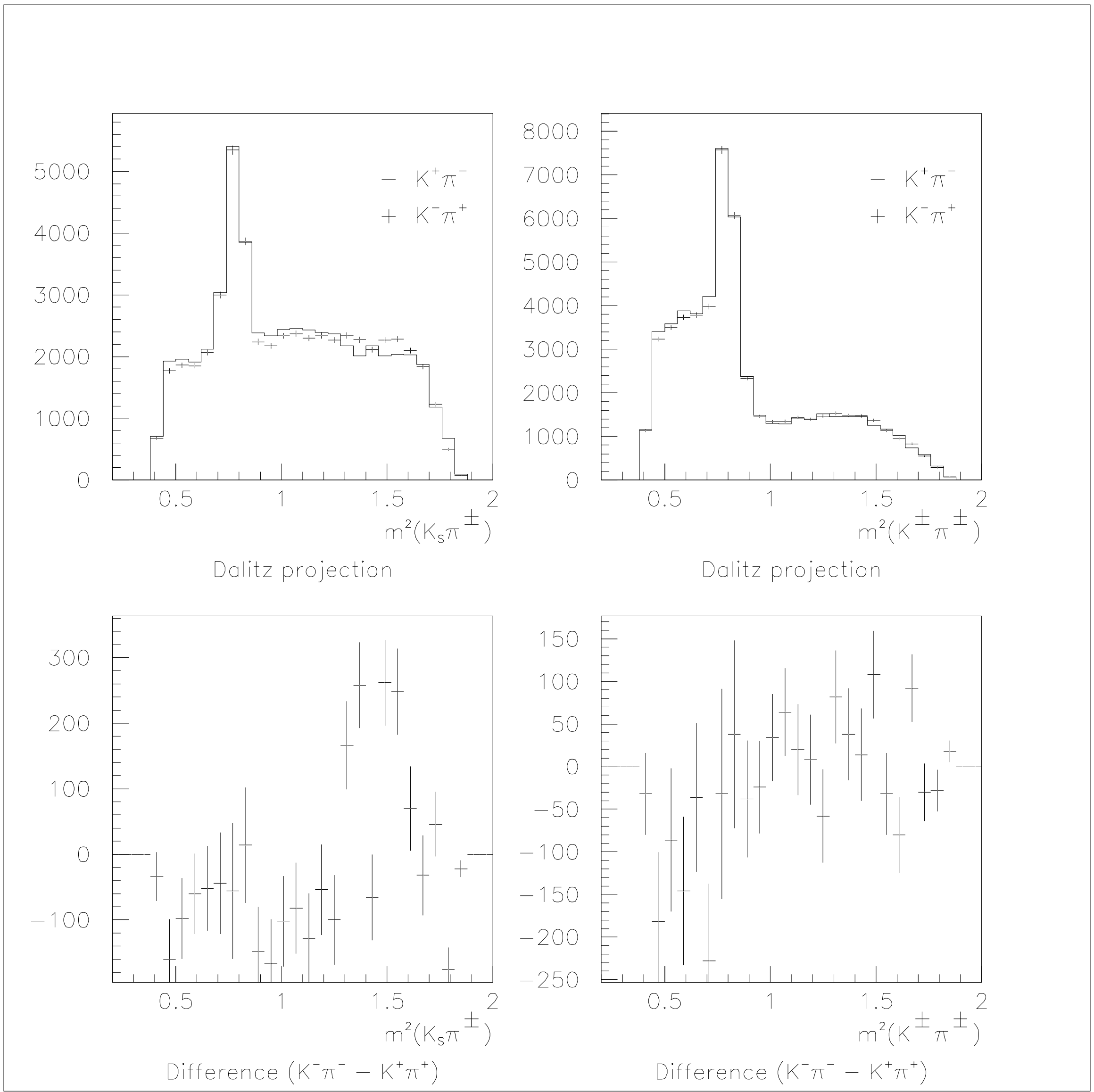

Figure 5.22: The Dalitz plot projections for each charge configuration, $K_SK^+\pi^-$ and $K_SK^-\pi^+$at top, and the differences between the two configurations at bottom. Note that only the error bars for $K_SK^-\pi^+$ are shown in the top projections; the error bars for $K_SK^+\pi^-$ are of approximately equal size. The error bars in the difference plots take into account both individual errors.

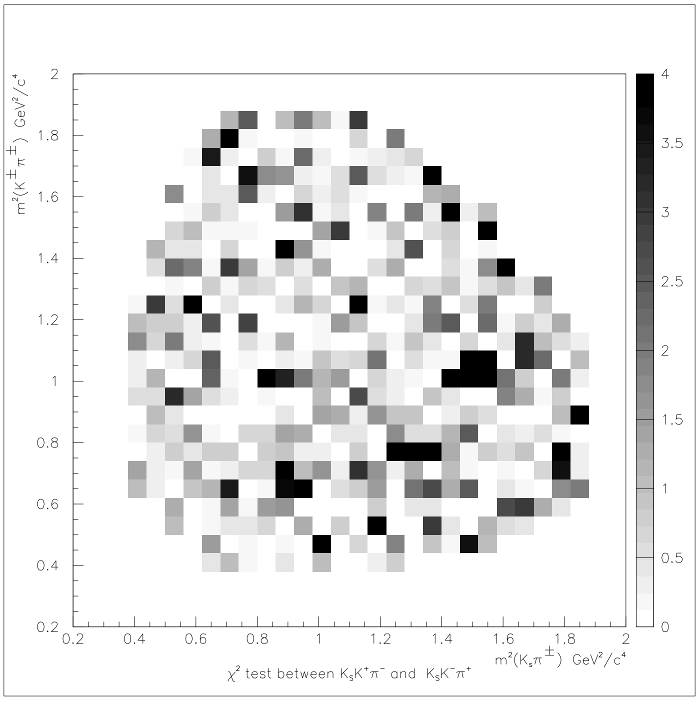

Figure 5.23: The χ^2 test between $K_S K^+\pi^-$ and $K_S K^-\pi^+$. The maximum is set to χ^2=4.0

Chapter 6

Monte Carlo Simulation

A good simulation of the experiment is necessary for several reasons.

1. Determination of corrections to the measured momenta, caused by losses in the detector.
2. Determination of overall efficiency for branching ratio calculations.
3. Determination of momentum dependent acceptance corrections to be applied to the Dalitz plot
4. Estimation of backgrounds

The first point has been discussed already in the data selection chapter 5. The second point is discussed in the branching ratio chapter 7. The final two points are discussed in this chapter, along with a discussion on the SVX positioning.

The Monte Carlo program, CBGEANT[39], is based on the general detector simulation program GEANT[40] from CERN. The program fully simulates the passage of the initially generated particles and any decay particles through all matter of the detector volume, except for the ionization of the gas in the JDC. The full JDC simulation, with tracking of delta rays, is too computationally expensive. The "fast" simulation method simply generates a statistical "time" signal for each wire that the track passes. However, the electro-magnetic and hadron interactions with the crystals is fully simulated, using the FLUKA hadronic interaction package.

6.1 Channels simulated

The signal channel $K_S K^{\pm}\pi^{\pm}$ requires the most Monte Carlo statistics in order to get a smooth acceptance correction function. We generated 1,000,000 events of $K_S K^+\pi^-$ and 1,000,000 events of $K_S K^-\pi^+$. However, since the acceptance of the trigger and data selection is smaller (about 1.5%), only about 30K events survive in the final Monte Carlo data set. This is sufficient for constraining the acceptance function, which is discussed in section 6.4.

For the purpose of background estimation, we also generated 100,000 events of the type $\pi^+\pi^+\pi^-\pi^-\pi^0$, and 100,000 events of the type $K_S K^+\pi^-\pi^0$, 10,000 events of the type $K_S K_L\pi^+\pi^-$, 100,000 events of the type $K_S\pi^+\pi^-$, and 100,000 events of the type $K_S\pi^+\pi^-\pi^0$. The later two do not conserve strangeness unless the $\pi^+\pi^-$ pair originates from K_S, thus they are supersets of the $K_S K_S$ and $K_S K_S\pi^0$ channels.

The "K_S" was the standard GEANT K_S, which decays into both neutral pions ($K_S\rightarrow\pi^0\pi^0$) and charged pions ($K_S\rightarrow\pi^+\pi^-$) , and there was no radial cut on the annihilation vertex. This explains why the efficiency for all channels was so low, since 1/3 is lost to the neutral decay, and another half or so is lost to decays inside the SVX. We used the standard K_S because these Monte Carlo data sets were used in other analyses too.

6.2 Parameters of the Monte Carlo

The Monte Carlo software is CBGEANT which is the Crystal Barrel customization of the CERN library GEANT 3.21. It includes all detector and structural components of the experiment. Most of the precise positioning of large components is not absolutely critical to having a reasonable Monte Carlo. The critical positioning parameters are the JDC sense wire positions relative to each other and the positioning of the SVX detector relative to the annihilation spot. Because there are gaps in the SVX detector, annihilations that are far from the center of the SVX can produce tracks that leak through without being detected. Because of the handedness of the SVX detector planes, this can also create a charge asymmetry; positively charged particles are more likely to pass through this gap than negatively charged particles.

The position of the SVX can be measured directly only to within a few millimeters. A more accurate position can be determined by an iterative calibration using charged tracks, which minimizes the χ^2 of the helix fits to the SVX hits by adjusting the parameters of the SVX geometry. The position and pitch of each of the 15 segments was determined in this manner. These positions were then used to define the correct geometry in the Monte Carlo. The mean shift of the SVX relative to the external JDC was determined to be about 2.5 mm to the left.

The annihilation vertex ideally lies exactly at the center of the SVX detector.

However, because of the complications of beam steering and non-ideal beam shape, the distribution of annihilation vertices can be slightly skewed or shifted. Using 4-prong triggered data, we have determined the mean position of the annihilation vertex to be (-0.24, 0.02, 0.00) ± 0.01 cm and the Gaussian 1-sigma widths to be (0.20,0.22,0.40) ± 0.01 cm. See figure 6.1 The Gaussian width is due to both physical and reconstruction uncertainties. In the $x - y$ plane, the Gaussian width is due mostly to the beam profile, while in the z plane the width is due entirely to the limited precision of z-reconstruction. (The JDC produces hits with $x - y$ errors on the order of 200 microns and z errors on the order of 1 cm.)

We generated the Monte Carlo annihilation vertex distribution with the parameters given above, except that the z width was set to 0.20 cm. The reconstruction of this simulated data produced measured means and widths consistent with the 4-prong real data.

Note that the center of the SVX was at (-0.319, -0.012) cm which is slightly off from the center of the annihilation point.

6.2.1 Vertex position

The vertex (inner and outer) is reconstructed within typically 300 microns of the generated vertex. However, there are long tails that extend to 1 cm or more. On inspection with the event display, these are due to bad pattern recognition on the tracks, where the track finding algorithm missed several hits which would have dramatically moved the track. The common problem was that these tracks either crossed several boundaries or the track ran along a sense plane or field plane.

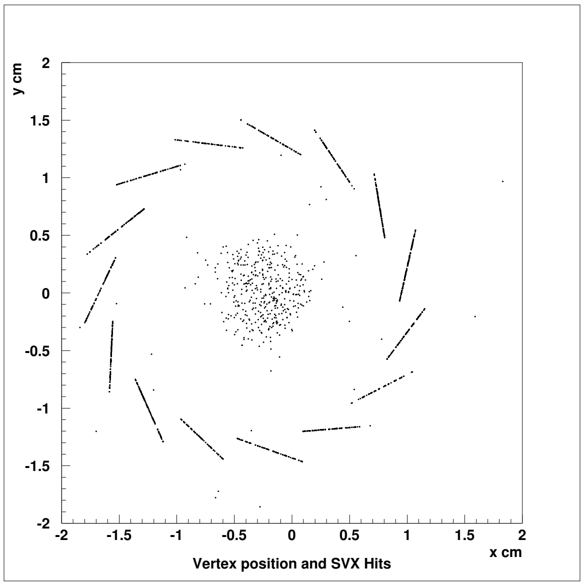

Figure 6.1: The positions of reconstructed vertices and SVX hits, showing the centering of the annihilation vertex distribution inside the SVX.

6.3 Background Estimation

The analysis channel is surprisingly low in backgrounds. The displaced vertex and mass of the $K_S \rightarrow \pi^+\pi^-$ decay is virtually background free. The biggest source of background comes from the signal channel itself, when the particles are misidentified. The remaining background comes from soft particles lost in the kinematic fit. The estimated total from all backgrounds is estimated to be no more than 0.44%. The total statistics is about 57K events, so there are about 250 background events over the entire Dalitz plot. With about 500 bins, that makes about 0.5 event per bin on average of background, while the Poisson noise of a typical bin will be $\sim \sqrt{57000/500} \sim 10$. Because the background is much smaller than the noise, no background subtraction is necessary.

Below we discuss the possible forms of background. In each case, we generate a

MC set	Efficiency	BR $[10^{-3}]$	Relative Intensity
$K_S K^{\pm}\pi^{\pm}$(signal)	1.5×10^{-2}	2.820	100.00 %
$K_S K^{\pm}\pi^{\pm}$($K\pi$ swap)	2.8×10^{-5}	2.820	0.19 %
$K_S K_S[\pi^0]$	6×10^{-5}	0.760	0.11 %
$K_S[K_L]\pi\pi$	$< 3 \times 10^{-6}$	2.600	< 0.02 %
$K\pi K_S[\pi^0]$	3×10^{-5}	5.500	0.02 %
$4\pi[\pi^0]$	$< 3 \times 10^{-8}$	178.500	< 0.01 %
$K_S K_S[\eta]$	$< 3 \times 10^{-6}$	0.410	< 0.003 %
$K_S K_S$	6×10^{-5}	0.005	0.0007 %
Total Background	–	–	0.32 to 0.44 %

Table 6.1: The estimates of primary background. The relative intensity is the product of the efficiency times the branching ratio, renormalized to the signal channel. The particles in [brackets] are lost particles.

number of Monte Carlo events of the specific background type and feed it into the same analysis chain, and count the number of events that survive all the cuts until the final Dalitz plot. This gives us the efficiency for that channel. We multiply this efficiency by the known branching ratios[1]. The results are in table 6.1.

6.3.1 $K_S K^{\pm}\pi^{\mp}(K\pi$ swapped)

This of course is the signal channel. Since the K_S is well tagged, the most likely background from the signal channel itself is reverse identification of the $K^{\pm}$ and $\pi^{\mp}$ at V0. Using Monte Carlo data, we find that only 28 ± 5 events are misidentified, which translates to 0.19 % of the Dalitz plot.

[1]Compiled by Lucien Montanet of CERN

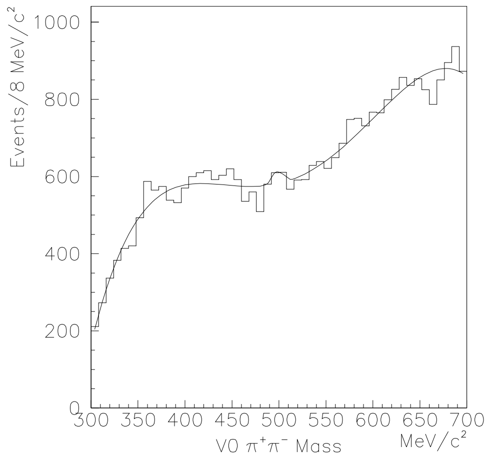

Figure 6.2: The small K_S contamination at V0. The curve is a Gaussian plus 4th order polynomial, with the small bump visible at 497 MeV.

6.3.2 $K_S K_S[\pi^0]$

The $K_S K_S[\pi^0]$ channel becomes a background when one of the K_S's decays inside the vertex. Because there is missing mass due to the lost π^0, one of the V0 pions could assume the missing energy and mimic a kaon in the kinematic fit. This turns out to be the largest background, with 0.10% of the data. Note that there is no visible π^0 peak in figure 5.21. However, we do see *some* events at the V0 vertex, which is due to the second K_S, which is seen in figure 6.2. There are 60 ± 40 events seen in the fitted Gaussian on top of the 4th order polynomial, which translates to 0.10 ± 0.07 % of the Dalitz plot. This agrees perfectly with the hypothesis that this peak is due sole to $K_S K_S[\pi^0]$.

6.3.3 $K_S[K_L]\ \pi^\pm\pi^\mp$

Out of 10000 events, no events survived into the Dalitz plot. Before the kinematic fit level, there were 4 events. The channel $K_SK_S[\pi^0]$ should have a similar kinematic fit efficiency, which was 6 out of 781 events. Thus the efficiency of $K_S[K_L]\pi^\pm\pi^\mp$ should be less than $4/10000 \times 6/781 = 3 \times 10^{-6}$.

6.3.4 $K\pi K_S[\pi^0]$

This is similar to the signal channel, except there is an additional π^0. If the π^0 is very soft and undetected in the kinematic fit, this channel can feed through. Three Monte Carlo events survived out of 100000.

6.3.5 $\mathbf{4}\pi^\pm[\pi^0]$

The $4\pi^\pm\pi^0$ channel is copiously produced in $p\overline{p}$ annihilation. However, because it lacks a tagging K_S, the feed-through is very small.

100K events were generated, but none survived all data processing cuts. We can put an upper limit on the efficiency. The last step where events existed was the after the "V0 inside target" cut, with 3 events. This is an efficiency of 3×10^{-5}. Now we compare to the $K_SK_S[\pi^0]$ channel, which should have a greater kinematic fit efficiency. This channel had 781 events at the "V0 inside target cut", and then 6 events in the Dalitz plot, or less than 10^{-3}. Thus the efficiency for $4\pi^\pm\pi^0$ should be less than 3×10^{-8}.

6.3.6 $K_S K_S[\eta]$

This is very similar to the preceding channel, $K_S[K_L]\pi^{\pm}\pi^{\mp}$; the lost η is nearly the same mass as the lost K_L, so the kinematics are the same. We didn't run any Monte Carlo for this channel, but use the same efficiency as $K_S[K_L]\pi^{\pm}\pi^{\mp}$.

6.3.7 $K_S K_S$

There is a small background from $K_S K_S$ Monte Carlo, but the branching ratio is very small. 6 events survived out of 100000 generated.

6.4 Acceptance Correction

The acceptance (or sometimes referred to the efficiency correction) of the detector varies as a function of the momenta of all particles. The biggest effect is the trigger acceptance, which is biased towards high momenta of the K_S. Also, the $\pi^{\pm}$ and $K^{\pm}$ are have low acceptances at low momentum because of curl ups or decays.

The partial wave analysis will only be accurate if the data is acceptance corrected. There are two methods of acceptance correction: The first method generates lots of Monte Carlo events, and divides the data by the Monte Carlo. The second method generates a smaller amount of Monte Carlo events and then fits a functional form, assuming some level of smoothness.

In order for the first method to work and not increase the statistical noise, the number of Monte Carlo events should be an order of magnitude more than the data. In this case, with roughly 50K data events in the Dalitz plot, we would like 500K MC events in the Dalitz plot. Our efficiency is on the order of 1.5%, so this would mean generating at least 30M MC events. With our fastest computer, we generate 100K events/day, so this would take 9 months of computing, which is clearly a waste of time.

Instead, we have generated 2M MC events of the form $K_S K^{\pm}\pi^{\pm}$ (in an equal ratio of both charge conjugate states). We then describe the net efficiency as a product of the efficiencies for each particle as a function of momentum, followed by an overall fudge-factor seventh-order polynomial. That is,

$$\epsilon_b = \frac{A_b}{A_0}\epsilon_{K^\pm}(p_{K^\pm})\epsilon_{K_S}(p_{K_S})\epsilon_{\pi^\pm}(p_{\pi^\pm})p_7(x,y) \tag{6.1}$$

where A_b is the area of bin b within phase-space, A_0 is the total area of a bin, $\epsilon_x(p_x)$ is the efficiency of particle x as a function of the momentum of particle x, and $p_7(x,y)$ is an overall seventh order polynomial in terms of the Dalitz plot variables (x,y), given in equation 6.6.

In most fits, the coefficients of the polynomial $p_7(x,y)$ are free. In a fit to just the Monte Carlo gives $(\chi^2)^{\mathrm{mc}} = 630$. When both the Monte Carlo and data are fitted simultaneously, the χ^2 due to the Monte Carlo increases, of course, to compensate for a decrease in the χ^2 due to the data. This increase, is typically small, about $\Delta\chi^2 = 20 - 30$ for the best fits.

$$E(m_{12}, m_{23}) = E_1(p_1)E_2(p_2)E_3(P_3)p_7(m_{12}, m_{23}) \tag{6.2}$$

To determine the momentum efficiency from MC, we start with the fact that the MC is generated flat in phase space. The phase space factor for a dalitz plot is

$$dLIPS = dm_{12}^2 dm_{23}^2$$

which may be also written as

$$dLIPS = dE_3 dm_{23}^2$$

or

$$dLIPS = \frac{P_3}{E_3} dp_3 dm_{23}^2$$

If we plot p_3 for each generated MC event with the weight

$$w = \frac{E_3}{p_3 \int dm_{23}^2},$$

this weighted distribution will be a constant within the limits of phase space. Deviations from this constant factor give the momentum dependence. Note that the integral is

$$\int dm_{23}^2 = m_{23}^2(max, m_{12}) - m_{23}^2(min, m_{12})$$

A plot of the weighted K_S momentum distribution is given in figure 6.3. The efficiency is zero at zero momentum, and rises roughly linearly with momentum. (The last point at the end of the plot near 750 MeV has not been weighted correctly because the bin exceeds phase space, so it should be ignored. The same would go for the lowest momentum bin, but it has zero events.) The probability of a K_S to decay outside a cylinder of radius $\rho = 1.2$ cm is

$$E_{\mathrm{SVX}}(p) = \int_{4\pi} d\Omega \exp\left(-\frac{\rho m}{p\tau \sin\theta}\right) \tag{6.3}$$

where $m = 497.672$ MeV, $\tau = 2.6762$ cm (in units where $c = \hbar = 1$). The limits of θ are determined by the JDC geometrical acceptance, but the functional form is relatively insensitive for values of $\theta = (0, 30°)$.

We plot the form of E_{svx} in figure 6.3 with the appropriate normalization to the MC distribution. We see that the E_{svx} functional form describes the MC well.

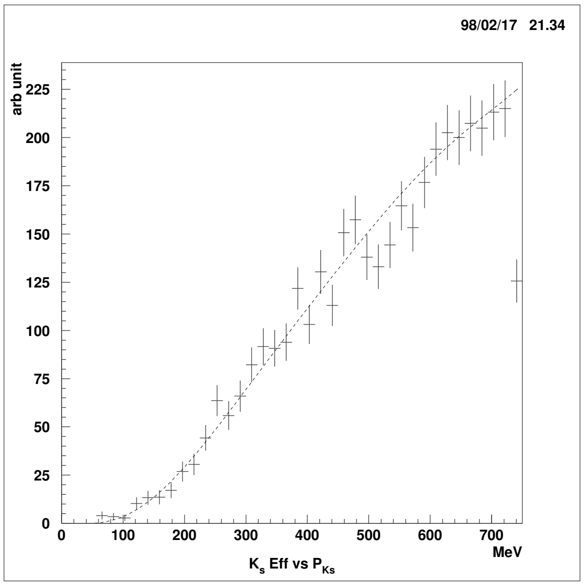

Figure 6.3: The efficiency as a function of K_S momentum. The histogram is due to the MC, while the smooth line is the functional form described in the text.

There are additional corrections from the reconstruction efficiency of each track. To put these corrections in functional form, we generated 10000 Monte Carlo events each of K^+ and π^+, distributed evenly in momentum space between 0 and 750 MeV. We then fit a parabolic function to each, with the following results.

$$E_\pi(p) = \begin{cases} (275.0 + 0.1p - 0.0002p^2)/333.3 & 125 < p \\ 275.0/333.3(p - 50.0)/75.0 & 50 < p < 125 \\ 0 & p < 50 \end{cases}$$

$$E_K(p) = \begin{cases} (84.0 + 0.47p - 0.00037p^2)/333.3 & 180 < p \\ (84.0 + 0.47p - 0.00037p^2)/(p - 140.0)/40.0/333.3 & 140 < p < 180 \\ 0 & p < 140 \end{cases}$$

$$E_{K_s}(p) = 1.0 + 0.0004p$$

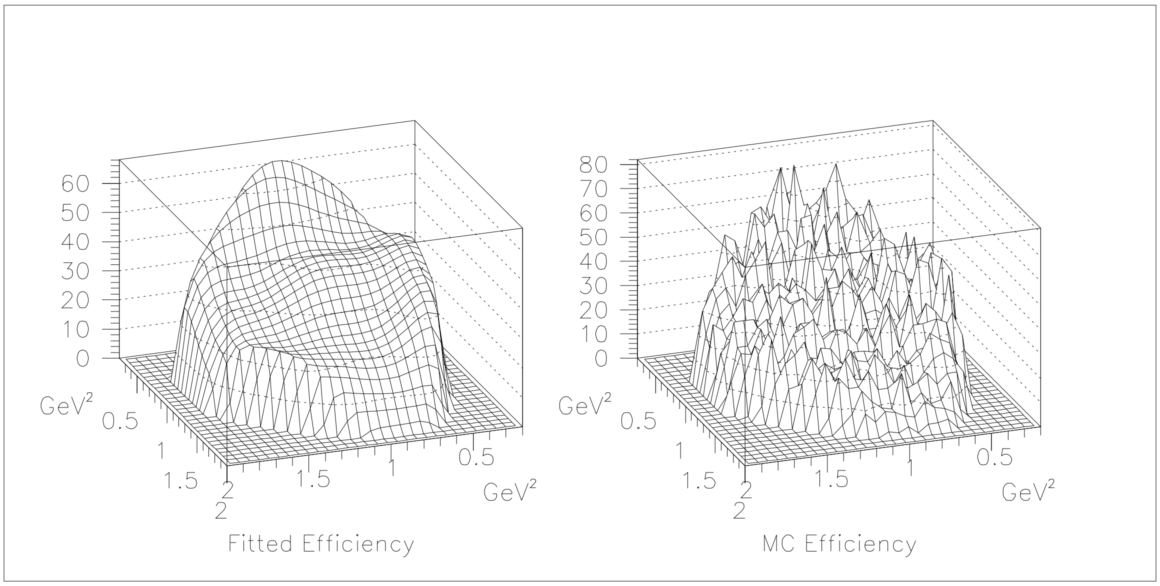

Figure 6.4: The acceptance function for the Dalitz plot. The fitted function (at left) is the result of a polynomial fit to the MC distribution (at right). The vertical scale is events per 0.06×0.06 GeV$^4/c^8$.

The seventh order polynomial is found by simultaneously fitting the Monte Carlo and the data with the same function. In truth, since there are more statistics in the data, the data probably constrains the efficiency more than the Monte Carlo. The zeroth order term of the polynomial is set to 1, so there are $7(7+1)/2 - 1 = 35$ parameters. The fitted efficiency function (6.2) is shown in figure 6.4. The polynomial is a function of x, y which are

$$x = m_{12}^2 - 1.1\text{GeV}^2/c^4 \tag{6.4}$$

$$y = m_{23}^2 - 1.1\text{GeV}^2/c^4 \tag{6.5}$$

$$p_7(x,y) = 1 + \sum_{i=1}^{7}\sum_{j=0}^{i} c_{i-j,j}\, x^{i-j} y^j \tag{6.6}$$

The coefficients are given in table 6.2. We chose a seventh order polynomial, since seven

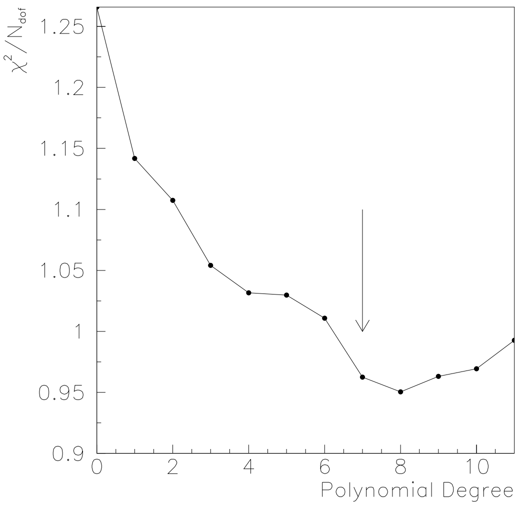

Figure 6.5: The pure efficiency fit as a function of polynomial degree

was the minimum order that gave the best χ^2/N to the data. We show the efficiency fit for orders zero through eleven in figure 6.5.

We discovered quite late into the analysis that the random number seeds used for the various runs comprising this 2 million event Monte Carlo set were not adequately "random", and that there were correlations between events. This caused the fit of the efficiency function to have an abnormally high $\chi^2/N \sim 1.7$, even when the function was expanded to 11th order. When each individual Monte Carlo run was individually fit (each with its own seed), the $\chi^2/N \sim 0.96$ to 1.2 at 7th order, regardless if the run was 100K, 200K, 300K or 500K events. Any combination of two runs caused the χ^2 to increase enormously to $\chi^2/N \sim 1.4$ to 1.6. In the interest of time, we did not regenerate the full statistics using the correct seeds, but used the only 500K event set of $K_S K^- \pi^+$, which fit the efficiency function with $\chi^2/N = 0.96$. We have shown in chapter 5 that the data is charge independent, so

Term	Coefficient	Term	Coefficient	Term	Coefficient
x	-0.07 ± 0.24	y	-0.95 ± 0.22	x^2	-1.5 ± 0.65
xy	-0.67 ± 0.72	y^2	-2.2 ± 0.73	x^3	-3.0 ± 3.1
x^2y	9.2 ± 2.9	xy^2	-1.3 ± 3.4	y^3	8.1 ± 2.3
x^4	8.1 ± 3.5	x^3y	1.9 ± 5.5	x^2y^2	10.5 ± 8.5
xy^3	-6.7 ± 6.4	y^4	17.1 ± 4.0	x^5	16.1 ± 13.
x^4y	-19.0 ± 12.	x^3y^2	-21.7 ± 20.	x^2y^3	-55.7 ± 17.
xy^4	35.5 ± 15.	y^5	-33.8 ± 8.4	x^6	-12.5 ± 5.7
x^5y	-1.0 ± 12.	x^4y^2	-14.5 ± 20.	x^3y^3	18.1 ± 23.
x^2y^4	-13.9 ± 25.	xy^5	27.6 ± 14.	y^6	-29.0 ± 6.0
x^7	-23.0 ± 16.	x^6y	7.8 ± 19.	x^5y^2	54.3 ± 33.
x^4y^3	76.5 ± 40.	x^3y^4	23.3 ± 46.	x^2y^5	110.0 ± 34.
xy^6	-66.4 ± 23.	y^7	43.6 ± 10.		

Table 6.2: The coefficients for the seventh order “fudge-factor” polynomial

this single run is equivalent to using both $K_SK^-\pi^+$ and $K_SK^+\pi^-$.

Chapter 7

Absolute branching ratio measurement

In order to calculate the total branching ratio, minimum bias events are counted and then corrected for acceptance. To select the proper events, we use the same cuts as in chapter5, except for one difference. Because we do not need to simulate the online K_S trigger, we do not apply the trigger simulator to the Monte Carlo.

Of 154 300 generated $K_S K^{\pm}\pi^{\pm}$ Monte Carlo events, 5660 are accepted into the final Dalitz plot.

There were 867 995 minimum bias events collected during the April 1996 run. The minimum bias trigger simply requires an incoming $\bar{p}$ and no outgoing $\bar{p}$ downstream. Of these, 86 survive into the $K_S K^{\pm}\pi^{\pm}$ Dalitz plot after applying all of the same cuts there were applied to the triggered data, except for the online trigger condition. These 86 events are well spread over the Dalitz plot, as shown in figure 7.1.

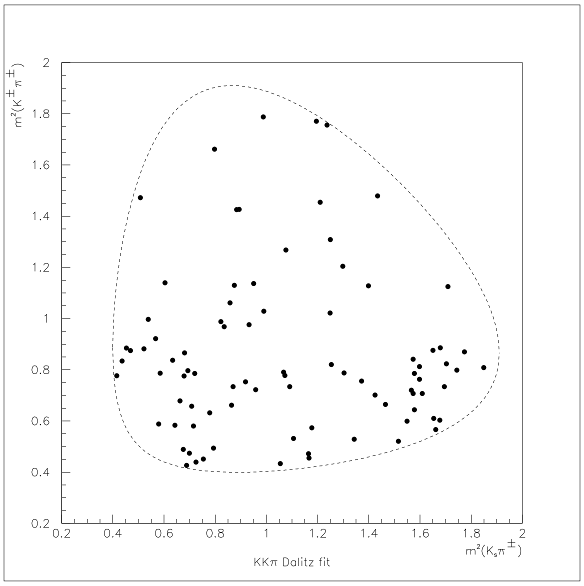

Figure 7.1: The Dalitz plot from 86 minimum bias events. The rightmost data point is discussed in the text.

Because the acceptance varies considerably, each event must be individually corrected, rather than taking the total number of events and dividing by the acceptance.

To correct for the acceptance variation, the

$$N_{\text{mb-cor}} = \frac{N_{\text{mc-tot}} A_i}{A_{\text{tot}}} \sum_{\text{events}\, i} \frac{1}{n_i}$$

where A_{tot} and A_i are the areas of the total Dalitz plot and the bin, respectively,

$$A_{\text{tot}} = 1.71126\,\text{Gev}^4/c^8 \tag{7.1}$$

$$A_i = 0.06\,\text{GeV}^2/c^4 \times 0.06\,\text{GeV}^2/c^4 = 0.0036\,\text{Gev}^4/c^8 \tag{7.2}$$

$$N_{\text{mc-tot}} = 154\ 300, \tag{7.3}$$

and n_i is the number of Monte Carlo events in the closest bin to the i-th minimum bias event. For bins on the boundary of phase space, the value of n_i is corrected by dividing by the fractional area within phase space. This gives

$$N_{\text{mb-cor}} = 2390^{+330}_{-260}$$

where the negative error is statistical and the positive error is due to one specific minimum bias event that appears to be an outlier. This event is the right-most dot on the Dalitz plot in figure 7.1.

Thus the branching ratio is

$$\begin{aligned} BR(K_S K^{\pm}\pi^{\pm}) &= \frac{N_{\text{mb-cor}}}{N_{\text{mb-tot}}} && (7.4)\\ &= \frac{2390^{+330}_{-260}}{867\,995} && (7.5)\\ &= (2.7^{+0.4}_{-0.3}) \times 10^{-3} && (7.6) \end{aligned}$$

This agrees within 2σ with Baresh *et al.* [41] ($\frac{1}{2}\text{BR}(K^0 K^{\pm}\pi^{\mp}) = (2.13 \pm 0.28) \times 10^{-3}$), and within 1σ with Armenteros *et al.* [20] ($\text{BR}(K_S K^{\pm}\pi^{\pm}) = (2.82 \pm 0.11) \times 10^{-3}$) and with the equivalent Crystal Barrel result[21] $\text{BR}(K_L K^{\pm}\pi^{\mp}) = (2.91 \pm 0.34) \times 10^{-3}$).

As these are all independent measurements, the error-weighted average of all four measurements is

$$\text{BR}(K_S K^{\pm}\pi^{\pm}) = (2.68 \pm 0.14) \times 10^{-3}. \qquad (7.7)$$

Chapter 8

Partial Wave Analysis

8.1 Introduction to Partial Wave Analysis

The primary purposes of this analysis are to quantitatively measure the masses, widths and branching ratios of the intermediate isobar resonances involved in the reaction $K_S K^{\pm}\pi^{\pm}$. Up to this point, the data selection has worked to select out the three final state particles, but has not made any requirements on the isobars.

Selection of the isobars is not a trivial task. Because the isobars decay via the strong interaction, their lifetimes are very short and hence widths are very wide. A typical isobar width is on the order of 100 MeV, much wider than the experimental resolution. Therefore one can not simple count the number of events in a narrow mass window to measure the isobars. More importantly, since there are many wide isobars in the same reaction, there is a lot of overlap, causing quantum mechanical interferences between the resonances.

Thus in order to determine the masses, widths and especially branching ratios of the resonances, a full theoretical calculation of the quantum mechanical amplitude is necessary. Each amplitude due to each resonance must be carefully summed, either coherently or incoherently as necessary.

We wish to calculate this amplitude using the fewest number of independent observables. For this, we use a Dalitz plot.

8.1.1 Dalitz plot

The differential Lorentz Invariant Phase Space (dLIPS) is given by

$$d\Phi(P;p_1,\ldots p_n) = \prod_{i=1}^{n} \frac{d^3p_i}{(2\pi)^3 2E_i}$$

where P is the total four-momentum and p_i the four-momentum of particle i. Since $n = 3$ for $p\overline{p}\rightarrow K_S K^{\pm}\pi^{\pm}$, there are 12 parameters (p_i^{μ}) describing phase space. Since all of the particles are identified and have a unique mass, this removes 3 arbitrary parameters ($p_0 = \sqrt{p_i p^i + m^2}$), leaving 9 parameters. We have applied a 4C kinematic fit to the data, requiring total energy and momentum conservation. Thus the number of parameters describing the phase space is further reduced by 4 to 5, and dLIPS becomes

$$d\Phi(p_1,\ldots p_n) = \int_P \delta^4(P - \sum_{i=1}^{n} p_i) d\Phi(P;p_1,\ldots p_n)$$

which simplifies to the 5 parameter expression

$$d\Phi(E_1,E_3,\alpha,\beta,\gamma) = \frac{1}{8(2\pi)^9} dE_1\ dE_3\ d\alpha\ d(\cos\beta)\ d\gamma$$

where E_1, E_3 are the energies of two of the three particles and α,β,γ are the Euler angles that describe the plane of the final three particles. At-rest annihilation is not polarized, so there is no external orientation that affects the physics, so we integrate over the three Euler angles, reducing the parameters to only 2,

$$d\Phi(E_1, E_3) = \frac{1}{4(2\pi)^7} dE_1\ dE_3.$$

The energy values E_i are dependent on the total center-of-mass energy, but we prefer Lorentz invariant quantities. We note that in the center of mass system where $P = (\sqrt{s}; 0, 0, 0) = p_1 + p_2 + p_3$,

$$\begin{aligned} m_{12}^2 &= (p_{12})^2 && (8.1) \\ &= (P - p_3)^2 && (8.2) \\ &= P^2 + p_3^2 - 2(EE_3) + 2\vec{P}\cdot\vec{p_3} && (8.3) \\ &= \sqrt{s}^2 + m_3^2 - 2(\sqrt{s}E_3) && (8.4) \\ d(m_{12}^2) &= 0 + 0 - 2\sqrt{s}\ dE_3. && (8.5) \end{aligned}$$

Thus were can substitute $dE_1 = -\frac{1}{2\sqrt{s}} m_{23}^2$ and $dE_3 = -\frac{1}{2\sqrt{s}} m_{12}^2$ and get

$$d\Phi(m_{12}^2, m_{23}^2) = \frac{1}{16(2\pi)^7\sqrt{s}^2} dm_{12}^2\ dm_{23}^2.$$

Then the rate of the process is just

$$\begin{aligned} \Gamma &= \frac{(2\pi)^4}{2\sqrt{s}}\ |\mathbf{M}|^2\ d\mathrm{LIPS} && (8.6) \\ &= \frac{1}{(2\pi)^3 32\sqrt{s}^3}\ |\mathbf{M}|^2\ dm_{12}^2\ dm_{23}^2 && (8.7) \end{aligned}$$

where the coefficient is a constant over the Dalitz plot. This simple expression shows that the intensity of the Dalitz plot at a point (m_{12}^2, m_{23}^2) is directly proportional to the matrix element squared. There is no additional phase space term.

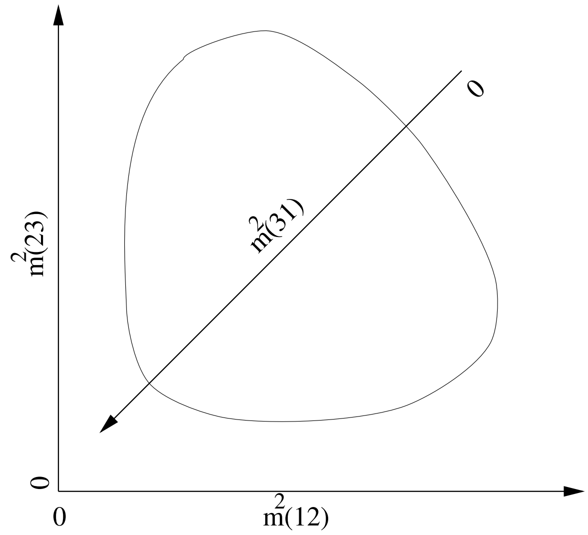

Figure 8.1: The Dalitz plot m^2 axes.

The particles are labeled in this fashion: 1=a=K_S, 2=b=$\pi^{\pm}$, 3=c=$K^{\pm}$. The Dalitz plot has two orthogonal axes, m_{12}^2 and m_{23}^2; the third axis m_{31}^2 is measured diagonally, starting with zero at upper-right and increasing while moving to the left and down, as seen in figure 8.1. In this Dalitz plot,

Axis	Equivalent	Example Isobar
m_{12}^2	$m^2(K_S\pi^{\pm})$	$K^*(892)^{\pm}$
m_{23}^2	$m^2(K^{\pm}\pi^{\mp})$	$K^*(892)^0$
m_{31}^2	$m^2(K_SK^{\pm})$	$a_2(1320)^{\pm}$

8.2 The total intensity

As discussed in chapter 3, the different initial states of $p\overline{p}$ are produced incoherently. Thus each the contribution from each initial state is added incoherently. For a specific initial state, all amplitudes that produce the same final state are added coherently. The

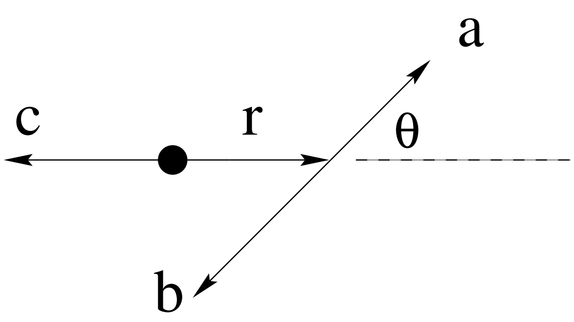

Figure 8.2: The isobar model showing $p\overline{p}\rightarrow r+c$, $r\rightarrow a+b$

intensity of the Dalitz plot is calculated as

$$I(m_{ab}^2, m_{bc}^2) = \sum_{\text{initial states},J_z} \left| \sum_{r,L,\text{axes}} A_r(\vec{J}, L, l, m_{ab}, m_{bc}) \right|^2 \tag{8.8}$$

The sum over axes represents the three pair-wise combinations of the final particles.

8.3 The matrix element

The matrix element A of the process (see figure 8.2)

$$\begin{aligned} p\overline{p}\rightarrow \quad & r + c \\ & \hookrightarrow a + b. \end{aligned}$$

is given by

$$A_r(\vec{J}, L, l, m_{ab}, m_{bc}) = Z(\vec{J}, L, l, \cos\theta) F_L(p_{rc}) \hat{T}_r(m_{ab}), \tag{8.9}$$

where

r	is the resonance particle
a,b	are the decay particles of the resonance r
c	is the spectator particle
J	is the total angular momentum of entire system ($p\overline{p}$ or rc)
L	is the orbital angular momentum between r and c
l	is the orbital angular momentum between a and b
$\vec{p}_{rc}$	is the break-up momentum in the $r-c$ system
$\vec{q}_{ab}$	is the break-up momentum in the $a-b$ system
$\cos\theta_{ac}$	is the angle between $\vec{p}$ and $\vec{q}$ in the $a-b$ system.
m_{ab}	is the invariant mass of the $a-b$ system
$Z()$	is the Zemach function which describes the angular distribution of the particles
$F()$	is the Blatt-Weisskopf barrier factor for the production of $r-c$ with angular momentum L
$\hat{T}_r()$	is the dynamical function describing the width of resonance r

Note that some of these parameters are redundant. $\cos\theta$ is derived from $\vec{p}$ and $\vec{q}$, which are in turn derivable from m_{12}^2 and m_{23}^2.

8.4 The Zemach formalism

The Zemach functions[42] are used to describe the angular distributions of the decays of the resonances. An unpolarized particle in free space decays uniformly. However, because of the coupling of the two orbital angular momenta L and l to J, certain magnetic sub-states are forbidden by the Clebsch-Gordan coefficients. For example, let us pick a reaction with $L = 1$ and $\hat{z}$ defined along the direction of $\vec{p}$, the resonance momentum. Then

$$L_z = \hat{z} \cdot \vec{L} \sim \vec{p} \cdot (\vec{p} \times \vec{r}) = 0.$$

Then the state $|L\ L_z\rangle = |1\ 0\rangle$ is empty while the states $|1\ \pm 1\rangle$ are not. This essentially polarizes the resonances along their momentum direction, and thus the decay pattern is governed by the shapes of the $Y_l^m(\theta\,\phi)$ spherical harmonics. In general the magnetic states are populated symmetrically in m, so all distributions are symmetric in $\cos\theta$. In addition, because there is only one axis of polarization $\hat{z}$, the azimuthal decay distribution is flat. The distributions as calculated by Zemach are given in table 8.2 if one sets the relativistic correction parameter z to zero, see (8.10).

The formalism is based on the Wigner-Eckart theorem, which separates a matrix element into the angular part (which is the Zemach tensor) and into the the reduced matrix element which does not depend on the orientation in space. The recipe for forming the Zemach tensor is as follows.

Construct a representation of the angular momentum group, and then form combinations of the elements that transform in the desired way. For instance, consider coupling $L = 1$ (quantized on the $\hat{\vec{p}}$ axis) with $L = 1$ (quantized on the $\hat{\vec{q}}$ axis to get $L = 0$ (on any axis). An $L = 1$ state transforms as a 3-component vector (e.g. Y_1^m with $m = -1, 0, +1$); let us choose the axis of quantization to represent it. The final $L = 0$ transforms as a scalar; $\hat{\vec{p}} \cdot \hat{\vec{q}} = \cos\theta$ also transforms as a scalar. Then the amplitude due to coupling transforms as that scalar, and the intensity $|A|^2$ transforms as $\cos^2\theta$, which is the right answer. An $L = 2$ state transforms as a 5-component tensor (e.g. Y_2^m with $m = -2, -1, 0, +1, +2$).

First construct the Zemach tensors for $L = 0, 1, 2$ and $l = 0, 1, 2$ S(see table 8.1). Then contract the tensors together, using δ_{ij} or ϵ_{ijk} as necessary, to get a tensor with the proper rank of J. For rank-2 tensors, take linear combinations to verify that the final tensor is traceless and symmetric. This final tensor i

The components of the coupled tensor are amplitudes of each of the components of angular momentum J. Because the coherence between different $|J_z\rangle$ states of the same J is destroyed by the $p\overline{p}$ annihilation cascade, the amplitudes due to each state of J_z are summed incoherently.

The Zemach formalism is restricted to reactions where a, b and c are spin-0 particles, which applies in this case. For final states with vector particles (ω, γ), the helicity formalism is needed.

Even though the Zemach formalism has been used successfully in $p\overline{p}$ annihilation analyses for thirty years, it is not covariant. A covariant form (the Rarita-Schwinger form) has been given by Filippini *et al.*[43]. The authors suggest that there can be significant differences for certain resonances in certain initial states due to the relativistic corrections. The fact there are non-uniform distributions at all is given by the fact that certain magnetic sub-states of the angular momentum are not populated evenly. The relativistic effect causes even more uneven population of the magnetic states because of the Lorentz boost.

The present analysis has been done using the non-relativistic Zemach functions. In table 8.2 we show the relativistic Zemach functions. They are functions of z,

$$z = |p_{rc}|/m_r = \sqrt{\gamma^2 - 1} \tag{8.10}$$

In the non-relativistic limit of $\beta \rightarrow 0$ or $\gamma \rightarrow 1$, then $z = 0$. The largest z comes from the lightest and fastest moving resonances, i.e. the $K^*(892)$. The following table gives the z^2 values for the different spin-1 or spin-2 isobars. Spin-0 isobars always decay uniformly.

Intermediate	p	m range	z^2
K_1^*K	618	865 to 915	0.53 to 0.43
$a_2(1320)\pi$	458	1220 to 1420	0.19 to 0.07
$\rho(1450)\pi$	357	1350 to 1550	0.10 to 0.03
K_2^*K	0	1330 to 1430	0.02 to 0.00

Looking at table 8.2, one can see that there are *no* relativistic corrections for any state coming from $^1S_0$. From $^3S_1$ annihilation there is only one function that is affected by the relativistic correction ($\langle J|L\ l\rangle = \langle 1|2\ 2\rangle$). The $a_2(1320)\pi$ contribution from this initial

Rank (L)	N_F $(2L+1)$	Tensor
0	1	$P = 1$
		$Q = 1$
1	3	$\overline{P}_i = \hat{\vec{p}}_i$
		$\overline{Q}_i = \hat{\vec{q}}_i$
2	5	$\overline{\overline{P}}_{ij} = \hat{\vec{p}}_i\hat{\vec{p}}_j - \frac{1}{3}\delta_{ij}$
		$\overline{\overline{Q}}_{ij} = \hat{\vec{q}}_i\hat{\vec{q}}_j - \frac{1}{3}\delta_{ij}$

$J = L \oplus l$	Coupled Tensor
$0 = 0 \oplus 0$	$Z = PQ$
$0 = 1 \oplus 1$	$Z = \overline{P}_i\overline{Q}_i$
$0 = 2 \oplus 2$	$Z = \overline{\overline{P}}_{ij}\overline{\overline{Q}}_{ij}$
$1 = 0 \oplus 1$	$\overline{Z}_i = P\overline{Q}_i$
$1 = 1 \oplus 0$	$\overline{Z}_i = \overline{P}_i Q$
$1 = 1 \oplus 1$	$\overline{Z}_i = \epsilon_{ijk}\overline{P}_j\overline{Q}_k$
$1 = 2 \oplus 1$	$\overline{Z}_i = \overline{\overline{P}}_{ij}\overline{Q}_j$
$1 = 1 \oplus 2$	$\overline{Z}_i = \overline{P}_j\overline{\overline{Q}}_{ji}$
$2 = 0 \oplus 2$	$\overline{\overline{Z}}_{ij} = P\overline{\overline{Q}}_{ij}$
$2 = 2 \oplus 0$	$\overline{\overline{Z}}_{ij} = \overline{\overline{P}}_{ij}Q$
$2 = 1 \oplus 2$	$\overline{\overline{Z}}_{ij} = T \cdot S(\epsilon_{ikl}\overline{P}_k\overline{\overline{Q}}_{lj})$
$2 = 2 \oplus 1$	$\overline{\overline{Z}}_{ij} = T \cdot S(\epsilon_{jkl}\overline{\overline{P}}_{ik}\overline{Q}_l)$
$2 = 2 \oplus 2$	$\overline{\overline{Z}}_{ij} = T \cdot S(\overline{\overline{P}}_{ik}\overline{\overline{Q}}_{kj})$

Table 8.1: The definitions of the P and Q Zemach tensors (left) and the coupling of the P and Q tensors to form the Z tensor (right). $S()$ is the symmetrization operator $S(X_{ij}) = \frac{1}{2}(X_{ij} + X_{ji})$, and $T()$ is the trace-removing operator, $T(X_{ij}) = X_{ij} - \frac{1}{3}\delta_{ij}\mathrm{Tr}(X)$

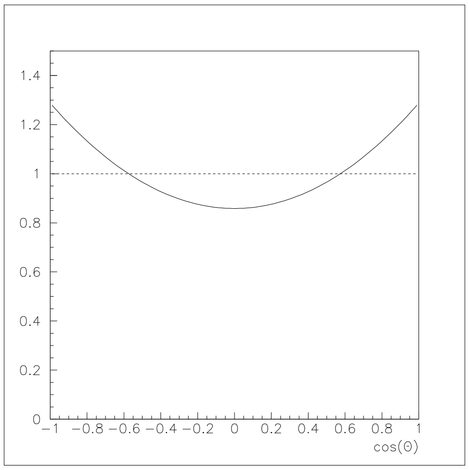

Figure 8.3: The decay distribution of the K^* from $^1P_1$ or $^3P_1$, calculated non-relativistically (dotted line) and relativistically (solid line)

state is about 2% according to the partial wave analysis, and the $z^2 \sim 0.13$ so this is a small effect.

In P-wave annihilation, only the $\rho(1450)\pi$ and K_1^*K isobars have significant amplitude, and of these two only the K_1^*K amplitude has a significant z factor for relativistic distortion of the angular amplitude, shown in figure 8.3. The non-relativistic flat distribution begins to look more like $\sim 1 + \cos^2\theta$. Because the K_1^*K also originates from $^1S_0$ and $^3S_1$ initial states, this error can be compensated in the fit by increasing the $^1S_0$ contribution.

In order to determine the impact on the K_1^*K branching ratio, we have repeated the fit using *no* $K_1^*(892)K$ contribution from $^1P_1$. The total branching ratio for the $K_1^*(892)K$ decreased by only 5%. Because the relativistic distortion effect is much smaller than total removal of the entire partial wave, we estimate that the error that the distortion brings to the branching ratio at less than 2%, which is smaller than the statistical error in table 9.2.

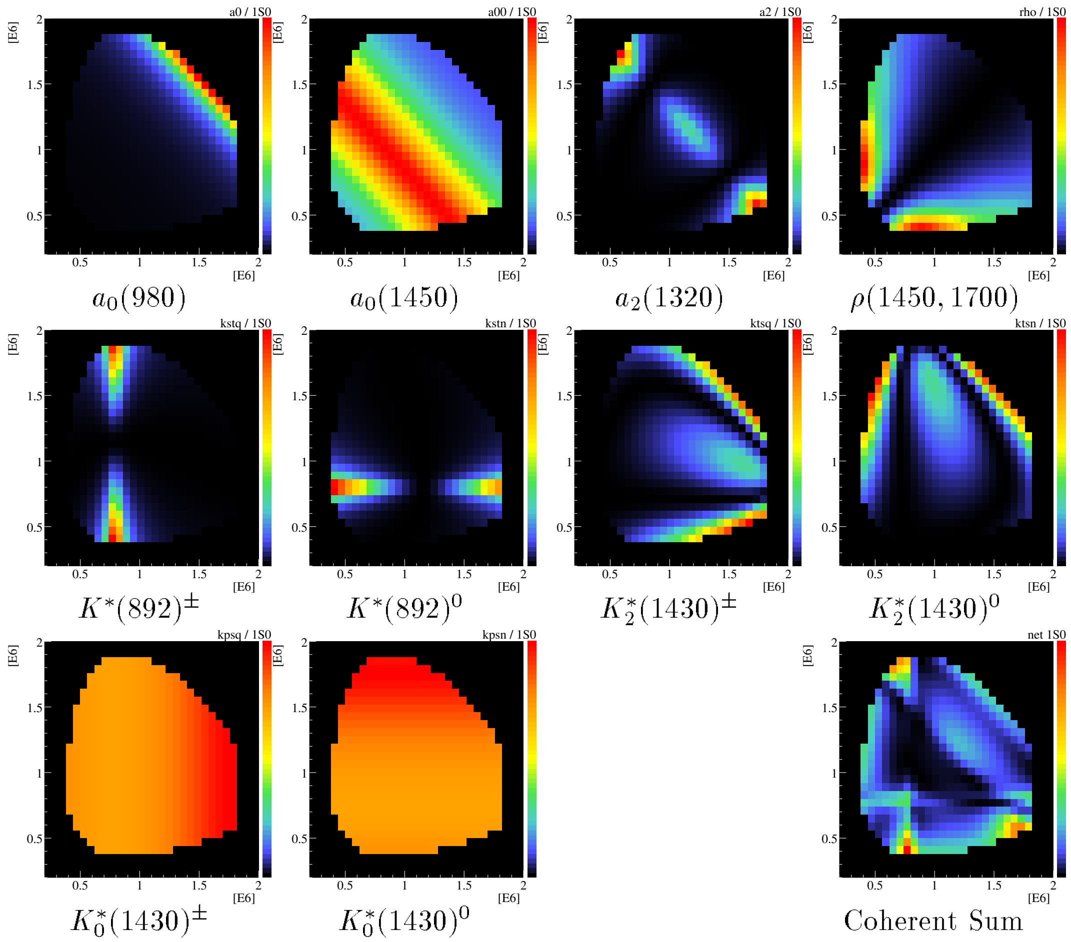

Figure 8.4: The ${}^1S_0$ Partial Waves

State	J	L	l	Angular distribution	$z \neq 0$?	Isobars
$^1S_0$	0	0	0	1		K_0^*K, $a_0\pi$
	0	1	1	$\cos^2\theta$		K_1^*K, $\rho\pi$
	0	2	2	$(\cos^2\theta - \frac{1}{3})^2$		K_2^*K, $a_2\pi$
$^3S_1$	1	1	1	$\sin^2\theta$		K_1^*K, $\rho\pi$
	1	2	2	$-(1+z^2)-2+4z^4\cos^4\theta+4z^2\cos^2\theta+(1+z^2)^2+16(1+z^2)\cos^2\theta-16(1+z^2)^2\cos^4\theta$ which simplifies to $(\cos\theta\sin\theta)^2$ if $z=0$	•	K_2^*K $a_2\pi$
$^1P_1$ and $^3P_1$	1	0	1	$1+z^2\cos^2\theta$	•	K_1^*K, $\rho\pi$
	1	2	1	$1+(3+4z^2)\cos^2\theta$	•	–
	1	1	0	1		K_0^*K, $a_0\pi$
	1	1	2	$(1+z^2)\left[\frac{1}{3}\cos^2\theta+3z^2(\cos^2\theta-\frac{1}{3})^2\right]$	•	K_2^*K $a_2\pi$

Table 8.2: Relativistic Zemach Angular distribution functions. Those which depend on z are marked with a bullet.

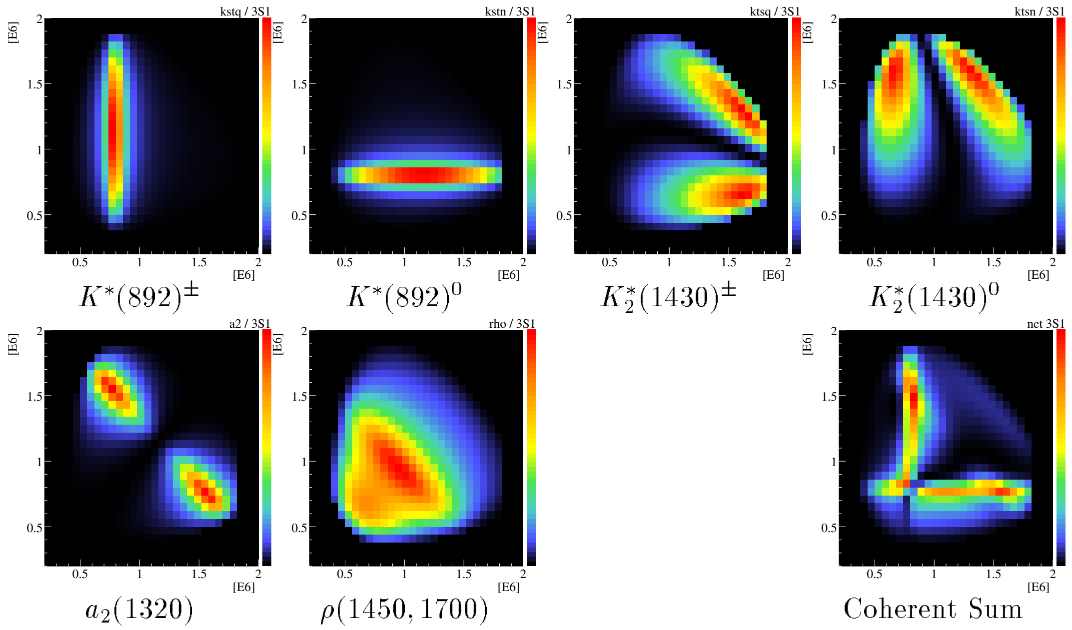

Figure 8.5: The $^3S_1$ Partial Waves

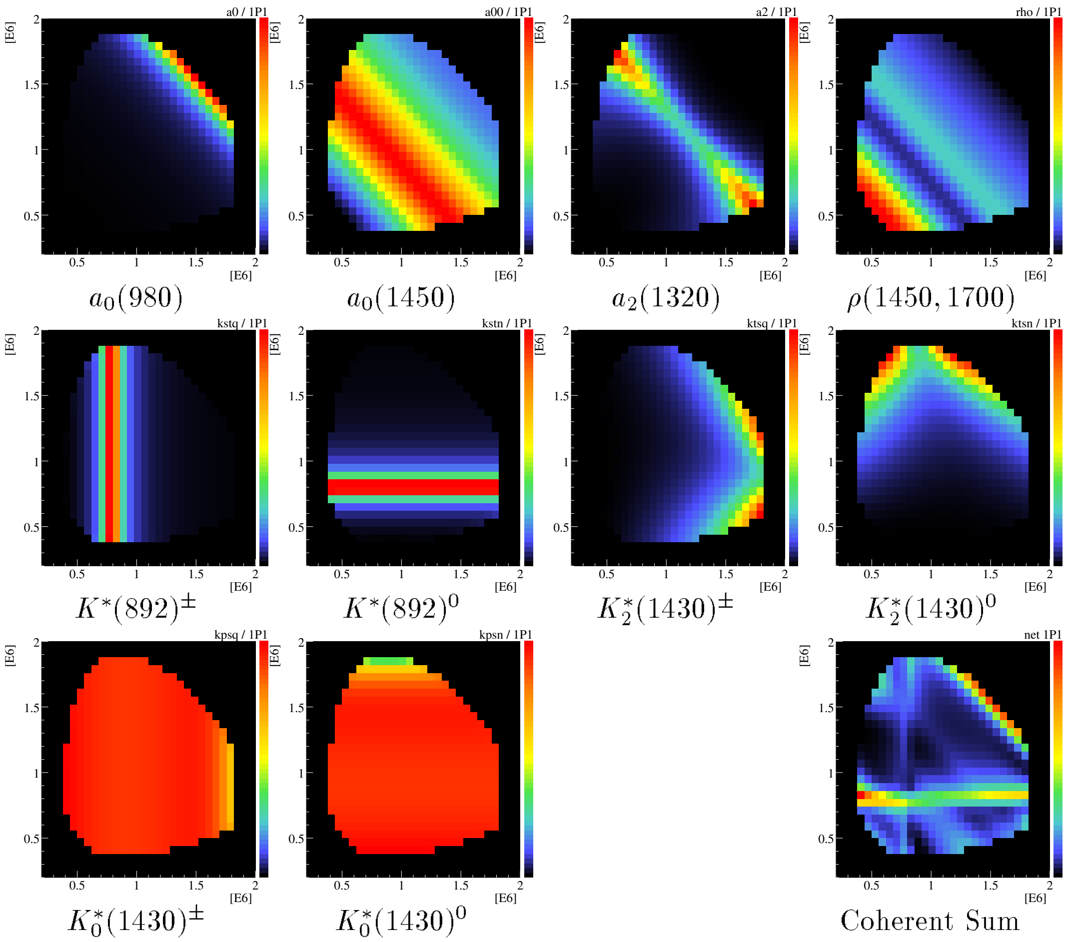

Figure 8.6: The $^1P_1$ and $^3P_1$ Partial Waves

8.5 Two-body breakup momentum and phase space

The breakup momentum for a system into two particles with masses m_a and m_b is

$$q_{ab} = \frac{\sqrt{[m_{ab}^2 - (m_a + m_b)^2]\,[m_{ab}^2 - (m_a - m_b)^2]}}{2m_{ab}}$$

where m_{ab} is the invariant mass of the system.

The phase space of a two body decay is

$$\rho(m_{ab}) = \frac{2q_{ab}}{m_{ab}}.$$

8.6 Angular barrier factor

Because the strong force only works over small distances, i.e. 1 fm, the maximum angular momentum L possible in a strong decay is limited by the linear momentum p

$$\vec{L} = \vec{r} \times \vec{p} \tag{8.11}$$

$$L = (1\ \text{fm}) \cdot |p|. \tag{8.12}$$

In other words, decay particles moving very slowly with an impact parameter of order of the size of the resonance (i.e. 1 fm) can not generate enough angular momentum to conserve the spin of the resonance. The functions calculated by Blatt and Weisskopf[44] weight the reaction amplitudes to account for this spin-dependent effect. The functions $F_L(z)$ for resonances with $L = 0, 1, 2$ are

$$F_0(q) = 1 \tag{8.13}$$

$$F_1(q) = \sqrt{\frac{z}{z+1}} \tag{8.14}$$

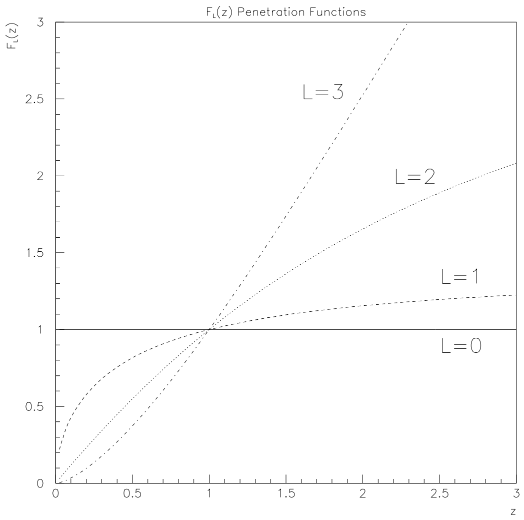

Figure 8.7: The Blatt-Weisskopf functions for $L = 0, 1, 2$

$$F_2(q) \quad = \quad \sqrt{\frac{13z^2}{(z-3)^2 + 9z}} \tag{8.15}$$

where the unitless quantity $z = (qR)^2$ is in terms of the breakup momentum q and the range of the interaction, 1 fermi or $R = 1/200\ \mathrm{MeV}^{-1}c$. See figure 8.7 for the shape of these functions.

It is convenient to define the normalized Blatt-Weisskopf functions

$$B^L(q, q_0) = \frac{F_L(q)}{F_L(q_0)} \tag{8.16}$$

where q_0 is the value of q on resonance.

These functions appear in two places. The first place is as a momentum-dependent correction to the "width" of a resonance Γ_0. The second is as a momentum-dependent correction to the overall amplitude, which appears in the production factors.

8.7 Dynamical functions $\hat{T}_r(m)$

Nearly all resonances in $p\overline{p}$ physics are characterized by the complex energy poles (E_0) of the transition matrix $\hat{T}$,

$$E_0 = m_0 - i\Gamma_0/2 \tag{8.17}$$

where the real part m_0 is the central resonance mass and the imaginary part $i\Gamma_0/2$ contains the defined width.

8.7.1 Breit-Wigner

One of the simplest forms for T is the Breit-Wigner form, which is derived from 2-particle partial wave scattering phenomenology for narrow resonances ($\Gamma \ll m_0$). Briefly, the elastic scattering amplitude (non-relativistic) is

$$f = \frac{1}{\cot\delta - i}$$

which has a maximum at $\delta = \pi/2$. If $\Gamma_0/m_0 \ll 1$, and defining $2/\Gamma = d\ \cot\delta/d\ m|_{m=m_0}$, this can be written as

$$f \approx \frac{\Gamma_0/2}{(m_0 - m) - i\Gamma_0/2}$$

where m is the invariant mass of the decay particle system, where Γ is defined in terms of a fast moving phase. Note the pole positions are in the correct place, as given by (8.17). The relativistic form is written as

$$f = \frac{\Gamma_0 m_0}{(m_0^2 - m^2) - i m_0 \Gamma_0}, \tag{8.18}$$

again with the T pole position in the same spot (but only if $\Gamma_0 \ll m_0$).

Of course, since many resonances are wide, the assumption $\Gamma_0 \ll m_0$ does not hold well. This was first noted in the ρ-meson ($\Gamma_0/m_0 = 150/770 = 19\%$) where deviations from the Breit-Wigner are visually apparent. In this case, the Breit-Wigner is given a varying width, which is usually proportional to the phase-space of the decaying particles. In addition, resonances with spin have a dependence on momentum due to the centrifugal barriers (equation 8.16). Thus the improved Breit-Wigner looks like

$$f = \frac{\Gamma_0 m_0 B^l(q, q_0)}{(m_0^2 - m^2) - i m_0 \Gamma_0 \left[\frac{\rho(m)}{\rho(m_0)}\right] \left[B^l(q, q_0)\right]^2} \tag{8.19}$$

where $\rho(m)$ is the phase space and $B^l(q, q_0)$ are the normalized Blatt-Weisskopf functions given in (8.16).

For this analysis, the Breit-Wigner function is used to parameterize all resonances except for the $a_0(980)$ which requires a Flatté distribution and for the $\rho(1450)$ and $\rho(1700)$ which require the K-matrix because of the proximity of the resonance poles.

A variation of the Breit-Wigner uses m instead of m_0 in the numerator and in the third term of the denominator. A refit of fit #81 using this hypothesis insignificantly changed the χ^2 by 1.99 less, and did not change any of the branching ratios by more than ~ 10 % except for the ${}^1S_0$ contribution from $a_2(1320)$ which decreased by 21%.

8.7.2 K-matrix

The K-matrix formalism is more general than that the Breit-Wigner function. It allows having more than one T matrix pole and coupled channels, while preserving unitarity. In fact, the Breit-Wigner function is equivalent to a one-pole, one-channel K-matrix and the Flatté function is equivalent to a one-pole, two-channel K-matrix. The derivation of the Flattè form from the K-matrix is given in [45]. Here we just give the 1×1 description of the K-matrix, which is used for the $K_0^*(1430)$ S-wave and the multiple pole ρ resonance.

In scattering applications, the T matrix looks like

$$\hat{T} = (1 - i\rho\hat{K})^{-1}\hat{K} \tag{8.20}$$

where the 1×1 K matrix is a summation of pole terms,

$$\hat{K} = \sum_{i=\text{poles}} \frac{(gB^L(q))^2}{m_i^2 - m^2} + c \tag{8.21}$$

where $g = \sqrt{m_i\Gamma_i/\rho}$, ρ is the decay phase space, $B^L(q)$ is the Blatt-Weisskopf factor, m_i is the resonance mass, m is the invariant mass of the system and c is an optional background term.

In production applications, such as in $p\overline{p}$ annihilation, the T matrix is written as

$$\hat{T} = (1 - i\rho\hat{K})^{-1}\hat{P}, \tag{8.22}$$

the only difference being the production vector P replacing the K matrix. The production vector is defined as

$$\hat{P} = \sum_{i=\text{poles}} \beta_i \frac{g^2 B^L(q)}{m_i^2 - m^2} + c \tag{8.23}$$

which is nearly the same as the K matrix, except there is a production coefficient β_i and one power of $B^L(q)$ is suppressed.

Flatté

The Flatté distribution is used to parameterize the $a_0(980)$. Because the a_0's mass is on top of the KK threshold and it can also decay into $\pi^0\eta$, the shape is affected in a somewhat weird way. See the discussion around equation (3.18) for a description of the dynamical form,

$$\hat{F}(s) = \frac{g_1}{m_0^2 - m^2 - i(\rho_1 g_1^2 + \rho_2 g_2^2)}.$$

The ρ P-wave

The ρ is described by a two pole K-matrix, with

$$(m_1, \Gamma_1) = (1430, 170)\,\text{MeV} \tag{8.24}$$

$$(m_2, \Gamma_2) = (1740, 190)\,\text{MeV}, \tag{8.25}$$

the values taken from [21].

$K - \pi$ S-Wave

The LASS parameterization of the $K - \pi$ S-wave requires a broad background term c to be added to the pole term. The value of c in (8.21) and (8.23) is defined as

$$c = \frac{am}{2 + abq^2(m)}. \tag{8.26}$$

It turns out that the fit is not very sensitive to the exact parameterization of the background term. The negative log-likelihood actually drops slightly (by 15) if the background term is not included. The dynamical form is discussed in section 3.11.2.

8.8 Fit algorithm

In most analyses, the efficiency function is calculated from the Monte Carlo, and then held constant in the fits. In this analysis however, because the statistics of the data are much higher than the statistics of the Monte Carlo, the efficiency can be better determined by using the *data* rather than the Monte Carlo. Of course, the data reflects both the efficiency and the dynamics. For this reason, we simultaneously fit the Monte Carlo (for the efficiency) and the data (for the efficiency and the dynamics).

MINUIT was used to minimize our χ^2 value,

$$\chi^2 = \chi^2_{\mathrm{mc}} + \chi^2_{\mathrm{data}} \tag{8.27}$$

where

$$\chi^2_{\mathrm{mc}} = \sum_{b=bins} \chi^2(N_b^{\mathrm{mc}}, \epsilon_b \cdot c) \tag{8.28}$$

and

$$\chi^2_{\mathrm{data}} = \sum_{b=bins} \chi^2(N_b^{\mathrm{data}}, \epsilon_b \cdot I_b) \tag{8.29}$$

where b is the bin index, N_b is the number of events in bin b, ϵ_b is the net detector and reconstruction efficiency of bin b, c is an overall normalization constant and I_b is the total theoretical intensity of bin b. The χ^2 for binned Poisson data is the same as twice the negative log-likelihood,

$$\chi^2(N^{\mathrm{obs}}, N^{\mathrm{th}}) = -2LL = 2(N^{\mathrm{th}} - N^{\mathrm{obs}} + N^{\mathrm{obs}} \ln(N^{\mathrm{obs}}/N^{\mathrm{th}})) \tag{8.30}$$

where N^{obs} is the observed integral number of events and N^{th} is the theoretically expected real number of events. If $N^{\mathrm{obs}} = 0$, then the second term is zero.

Both ϵ_b and I_b are calculated at the phase-space center-of-gravity of each bin. For bins whose perimeter lies entirely within phase space, this point is simply the center of the square bin. For bins on the edge of the dalitz plot, this point is not at the center of the bin.

The efficiency function is described in chapter 6.

Table 8.3: Results of every fit, with percentages of each resonance

8.9 The reduced χ^2

Because the fits are done simultaneously on the data and the Monte Carlo, the total χ^2 is due to both sources. The best χ^2 fit to the Monte Carlo alone gives $\chi^2 = 438$, for 490 bins with 36 free parameters, or a reduced $\chi^2/N = 0.96$. To get the χ^2 due to the data alone, we subtract the expected contribution from the efficiency. Since the 36 efficiency parameters are shared between the data and the efficiency fit, we divide this count by 2, and then subtract from the number of bins to arrive at the expected contribution due to the efficiency alone, 490-36/2 = 472. The degrees of freedom of the fit include all the dynamic parameters and half of the efficiency parameters, since again the later are shared with the pure efficiency fit.

$$\chi^2/N_{\text{dof}} = \frac{\chi^2 - 472}{472 - N_{\text{par}}} \tag{8.31}$$

where N_{par} are the number of free parameters in the theoretical dynamic function.

8.10 Results

The Dalitz plot has one obvious resonance, the $K^*(892)$, appearing as a horizontal and vertical band. Thus this resonance is in all fits. The other resonances are not so immediately evident, and we must develop an algorithm to discover the remaining resonances.

Resonance	Mass [MeV/c^2]	Width [MeV/c^2]
$K^*(892)^{\pm}$	891.921	54.7
$K^*(892)^0$	896.056	53.4
$K_0^*(1430)$	1342	400
$a_0(980)$	999	353,353 *
$a_0(1450)$	1489	265
$a_2(1320)$	1318.1	107
$\rho(1450)$	1430	170
$\rho(1700)$	1740	190

Table 8.4: The reference masses and widths of fit #81, taken from [21].

First, we examine the $K\pi$ wave, then we examine the $K\bar{K}$ wave. For reference, for a fit to the data assuming a "phase space" hypothesis, that is the dynamical function is simply a constant, the $\chi^2 = 23924$ for 489 degrees of freedom, or a reduced $\chi^2/N_{\mathrm{dof}} = 49$. This number is meant to set a scale for a "bad" fit, compared to 1.0 being a "good" fit.

We also attempted a fit without any interferences between the different resonances. This gave a totally unacceptable fit of $\chi^2/N \sim 10$; allowing some interference between the $K\bar{K}$ components improved the fit to a still unacceptable $\chi^2/N \sim 5$. Thus the interferences between the $K\pi$ and $K\bar{K}$ waves are a critical ingredient in the Dalitz plot. This also means that it is difficult to determine the branching ratios of individual components because there is so much interference.

For comparison purposes, the fits in table 8.5 were done with all masses and widths fixed to those of table 8.4, and the $K\bar{K}$ wave included all five resonances: $a_0(980)$, $a_2(1320)$, $a_0(1450)$, $\rho(1450)$, $\rho(1700)$. The fits in table 8.6 were done with all masses and widths free, except for those of the $K_0^*(1430)$ and $K_2^*(1430)$, and the $K\pi$ wave included all three resonances, $K^*(892)$, $K_2^*(1430)$ and $K_0^*(1430)$.

Fit	χ^2	χ^2/N_{dof}	$K^*(892)$	$K_2^*(1430)$	$K_0^*(1430)$	$K^*(1410)$
0/201	994	1.29	•	•	•	•
1/81	1032	1.34	•	•	•	
2/156	1112	1.53	•	•		
3/80	1290	1.91	•		•	
4/159	1547	2.45	•			
5/157	12800	28.7		•	•	
6/160	13000	28.8		•		
7/161	13300	29.1			•	

Table 8.5: The components of the $K\pi$ wave. See figure 8.8

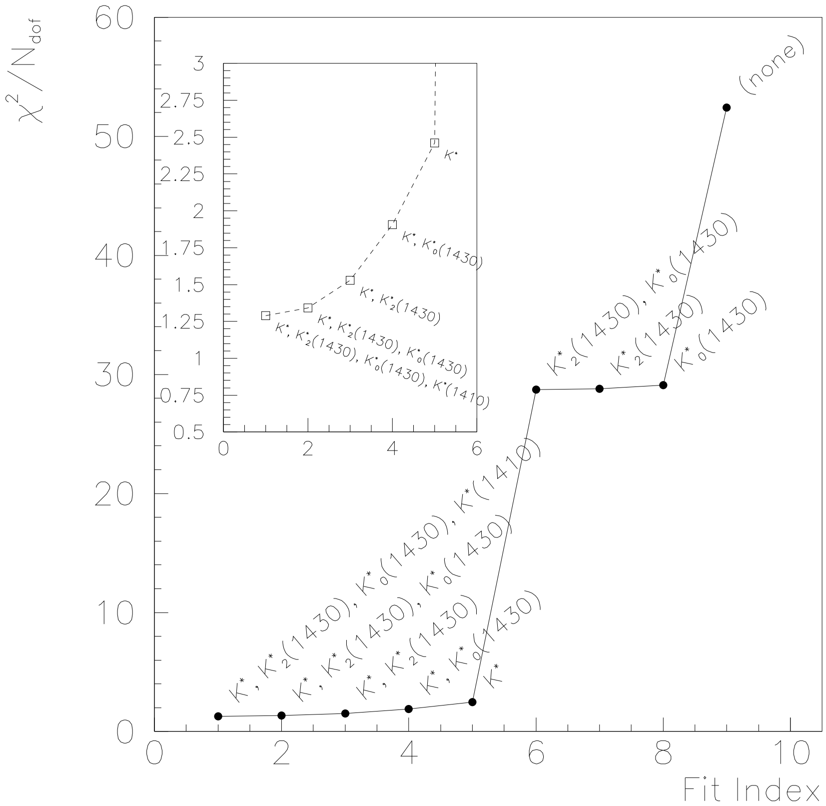

Figure 8.8: The fits of the $K\pi$ wave. See table 8.5

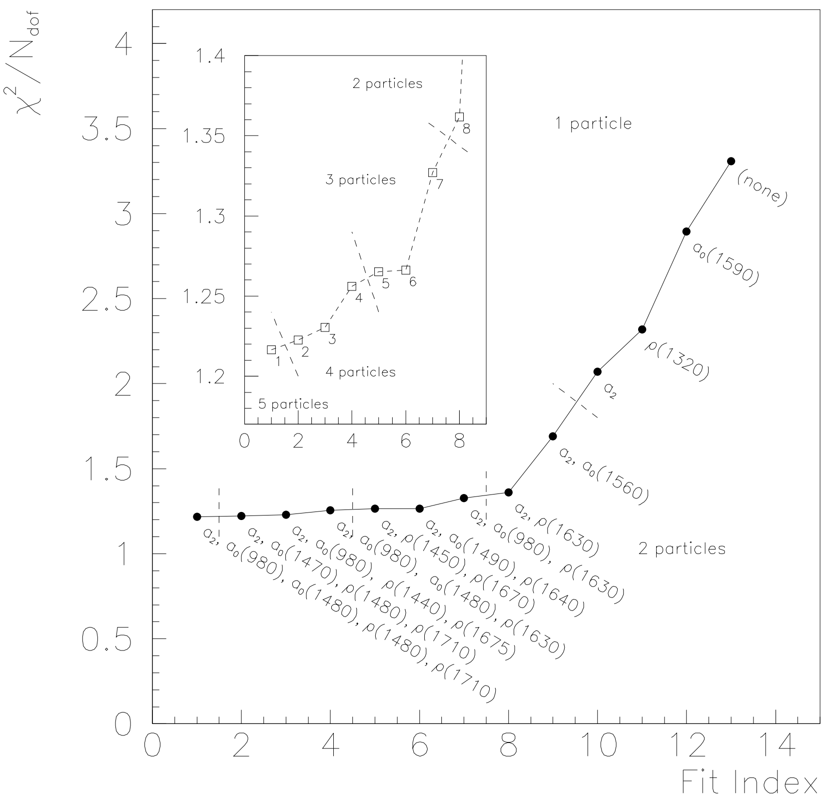

Figure 8.9: A graphical display of table 8.6.

		$a_0(980)$		$a_2(1320)$		$a_0(1450)$		$\rho(1450)$		$\rho(1700)$	
Fit	-LL	m	$\begin{pmatrix} g_{K\overline{K}} \\ g_{\eta\pi} \end{pmatrix}$	m	Γ	m	Γ	m	Γ	m	Γ
		MeV/c^2	MeV/c^2	MeV/c^2	MeV/$\hbar$	MeV/c^2	MeV/$\hbar$	MeV/c^2	MeV/$\hbar$	MeV/c^2	MeV/$\hbar$
1/144	961	1004 ± 2	$\begin{pmatrix} 396 \pm 55 \\ 1.5 \pm 61 \end{pmatrix}$	1308 ± 3	112 ± 6	1488 ± 14	144 ± 30	1478 ± 17	277 ± 29	1701 ± 13	225 ± 24
2/145	973			1309 ± 3	109 ± 7	1481 ± 13	132 ± 30	1488 ± 17	258 ± 33	1705 ± 16	231 ± 31
3/89	974	1023 ± 21	$\begin{pmatrix} 300 \pm 80 \\ 480 \pm 60 \end{pmatrix}$	1308 ± 3	102 ± 7			1438 ± 24	222 ± 26	1668 ± 15	177 ± 20
4/141	987	919 ± 22	$\begin{pmatrix} 73 \pm 8 \\ 0.1 \pm 440 \end{pmatrix}$	1312 ± 3	112 ± 8	1472 ± 15	204 ± 40			1624 ± 7	140 ± 14
5/146	997			1308 ± 3	105 ± 6			1452 ± 18	203 ± 24	1669 ± 13	179 ± 22
6/147	1000			1314 ± 3	107 ± 7	1491 ± 12	122 ± 27			1634 ± 10	174 ± 21
7/96	1025	1042 ± 13	$\begin{pmatrix} 683 \pm 75 \\ 11 \pm 307 \end{pmatrix}$	1311 ± 3	106 ± 6					1625 ± 6	176 ± 15
8/ 148	1048			1315 ± 3	109 ± 6					1633 ± 9	226 ± 30
9/155	1190			1304 ± 3	98 ± 6	1553 ± 12	258 ± 21				
10/151	1364			1302 ± 3	83 ± 6						
11/149	1471							1319 ± 5	88 ± 7		
12/152	1725					1593 ± 7	182 ± 13				
13/150	1924										
PDG		983.4 ± 0.9	n/a	1318.1 ± 0.6	107 ± 5	1474 ± 19	265 ± 13	1465 ± 25	310 ± 60	1700 ± 20	240 ± 60

Table 8.6: The components of the $K\bar{K}$ wave. Blank entries mean that that resonance was not used in the fit. See figure 8.9.

8.10.1 Standard Fit

The reference fit is fit # 81 in table 8.5 with a reduced $\chi^2/N = 1.34$. Releasing the masses and widths improves the fit to $\chi^2/N = 1.22$, in fit #144. The Dalitz plot of the theoretical fit and the projections of the Dalitz plot are shown in figure 8.10. The fit quality is visually excellent. The χ^2 plot, showing areas of bad fit, is given in figure 8.13.

Because the angular decay distributions of the ${}^1P_1$ and ${}^3P_1$ initial states are exactly the same for each final state, we use only ${}^1P_1$ in the fit for computational and convergence reasons. However,if the relative productions of each isobar is different from these two initial states, then there can be a net difference between ${}^1P_1$ and ${}^3P_1$, but only due to the *interferences* between the isobars.

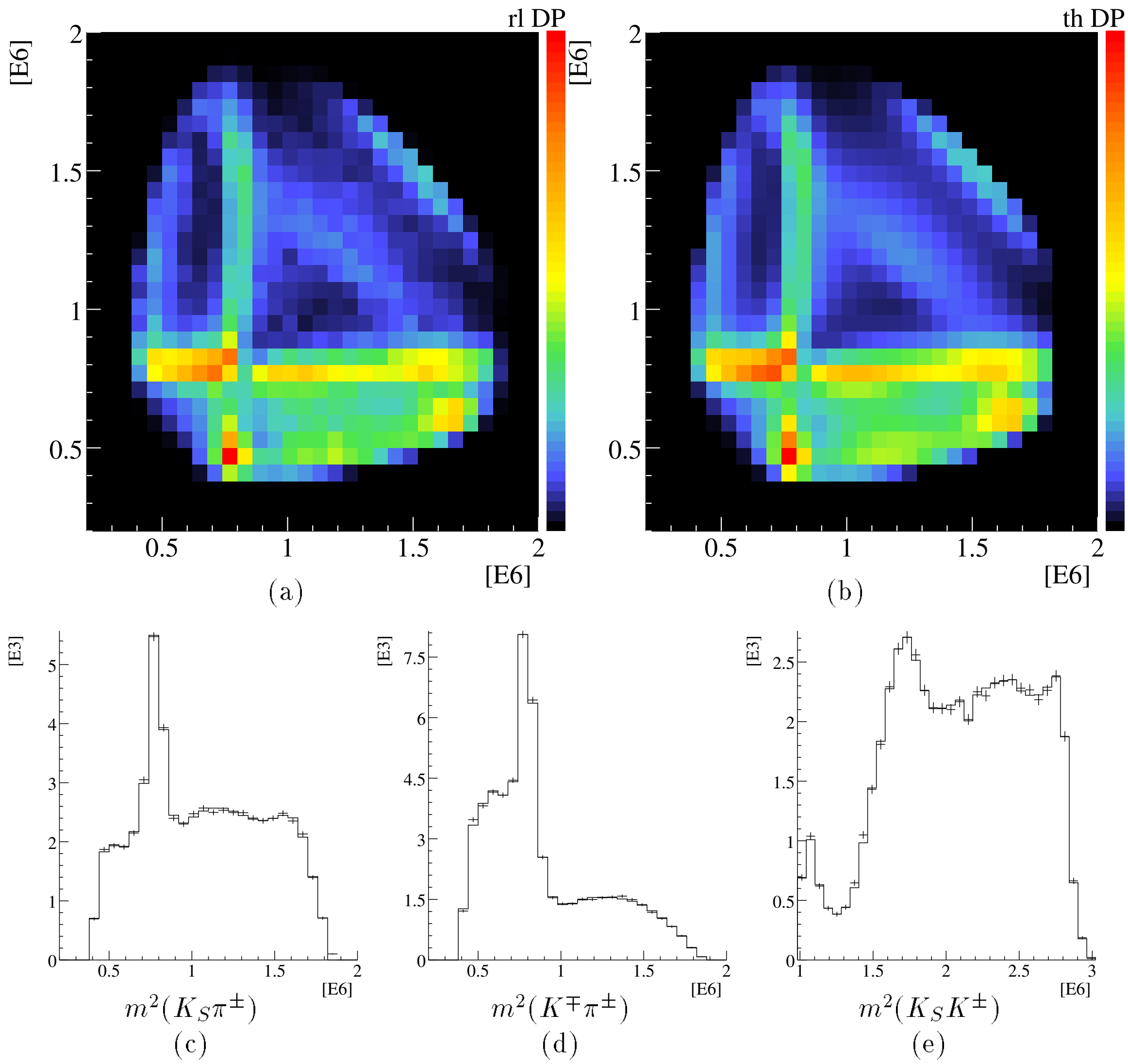

Figure 8.10: Fit 144, the standard fit. (a) Data Dalitz plot, (b) Fitted Dalitz plot, (c,d,e) The projections of the Dalitz plot. The solid line is the fitted function and the error bars are the data.

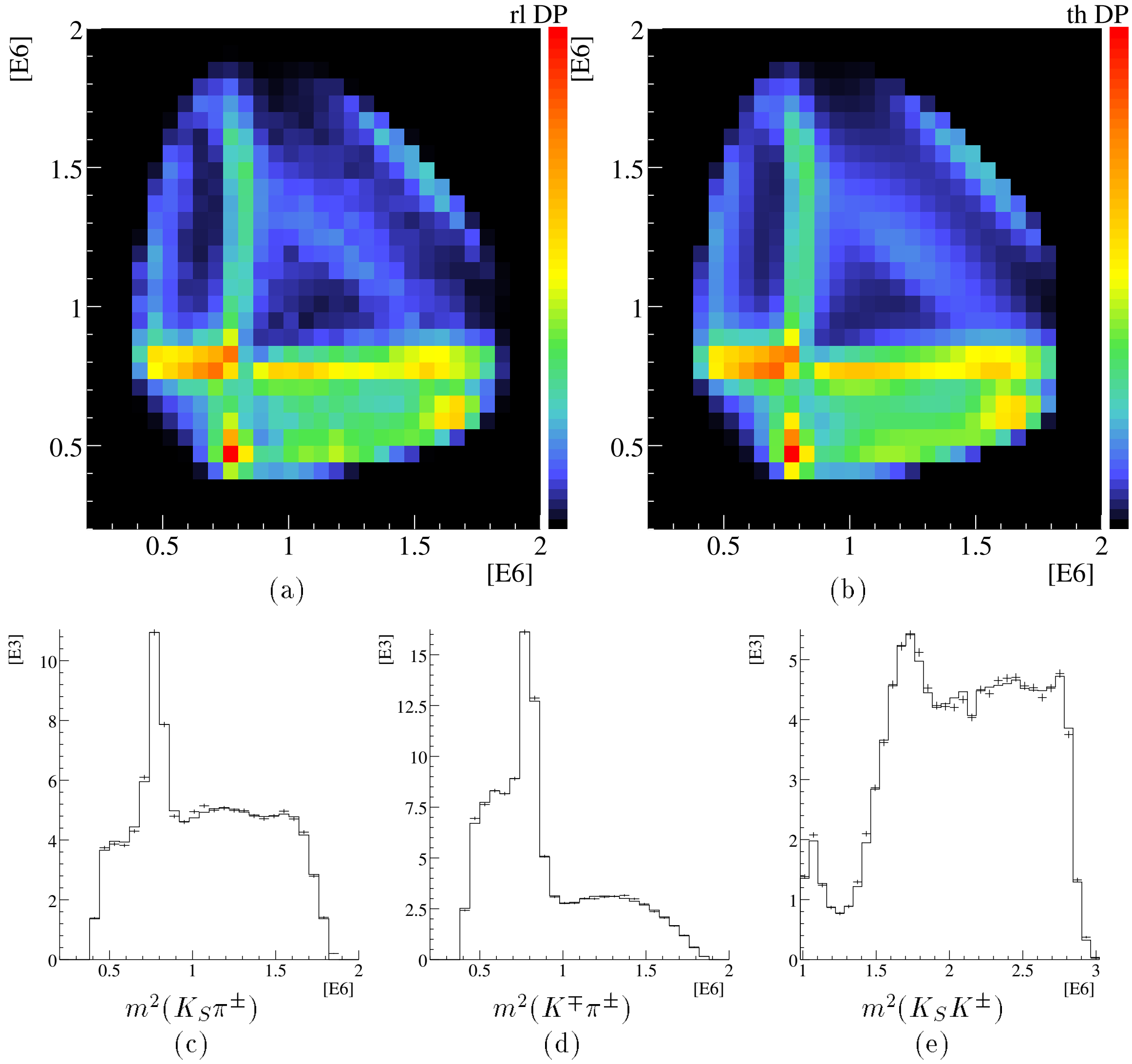

Figure 8.11: Fit 148, the minimal fit. (a) Data Dalitz plot, (b) Fitted Dalitz plot, (c,d,e) The projections of the Dalitz plot. The solid line is the fitted function and the error bars are the data.

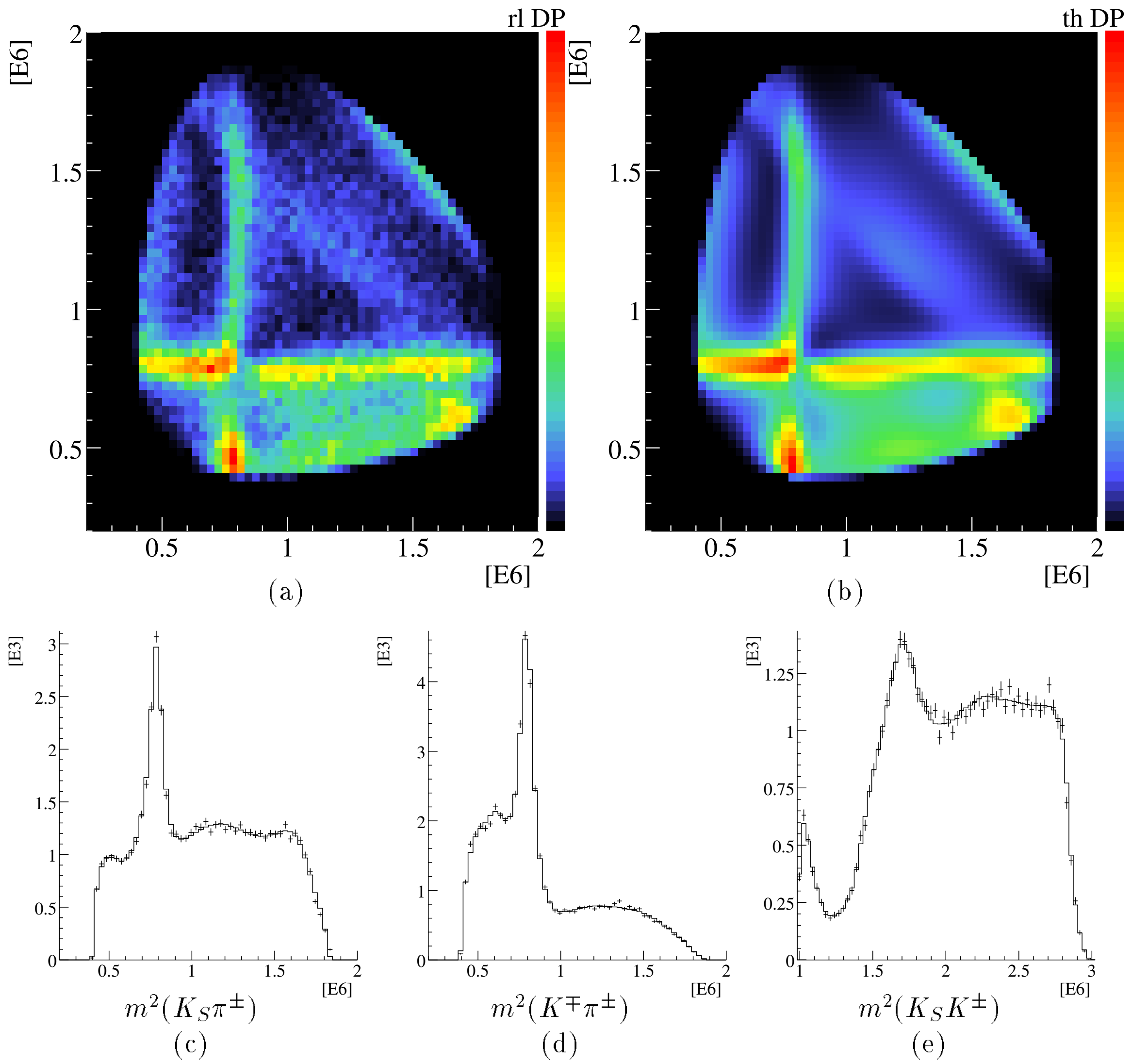

Figure 8.12: Fit 123, the fit without the $a_0(980)$ on a fine grid. (a) Data Dalitz plot, (b) Fitted Dalitz plot, (c,d,e) The projections of the Dalitz plot. The solid line is the fitted function and the error bars are the data.

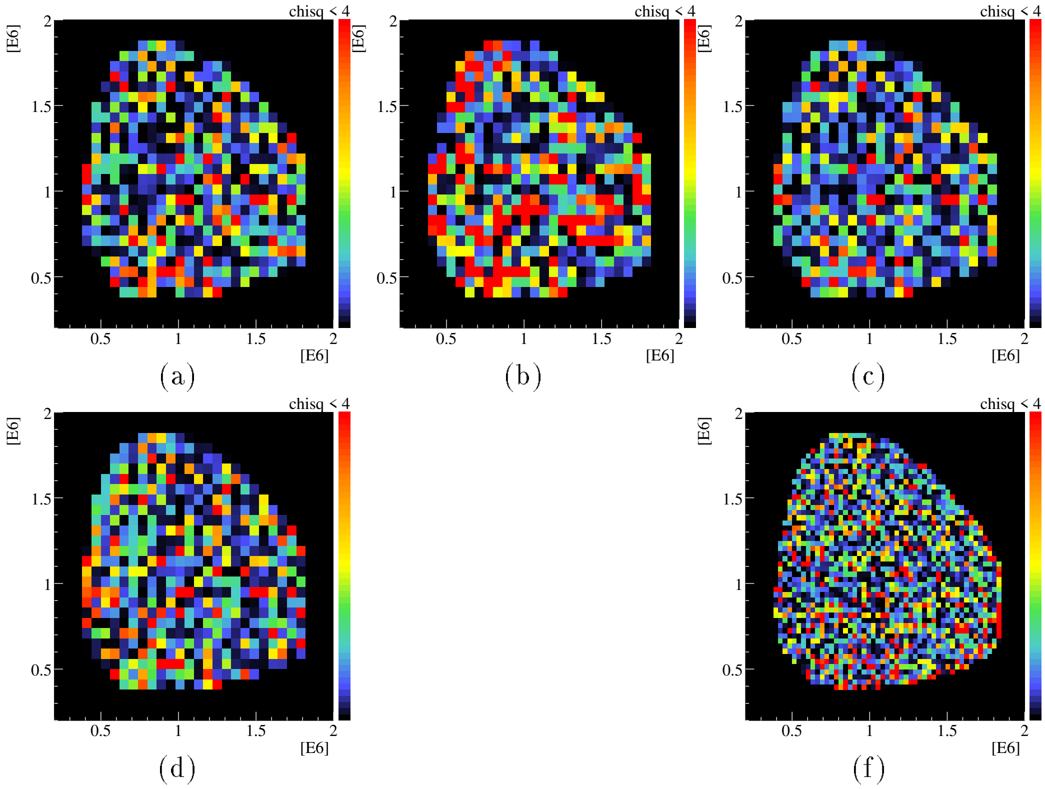

Figure 8.13: The χ^2 plot for (a) the standard fit # 81, (b) fit #87 with no P-wave or $K_2^*(1430)$, (c) the standard fit # 144, (d) the minimal fit # 148, (f) fit #123, without any $a_0(980)$ on a fine grid. Values of $\chi^2 > 4.0$ are truncated to 4.0, shown in red.

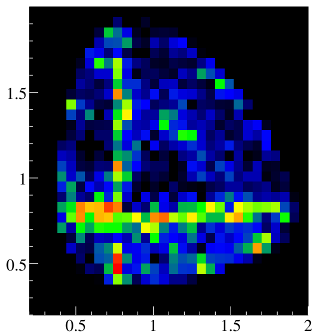

Figure 8.14: The $K_S K^{\pm}\pi^{\pm}$ Dalitz plot, taken at the Saclay 81 cm bubble chamber in the 1960's [19]. The data is not acceptance corrected, but the acceptance is nearly flat for the bubble chamber. The units of the axes are GeV^2/c^4

Chapter 9

Discussion

9.1 Systematic errors

9.1.1 Masses and widths

For the masses of resonances, we assign 2 MeV of systematic error based on the comparison of the $K^*(892)$ mass in section 9.2.1. For the widths, we subtract 30 MeV in quadrature from the fitted widths and assign 8 MeV of systematic error, also based on the result for the $K^*(892)$.

9.1.2 Goodness of fit

The best fit (fit #144) to the data has $\chi^2/N = (961-472)/(490-88) = 1.22$. An ideal fit would have given a reduced $\chi^2/N = 1$, so this fit is still not ideal. A toy Monte Carlo fit (see next subsection) shows that a fit to ideal data does indeed return a reduced $\chi^2/N = 1.0$. The additional χ^2 in our best fit should be due to one of the following reasons:

1. There is something wrong with the data, i.e. a background that has not been subtracted.

2. There is another isobar that needs to be put in the fit.

3. The isobar model has limited accuracy.

4. The detector resolution is not convoluted with the theoretical shape.

5. The theoretical intensity is not adequately linear across a single bin, so there is a second order error induced when the intensity is only calculated at the center of the bin.

We have attempted to eliminate item 1, by the careful checking of the data. We do not see any obvious clustering of the χ^2 across the Dalitz plot, so there doesn't not seem to be any localized background.

Item 2 is unlikely, because we have tried all well known resonances and the incremental improvement in the fit is small, indicating that adding more resonances is not going to help the fit.

Item 3 is a definite possibility. The isobar model does not take into account final state interactions. There are limitations to the accuracy of the Breit-Wigners used, especially in the width characterization.

Item 4 should only apply to the narrow $K^*(892)$ and its interferences, but because this isobar is strong, it could account for a large part of the additional χ^2. We have noted that some of the detector resolution is compensated for by the widening of the $K^*(892)$. However, this is not equivalent to detector resolution convolution, because widening the physical width changes the interference with other resonances, while simple Gaussian blurring does not. It is not a big effect, since the fitted width is only 8 MeV larger than the physical width.

Item 5 can be addressed by smaller binning. We have repeated the fit using a smaller binning, with bins of size $(0.03\ \mathrm{MeV}^2/c^4)^2$ instead of $(0.06\ \mathrm{MeV}^2/c^4)^2$ which were used in all the other fits. The result is $\chi^2/N = (2645 - 472)/(1924 - 88) = 1.18$, which is indeed better than the coarse binned fit. The fine binning is computationally expensive, so we could not use this for all the fits and scans. If we naively interpolate to zero bin size, we still are left with a $\chi^2/N \sim 1.14$.

In our opinion, the poorness of the fit is due primarily to the limitation of the isobar model and the parameterization of broad resonances. We note that other Crystal Barrel analyses have similarly high χ^2/N with similar statistics to this analysis of 57 Kevents, with Abele[9] having a final fit of $\chi^2/N = 1.32$ with 37 Kevents, Aker[46] having $\chi^2/N = 1.27$ with 55 Kevents, Amsler[47] having $\chi^2/N = 1.15$ with 22.5 Kevents.

9.1.3 Toy Monte Carlo and branching ratios

To test the reproducibility of the fit, we took the theoretical Dalitz plot of standard fit #81, smeared each bin using a Poisson distribution, and refit the smeared theoretical data. The χ^2 before minimization was 418 for 417 degrees of freedom, which is exactly what it should be since that was what was generated. This proves that the χ^2 is correctly calculated and that it can be used as a goodness of fit estimate. However, the χ^2 could be further minimized considerably. Holding the efficiency function fixed, the fit found $\chi^2/N = 373/417 = 0.89$, or a change of 45 units of χ^2.

Since we know what ingredients went into the fit, we can see how well the fit extracts those values. In table 9.1, we show the generated (input) Dalitz plot contributions and the fitted (output) Dalitz plot contributions.

It is clear that it is difficult to accurately measure the branching ratios when there are so many interfering amplitudes. We estimate the error for the total branching ratios (summed over initial states), is about 25%. The errors for the branching ratios of individual initial states is realistically about 50%.

In order to get a better constraint on the branching ratios, we have tried an additional symmetry, described in section 9.2.4.

9.2 The $K\pi$ wave

9.2.1 The $K\pi$ wave: The strange vector $K^*(892)$

The strange vector $K^*(892)$ is the most important resonance in this analysis. In a fit with all resonances *except* the $K^*(892)$ gives a humorous $\chi^2/N \sim 29$; that the $K^*(892)$ exists is obvious by inspection of the Dalitz plot.

The $p\overline{p}$ annihilation branching ratio is determined to be (see table 9.2)

$$\mathrm{BR}(p\overline{p}\rightarrow K\overline{K}^*(892)) = (4.4 \pm 0.3) \times 10^{-3} \tag{9.1}$$

when the interference at the band crossing is assumed to integrate to zero. We compare this to Conforto[19], again assuming the interference between I=0 and I=1 integrates to zero, which found $\mathrm{BR}(p\overline{p}\rightarrow K\overline{K}^*(892)) = (3.5 \pm 0.3) \times 10^{-3}$. This is somewhat smaller, but may be due to the following reasons. The bubble chamber analysis assumed no P-wave

$^{2s+1}L_J$	Isobar	% of Dalitz plot		Change	
		Before Fit	After Fit	Relative	Absolute
$^1S_0$	$K^*(892)^{\pm}K^{\mp}$	4.2	4.0	-5%	-0.2
	$K^*(892)^0K^0$	6.9	5.8	-16%	-1.1
	$K_0^*(1430)^{\pm}K^{\mp}$	0.2	1.4	+500%	+1.2
	$K_0^*(1430)^0K^0$	6.3	5.0	-21%	-1.3
	$a_0(980)\pi$	1.4	0.9	-36%	-0.5
	$a_0(1450)\pi$	0.9	1.1	+22%	+0.2
	$a_2(1320)\pi$	22.8	22.2	-3%	-0.6
	$\rho\pi$	9.5	7.1	-25%	-1.4
	$K_2^*(1430)^{\pm}K^{\mp}$	1.6	1.7	+ 6%	+0.1
	$K_2^*(1430)^0K^0$	7.2	6.9	-4%	-0.3
$^3S_1$	$K^*(892)^{\pm}K^{\mp}$	14.8	15.9	+7%	+1.1
	$K^*(892)^0K^0$	11.8	12.3	+4%	+0.5
	$a_2(1320)\pi$	2.2	1.9	-14%	-0.3
	$\rho\pi$	2.6	2.8	+8%	+0.2
	$K_2^*(1430)^{\pm}K^{\mp}$	1.6	1.7	+6%	+0.1
	$K_2^*(1430)^0K^0$	0.4	0.7	+75%	+0.3
$^1P_1$	$K^*(892)^{\pm}K^{\mp}$	1.4	2.0	+43%	+0.6
$^3P_1$	$K^*(892)^0K^0$	9.1	10.8	+13%	+1.7
	$K_0^*(1430)^{\pm}K^{\mp}$	17.3	19.6	-3%	-2.3
	$K_0^*(1430)^0K^0$	6.9	4.3	-38%	-2.6
	$a_0(980)\pi$	5.7	4.8	-16%	-0.9
	$a_0(1450)\pi$	0.2	0.1	- 50%	-0.1
	$a_2(1320)\pi$	0.5	1.1	+120%	+0.6
	$\rho\pi$	17.8	21.5	+21%	+3.7
	$K_2^*(1430)^{\pm}K^{\mp}$	1.6	1.2	-25%	-0.4
	$K_2^*(1430)^0K^0$	1.4	2.5	+79%	+1.1
Sum	$K^*(892)^{\pm}K^{\mp}$	20.4	21.9	+4%	+1.5
	$K^*(892)^0K^0$	27.8	28.9	+4%	+1.1
	$K_0^*(1430)^{\pm}K^{\mp}$	17.5	21.0	+20%	+3.5
	$K_0^*(1430)^0K^0$	13.2	9.3	-30%	-3.9
	$a_0(980)\pi$	7.1	5.7	-20%	-1.4
	$a_0(1450)\pi$	1.1	1.2	+ 9%	+0.1
	$a_2(1320)\pi$	25.5	25.2	-1%	-0.3
	$\rho\pi$	29.9	31.4	+5%	+1.5
	$K_2^*(1430)^{\pm}K^{\mp}$	4.8	4.6	-4%	-0.2
	$K_2^*(1430)^0K^0$	9.0	10.1	+12%	+1.1

Table 9.1: The Toy MC, before and after fitting

annihilation, but we see that $\sim 30\%$ of our branching ratio comes from P-wave. This will change the interference pattern significantly. Also, the $K^*(892)$ was parameterized via $I = 0$ and $I = 1$ in the previous analysis, while it was parameterized via horizontal and vertical bands in our analysis. There is a clear strong interference effect at the crossing of the bands, which may explain the difference in branching ratios if the integrated interference is not zero.

From the best fit (#144) with the masses and widths of all resonances freely varying in the fit (except the broad K_2^* and K_0^*), we find (quoting statistical errors only)

$$\begin{aligned} m(K^*(892)^{\pm}) &= 890.0 \pm 0.8 \quad \Gamma(K^*(892)^{\pm}) = 56 \pm 2 \\ m(K^*(892)^{0}) &= 894.0 \pm 0.6 \quad \Gamma(K^*(892)^{0}) = 60 \pm 2. \end{aligned} \tag{9.2}$$

The Particle Data Group[38] reports the mass and width of the $K^*(892)$ as $m(K^*(892)^{\pm}) = 891.66 \pm 0.26$ MeV/c^2, $m(K^*(892)^0) = 896.10 \pm 0.28$ MeV/c^2 and $\Gamma(K^*(892) = 50.6 \pm 0.5$ MeV/c^2 (charge independent).

Our measurements of masses are 1.7 and 2.1 MeV/c^2 lower, respectively, in the masses. The mass difference is not surprising, because the binning in the histogram is rather coarse, (0.06 GeV^2/c^4), which corresponds to a mass range of $\delta m \sim 33$ MeV/c^2 at the $K^*(892)$ mass. Because the theoretical intensity is calculated only at the center of a bin, there is a significant undersampling of the theoretical shape over a single bin. But rather than assign a $\pm 33/2$ MeV/c^2 error to the result, we see that the systematic error of the coarse binning is only about ± 2 MeV/c^2. The testifies to the influence of the K^* on the entire Dalitz plot far beyond the narrow peak region. We assign a systematic error of 2 MeV/c^2 in mass to all other mass measurements.

The measured width is about 8 MeV higher than the Particle Data Group's value, and this is simply a result of the fact that the theoretical intensity is not convoluted with the detector resolution. Doing so requires an inordinate amount of computational time, and we can see that the error is only $8MeV$ for the narrowest resonances, so the effect is even smaller for all the other much wider resonances. The $8MeV$ net difference implies a detector resolution of $\sqrt{58^2 - 50^2} \sim 30$ MeV, which is about 3% of the K^* mass. We thus subtract (in quadrature) 30 MeV from all fitted widths to remove the detector resolution, and assign 8 MeV of systematic error to all measured widths.

We attempted adding a second pole to the strange vector wave, the $K^*(1410)$ with a mass of 1414 MeV/c^2 and a width of 232 MeV/c^2. The χ^2 dropped by 37 with 12 extra free parameters, meaning that this is a $\sqrt{37 - 12} = 5\sigma$ effect. Because this particle is well established by the Particle Data Group, this result is not surprising. However, the additional calculational overhead has meant that we refrained from using it in other fits.

9.2.2 The $K\pi$ wave: The strange tensor $K_2^*(1430)$

To our knowledge, the $K_2^*(1430)$ has not been used before in any $p\overline{p} \rightarrow KK\pi$ (at rest) analysis. This is due, presumably, because the mass of 1430 MeV/c^2 is higher than the edge of the Dalitz plot, 1240 MeV/c^2 and its width of 100 MeV/c^2 seems narrow. However, the tails of a Breit-Wigner are very long and do not drop rapidly after going beyond one standard width. Of course to be significant, the resonance needs to be very strong so that the tails have any significant intensity.

The LASS spectrometer at SLAC[22] studied $K\pi$ scattering at energies from threshold to 4 GeV. They noted two very strong resonances, the $K^*(892)$ and the $K_2^*(1430)$, as well as the next three higher excited ($L = 3, 4, 5$) states of the K^*. The $K^-\pi^+$ invariant

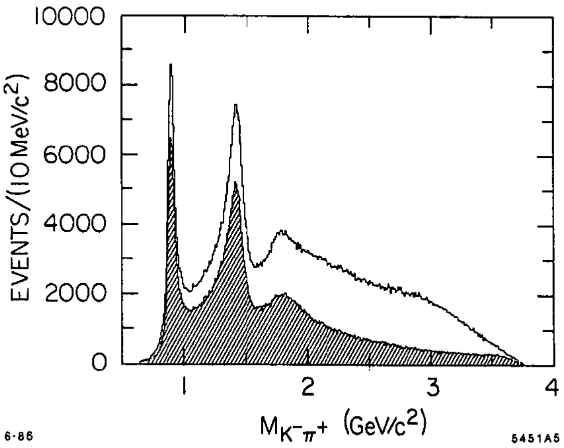

(a)

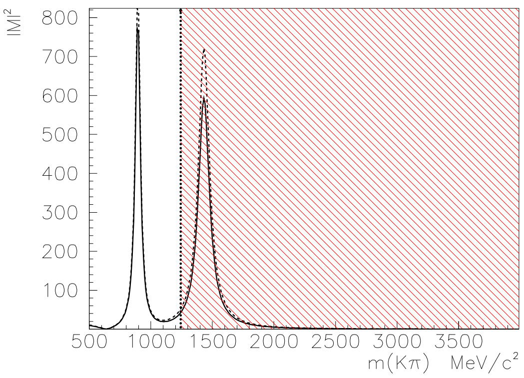

(b)

Figure 9.1: (a) the $K\pi$ invariant mass distribution seen in the LASS experiment (taken from [22], figure 3), for events with $|t'| \leq 1.0$ GeV/c^2). The shaded region contains events with nπ^+ mass greater than 1.7 GeV/c^2 (the difference between the shaded and unshaded regions is unimportant for the purposes of this comparison). (b) the fitted $K\pi$ invariant mass distribution as seen in this analysis, when phase space and angular barrier functions are *not* included. The two curves are the $\pm1\sigma$ limits of the fitted values. The hatched region is outside of the $KK\pi$ at-rest phase space.

mass distribution is shown in figure 9.1a. The height of the $K^*(892)$ and $K_2^*(1430)$ peaks are in a ratio of 1:0.63, while the ratio of widths is 50.8:116.5. This means that the ratio of events due to the tensor to events due to the vector is about 1.44; in other words, the tensor intensity is *greater* than the vector; since the vector is the most visible component of the Dalitz plot, the tensor *must* have a significant contribution, even though the mean lies outside of phase space.

The actual contribution of the tensor in the $p\overline{p} \rightarrow KK\pi$ Dalitz plot is smaller than the vector, of course, because it is outside of space space and along the edge of phase space, the angular momentum barrier causes production of $p\overline{p} \rightarrow KK_2^*(1430)$ to be suppressed. This is why the $K_2^*(1430)$ is not immediately obvious by eye in the Dalitz plot as vertical and horizontal bands. However, there are visible effects that are due to interference effects of the $K_2^*(1430)$ with other resonances in the Dalitz plot, for example the KK threshold enhancement in the upper-right part of the Dalitz plot, which is discussed below.

However, we can remove the phase space restriction and angular barrier from the partial-wave analysis and simply plot the Breit-Wigners of the $K^*(892)$ and $K_2^*(1430)$ using the production amplitudes. We can then compare this plot with the LASS data which is essentially not limited by phase space or angular momentum. The plot of

$$|M(m)|^2 = \sum_{i={}^1S_0,{}^3S_1,({}^1P_1 \text{ and } {}^3P_1)} \left| \beta_i^{K^*(892)} BW^{K^*(892)}(m) + \beta_i^{K_2^*(1430)} BW^{K_2^*(1430)}(m) \right|^2 \tag{9.3}$$

is shown in figure 9.1b, where β_i is the fitted production amplitude in the i-th initial state (taken from fit #130), $BW(m)$ is the relativistic Breit-Wigner used in the PWA, and m is the invariant mass of the $K\pi$ system. The dashed line is drawn with all the $\beta_i^{K_2^*(1430)}$ set to their $+1\sigma$ upper limits, while the solid line is drawn with all the $\beta_i^{K_2^*(1430)}$ set to their -1σ lower limits. The ratio of peak heights $[K^*(892) : K_2^*(1430)]$ is 0.83 ± 0.12, which is in reasonable agreement with the LASS data, which found a ratio of 0.63 ± 0.03. Note that our fit is only sensitive to the region *within* phase space ($m(K\pi) < 1242$ MeV$/c^2$), which is the unhatched region in the figure. The peak height ratio agreement is amazing since it is extrapolated from just the small portion within phase space.

The χ^2/N drops from 1.91 to 1.34 when the $K_2^*(1430)$ is introduced (compare fit #80 and #81 in table 8.5). In fact, the tensor $K_2^*(1430)$ is more important than the scalar $K_0^*(1430)$, as seen in the table. This, in addition to excellent agreement with the LASS $K\pi$ scattering data, proves that the $K_2^*(1430)$ is vital in a description of the $KK\pi$ system at rest.

9.2.3 The $K\pi$ wave: The scalar $K_0^*(1430)$

The $K_0^*(1430)$ resonance (with the additional background term) is not as significant as the $K^*(892)$ or the $K_2^*(1430)$. This can be expected from the results of the LASS experiment[22] which saw much more evidence for the later two resonances than this scalar. However, the fit is still significantly improved by including this resonance, by dropping the χ^2/N from 1.53 (fit # 156) to 1.34 (fit# 81) in table 8.5.

9.2.4 Ratio of charged to neutral strange resonances

As can be seen by scanning table 9.1, the percentage attributed to charged or neutral ($K\pi$) resonances seems to vary in a random pattern. In some cases the intensity of the charged resonance exceeds that of the neutral resonance, and in other cases, the reverse is true. This variation changes from fit to fit.

We have hypothesized that the there may be an additional constraint we can impose in the fit. We have imposed a fixed ratio on the production amplitudes of the neutral $K\pi$ waves to the charged $K\pi$ waves. This ratio was then allowed to vary. This removes 8 degrees of freedom (now all the $(K\pi)^{\pm}$ and $(K\pi)^0$ waves are in a fixed ratio), and added one (the ratio). The phase of each production amplitude is still a free parameter in the fit.

The result of the fit # 202 (see table 9.2 for the full results) is an intensity ratio

$$\left|\frac{\beta[(K\pi)^0]}{\beta[(K\pi)^{\pm}]}\right|^2 = 1.39 \pm 0.14. \tag{9.4}$$

The χ^2 increases by 17 units after the removal of 7 parameters, so the significance of this is $\sqrt{17-7} \sim 3\sigma$. Because the branching ratios from each initial state vary considerably if this constraint is not imposed, we use this fit to give the values of the branching ratios, in table 9.2.

Conforto[19] found a charge asymmetry of $(500 \pm 50) : (300 \pm 30) = 1.67 \pm 0.24$ between $K^{*0}(892)K^0$ and $K^{*\pm}(892)K^{\mp}$. Our result is consistent with this, even though we have introduced P-wave, the tensor $K_2^*(1430)$ and the $a_0(1450)$.

9.3 The $K\bar{K}$ wave

There are five candidate resonances in the $K\bar{K}$ wave, which are given in the heading of table 8.6. To determine which of these particles is required requires testing all combinations. The table gives nearly all combinations of 0,1,2,3,4 or 5 resonances; because the $a_2(1320)$ is clearly needed, some combinations without the $a_2(1320)$ are omitted for clarity. The fits are sorted in order of increasing χ^2. In all fits, the masses and widths of the $K\bar{K}$ resonances were allowed to vary freely, in addition to the masses and widths of the $K^*(892)^{\pm}$ and $K^*(892)^0$. The remaining resonances: $K_0^*(1430)$ and $K_2^*(1430)$ are too broad to allow to vary.

At the bottom of table 8.6 are the values from the Particle Data Group[38]. The g widths for the $a_0(980)$ are not applicable, because they are model dependent. The mass and width of the ρ's are for their decays into non-$K\bar{K}$ channels. In the figure 8.9, the same data is displayed graphically, where the reduced χ^2 is displayed, as defined in (8.31).

In figure 8.9, one can clearly see that there is a knee in the χ^2 plot at fit #8/148, which requires simply two resonances, the $a_2(1320)$ and a $\rho(1630)$. This is our minimal fit, which is shown in figure 8.11. This fit is acceptable, with no clustering of χ^2 over the Dalitz plot (shown in figure 8.11), but further improvements can be made.

We first attempt to add one extra resonance, shown in fits #5, #6 and #7. There is not a significant different between fit #5 (which added the $\rho(1450)$) and #6 (which added the $a_0(1450)$), but the improvement over fit #8 is significant. Adding both $a_0(1450)$ and $\rho(1450)$ simultaneously again improves the χ^2 in fit #2, favoring them over the $a_0(980)$ as the fourth particle. However, adding the $a_0(980)$ to the other four does not significantly change the χ^2 in fit #1. It is our opinion that while the $a_(980)$ has been seen in decays to $\eta\pi$, the decay into $K\bar{K}$ could be much smaller than previously believed.

In defense of the $a_0(980)$ and its wild variations in mass and g couplings as seen in the table, the shape in this analysis is dictated primarily by the opening of phase space, and not the Flatté formula. The coupling $g_{K\overline{K}}$ is almost entirely independent of the data, so the values of -1 are not surprising. The coupling value essential gets absorbed into the production amplitude, so the sign of -1 reflects simply an arbitrary change of phase of the amplitude.

The $a_2(1650)$ resonance was attempted, but gave absolutely no improvement in the fit.

9.3.1 Is there an second isovector? Is there *any* isovector?

One of the main goals of this analysis is to find the isovector member of the $q\overline{q}$ scalar nonet. There are now three candidates for this position, the $a_0(980)$, the $a_0(1300)$ and the $a_0(1450)$. Because the $a_0(980)$ has other weird properties, many believe it is not the isovector member. The OBELIX favors the $a_0(1300)$ while the Crystal Barrel favors the $a_0(1450)$.

The first question is, is this isovector statistically significant? We attempt to answer this question in this section. The second question is why do we get a different result from OBELIX and from the previous Crystal Barrel analysis, the second question is, what are the pole parameters? We attempt to answer the first question in this section, and the second question in section 9.3.2.

Our fits offer the surprising conclusion that *there may not be any isovector contribution at all* to the $KK\pi$ Dalitz plot. The minimal fit requires only a $a_2(1320)$ and a single vector $\rho(1670)$ in the $K\bar{K}$ wave to get a reasonable reduced $\chi^2/N = 1.27$. Adding one particle to this favors another vector ρ over a scalar a_0, with a change in $\delta\chi^2 = -51$ for 8 extra free parameters. The significance of this is $\sqrt{63-8} \sim 6.6\sigma$.

The (masses,widths) of these two ρ's are (1452±18,204±24) and (1669±13,170±22)

MeV/c^2, respectively, consistent with the Particle Data Group's values of (1465±25,310±60) and ($1700 \pm 20{,}240 \pm 60$) MeV/c^2, respectively. The change in χ^2 and confirmation by the PDG of the masses speaks for inclusion of two vector resonances in the $K\bar{K}$ wave. We emphasize the statement that the $K\bar{K}$ wave favors two vector ρ poles rather than one vector ρ pole and one scalar a_0 pole.

We then proceeded to add a scalar resonance (an a_0) and the fit found an improvement of $\delta\chi^2 = -25$ with 6 extra parameters. Thus the χ^2 drops by an additional 19 units over statistics alone, which is roughly a $\sqrt{19} = 4.4\sigma$ effect. The range of 3 to 5 σ's is traditionally a gray area of acceptance, and this result is thus gray. The parameters for the mass are relatively stable (ranging from 1472 to 1488 MeV/c^2 over fits 1-8 which returned a statistical error of about 10 MeV/c^2) but the width is not stable, varying from 100 to 250 MeV/c^2 with only a maximum change in χ^2 of 10, as can be seen in figure 9.3. In any case, here are the pole position parameters, the average of fits 1/144, 2/145, 4,/141 and 6/147 in table 8.6 followed by the corrections discussed in section 9.1.

$$m(a_0(1450)) = 1481 \pm 17 \text{ MeV}/c^2 \qquad \Gamma(a_0(1450)) = 100 \text{ to } 250 \text{ MeV}/c^2 \quad (9.5)$$

The much heralded $a_0(980)$ is the weakest resonance in the entire Dalitz plot, with no statistical significance at all based on the change of χ^2. The reduced χ^2/N (fit #144) is 1.216 with the $a_0(980)$ and 1.222 without. The raw χ^2 drops by 11 with the addition of 7 extra parameters, thus only $\delta\chi^2 = 4$ can be attributed to the significance of the $a_0(980)$. This change of 4 is about a 2 σ effect, assuming perfect statistics.

In the previous Crystal Barrel result, a fit with the double-pole ρ alone (not $a_0(1450)$) was not reported. The ρ poles were added to the fit after the $a_0(1450)$, thus it is not clear if the net improvement in the fit was due mostly due to the ρ poles *helping* the $a_0(1450)$ or *replacing* the $a_0(1450)$. In the OBELIX result, only a single pole ρ was used with the a_0. However, we have shown that a two pole ρ is favored over a single pole ρ and a_0.

We summarize in saying that the fit does not require any $a_(980)$, but is consistent with an $a_0(1450)$ although it is not inconsistent either.

9.3.2 Where is the second isovector, $a_0(1450)$?

We now ask why this analysis, with a factor of 5-6 more statistics than either previous analysis, finds less statistic significance for the $a_0(1450)$ than they did. The answer is that the previous analyses did not use the $K_2^*(1430)$ in the fits. In this section, we will show that the inclusion of this tensor resonance affects the results of the $a_0(1450)$.

9.3.3 The Crystal Barrel Analysis of $K_L K^{\pm}\pi^{\mp}$

In Abele[21], the Crystal Barrel collaboration found evidence for a second isovector with $m = 1480 \pm 30$ MeV/c^2 and $\Gamma = 265 \pm 15$ MeV/c^2. The analysis claimed that the mass was not very sensitive to the χ^2, that the mass could be varied between 1450 and 1510 MeV/c^2 with a maximum change in χ^2 of 20.

9.3.4 The OBELIX Analysis

The conclusion of the OBELIX collaboration in [48] is that there is a new isovector with $m = 1290 \pm 10$ MeV/c^2 and $\Gamma = 80 \pm 5$ MeV/$\hbar$, which they call the $a_0(1300)$. They note that this is not consistent with the Crystal Barrel result.

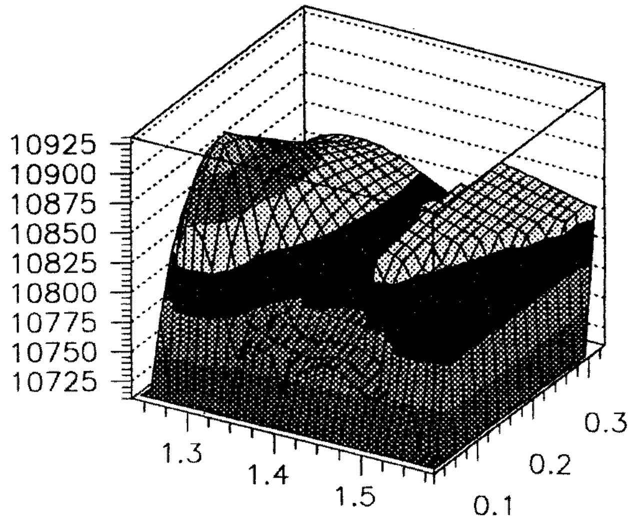

Figure 9.2: OBELIX: Likelihood scan over mass (1200→1600 MeV) and width (0→300 MeV) of second isovector, reproduced from OBELIX[48] (units are in GeV).

In order to disentangle this problem, the OBELIX analysis scanned the mass from 1200 to 1600 MeV/c^2 and the width from 40 to 320 MeV/c^2 of the isovector (see figure 9.2). They found two solutions. Solution 1 has $m_1 = 1290 \pm 10$ MeV, $\Gamma_1 = 90 \pm 10$ MeV, $LL_1 = 10910$, and solution 2 has $m_2 = 1480 \pm 40$, $\Gamma = 200 \pm 60$ MeV, $LL_2 = 10845$. They point out that solution one has a better Log-Likelihood and the shape of the likelihood curve is better behaved at solution 1. In their plot of the Log-Likelihood scan, there is a valley of about -100 LL between the two solutions.

We note that the shape of the second solution is not a good parabolic log-likelihood surface, but features a sharp discontinuity at 1480 MeV/c^2. We fear that this is not a physical maximum in the likelihood but a *gestalt* change in choice of solutions. We believe that this cliff in likelihood is an artifact of the direction of the scanning of mass (from small mass to large mass, rather than from large mass to small mass). This is demonstrated in

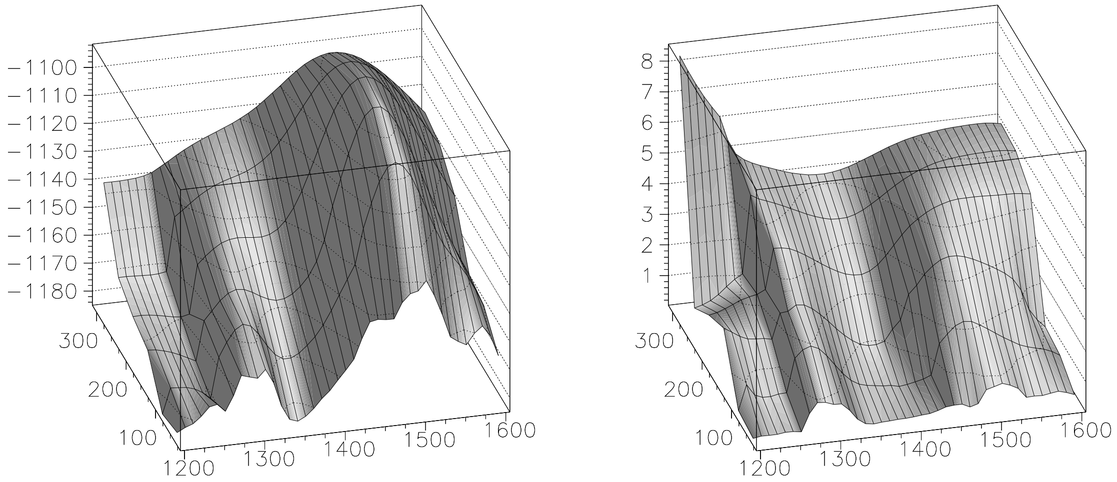

(a) $-\chi^2$ (b) % of Dalitz Plot

Figure 9.3: A scan over the mass and width of a second isovector, assuming P-wave annihilation and $K_2^*(1430)$ contributions. (a) $-\chi^2$ from this analysis (b) percentage of Dalitz plot due to isovector. Horizontal axes units are MeV/c^2.

figure 9.4 and 9.6.

9.3.5 Comparisons to $K_L K^\pm \pi^\mp$ and OBELIX

We have repeated the same mass and width scan for four different hypotheses. The first hypothesis includes P-wave annihilation and the $K_2^*(1430)$ in the fit. This scan is shown in figure 9.3. This hypothesis results in our best fit. The second hypothesis includes P-wave annihilation, but no $K_2^*(1430)$, which is the hypothesis used in the OBELIX analysis. This scan is shown in figure 9.4. The third hypothesis is the complement of the latter, with no P-wave annihilation but with $K_2^*(1430)$. This hypothesis was done for completeness, and is shown in figure 9.5. The fourth and final hypothesis contains no P-wave and no $K_2^*(1430)$, shown in figure 9.6. This is the hypothesis of the previous Crystal Barrel analysis.

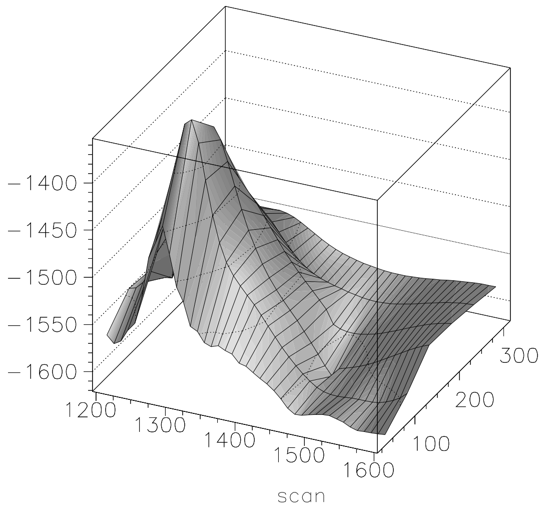

(a) $-\chi^2$

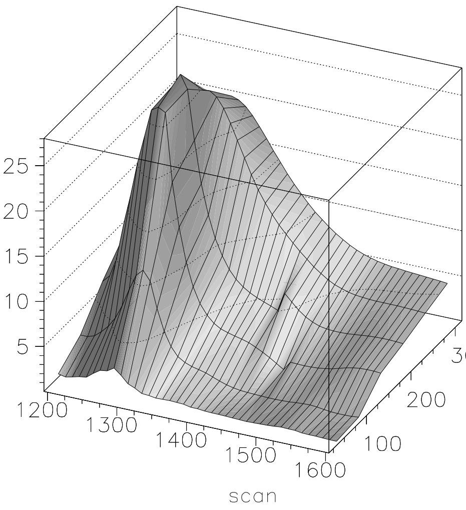

(b) % of Dalitz Plot

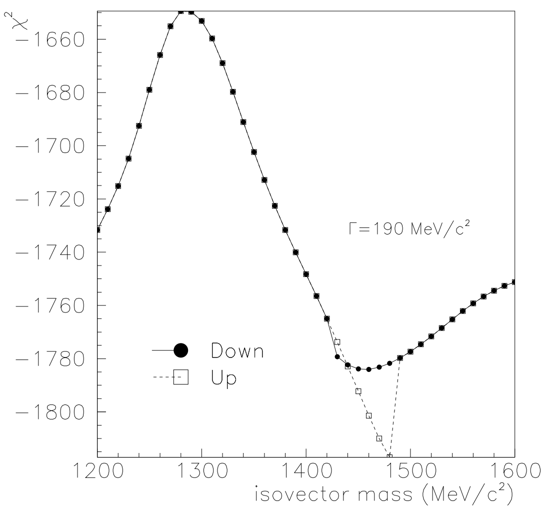

(c)

Figure 9.4: A scan over the mass and width of a second isovector, assuming P-wave annihilation but no $K_2^*(1430)$ contributions. (a) $-\chi^2$ from this analysis (b) percentage of Dalitz plot due to isovector. Horizontal axes units are MeV/c^2. (c) Discontinuity in χ^2, depending on scan direction, along $\Gamma = 190$ MeV/c^2.

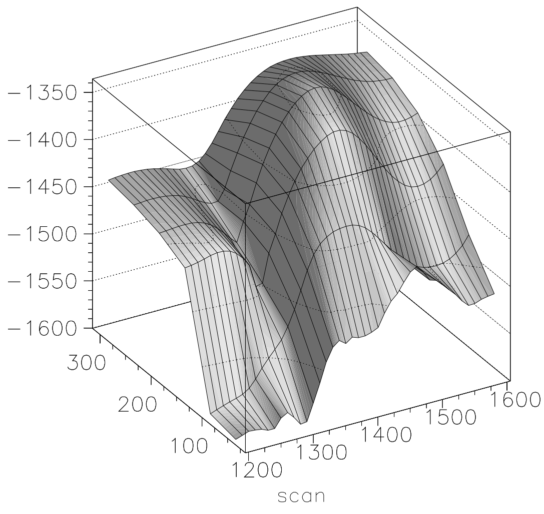

(a) $-\chi^2$

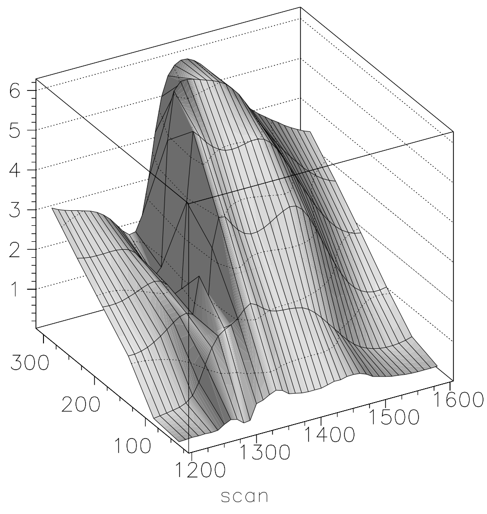

(b) % of Dalitz Plot

Figure 9.5: A scan over the mass and width of a second isovector, assuming $K_2^*(1430)$ but no P-wave annihilation contribution. (a) $-\chi^2$ from this analysis (b) percentage of Dalitz plot due to isovector. Horizontal axes units are MeV/c^2.

The masses of all other resonances (which include $a_2(1320)$, $\rho(1630)$, $K^*(890)$, $K_2^*(1430)$ and $K_0^*(1430)$) were kept fixed. The $a_0(980)$ was not used in the fit with the $K_2^*(1430)$ and P-wave annihilation. The efficiency function was fixed to the best fit to just Monte Carlo data and not varied as in other fits for faster fitting. Because it was fixed, the absolute χ^2's of these scans are somewhat higher and can not be compared to the fits in tables 8.5 and 8.6. Also, relative differences of less than ~ 50 units of χ^2 are not likely not to be statistically significant, as we see for the case of no P-wave and no $K_2^*(1430)$ at the end of this section.

In our scan including the $K_2^*(1430)$ and P-wave annihilation, we see one solution at $m = 1490 \pm 10$ MeV/c^2 and $\Gamma = 240 \pm 50$ MeV/$\hbar$. (We note that this is not our final solution of the mass and width, because the masses and widths of the other $K\bar{K}$ resonances

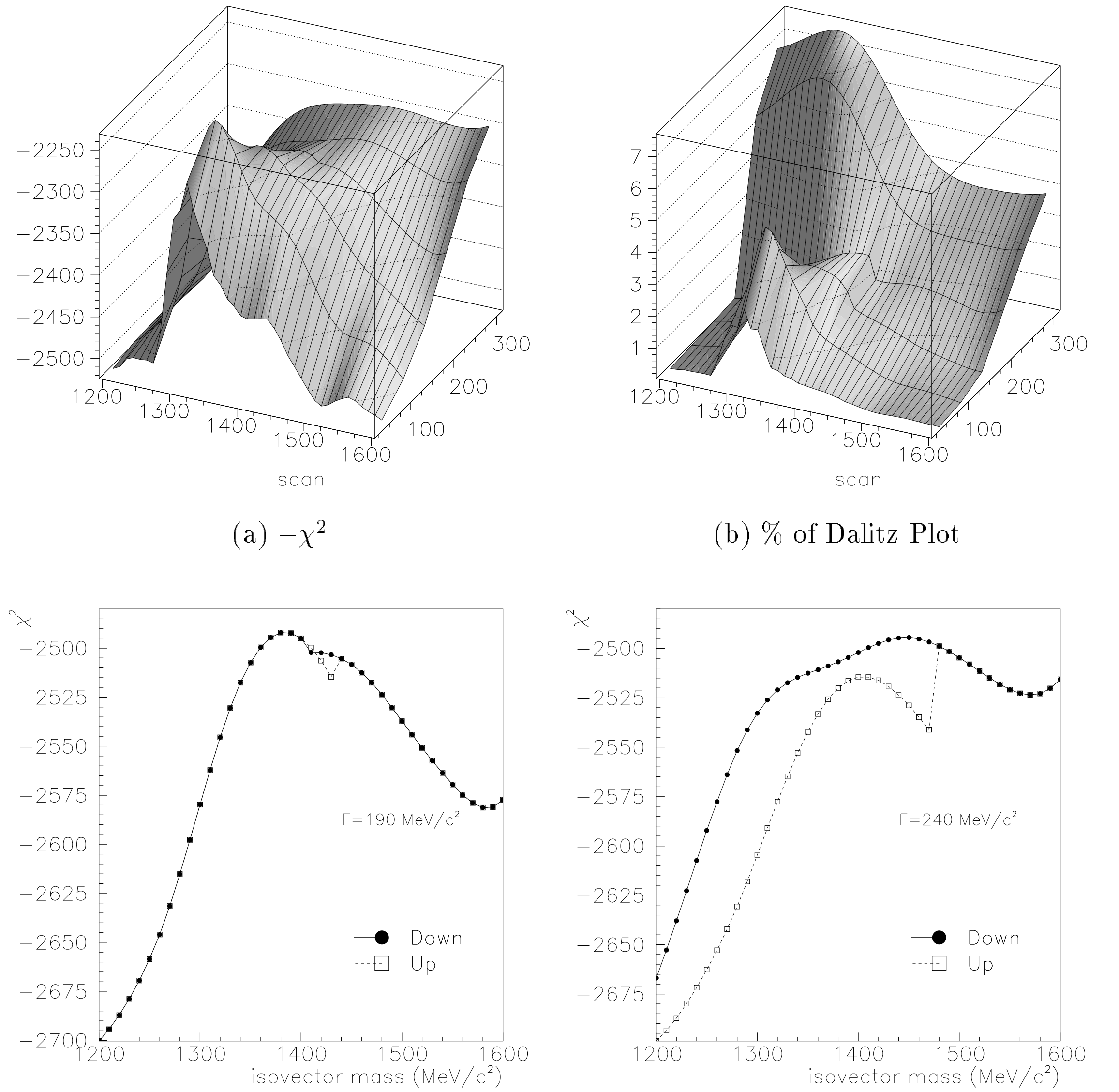

(a) $-\chi^2$

(b) % of Dalitz Plot

(c)

(d)

Figure 9.6: A scan over the mass and width of a second isovector, assuming no P-wave annihilation nor $K_2^*(1430)$ contributions. (a) $-\chi^2$ from this analysis (b) percentage of Dalitz plot due to isovector. Horizontal axes units are MeV/c^2. (c,d) Discontinuity in χ^2, depending on scan direction, along $\Gamma = 190, 240$ MeV/c^2 respectively.

were not allowed to vary. However, the pole position in this scanned solution is similar to that of our best fit). There is a ridge at $m = 1300 \pm 10$ at $\Gamma = 90$ MeV/c^2, but the ridge disappears into the global maximum. If we examine the percentage of the isovector contribution to the Dalitz plot, we see that there is a two ridge structure, with one around $m = 1290$ MeV/c^2 and one around $m = 1500$ MeV/c^2.

In our scan including the $K_2^*(1430)$ and but with no P-wave annihilation (figure 9.5), we see a very broad minimum in the χ^2, roughly centered at $m = 1450$ MeV/c^2 and $\Gamma = 190$ MeV/c^2. This solution is consistent with the best fit, albeit the χ^2 is worse by +270.

In our scan which mimics the OBELIX analysis, using P-wave but no $K_2^*(1430)$, we get a very clear minimum of the χ^2 at $m = 1285 \pm 15$ MeV/c^2 and $\Gamma = 90 \pm 20$ MeV/c^2 (see figure 9.5). This is in perfect agreement with the OBELIX analysis. However, we do not see the secondary solution at $m = 1480$ that they report. We postulate in subsection 9.3.6 that the secondary solution in OBELIX is an artifact of the fit procedure, and not a physical minima.

Finally, in our scan which mimics the previous Crystal Barrel analysis, using no P-wave annihilation and not any $K_2^*(1430)$, we get a first solution at $m = 1300 \pm 10$ MeV/c^2 and $\Gamma = 90 \pm 20$ MeV/c^2 at $\chi^2 = 2458$. There is second solution at $m = 1450$ MeV/c^2 and $\Gamma = 240$ MeV/c^2 with $\chi^2 = 2495$. The difference in these two solutions is 37, which is not very significant. In fact, we have repeated the fits at these two solution positions, except with a freely varying efficiency function. The results are $\chi_1^2 = 1954$ and $\chi_2^2 = 1863$, respectively; the second solution is now better than the first by $\delta\chi^2 = 91$.

9.3.6 Two solutions, One χ^2 Minimum

A local minimum in the χ^2 may be simply a manifestation of a discontinuity in the χ^2 surface, causing a "fake" local minimum. There may be two very different solutions to the fit, but which have similar χ^2 values. If the fit gets "caught" in one solution, it may not find the other solution because the χ^2 barrier between the two solutions is too high, even though the other solution may be a better solution. In a scan of a parameter, the fit might need to jump from one solution to the other as the parameter is changed. However, if the parameter is varied slowly from a to b, this jump may not happen until the parameter goes far enough to make the barrier small. At this point, the change in χ^2 may be very dramatic. If the scan of the parameter is reversed back towards a, the new minimum may be continue to be a better solution than the previous solution. Thus it is important to be aware of sharp discontinuities in the χ^2 surface and reverse the direction of the scan of the parameter if such a discontinuity is seen, to see if the discontinuity will go away.

In fact, we see just such a discontinuity as a scan of the mass of the isovector passes through $m \sim 1480$ MeV/c^2. This discontinuity can be seen in figures 9.4 and 9.6, where the tensor $K_2^*(1430)$ has been omitted from the fit. In all these cases, a dramatic drop in χ^2 occurs when the mass steps from 1480 to 1490, but there is no drop in χ^2 when then mass steps from 1490 to 1480.

This discontinuity seems to shown in the OBELIX scan of mass too, in figure 9.2 at $m \sim 1480$ MeV/c^2. We believe that the OBELIX scan was done sequentially with increasing mass, i.e. in steps of $\delta m = +10$ MeV/c^2, and that they encountered the same discontinuity in the fit. If that is what they observed, then the second solution that they propose is just an artifact of the fit procedure, and there is only one solution at $m = 1290$ MeV$/c^2$.

Thus to summarize, we observe an unphysical discontinuity at $m \sim 1480$ MeV$/c^2$ in fits with and without P-wave annihilation, OBELIX shows a χ^2 surface with a discontinuity at the same place, and the Crystal Barrel previously declared a resonance at the same place as the discontinuity. These observations suggest that the solution at $m \sim 1480$ MeV$/c^2$ is due to the same systematic effect, which is unphysical. However, there is something interesting going on at $m = 1480$ which causes the *gestalt* shift in the fit.

We note, perhaps as a curiosity, that the discontinuity only occurs if the $K_2^*(1430)$ is omitted from the fit; it is not seen in figures 9.3 and 9.5, where the $K_2^*(1430)$ is included in the fit.

9.3.7 $^3S_1$ versus $^1S_0$

We get about 42% annihilation from $^1S_0$, 27% from $^3S_1$ and 31% from $^1P_1$ and $^3P_1$. The ratio of $^1S_0$ to $^3S_1$ is 1.56, in good agreement with 1.5 seen in [21]. The relative production of $K^*(892)K$ between the two initial states, $^3S_1$ to $^1S_0$ is 1.9 ± 1.0, in agreement with 2.4 ± 0.5 from Bettini[49], 2.6 ± 0.5 from Conforto[19] and 3.0 ± 0.6 from Abele[21]. The relative production of $a_2(1320)\pi$ from $^3S_1$ to $^1S_0$ is 0.05 ± 0.02, compared to 0.14 ± 0.06 (Bettini), 0.12 ± 0.05 (Conforto) and 0.24 ± 0.09 (Abele). This lower ratio is partially explained by transfer of intensity to the P-wave component, which was not used in the fits of these comparison papers. If we take the ratio of everything but $^1S_0$ to $^1S_0$, we get 0.12 ± 0.03.

9.3.8 $a_2(1320)$

We find

$$\mathrm{BR}(p\overline{p}{\rightarrow}a_2(1320)\pi, a_2(1320){\rightarrow}K\bar{K}) = (1.73 \pm 0.10_{\mathrm{stat}} \pm 0.50_{\mathrm{sys}}) \times 10^{-3} \tag{9.6}$$

which is higher than Bettini[49] which found $(1.24 \pm 0.19) \times 10^{-3}$, higher than Conforto[19] which found $(1.3{\pm}0.4){\times}10^{-3}$ [1] and slightly higher than [21] which found $(1.49{\pm}0.19){\times}10^{-3}$. The statistical error given in (9.6) is simply the statistical error from fit # 202 (6%). The standard deviation among different reasonable fit hypotheses, that is $\Delta\chi^2 < +30$ from the reference fit, is 17%. When we change the parameterization of the Breit-Wigner to include additional kinematic factors (see section 8.7.1), we see the branching ratio drop by 21%. We add these last two systematic errors in quadrature to arrive at the total systematic error, which dominates the total error.

In a Crystal Barrel coupled-channel analysis of $\pi^0\pi^0\pi^0$, $\pi^0\pi^0\eta$, and $\pi^0\eta\eta$ [27], the value $\mathrm{BR}(p\overline{p}{\rightarrow}a_2(1320)^0\pi^0,\ a_2(1320)^0{\rightarrow}\pi^0\eta) = (2.05 \pm 0.40) \times 10^{-3}$ was determined. If we divide by (9.6) and by 3 because only π^0 was seen in [27], we find the ratio

$$r_1 = \frac{\mathrm{BR}(a_2{\rightarrow}K\bar{K})}{\mathrm{BR}(a_2{\rightarrow}\pi\eta)} = 0.29 \pm 0.10 \tag{9.7}$$

which agrees well with the Particle Data Group, $r_1(a_2(1320)) = 0.34 \pm 0.06$ [38]. A similar exercise can be done using the $p\overline{p}{\rightarrow}\pi^0\pi^0\eta$ result [23], looking only at singlet S-wave annihilation. We found in this analysis $\mathrm{BR}(p\overline{p}(^1S_0){\rightarrow}a_2(1320)^0\pi^0,\ a_2(1320)^0{\rightarrow}\pi^0\eta) = (1.9 \pm 0.3) \times 10^{-3}$. From table 9.2 we find the value for $\mathrm{BR}(p\overline{p}(^1S_0){\rightarrow}a_2(1320)\pi,\ a_2(1320){\rightarrow}K\bar{K})$ (with a 50% systematic uncertainty). We find the ratio (noting a hidden factor of 3 in the

[1] The value on page 495 was corrected to be independent of charge

denominator to remove the charge dependence of [23])

$$r_2 = \frac{\mathrm{BR}(p\overline{p}(^1S_0)\rightarrow a_2\pi,\, a_2\rightarrow K\bar{K})}{\mathrm{BR}(p\overline{p}(^1S_0)\rightarrow a_2\pi,\, a_2\rightarrow \pi\eta)} = 0.26 \pm 0.13 \tag{9.8}$$

which also agrees well with the PDG.

9.3.9 The Branching ratio of $a_0(980)\rightarrow K\bar{K}$

The $K_2^*(1430)$, being a tensor resonance, has a complicated dynamical shape. In the $^1S_0$ initial state, it has a characteristic "W" shape in its angular projection of the Dalitz plot. It is the tail of each "W" from the charge and neutral $K_2^*(1430)$ that overlap along the $K\bar{K}$ threshold, forming an even sharper peak because of constructive interference. This interesting structure is seen in figures 8.4 and 8.6. This edge enhancement is seen in $^1S_0$ and $^1P_1$ initial states.

This threshold enhancement fits the data perfectly, obviating the need for the $a_0(980)$ which requires a more complicated coupled-channel (Flatté) description in order to get the shape correct. In fact, the χ^2 only increases by +2.87 when the $a_0(980)$ is removed, when it should increase by about +4 because four free parameters are removed. A scan of χ^2 versus the $a_0(980)$ contribution to the Dalitz plot is given in figure 9.7. Note that the change in χ^2 is very small over the range 0 to 10% of the Dalitz plot. Figure 8.12 shows the fit result also, but on a fine 60x60 grid. The edge enhancement is very well described *without* the $a_0(980)$.

The $a_0(980)$ is prominently seen in its decay to $\pi\eta$. Amsler[50] sees the characteristic cusp shape predicted by the Flatté formula with very high statistics in $\pi^0\pi^0\eta$. However, the decay into $K\bar{K}$ is not as prominent. In fact, nearly every measurement of the $K\bar{K}$ decay channel could have been contaminated in the same way by the $K_2^*(1430)$, because nearly all of them are measuring the 3-body system $K\bar{K}\pi$. A search of the literature could not find any evidence for $a_0(980)\rightarrow K\bar{K}$ without a π spectator or without a possible contribution from $I = 0$ $f_0(980)\rightarrow K\bar{K}$.

The $K_2^*(1430)$ phenomenon may explain one of the big puzzles associated with the $a_0(980)$. Cahn and Landshoff[10] note the puzzling situation that the relative branching ratio of $a_0(980)$ into $K\bar{K}$ versus into $\eta\pi$ varies by an order of magnitude, depending on whether the $a_0(980)$ was produced from $\eta(1440)$ or $f_1(1285)$. If the $a_0(980)$ branching ratios are to believed when produced in $f_1(1285)$, then they claim that the large $K\bar{K}$ threshold enhancement in $\eta(1440)\rightarrow K\bar{K}\pi$ "cannot be ascribed to the [$a_0(980)$][2]" Our explanation agrees with this assessment, that the "$a_0(980)$" seen in the $\eta(1440)$ decays is not due to the $a_0(980)$ at all, but due to the tails of the $K_2^*(1430)$. This is the same effect seen here in this analysis in $p\overline{p}\rightarrow K\overline{K}\pi$. Because the $\eta(1440)$ has higher mass than the $f_1(1285)$, there will be more $K_2^*(1430)$ in the $\eta(1440)$ decay than in the $f_1(1285)$.

In figure 9.7, we see that the $a_0(980)$ contribution to the Dalitz plot can take on the range of 0.5 to 10%, with 4% preferred. Since 0% contribution is statistically allowed, we take the 10% contribution as the upper limit at 85% confidence level. At this point, the fit reports 2.0% from ${}^1S_0$ and 7.9% from ${}^1P_1$. The branching ratio is then

$$\mathrm{BR}(p\overline{p}\rightarrow a_0(980)\pi, a_0(980)\rightarrow K\bar{K}) = 0.3^{+0.4}_{-0.3} \times 10^{-3} \tag{9.9}$$

Using the branching ratio $\mathrm{BR}(p\overline{p}\rightarrow a_0(980)\pi, a_0(980)\rightarrow \pi\eta) = (2.6 \pm 0.5) \times 10^{-3}$

[2]The official names of the particles have changed since 1986. The $a_0(980)$ was previously the δ, the ι is now the $\eta(1440)$ and the $D(1285)$ is now the $f_1(1285)$.

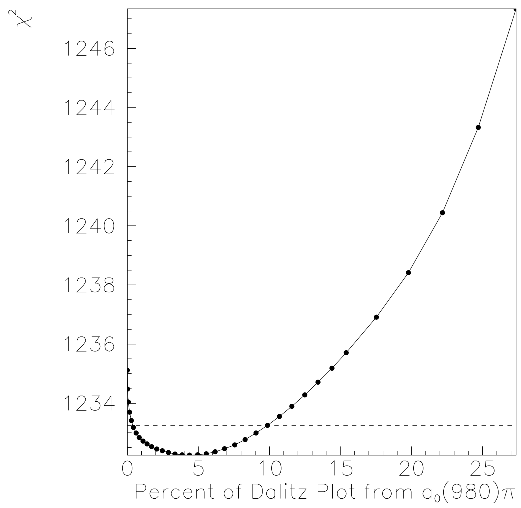

Figure 9.7: χ^2 versus the percentage contribution of $a_0(980)$ to the Dalitz plot. The dashed line is $\Delta\chi^2 = +1$ above the minimum.

[23], we find

$$\frac{\mathrm{BR}(a_0(980)\to K\bar{K})}{\mathrm{BR}(a_0(980)\to\pi\eta)} = 0.12^{+0.15}_{-0.12}. \tag{9.10}$$

Teige[51] calculates the $K\bar{K}$ coupling based on a fit to the Flatté line shape of the $\eta\pi$ channel measured by the E852 collaboration, and finds that the branching ratio $\mathrm{BR}(a_0(980)\to K\bar{K}) = 0.14\pm0.02$. If we assume that the $\eta\pi$ and $K\bar{K}$ modes are the dominant decay modes of the $a_0(980)$, we get $\mathrm{BR}(a_0(980)\to K\bar{K}) = 0.11^{+0.10}_{-0.11}$, in agreement with Teige.

We also attempted to see if the $K\overline{K}$ threshold enhancement could be faked by a suitable combination of the rest of the other resonances. Fit #126 without the $a_0(980)$ and without $K_2^*(1430)$ is unacceptable, with an increase of negative log-likelihood of 635.

In fits where the mass and two width parameters of the $a_0(980)$ were freed, the results did not settle on values compatible with previous analyses or with each other (see table 8.6). This is not surprising, since we have shown that the $K_2^*(1430)$ can entirely

Channel $p\overline{p}\to X$	$^1S_0$ % DP	BR $[10^{-4}]$	$^3S_1$ % DP	BR $[10^{-4}]$	$^1P_1$ and $^3P_1$ % DP	BR $[10^{-4}]$	Total BR $p\overline{p}\to X\to K\overline{K}\pi$ $[10^{-3}]$
$K^*(890)K$	5.6 7.4	10.5 ± 1.0	10.7 14.2	20.0 ± 1.2	6.3 8.4	11.9 ± 2.7	4.2 ± 0.3
$K_0^*(1430)K$	2.9 3.9	5.5 ± 0.8	–	–	13.5 18.5	25.6 ± 5.0	3.1 ± 0.5
$K_2^*(1430)K$	2.9 4.5	5.9 ± 0.8	0.3 0.4	0.5 ± 0.4	2.0 3.0	4.0 ± 1.7	1.04 ± 0.2
$a_0(980)\pi$	3.9	3.1 ± 0.9	–	–	9.3	6.2 ± 2.2	0.9 ± 0.2
$a_0(1450)\pi$	1.0	0.8 ± 0.3	–	–	2.6	1.7 ± 1.1	0.25 ± 0.11
$a_2(1320)\pi$	19.1	15.4 ± 0.9	1.5	0.8 ± 0.2	1.6	1.1 ± 0.5	1.73 ± 0.10
$\rho(1450,1700)\pi$	6.8	3.6 ± 0.7	4.5	3.6 ± 0.7	8.1	5.4 ± 2.4	1.3 ± 0.3
Coh. Total	42		27		31		–
Incoh. Total	58		32		73		–

Table 9.2: The fit results of fit # 202. The percentages of the Dalitz plot are given and the branching ratios from $p\overline{p}$ are given. When two percentages are given, the upper value is for $K^{*\pm}K^{\mp}$ and the lower for $K^{*0}\overline{K}^0$, in a ratio of 1:1.39 (see section 9.2.4). The total branching ratio is corrected by charge multiplicity factors (see text). The errors given are statistical only; the systematic error is estimated to be 50%.

replace the $K\bar{K}$ threshold enhancement. The fit is not very sensitive to the $g_{K\overline{K}}$ coupling, so the enormous variation in the fit result is not surprising.

9.4 Branching Ratios from $p\overline{p}$

To calculate the branching ratio, three values are needed. First, the total branching ratio was calculated in (7.7), being

$$\mathrm{BR}(K_S K^{\pm}\pi^{\pm}) = (2.68 \pm 0.14)\times 10^{-3}.$$

Second, since we are interested in the branching ratios into the strong eigenstates, regardless of charge, i.e. "$K^{\pm 0}K^{\pm 0}\pi^{\pm 0}$", we require the BR scaling factors given in table 3.3, which account for unobserved final states and the CG decomposition of the weak states, K_S and

K_L, into the strong states, K^0 and $\overline{K}^0$. Third, we require the percentage of the Dalitz plot returned by the fit due to each channel. This is simply a defined quantity, the integral of the particular wave intensity divided by the number of events of the whole Dalitz plot. Because this ignores interferences, the sum of all contributions will be not equal to 100%.

The calculated branching ratios are summarized in table 9.2. For the channels with two charge variations i.e. $K^{*\pm}K^{\mp}$ and $K^{*0}K^0$, both percentages of the Dalitz plot are given, with the charged value above the neutral value. These values come from fit #202, which provided an additional hypothetical constraint on the fit, as described in section 9.2.4. From the discussion on the toy Monte Carlo fits (see table 9.1), the systematic errors are very large, estimated to be about 50%.

This large fluctuation is caused by the way amplitudes are added. The contribution of one wave can dramatically drop if another interfering wave's contribution increases only slightly. Let us consider a single bin with 2 resonances coherently contributing to 121 events. Let A be the background amplitude, $A = 1$, and B be the signal amplitude, $B = 10$, so that the total intensity is

$$|A + B|^2 = |1 + 10|^2 = 121.$$

The number of events attributed to the background is $|A|^2 = 1$, and the number attributed to the signal is $|B|^2 = 100$. Now let us attribute 2 events to the background, so $|A|^2 = \sqrt{2}$. If the two channels were added incoherently, this additional event added to the background would take one event from the signal. But since they add coherently, we must decreased the signal amplitude to $B = 11 - \sqrt{2}$, which give $|B|^2 = 91.9$, or a loss of 9.1 events. Thus a gain of 1 event in the background gets magnified to loss of 9 events in the signal. This situation

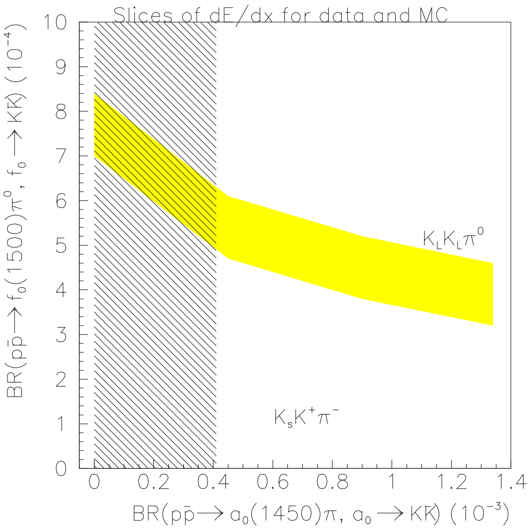

Figure 9.8: Determination of the branching ratio of $f_0(1500)$ in the reaction $p\overline{p}\rightarrow K_L K_L \pi^0$. The light shaded region was determined in [9], while the dark region was determined in the present analysis.

becomes even more unstable when adding 11 amplitudes (in the case of $^1S_0$ for example). That is why the toy MC shows such large variations in branching ratio measurements, and why we assign 50% systematic error to all branching ratio measurements from particular initial states.

The total branching ratio values given in table 9.2 should be not be taken too seriously, because of massive amounts of interference. For example, the sum of all the P wave components is 73% of the Dalitz plot, but the total P wave contribution is only 31%. This means that the interference terms are greater than the direct terms! A more reasonable number would be the coupling constants, which relate directly to the interesting physics, but these have not been calculated.

9.4.1 Determination of $f_0(1500)\rightarrow K\overline{K}$

In a previous Crystal Barrel analysis, the components of $f_0(1500)$ and $a_0(1450)$ were measured in $p\overline{p}\rightarrow K_L K_L \pi^0$. Because of the similar masses and the same spin, the results were correlated. This is shown in figure 9.8. By intersecting the present result for $a_0(1450)$, the branching ratio for f_0 is constrained. We do not believe there is convincing evidence for the existence of the $a_0(1450)$, but if we include the resonance, we get a branching ratio of $(0.25 \pm 0.13) \times 10^{-3}$. Thus we take the region from zero to the upper limit of this value as the possible range for the branching ratio. From the figure, we see that the intersection region gives

$$\mathrm{BR}(p\overline{p}\rightarrow f_0(1500)\pi^0, f_0(1500)\rightarrow K\overline{K}) = (5.0 \text{ to } 8.4) \times 10^{-4} \tag{9.11}$$

With $\mathrm{BR}(p\overline{p}\rightarrow f_0(1500)\pi^0, f_0(1500)\rightarrow \pi^0\pi^0) = (8.1 \pm 2.8) \times 10^{-4}$ from Ref. [52], we calculate

$$r = \frac{BR(f_0(1500)\rightarrow K\overline{K})}{3 \cdot BR(f_0(1500)\rightarrow \pi^0\pi^0)} \frac{\rho(f_0(1500)\rightarrow \pi^0\pi^0)}{\rho(f_0(1500)\rightarrow K\overline{K})} = 0.27 \text{ to } 0.45 \tag{9.12}$$

SU(3) flavor symmetry predicts a coupling ratio $r = 1/3$ for a $(u\overline{u} + d\overline{d})$ state and $r = \infty$ for a $s\overline{s}$ state. This highly favors a $(u\overline{u} + d\overline{d})$ interpretation over a $s\overline{s}$ interpretation, the same conclusion of Abele[21]. Because the 0^{++} nonet already appears to have the $(u\overline{u} + d\overline{d})$ state occupied by the $f_0(1370)$, the $f_0(1500)$ is supernumerary, making it a likely glueball or other non-$q\overline{q}$ state.

9.4.2 Absence of ${}^3P_2$

The fit does not apparently want any annihilation from the ${}^3P_2$ initial state. When it is added to the reference fit (# 81), the negative log-likelihood only drops by 10 units.

This is not significant after the addition of 13 extra parameters. It takes on $(4 \pm 2)\%$ of the total Dalitz plot, where the ${}^1P_1$ and ${}^3P_1$ contribution is 21.9%, for a total of about 26%. In fit #142, which imposes charge symmetry for $K\pi$, the contribution from ${}^3P_2$ is $(2 \pm 2)\%$, consistent with zero, and the contribution from ${}^1P_1$ is about 33%.

This is in marked contrasted to the OBELIX analysis[48], which found a that ${}^3P_2$ accounted for $(5 \pm 1)\%$ of the Dalitz plot while ${}^1P_1$ accounted for only $(8 \pm 1)\%$.

If the ${}^1P1$ initial state is removed from the fit and the ${}^3P_2$ is kept (fit #143), then the negative log-likelihood rises by 172 compared to fit # 142 which used both P-waves. Thus the fit clearly demands ${}^1P_1$ and does not demand any ${}^3P_2$.

9.5 Comparison to earlier Crystal Barrel Fit

The $K_L K^{\pm}\pi^{\mp}$ Dalitz plot should be very similar to this Dalitz plot. In [21], only S-wave annihilation was used and the $K_2^*(1430)$ was not used. This hypothesis was used in fit #87, with very poor results. The χ^2 increased by 622 with $980 - 62$ degrees of freedom. The χ^2 plot, showing areas of bad fit, is given in figure 8.13. Adding only P-wave or only $K_2^*(1430)$ to the fit improves things (Fits #80 and #84), but the χ^2 is still poor, with increases in +194 and +304 respectively. The data clearly demands both at least ${}^1P_1$ or ${}^3P_1$ initial state annihilation and the $K_2^*(1430)$ resonance.

Chapter 10

Conclusion

We summarize the results of the analysis of the $K_S K^{\pm}\pi^{\mp}$ Dalitz plot.

1. The $K_S K^{\pm}\pi^{\pm}$ Dalitz plot requires the following resonances to minimally fit the data: $K^*(892)$, $K_2^*(1430)$, $K_0^*(1430)$, $a_2(1320)$, and $\rho(1650)$, originating from $^1S_0$, $^3S_1$, $^1P_1$ and $^3P_1$ initial states. There is some additional evidence for two ρ resonances, $\rho(1450)$ and $\rho(1700)$, which would replace the $\rho(1650)$. There is minimal evidence for the $a_0(1450)$. There is some evidence for the $K^*(1410)$. There is no evidence for the $a_0(980)$ nor for the $a_2(1620)$.

2. The $K_2^*(1430)K$ wave is an important part of $p\overline{p}$ annihilation at rest, and it creates the $K\bar{K}$ edge enhancement.

3. The decays of the $f_0(1500)$ are not consistent with an $s\overline{s}$ interpretation, and thus it is not the $s\overline{s}$ member of the 0^{++} $q\overline{q}$ nonet.

4. The $a_0(980)$ branching ratio into $K\bar{K}$ is consistent with zero, but is also consistent with that determined by the E852 collaboration based on the line shape of the $\eta\pi$ decay channel.

We are not able to accurately determine the branching ratios of many of the resonances from different initial states, because there are not enough constraints in the fits. To determine the branching ratios more accurately, a coupled channel analysis using other reactions not included in this thesis (*e.g.* $p\overline{p}\rightarrow K_S K_S \pi^0$) must be done. This will be done by the author and other collaborators in the near future.

Part III

$\omega \rightarrow \eta\gamma$ Analysis

Chapter 11

Introduction

The radiative decays of mesons are a useful source in testing various theories of low energy physics, i.e. the quark model and the vector dominance model. For example, in both models, decays from and to nonet central states (i.e. η, η', ω, ϕ) are dependent on the pseudoscalar and vector mixing angles. For a review of radiative meson decays see [53]. All of the relevant low mass radiative meson decays have been observed, yet measurements of

$$\omega \rightarrow \eta\gamma \tag{11.1}$$

have been by far the poorest. In the neutral decay mode of the ω, the branching ratio of $\omega \rightarrow \eta\gamma$ is nearly three orders of magnitude less than $\omega \rightarrow \pi^0\gamma$. This large factor is due nearly equally to both phase space and matrix element factors.

The all-neutral sources of ω production in $p\overline{p}$ annihilations are given in table 11.1. In this paper, the branching ratio of the decay of reaction 11.1 was measured using ω mesons from the two-body reaction

$$p\overline{p} \rightarrow \eta\omega \tag{11.2}$$

Channel	BR	Ref	Comment
$p\overline{p}\to\gamma\omega$	$(6.8\pm 1.9)\times 10^{-5}$	[54]	Too small
$p\overline{p}\to\pi^0\omega$	$(5.73\pm 0.47)\times 10^{-3}$	[55]	Large $\pi^0\pi^0\eta$ background
$p\overline{p}\to\eta\omega$	$(1.51\pm 0.12)\times 10^{-2}$	[55]	*Desired channel*
$p\overline{p}\to\omega\omega$	$(3.32\pm 0.34)\times 10^{-2}$	[55]	Extra ω decay lowers efficiency
$p\overline{p}\to\eta'\omega$	$(7.8\pm 0.8)\times 10^{-3}$	[55]	η' hard to tag
$d\overline{p}\to\omega$n	$(2.28\pm 0.41)\times 10^{-5}$	[56]	Too small
$p\overline{p}\to\pi^0\pi^0\omega$	$(2.57\pm 0.17)\times 10^{-2}$	[57]	Many combinatorics
$p\overline{p}\to\pi^0\eta\omega$	$(6.8\pm 0.5)\times 10^{-3}$	[58]	Many combinatorics
$p\overline{p}\to\rho^0\eta$	$(3.9\pm 0.3)\times 10^{-3}$	[59]*	ρ^0 background.
$p\overline{p}\to\rho^0\pi^0$	$(1.7\pm 0.1)\times 10^{-2}$	[60]*	ρ^0 background.
$p\overline{p}\to\pi^+\pi^-\omega$	$(6.6\pm 0.6)\times 10^{-2}$	[61]	Charged split-offs

Table 11.1: Branching ratios of channels containing ω's or ρ^0's. * Indicates averages of many measurements.

measured with the Crystal Barrel spectrometer[2] (PS197) at CERN. This $p\overline{p}$ annihilation channel was the choice for analysis because, as a source for ω's, it has one of the highest branching ratios, has low combinatorics and is all neutral. The Crystal Barrel is especially suited for high precision gamma measurements. The channel $\eta\omega$ was chosen over $\pi^0\omega$ for two reasons. First, the former channel contains no π^0's at all. Any π^0's that are seen are feed-through from the reaction $\omega\to\pi^0\gamma$. Second, the potential ρ^0 backgrounds are a relative factor 9 times less in $\eta\omega/\eta\rho^0$ than in $\pi^0\omega/\pi^0\rho^0$.

The $p\overline{p}\to\pi^+\pi^-\omega$ annihilation channel was not used, even though it has a high branching ratio, because of additional spurious EM showers created by charged particles. Because this analysis is looking for a rare decay into a single photon, the background from these so-called hadronic "split-offs" was unacceptable.

In the analysis, the ratio of rates of $\omega\to\eta\gamma$ to $\omega\to\pi^0\gamma$ was measured to cancel many common systematics, such as the overall $p\overline{p}$ annihilation rate. All η's and π^0's were detected in their neutral 2γ decay mode. Once the π^0's and η's were identified from pairs of γ's, they were combined with the remaining unpaired gamma to form ω candidates. Figure 11.1 shows the decay chain graphically for the signals and the backgrounds.

Because the $\omega \rightarrow \eta\gamma$ is very rare, it is nearly lost to background. Thus great effort was taken to minimize this background as much as possible, while not totally killing the signal.

11.1 Report Outline

1. We provide a introduction to the theory of radiative meson decays,

2. We then describe the Monte Carlo calculations done to simulate the important physics channels and their special properties (chapter 13).

3. We continue with the two data reduction passes on the data (chapters 14 and 15).

4. Finally, we summarize the last cuts (chapter 15) and the fits to the data versus the Monte Carlo simulations (chapter 16).

5. The Appendix contains information on algorithms for kinematic fitting and the fitting of real data to a linear sum of MC data, as well as a calculation of angular distributions and a summary of the 0-prong DLT's.

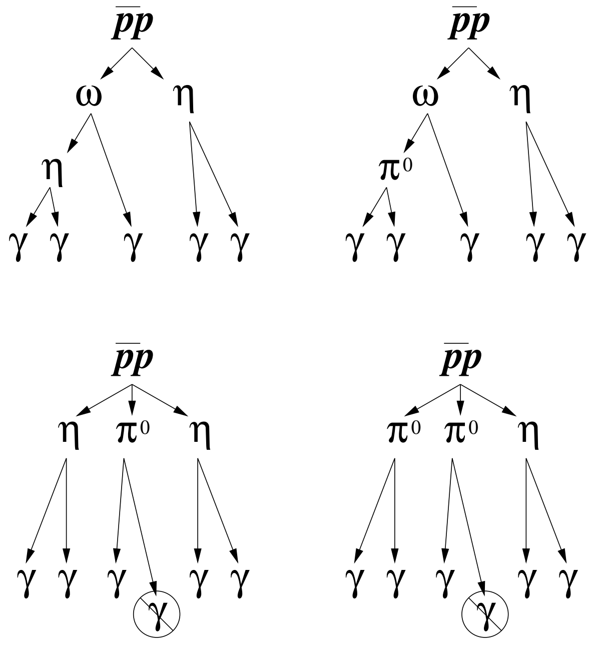

Figure 11.1: Decay chain of four most important channels, the two signal channels $\eta\omega\rightarrow\eta\eta\gamma$ (above left) and $\eta\omega\rightarrow\eta\pi^0\gamma$ (above right), and the two background channels $\pi^0\eta\eta$ (below left) and $\pi^0\pi^0\eta$ (below right)

Chapter 12

Theory

12.1 Introduction

A radiative decay of a particle means that the particle decays into another particle and a high-energy γ ray (photon). Because the photon is spin 1 and thus carries away some angular momentum from the system, there must be a change in spin between the original particle and the final particle. For low mass mesons, this implies spin-1 particles decaying to spin-0 particles, or spin-0 particles decaying to spin-1 particles. The family of all energetically possible decays in this scheme is given in table 12.1. Energy conservation requires that the final particle be less massive than the original.

The measured rates of radiative decays of mesons are a useful observable for testing low energy models of non-perturbative QCD. These models describe the coupling of the radiated photon to the mesons. To first order in the fine structure constant ($\alpha \equiv 1/137$), the general decay rate is written as

Decay	Γ [KeV]	Decay	Γ [KeV]
$\eta'\rightarrow\rho^{0^0}\gamma$	$60.7\pm\ 4\%$	$\eta'\rightarrow\omega\gamma$	$6.07\pm10\%$
$K^{*\pm}\rightarrow K^{\pm}\gamma$	$50.3\pm\ 9\%$	$K^{*0}\rightarrow K^{0}\gamma$	$116.\pm\ 9\%$
$\phi\rightarrow\pi^0\gamma$	$5.80\pm10\%$	$\phi\rightarrow\eta\gamma$	$56.7\pm\ 5\%$
$\omega\rightarrow\pi^0\gamma$	$717.\pm\ 6\%$	$\omega\rightarrow\eta\gamma$	$7.0\ \pm25\%$
$\rho^{\pm}\rightarrow\pi^{\pm}\gamma$	$68.\ \pm22\%$	$\rho^0\rightarrow\pi^0\gamma$	$119.\pm25\%$
$\rho^0\rightarrow\eta\gamma$	$57.5\pm28\%$		

Table 12.1: The eleven radiative meson decays and their rates. (See PDG[62])

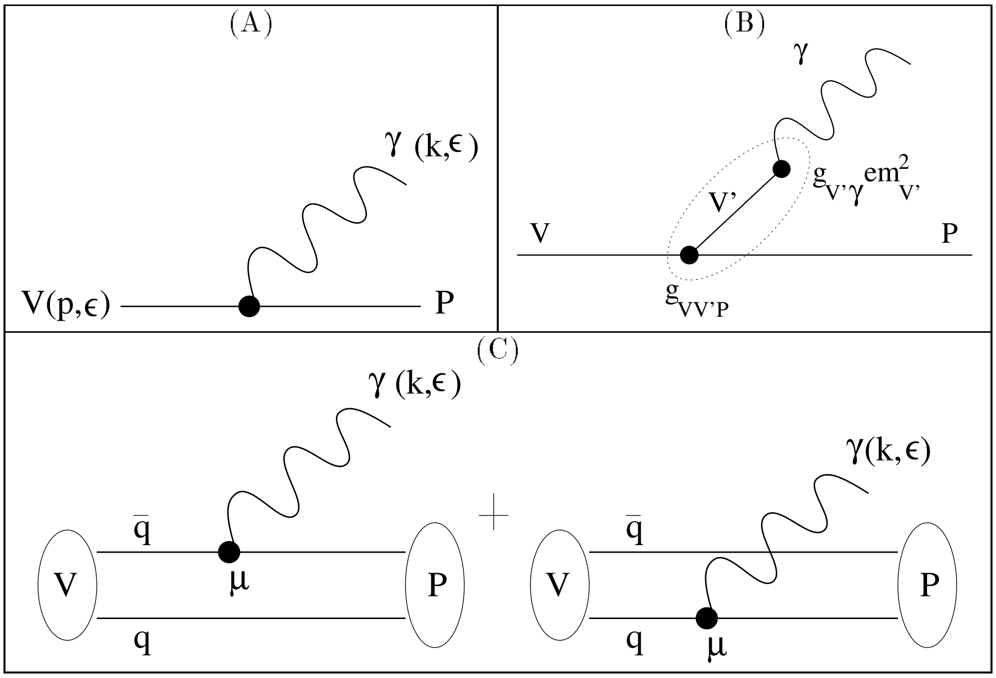

Figure 12.1: Decay mechanisms. (A) general scheme, to first-order in α (B) Vector Meson Dominance (C) Quark model

$$\Gamma(V \to P\gamma) = \frac{4}{3}\alpha k^3 |g_{VP\gamma}|^2$$

where k is the momentum of the radiated γ and

$$g_{VP\gamma} = g(\theta_P, \theta_V, \text{model}) \text{ MeV}^{-1}$$

is the theory dependent matrix element[53]. The convention for SU(3) octet/singlet mixing between $I = 0$ states is as follows[38].

$$\begin{pmatrix} \eta \\ \eta' \end{pmatrix} = \begin{pmatrix} \cos\theta_P & -\sin\theta_P \\ \sin\theta_P & \sin\theta_P \end{pmatrix} \begin{pmatrix} \eta_8 \\ \eta_1 \end{pmatrix}$$

$$\begin{pmatrix} \phi \\ \omega \end{pmatrix} = \begin{pmatrix} \cos\theta_V & -\sin\theta_V \\ \sin\theta_V & \sin\theta_V \end{pmatrix} \begin{pmatrix} \omega_8 \\ \omega_1 \end{pmatrix} \approx \begin{pmatrix} s\bar{s} \\ u\bar{u} + d\bar{d} \end{pmatrix}$$

The deviation from ideal mixing is by convention defined as $\alpha \equiv \theta - \arctan(1/\sqrt{2})$. Mixing in the vector nonet is nearly ideal, that is the value of α for the vector nonet $\alpha \approx -0.3°$. Mixing in the pseudoscalar nonet is not ideal, with $\theta_P \approx -20°$.

A large number of theoretical papers based on the constituent naive quark model, the phenomenological Lagrangian within the SU(3) unitary symmetry scheme, the bag-model and the potential model (see Barik[63] for a plethora of references) have been written providing a a considerable amount of understanding in this area. However there is no single theoretical or phenomenological description of one-photon radiative transition among the low-lying vector and pseudoscalar mesons which can successfully account for all the experimentally observed decay rates. most of these descriptions usually fail in some specific transitions such as $K^* \to K\gamma$ or $V \to \pi\gamma$.

$V \triangleright V' \otimes P$	coupling
$\mathbf{8} \triangleright \mathbf{8} \otimes \mathbf{8}$	$g_{V_i V'_j P_k} \sim g_{88} d_{ijk}$
$\mathbf{8} \triangleright \mathbf{8} \otimes \mathbf{1}$	$g_{V_i V'_j P} \sim g_{81} \delta_{ij}$
$\mathbf{8} \triangleright \mathbf{1} \otimes \mathbf{8}$	$g_{V_i V' P_j} \sim g_{81} \delta_{ij}$
$\mathbf{1} \triangleright \mathbf{8} \otimes \mathbf{8}$	$g_{V V'_i P_k} \sim g_{18} \delta_{ij}$
$\mathbf{1} \triangleright \mathbf{1} \otimes \mathbf{1}$	$g_{V V' P} \sim g_{11}$ ($= 0$ if $\gamma \neq \mathbf{1}$)

Table 12.2: The strong coupling constants are written in octet and singlet terms

12.2 Vector Meson Dominance

The theory of vector meson dominance (VMD), proposed by Gellman[64] and reviewed by Durso[65], states that electro-magnetic reactions between hadronic states proceed through vector meson intermediate states, (i.e. $\rho \rightarrow \gamma$) . Because the photon is not an isospin eigenstate, the three vector mesons (ρ^0, ω and ϕ) can contribute.

$$g_{VP\gamma} = \sum_{V'} \left(e m_{V'}^2 g_{V'\gamma} \right) \left(g_{VV'P} \right)$$

The decay is parameterized by a SU(3) interaction followed by transmutation of the intermediate vector into a photon. Assuming that the strong force symmetry is only broken between octet and singlet states and also that the photon is not a SU(3) singlet state, the unique coupling constants are at most three in number, as shown in table 12.2.

We can then write the measured coupling constants in terms of these octet/singlet constants and the nonet mixing angles,

$$\begin{aligned} g_{\omega\pi^0\gamma} &= \frac{\sqrt{2}}{3} \sin \alpha_V (g_{88} - g_{18}) + \\ &\quad \frac{1}{3} \cos \alpha_V (g_{88} + 2 g_{18}) \end{aligned}$$

$$\begin{aligned} g_{\omega\eta\gamma} &= \frac{1}{9}\cos\alpha_V \sin\alpha_P(g_{88} - 2g_{81} - 2g_{18}) + \\ &\frac{2}{9}\sin\alpha_V \cos\alpha_P(-g_{88} - g_{81} - g_{18}) + \\ &\frac{\sqrt{2}}{9}\sin\alpha_V \sin\alpha_P(g_{88} - 2g_{81} + g_{18}) + \\ &\frac{\sqrt{2}}{9}\cos\alpha_V \cos\alpha_P(-g_{88} - g_{81} + 2g_{18}). \end{aligned}$$

In a recent paper by Benayoun[66], 11 measured radiative decays are fitted to these constraints. The authors find that full nonet symmetry holds to an extent by noting that the fitted g values are nearly all equal.

coupling g_{VP}	All free GeV^{-1}	Two free ($g_{88} = g_{18}$) GeV^{-1}
g_{88}	0.74 ± 0.02	0.70 ± 0.02
g_{18}	0.67 ± 0.02	0.70 ± 0.02
g_{81}	0.64 ± 0.06	0.61 ± 0.03

12.3 Static quark model

In the static quark model (see Barik[63] for a more advanced treatment), the interaction that leads to decay is a M1 magnetic dipole quark-photon interaction with matrix element,

$$(H = \vec{\mu} \cdot \vec{B})$$

$$M = \mu_q \vec{\sigma}_q \cdot (\vec{k} \times \vec{\epsilon})$$

For example, here is a sketch of the calculation of the g constants for $\omega \rightarrow \pi^0\gamma$[67].

$$g_{\omega\pi^0\gamma} = \langle\omega|\hat{\mu}\hat{\vec{\sigma}} \cdot \vec{\epsilon}|\pi^0\gamma\rangle \tag{12.1}$$

$$\hat{\vec{\sigma}} \cdot \vec{\epsilon}|\gamma\rangle = \hat{\sigma}_+|\gamma\rangle \tag{12.2}$$

$$|\omega\rangle = |\left(\cos\alpha_V \frac{(u\bar{u}+d\bar{d})}{\sqrt{2}} - \sin\alpha_V(s\bar{s})\right)(\uparrow\uparrow)\rangle \tag{12.3}$$

$$|\pi^0\rangle = |\left(\frac{(u\bar{u}-d\bar{d})}{\sqrt{2}}\right)\left(\frac{(\uparrow\downarrow-\downarrow\uparrow)}{\sqrt{2}}\right)\rangle \tag{12.4}$$

$$g_{\omega\pi^0\gamma} = \left(\frac{2}{3}\mu_u + \frac{1}{3}\mu_d\right)\cos\alpha_V \tag{12.5}$$

$$\begin{aligned} g_{\omega\eta\gamma} &= -\frac{1}{3}(2\mu_u - \mu_d)\cos\alpha_V \sin\alpha_P \\ &\quad -\frac{2}{3}\mu_s \sin\alpha_V \cos\alpha_P \end{aligned} \tag{12.6}$$

12.4 Exact SU(3) Symmetry and Nonet Symmetry

If we impose exact SU(3) symmetry or exact nonet symmetry, that is

$$\mu_u = \mu_d = \mu_s$$

or

$$g_{88} = g_{18} = g_{81}$$

and assume the mixing is $\alpha_V = 0$ and $\alpha_P = -45°$, then the Vector Dominance Model and Static Quark Model give the same result, and agree reasonably well with the experimental data. Table 12.3 shows the prediction from such an assumption and the measured rates. We see good agreement within two sigmas for all measurements except for the decay $\phi \to \pi^0\gamma$ which is prohibited by exact SU(3) symmetry and ideal mixing. Note that the absolute rates are not predicted by theory, only the relative rates.

Decay	Rel. $\lvert M\rvert^2$	Phase Space	Rel. Ratio	PDG (keV)
$\omega\to\pi^0\gamma$	1	0.0549	720	720 ± 40
$\omega\to\eta\gamma$	$\frac{1}{18}$	0.0079	5	7 ± 2
$\rho\to\pi^0\gamma$	$\frac{1}{9}$	0.0527	80	120 ± 30
$\rho\to\eta\gamma$	$\frac{1}{2}$	0.0073	470	570 ± 110
$\phi\to\pi^0\gamma$	0	0.1258	0	5.8 ± 0.6
$\phi\to\eta\gamma$	$\frac{4}{18}$	0.0474	52	57 ± 3

Table 12.3: Exact SU(3) predictions for selected decays

12.5 Other theories

Agreement with data can be improved by breaking symmetry by different methods, including adding quark mass effects, direct strange quark symmetry breaking, and/or octet vs. singlet differences. Relativistic corrections can be included as well.

The Chanowitz Equations also allow an interesting modification to the quark model by setting its parameter $\xi = 2$, which gives the quarks integral charges rather than fractional charges[66].

The Cloudy Bag Model uses a Lagrangian which seems to be a mixture of QCD and ChPT at the same time, i.e. quark fields and meson fields, and the matrix element takes 2 pages to write down [68, 69].

However, the current data in general is not precise enough to really separate any of the models, as seen in table 12.4. Also, some of these models only provide constraints to the relative branching ratios and can arrive at predictions based on fits to a complete set of data. Thus the theoretical value is not unbiased towards the measurements.

Reference	*Model or ω source*	BR($\omega \rightarrow \eta\gamma$) [$10^{-4}$]	BR($\rho^0 \rightarrow \eta\gamma$) [$10^{-4}$]
Zhong[69] **	Exact SU(3)	10.1	
Zhong[69] **	Broken SU(3)	5.2	
Benayoun[66]	Fractional Quark Chrg	6.14 ± 0.58	
	Integral Quark Chrg	3.27 ± 0.44	
Barik[70]	Set "1"	6.5	
	Set "2"	6.76	
	Static	5.8	
Singer[68]	Cloudy Bag	2.7	
Zhong[69]	M1 Cloudy Bag	3.1 – 3.3	
Bramon[71]	Broken SU(3)	6.1 ± 0.7	
Dolinksy[72]	$e^+e^- \rightarrow \omega$	$6.4^{+7.0}_{-4.7}$	4.0 ± 1.1 (+)
Alde[73]	$\pi^- p \rightarrow \omega n$	8.3 ± 2.1	–
CB[74]	$p\overline{p} \rightarrow \omega\eta$	6.6 ± 1.7	–
This measurement	$p\overline{p} \rightarrow \omega\eta$	$(4.2^{+1.3}_{-1.8}) \times 10^{-4}$	N/A

Table 12.4: Various theories on radiative meson decays and their predictions for BR($\omega \rightarrow \eta\gamma$)

12.6 Polarized Decay

In general, a polarized spin particle will not decay isotropically. For spin-1 particles decaying into spin-0 particles, the following radiation patterns are observed:

$$|1 \pm 1\rangle = \tfrac{1}{2}(1 + \cos^2\theta) \tag{12.7}$$

$$|10\rangle = \sin^2\theta \tag{12.8}$$

Annihilations of $p\overline{p}$ occur primarily in low angular momentum states, written in ${}^{2s+1}L_J^{(PC)}$ format:

$${}^1S_0^{(-+)}, {}^3S_1^{(--)}, {}^1P_1^{(+-)}, {}^3P_0^{(++)}, {}^3P_1^{(++)}, {}^3P_2^{(++)}$$

When decaying into vector + pseudoscalar, i.e. $p\overline{p} \rightarrow \omega\eta$ or $p\overline{p} \rightarrow \omega\pi^0$, only ${}^3S_1$ and ${}^1P_1$ states are allowed by C-parity.

In the frame of the vector particle, the orbital angular momentum quantized along the motion axis of the vector particle always has $m_L = 0$, because $\vec{L} \cdot \vec{P} = (\vec{R} \times \vec{P}) \cdot \vec{P} = 0$.

Annihilation	Vector+Pseudoscalar System		
	J^{PC}	Orbital Ang. Mom. $\|Lm\rangle$	Spin Ang. Mom. (S)
$^1P_1$	1^{+-}	$\|00\rangle$	1
$^3S_1$	1^{--}	$\|10\rangle$	1
$^1P_1$	1^{+-}	$\|20\rangle$	1

We now examine the Clebsch-Gordan coefficients to couple $L+S = J$, where $J = 1$ in all cases.

$\langle LSm_Lm_s\|Jm_J\rangle$	value
$\langle 01\ 0\ 0\|1\ 0\rangle$	1
$\langle 11\ 0+1\|1+1\rangle$	$-\sqrt{1/2}$
$\langle 11\ 0\ 0\|1\ 0\rangle$	0
$\langle 11\ 0-1\|1-1\rangle$	$\sqrt{1/2}$
$\langle 21\ 0+1\|1+1\rangle$	$\sqrt{1/10}$
$\langle 21\ 0\ 0\|1\ 0\rangle$	$-\sqrt{2/5}$
$\langle 21\ 0-1\|1-1\rangle$	$\sqrt{1/10}$

Finally, the radiation distributions are as follows, obtained by multiplying the pure polarization distributions by the C-G coefficients squared and summing, then renormalizing to the form $1 + b\cos^2\theta$.

$p\overline{p}$	V+P System	Radiation Distribution
$^1P_1$	$L = 0$	1 (isotropic)
$^3S_1$	$L = 1$	$1 + \cos^2\theta$
$^1P_1$	$L = 2$	$1 - 3/5\cos^2\theta$

For antiproton annihilations in liquid hydrogen, the ratio of P to S wave annihilation has been measured in other experiments with values ranging from 0 to 10%, while in gaseous hydrogen annihilation it is closer to 50%. In this measurement of $\omega \to \pi^0\gamma$ decays, the decay angle distribution is consistent with mostly S-wave annihilation.

Chapter 13

Monte Carlo Simulation

13.1 Introduction

CBGEANT, version 5.05.04 was used to generate over a million MC events for this analysis. Over 97% of these events were simulations of backgrounds which have a small efficiency of being detected in the wrong final state but which are still large compared to the data; the remaining 3% of events are simulations of the signal channel ($(\eta\rho^0+\eta\omega)\rightarrow\eta\eta\gamma$). The statistics of each channel are given in table 13.1.

The two main background types are due to (a) mismatching $\gamma\gamma$ to fake η's or fake π^0's (in 5 γ states) and (b) 6 γ states that lose one γ and appear as 5 γ states. There are also 5 γ non-resonant backgrounds, as well as backgrounds from 4 γ final states that acquire a spurious split-off. Each of these channels is discussed below, and the cuts to suppress the backgrounds are discussed in chapter 15.

Short name	Events	Description
lbl	20,318,391	real data (from "LBLxxx" tapes)
eoeg	9,965	$p\overline{p}\to\eta\omega$, $\omega\to\eta\gamma$, $\eta\to\gamma\gamma$
eopg	568,928	$p\overline{p}\to\eta\omega$, $\omega\to\eta\gamma$, $\eta\to\gamma\gamma$, $\pi^0\to\gamma\gamma$
popg	99,963	$p\overline{p}\to\pi^0\omega$, $\omega\to\pi^0\gamma$, $\pi^0\to\gamma\gamma$
eep	1,104,150	$p\overline{p}\to\pi^0\eta\eta$, $\eta\to\gamma\gamma$, $\pi^0\to\gamma\gamma$
epp	788,911	$p\overline{p}\to\pi^0\pi^0\eta$, $\eta\to\gamma\gamma$, $\pi^0\to\gamma\gamma$
ppp	600,000	$p\overline{p}\to\pi^0\pi^0\pi^0$, $\pi^0\to\gamma\gamma$
epg	50,000	$p\overline{p}\to\pi^0\eta\gamma$, $\eta\to\gamma\gamma$, $\pi^0\to\gamma\gamma$
eeg	150,000	$p\overline{p}\to\eta\eta\gamma$, $\eta\to\gamma\gamma$
ppg	50,000	$p\overline{p}\to\pi^0\pi^0\gamma$, $\pi^0\to\gamma\gamma$
ee	100,000	$p\overline{p}\to\eta\eta$, $\eta\to\gamma\gamma$
pp	100,000	$p\overline{p}\to\pi^0\pi^0$, $\pi^0\to\gamma\gamma$

Table 13.1: List of Monte Carlo data sets

13.2 GEANT software

The CERN code package GEANT, version 3.21, is used to simulate the propagation of the initial annihilation particles through the detector, applying energy losses, and interactions with the active detector elements. Although not critical for this analysis because there are no direct hadrons interacting with the detector (only γ's), the GHEISHA package was used for tracking spurious hadrons. The events were generated using a hit/miss algorithm that results in the events being flat in phase space, that is each event has an inherent weight of unity. Resonances with a sufficiently wide width are generated with a non-relativistic Breit-Wigner distribution in mass. Because some events generated with this Breit-Wigner lie outside phase space, a very small fraction of events are rejected in the generation phase (for example 0.00036 in $\pi^0\omega\to\pi^0\pi^0\gamma$). Post-reconstruction weighting was done via a variety of methods for the different channels.

13.3 Dalitz plot weighting of 3 pseudoscalar channels

The background channels, $\pi^0\eta\eta$, $\pi^0\pi^0\eta$ and $\pi^0\pi^0\pi^0$, are rich in Dalitz plot structure, specifically, f and a scalar resonances. The Crystal Barrel has published analyses of all three channels, and the acceptance corrected Dalitz plots were used to weight these channels so that they reflect the resonance structure. Each Monte Carlo event is mapped to a bin in the Dalitz plot, using the initially generated momenta of the three mesons. The weights are normalized to average unity over the Dalitz plot. Edge bins which do not lie entirely in allowed phase-space are not corrected, but because of the small bin size, the net result is not significant, and because the effect is only on the edge, it is not correlated to the measurement of interest along the omega bands.

13.4 Angular dependence of ω decay

Because the ω does not decay isotropically in its rest-frame (because it is polarized by annihilation selection rules), the Monte Carlo must be weighted to reflect this. See appendix 12.6 for a theoretical description of the angular distributions. The angular distribution is of the form

$$f(\theta) = (1 + b\cos^2\theta)/(1 + b/3),$$

where b was measured to be $b = 1.04 \pm 0.03$. This value was determined by fitting the angular distribution of the data for the channel $\eta\omega \rightarrow \eta\pi^0\gamma$, after subtracting the expected background from $\pi^0\pi^0\eta$ and dividing by the efficiency for $\eta\omega \rightarrow \eta\pi^0\gamma$. The allowed physical range for b is $b \leq 1$, so the value of b is fixed to 1, and the error is increased to 0.04. This value is consistent with annihilation from $^3S_1$. The function is normalized to average one from $\theta = 0 \rightarrow \pi$.

13.5 Weighting the ρ^0/ω interference dynamics

Because isospin is not the decay, the decay $\omega \rightarrow \eta\gamma$ can interfere coherently with the decay $\rho^0 \rightarrow \eta\gamma$. In addition, there is direct mixing between ω and ρ^0 states by off-diagonal components of the mass matrix in the isospin eigenstate basis.

We write the net amplitude with the phenomenological model,

$$S = (A_{\rho^0{}_I} A_{\omega_I}) \left(m - \begin{bmatrix} m^*_{\rho^0{}_I} & -\delta \\ -\delta & m^*_{\omega_I} \end{bmatrix} \right)^{-1} \begin{pmatrix} T_{\rho^0{}_I} \\ T_{\omega_I} \end{pmatrix}$$

where A_x are the complex production amplitudes, T_x are the complex decay amplitudes, m is the $\eta\gamma$ or $\pi^0\gamma$ mass, m^*_x are the complex masses ($= m + i\Gamma/2$), and δ is the mass mixing term, measured to be $\delta = 2.5$ MeV from many experiments[75], [76]. The I subscripts indicate that these are isospin eigenstates, not the physical vector mesons. We can expand this equation to first order in δ/m_ω.

$$S = \frac{A_{\rho^0{}_I} T_{\rho^0{}_I}}{m - m^*_{\rho^0{}_I}} + \frac{A_{\omega_I} T_{\omega_I}}{m - m^*_{\omega_I}} + \frac{\delta(A_{\rho^0{}_I} T_{\omega_I} + A_{\omega_I} T_{\rho^0{}_I})}{(m - m^*_{\rho^0{}_I})(m - m^*_{\omega_I})}$$

or equivalently,

$$S = \frac{A_{\rho^0{}_I} T_{\rho^0{}_I}}{m - m^*_{\rho^0{}_I}} \left(1 + \frac{T_{\omega_I}\delta}{T_{\rho^0{}_I}(m - m^*_{\omega_I})} \right) + \frac{A_{\omega_I} T_{\omega_I}}{m - m^*_{\omega_I}} \left(1 + \frac{T_{\rho^0{}_I}\delta}{T_{\omega_I}(m - m^*_{\rho^0{}_I})} \right)$$

Most of the work in this area has concerned the not-so-rare decays into $\pi^+\pi^-$, rather than the rare decays into $\eta\gamma$.

In the absence of isospin breaking, the third term vanishes. In the approximation that $A_{\rho^0} \sim A_\omega$ and $T_{\rho^0} \sim T_\omega$, but $\Gamma_{\rho^0}/\Gamma_{om} = 20$, the third term is roughly a factor of 30 smaller than the second term at the omega mass. When the total amplitude is squared, this isospin term becomes smaller.

The complex phase of $\alpha = \arg(A_{\rho^0}/A_\omega)$ for the productions in $p\overline{p}{\rightarrow}\rho^0\eta$ and $p\overline{p}{\rightarrow}\omega\eta$ has been measured to be $\alpha = -5.4 \pm 4.3°$ [59]. This supports the quark model of $p\overline{p}$ annihilation, which predicts the phase to be zero. We fix $\alpha = 0$ in this analysis. We note in passing that this production phase in other processes ($e^+e^-{\rightarrow}\pi^+\pi^-$, $\pi^+p{\rightarrow}\pi^+\pi^-\Delta^{++}$, $\pi^-p{\rightarrow}\pi^+\pi^-n$) is always 0,$\pm\pi/2$ or π [77]. The low statistics do not allow a definitive determination of this phase, although some preliminary tests showed that $\alpha = 0$ was favored over $\alpha = \pi$.

The complex phase of $\phi = \arg(T_{\rho^0}/T_\omega)$ for the decays $V{\rightarrow}P\gamma$ ($V{=}\rho^0$ or ω, $P{=}\eta$ or π^0) is either 0 or π, because the decay amplitudes are real in the quark model (the dipole spin-flip operator results in real magnetic moments). Using typical values for the pseudoscalar and vector mixing angles, the phase is zero. We fix this phase to zero also because we believe the quark model.

The production of ρ^0 and ω is believed to be totally coherent in the case where the particles are created and decay in strong reactions [59]. We call this theory type I, which is strictly used in a previous paper by the Crystal Barrel[74] for $(\eta\rho^0{+}\eta\omega){\rightarrow}\eta\eta\gamma$.

However, the decay into $\pi^+\pi^-$ is very different from the decay into $\eta\gamma$. The former decay is a strong decay which occurs very near the original $p\overline{p}$ annihilation. Because ω is forbidden to decay into $\pi^+\pi^-$ by isospin conservation, it can only decay if it mixes into a ρ^0. However, the decay $\eta\gamma$ is electro-magnetic and does not need to conserve isospin in the decay. Also because the radiative decay happens far from the initial $p\overline{p}$ annihilation, the amount of interference between ρ^0 and ω is limited to the relatively small amount of eigenstate mixing between the two. If there is no isospin mixing of eigenstates, then the two channels of $\omega \rightarrow \eta\gamma$ and $\rho^0 \rightarrow \eta\gamma$ may proceed totally incoherently. Thus the slight correction for interference only happens for the small fraction of mixed state. We label this intensity type II.

For comparison and to show that the intrinsic isospin mixing is small, a third assumption is created where there is no interference and no mixing between ρ^0 and ω is labeled type III. Fits to these three types (I,II and III) are given in chapter 16.

We generate the decay particles flat in phase space (i.e. $\eta\eta\gamma$ and $\eta\pi^0\gamma$). We then calculate the intensity for each event using the following amplitudes,

$$S \sim \langle \eta\gamma | T | x' \rangle \langle x' | H | x \rangle \langle x | A | p\overline{p} \rangle . \tag{13.1}$$

where x and x' are mixed states of ω and ρ^0, and the spectator η meson has been suppressed from the equation for clarity. We assume that all the mass-dependent dynamics are contained only in the middle propagator term, which we parameterize with a mass matrix with off-diagonal terms, δ.

$$S = \begin{pmatrix} T_\omega & T_\rho \end{pmatrix} \left(m - \begin{bmatrix} m_\omega - i\Gamma/2 & \delta \\ \delta & m_\rho - i\Gamma/2 \end{bmatrix} \right)^{-1} \begin{pmatrix} A_\omega \\ A_\rho \end{pmatrix} \tag{13.2}$$

Thus the net intensity I is calculated as

$$I = \sum_{\lambda=\pm 1} |d^1_{1,\lambda}(S_\omega + e^{i\alpha} e^{i\phi} S_\rho) + C/\sqrt{2}|^2 \tag{13.3}$$

$$S_x = \frac{\mu_x}{\sqrt{2\pi}} \frac{|A_x||T_x|}{m - m_x + i\Gamma_x/2} \tag{13.4}$$

$$\times \left(1 - \frac{|A_y|}{|A_x|} \frac{e^{\pm i\alpha}\delta}{m - m_x + i\Gamma_x/2}\right) \tag{13.5}$$

$$|A_x| = \sqrt{BR(p\overline{p}\rightarrow x\eta)} \tag{13.6}$$

$$|T_x| = \sqrt{BR(x\rightarrow\eta\gamma)\Gamma_x} \tag{13.7}$$

where $x(y)$ is $\omega(\rho^0)$ or $\rho^0(\omega)$. The helicity formalism gives the angular dependence of the ω decay. The rotation d matrices are $d^1_{1,\pm\lambda} = (1 \pm \cos\theta)/2$, where λ is the J_z component of the initial $p\overline{p}$ state along the ω momentum axis and θ is the Gottfried-Jackson angle. The decay phase ϕ is the phase difference between the $\omega\rightarrow\eta\gamma$ and $\rho^0\rightarrow\eta\gamma$ decays, and is set to zero based on the quark model. The production phase α is the phase difference between the $p\overline{p}\rightarrow\eta\omega$ and $p\overline{p}\rightarrow\eta\rho^0$ production amplitudes, and is set to zero, based on a Crystal Barrel measurement of this quantity which was consistent with zero.[59]. The complex constant C describes the flat $\eta\eta\gamma$ background. The $\pm$ sign in $e^{\pm i\alpha}$ is $+$ for $x = \omega$ and $-$ for $x = \rho$. The mixing parameter is $\delta = 2.5$ MeV[78]. Numerical values for the remaining values are given in table 13.2[74]. The μ_x are normalization factors, such that the integral over the Dalitz plot of the $|S_x|^2$ with $\delta = 0$ and $\Gamma\rightarrow 0$ equals the net branching ratio, BR($p\overline{p}\rightarrow$X$\rightarrow\eta\eta\gamma$). We chose this definition of normalization to be consistent with e^+e^- experiments which generate ω's directly at 781 MeV, i.e. at the nominal mass with an energy spread small compared to the ρ^0 width. When $\Gamma \neq 0$, the Monte Carlo efficiency automatically takes care of the phase space correction, so no explicit correction is needed for the amplitude. Annihilation branching ratios as determined by the Crystal Barrel and used in this analysis are integrated over available phase space which may not completely cover the resonance width. In the case of the ρ^0, about 3% of the resonance is outside of phase space. This effect is small enough to be ignored in this analysis, but becomes more significant if resonances are on or near the edge of phase space.

The α_x is a normalization factor, such that the integral over the Dalitz plot of the $|S_x|^2$ with $\delta = 0$ and $\Gamma \rightarrow 0$ is simply the net branching ratio, that is

$$\alpha_x \int \int_{dalitz} dLIPS|S-x|^2 = \beta_x \mathrm{BR}(pbarp \rightarrow X\eta \rightarrow \eta\eta\gamma)$$

When $\Gamma \neq 0$, the Monte Carlo efficiency automatically takes care of the phase space correction, so no additional correction is needed. The β_x is a correction coefficient to tabulated production branching ratios. Crystal Barrel production branching ratios are the integrated intensity over all of phase space of the resonance (ω or ρ^0 in this case), and thus have an inherent phase-space correction that must be removed in order to get the correct amplitude. The correction is calculated by comparing the integrated infinite-phase-space Breit-Wigner to the integrated Dalitz-limited-phase-space Breit-Wigner.

$$\beta_x = \frac{\int_{-\infty}^{\infty} |\mathrm{BW}_x(m)|^2 p(m_x) dm}{\int_{-\infty}^{\infty} |\mathrm{BW}_x(m)|^2 p(m) dm} \tag{13.8}$$

where $p(m)$ is the momentum of the $(\eta\gamma)$ system in the $p\overline{p}$ rest frame as a function of mass $m(\eta\gamma)$, and $p(m_x)$ is evaluated at the mass of x. We define the decay branching ratio of a broad resonance x at the standard mean mass of the resonance m_x, and allow the phase-space corrections to be calculated directly by the Monte Carlo, so no additional corrections are needed for the amplitude or for a mass dependent width; these are included in the Monte Carlo efficiency. These corrections, of course, apply mostly to the ρ^0 whose width significantly exceeds the limits of 3-body phase space.

On top of this intensity weighting, the events are also weighted according to their decay angle distribution, as in section 13.4.

process	BR (10^{-3})	Ref	process	BR (10^{-3})	Ref
$p\overline{p}\rightarrow\eta\omega$	15.1 ± 1.2	[55]	$p\overline{p}\rightarrow\eta\rho^0$	3.9 ± 0.3	[59]
$p\overline{p}\rightarrow\pi^0\omega$	5.7 ± 0.3	[55]	$p\overline{p}\rightarrow\pi^0\rho^0$	17 ± 3	[60]
$\omega\rightarrow\eta\gamma$	0.83 ± 0.21	[62]	$\rho^0\rightarrow\eta\gamma$	0.38 ± 0.07	[62]
$\eta\rightarrow\gamma\gamma$	392.5	[62]			
Parameter	value	Ref	Parameter	value	Ref
Γ_ω	8.43 MeV	[62]	Γ_{ρ^0}	150.7 MeV	[62]
$\alpha_{\eta\omega}$	771.7 MeV		$\alpha_{\eta\rho^0}$	804.0 MeV	
$\alpha_{\pi^0\omega}$	1423.0 MeV		$\alpha_{\pi^0\rho^0}$	1487.9 MeV	
$\beta_{\eta\omega}$	1.002		$\beta_{\eta\rho^0}$	1.039	
$\beta_{\pi^0\omega}$	1.001		$\beta_{\pi^0\rho^0}$	1.023	

Table 13.2: BW parameters

13.6 The flat 3-body channels, $p\overline{p}\rightarrow\eta\eta\gamma$, $\pi^0\eta\gamma$ and $\pi^0\pi^0\gamma$

The non-resonant channels, $p\overline{p}\rightarrow\eta\eta\gamma$, $\pi^0\eta\gamma$ and $\pi^0\pi^0\gamma$, have not been previously measured because they are predicted to be rare and also impossible to measure in bubble chamber experiments.

The rate of $p\overline{p}\rightarrow\eta\eta\gamma$ can be estimated by invoking vector dominance, which relates EM rates to QCD rates with a factor of the fine structure constant. In this case, we would want to know the rates of $p\overline{p}\rightarrow\eta\eta\omega$ and $p\overline{p}\rightarrow\eta\eta\rho^0$, then use the couplings of ω or ρ^0 to γ, which is

$$g_{\rho\gamma} = 3g_{\omega\gamma} = 3.03 \times 10^{-3}$$

and then multiply by phase space corrections. The measurements of the ρ^0 channels are not available, but we can guess that they are approximately the same, since the rate for $p\overline{p}\rightarrow\omega\pi^+\pi^-$ and the rate for $p\overline{p}\rightarrow\rho^0\pi^+\pi^-$ are approximately the same. If they are indeed the same, then the coupling factor is simply $g_{\rho\gamma}^2$ because $g_{\omega\gamma}^2$ is an order of magnitude smaller. The phase space ratios are approximately LIPS($\pi^0\pi^0\gamma$)/LIPS($\pi^0\pi^0\rho^0$) $\approx$ 2 and LIPS($\pi^0\eta\gamma$)/LIPS($\pi^0\eta\rho^0$) $\approx$ 4.

[branching ratios from [55]]

Reaction $p\overline{p}\to$	BR (10^{-3}) X = ρ^0	PS(X=γ)/PS(X=ρ^0) factor	BR (10^{-5}) X=γ
$\pi^0\pi^0$X	20.0	2	12
$\pi^0\eta$X	6.8	4	8

The reaction $p\overline{p}\to\eta\eta\omega$ has not been measured because it has nearly no available phase space. We can only relate $p\overline{p}\to\eta\eta\gamma$ to the other radiative annihilations via phase space ratios. (The phase space for $\eta\eta\gamma$ is much, much greater (perhaps 3-4 orders of magnitude) than $\eta\eta\omega$. It is curious to note that m(η) +m(η) + m(ω) = 1876.84, while m($p\overline{p}$) = 1876.54!)

Using LIPS($\eta\eta\gamma$)/LIPS($\pi^0\pi^0\gamma$) = 0.2 and LIPS($\eta\eta\gamma$)/LIPS($\pi^0\eta\gamma$) = 0.5, we get BR($\eta\eta\gamma$) = $(2-4)\times 10^{-5}$.

We compare our naive calculations to the values derived in chapter 16.

Reaction	BR (10^{-5}) prediction	BR (10^{-5}) seen
$p\overline{p}\to\pi^0\pi^0\gamma$	12	$8.8^{+6.2}_{-8.8}$
$p\overline{p}\to\pi^0\eta\gamma$	8	$25.0^{+5.0}_{-25.0}$
$p\overline{p}\to\eta\eta\gamma$	2 - 4	$1.9^{+1.6}_{-1.9}$

The agreement is okay for two cases, but poor for the third. However, we have neglected phase space factors and have been lazy in using the ρ^0 VMD constant instead of ω, so all of these numbers are just order of magnitude calculations.

The $\eta\eta\gamma$ background was included in the fits to improve their results. The χ^2 fell significantly (see table 16.2) and the dependence on the confidence level for the background $\pi^0\eta\eta$ vanished when the $\eta\eta\gamma$ background was included. The dependence vanished because of the difference in the confidence levels of $\pi^0\eta\eta$ vs. $\eta\eta\gamma$. Because $\pi^0\eta\eta$ is missing a photon, it is biased to have too low an energy and thus a bad confidence level distribution that falls with increasing confidence level. On the other hand, $\eta\eta\gamma$ is a perfect match for the kinematic fit and thus has a perfectly flat confidence level. By describing the background as a sum of $\pi^0\eta\eta$(with a falling CL) and $\eta\eta\gamma$(with a flat CL), the fit values were constant regardless of what CL was used. Without the $\eta\eta\gamma$ background, the fit value for $\pi^0\eta\eta$ rose significantly as the CL cut was increased.

Because the measurement of these backgrounds is highly correlated to the 3-pseudoscalar backgrounds and it is possible that the Monte Carlo simulation of the 3-pseudoscalar backgrounds could be inaccurate, we do not wish to claim discovery of these channels, but we do claim that the data supports their existence at the given intensities. We assign the largest portion of the systematic error later in this paper to our ignorance of whether or not these channels really exist, which amounts to an error of 20% because the shape of the background under the ω peak is slightly different.

The existence of the $\eta\eta\gamma$ background plays an enormous role in the alternate analysis by the Crystal Barrel [74], where the measured value of BR($\omega\rightarrow\eta\gamma$) changes by a factor of two if this background is included in the background subtraction. We note that the two analyses agree well if the $\eta\eta\gamma$ channel is included, but disagree if not. See the separate report [79] for a detailed comparison between the two analyses.

Chapter 14

First Skimming Pass

The first pass on the triggered data selected good 5 γ events. In this chapter we describe the trigger, data retrieval and the first pass data cuts.

14.1 Trigger and data retrieval

Antiprotons from the 200 MeV LEAR beam were captured in liquid hydrogen and annihilate at rest. The zeroth level trigger requires a signal in the entrance counter, but no trigger in the downstream veto counter. The first level trigger counts the multiplicity of hit clusters in the PWC, due to charged particles. Since this analysis requires all neutral particles, the "0-prong" trigger required no hit clusters in the PWC. These events were written to IBM tape cartridges. The data was collected over a 5 year period spanning December 1989 to June 1994, and archived. A total of 747 cartridges (approximately 200MB) were used for the 0-prong data.

With the advent of better storage technology, these cartridges as well as the rest of the Crystal Barrel data were transfered to several hundred DLT's (10 GB). Unfortunately, the list of runs and their trigger type was lost after the data archivist left the collaboration. The author was required to search partial catalogs, obsolete computer systems and various production log files to determine which DLT held which the desired 0-prong data. After weeks of such effort, a full catalog of every run of the Crystal Barrel was collected, and from this list, the 0-prong runs were extracted from approximately a hundred DLT's and written to a nine DLT set. This set held approximately 20 million events.

14.2 Cuts

The entire 0-prong data set was reconstructed using the standard Crystal Barrel software (see section 1.10). The result of this reconstruction is a list of particle energy deposits (PEDs) in the electro-magnetic calorimeters and a list of charged tracks (if any).

The choice of PED definition parameters affects the efficiency. A PED is defined as a local maximum in energy among a cluster of fired crystals. There can be more than one local maximum in a cluster, thus more than one PED. This can be caused by photons that hit the detector in close proximity, or it be caused by a statistical shower fluctuation.

In this first step of the processing, all local maxima greater than 20 MeV were kept as photons. This threshold is selected to minimize spurious PEDs caused by show fluctuations, but because it is high the reconstruction can miss low energy photons. To solve this problem, the PED thresholds were changed in the second data reduction pass, described in chapter 15.

Some events contained charged particles that somehow passed the 0-prong trigger.

cut	LBL	$\pi^0\eta\eta$	$\pi^0\pi^0\eta$	$\pi^0\pi^0\pi^0$	$\eta\omega\to\eta\eta\gamma$	$\eta\omega\to\eta\pi^0\gamma$
Event in	20298446	1104150	788911	600000	9965	568928
0 tracks	18223703	1006509	719152	530391	9398	523279
$\lvert\vec{p}\rvert < 200$ MeV	13525910	852225	616544	456845	8045	446242
$\lvert E - 1876\rvert < 200$ MeV	11699206	822935	596600	441654	7815	433559
5 gammas	1154964	109198	99961	87248	6754	355258
cut	$\pi^0\omega\to\pi^0\pi^0\gamma$	$\pi^0\pi^0$	$\eta\eta$	$\pi^0\pi^0\gamma$	$\eta\eta\gamma$	$\eta\pi^0\gamma$
Event in	99963	100000	100000	50000	150000	50000
0 tracks	90487	91932	93541	45268	138277	45789
$\lvert\vec{p}\rvert < 200$ MeV	77306	82323	79987	38954	116359	38904
$\lvert E - 1876\rvert < 200$ MeV	75177	79180	77875	37885	113012	37793
5 gammas	59555	4264	5885	29392	97205	30827

Table 14.1: Cut results for various data sets in “skim” pass

These were removed first, by rejecting any event with any reconstructed tracks, with a track defined as 3 or more hits on a helix.

Events with total energy and momentum, summed over all photon momenta, consistent with annihilation at rest ($p_{\text{tot}} = (0, 0, 0; 1876)$ MeV) are kept, if the difference for each component is less than 200 MeV. This removed approximately 40% of events. A tighter selection is done later by the kinematic fit. Events with exactly five gammas are retained. This removed approximately 90% of events. The number of final events in the skimming pass are given in table 14.1 and the statistics are shown in figure 14.1 .

These cuts reduced the data events from 20.3 million to 1.1 million events. The same procedure was applied to the Monte Carlo data sets, which statistics given in the table.

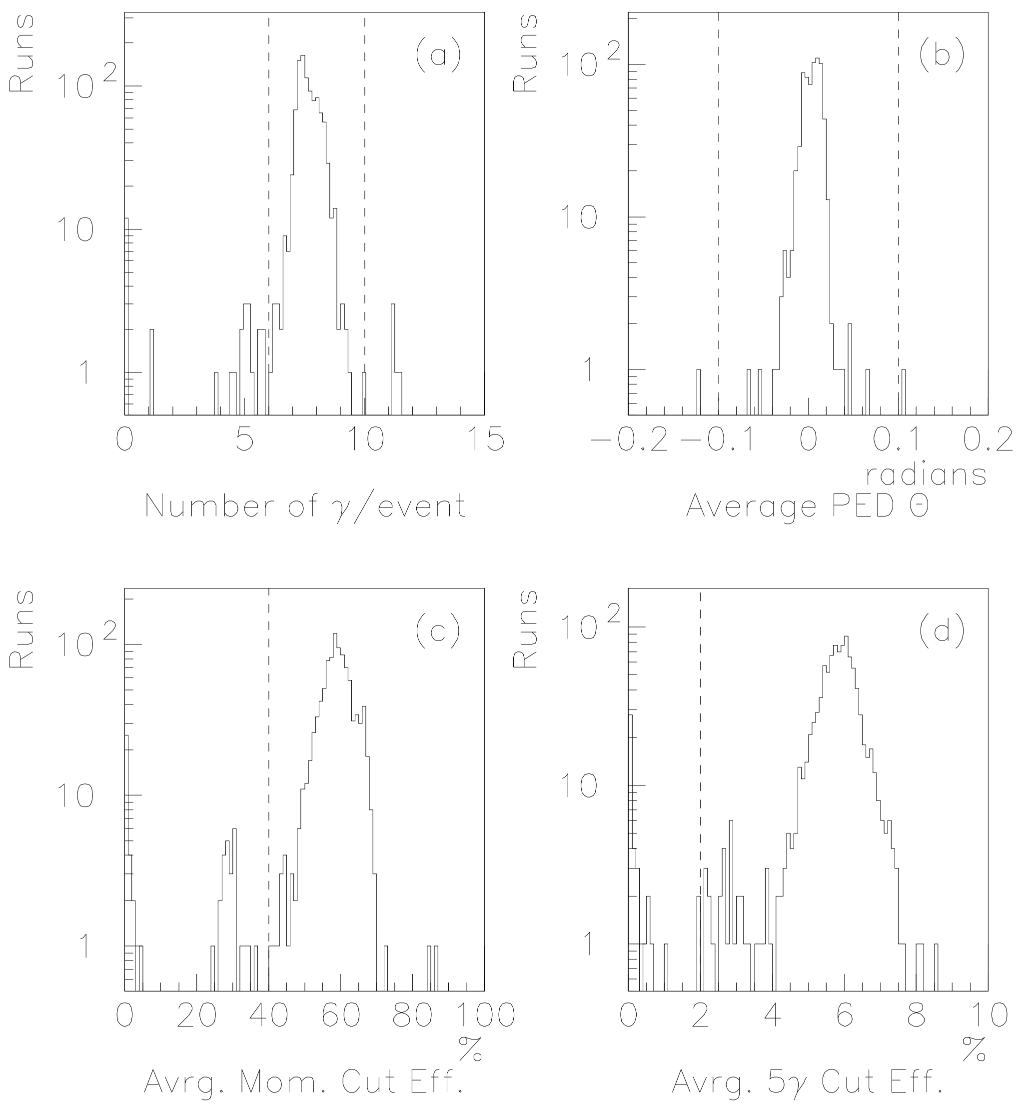

Figure 14.1: The run-averaged statistics from the skimming pass. (a) The number of photons per event (b) the average photon polar angle (c) the efficiency of the momentum cut (d) the efficiency of the 5 photon cut. The dashed lines indicate the "bad run" criteria.

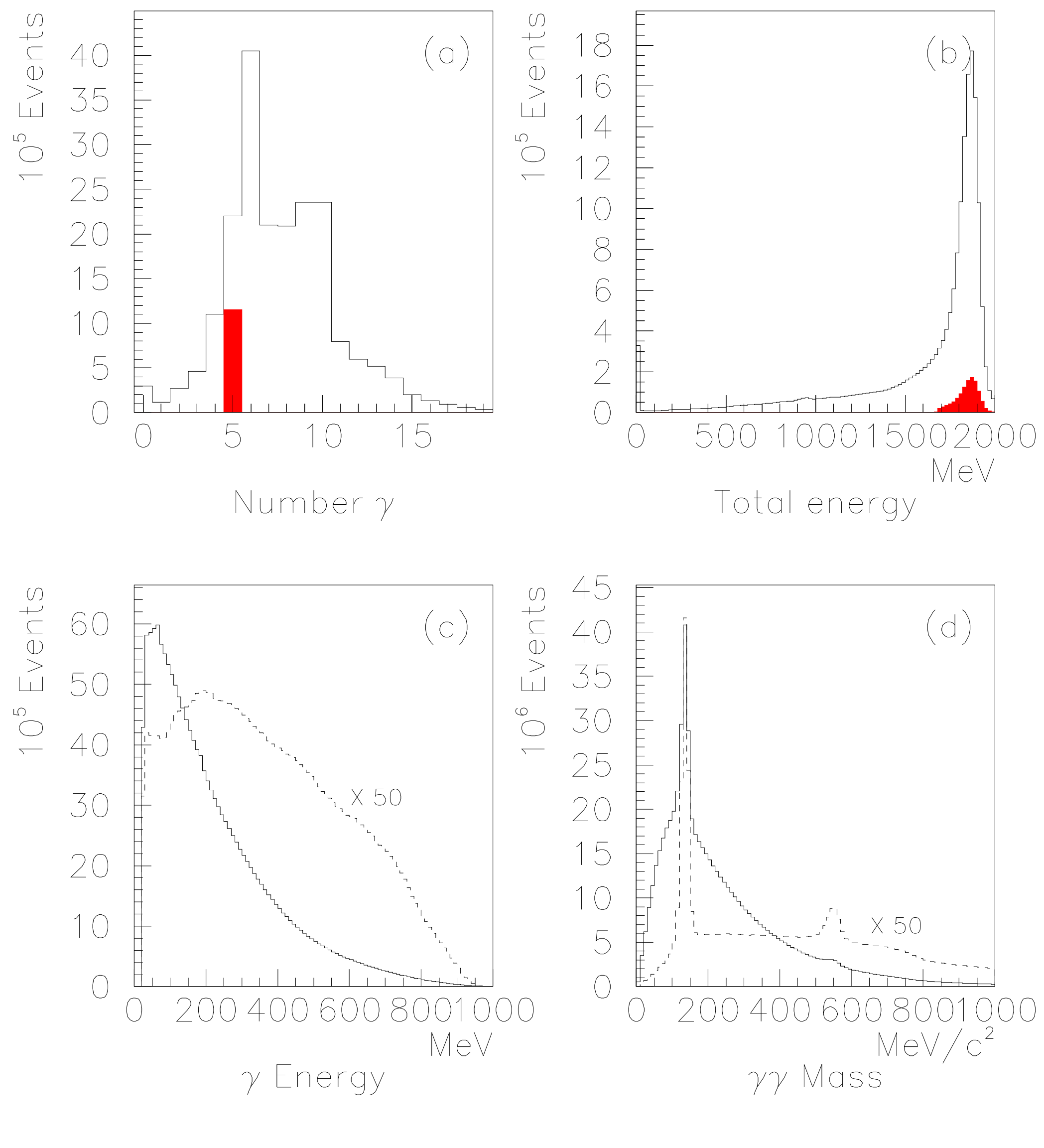

Figure 14.2: Event and particle statistics, before and after skimming cuts. (a) Number of photons per event (b) Total energy of event (c) Energy of single photon (d) Invariant mass of all $\gamma\gamma$ pairs. The solid-line histogram is before any cuts, and the filled or dashed histogram is after the skimming cuts. In (c) and (d), the dashed histogram is scaled by a factor of 50 to make it visible.

14.3 Data quality

In figure 14.2, the effects of the cuts can be seen. The 5 γ cut changes the energy spectrum of the photons significantly (fig. (c)). This is because 5 γ's is less than the average, thus by selecting fewer photons, the average energy of each photon must increase. In figure (d), the π^0's and η's can be more easily seen after the cuts, but this is only due to less combinatorial background.

Before the events were submitted to the second data reduction pass, bad runs were identified and rejected. There are two types of runs that are to be rejected, "wrong" runs and truly "bad" runs.

"Wrong" runs are runs that used a trigger that might not have been a real 0-prong trigger, based on the run database. These are listed in the appendix table A.7.

"Bad" runs were identified by looking at run averages of certain parameters, and requiring them to have some some sane values. The cuts are shown in figure 14.1 as dashed lines. The cuts and the resultant bad runs are listed in table A.8.

The number of bad events in data runs was estimated to be about 740,000 events out of 20.4 million total data events, or 3.6% of the data. The bad runs are assumed to be very bad, in other words the data is assumed to be so corrupt that they appear as random noise, and most would probably would not pass any Kinematic Fit. At worst, they would have formed a flat background to the data. The total number of events is corrected by subtracting 3.6%.

Chapter 15

Second Kinematic Fit Pass

15.1 Description

The purpose of the first pass on the data, described in the previous chapter, was to select out 5 γ events with good 4-momentum. The purpose of the second pass, described in this chapter, is to reduce background due to channels with lost γ's and to classify the 5γ events by kinematically fitting to three hypotheses.

In the first pass, all local maxima in the crystal matrix were identified as PEDs, as long as the energy of the PED was above 20 MeV. This high value is good for the signal, because it causes the reconstruction to ignore show fluctuations as fake photons. The photon energy spectrum of the signal does not drop below 100 MeV. However, the background channels, for instance $p\overline{p}\rightarrow\pi^0\eta\eta$, become backgrounds by losing one soft photon. This soft photon spectrum drops nearly to zero MeV, so the 20 MeV photon threshold causes additional background by not tagging these soft photons.

There are in fact two different thresholds, the threshold to create a cluster[1] and the threshold for secondary maximum[2]. In the previous analysis, both thresholds were set to 20 MeV. However, it is better to have a low threshold for the cluster creation, and a higher threshold for secondary maxima. This will increase the probability of tagging individual soft photons, which form a single cluster, but still keep shower fluctuations from mimicking a photon.

To minimize the statistical error of the signal required scanning both threshold parameters, and running the entire analysis on the Monte Carlo sets of the desired signal and expected background for each pair of thresholds. The statistical error of the signal was defined as

$$\frac{\sigma(s)}{s} = \frac{\sqrt{s+b}}{s}$$

where s is the number of signal events and b is the number of background events underneath the signal. The result of this scan was a cluster threshold of 11 MeV and a secondary maximum threshold of 18 MeV.

In previous tests, we set these reconstruction parameters to both 3 MeV. This very low value caused there to be lots of shower fluctuations to be seen as photons. Thus we separated the reconstructed photons into "hard" and "soft" photons, with 20 MeV as the dividing point. The analysis required exactly 5 hard photons, but also attempted to find π^0's and η's by pairing the hard photons with the soft photons. This technique worked, in the sense the background was cut, but the signal was cut too, and the net effect was not productive. Also, the efficiency of the Monte Carlo in the end was off by 10% to 20% of

[1] `ECLUBC`
[2] `EPEDBC`

expectations (based on known channels, such as $\omega\rightarrow\pi^0\gamma$) when these low 3 MeV thresholds were used. This is most likely because the Monte Carlo does not properly simulate very soft photons below 5-10 MeV.

Erratum: We have discovered two small problems in our final data set after the analysis was completed. Neither problem has a significant impact on the final value, and thus do not merit the work needed to correct them. The problems appear to be a result of changing the PED reconstruction thresholds. A discussion appears at the end of this chapter in section 15.3.

Since the photons were reconstructed from the raw data a second time, but with different thresholds, the photon multiplicity per event was no longer 5. The first cut on the second pass was to require exactly 5 photons.

The next step is application of the kinematic fit (see appendix A.1) to a phase space hypothesis,

$$p\overline{p}\rightarrow 5\gamma$$

and then three resonant hypotheses if the first fit succeeds,

$$p\overline{p}\rightarrow\pi^0\pi^0\gamma,$$

$$p\overline{p}\rightarrow\pi^0\eta\gamma,$$

$$p\overline{p}\rightarrow\eta\eta\gamma.$$

Events are accepted if and only if they pass the phase space hypothesis and exactly one of the three resonant hypotheses. The success of a fit is defined by a maximum allowed reduced $\chi^2/N_{dof} < 5$. At a slight cost of efficiency, there are no ambiguous events.

	Cut	Events		
0	All-neutral trigger			20298446
1	0 tracks in JDC			18223703
2	$\lvert p_i \rvert < 200$ MeV/c			13525910
3	$\lvert E - 1876 \rvert < 200$ MeV			11699206
4	$N\gamma = 5, E\gamma > 11$ MeV			748441
5	4C Kin. Fit, $\chi^2/4 < 5$			616155
		$\eta\eta\gamma$	$\eta\pi^0\gamma$	$\pi^0\pi^0\gamma$
6	6C Kin. Fit, $\chi^2/6 < 5$	113546	369689	380479
7	Only 1 solution	5763	136042	204297
8	6C CL > 10%	2260	93350	128838
9	$m(\gamma_{\text{pair}}\gamma_{\text{unpair}}) \notin [80, 180]$ MeV/c^2	2146	82349	100369
10	$\gamma_{\text{unpair}} > 200$ MeV	–	79588	–

Table 15.1: The event counts during the first and second passes on the data.

The $\pi^0\pi^0\gamma$, $\eta\pi^0\gamma$ and $\eta\eta\gamma$ events are written to HBOOK ntuples, along with some important cut variables discussed in the next chapter. The results of this pass are shown in table 15.1.

15.2 Scaling of errors for kinematic fit

The default database[3] contains the standard calibration constants. However, these calibration constants were obtained for unknown final states, and do not give perfect results in the kinematic fit. There are 3 types of parameters that can be varied to give better results.

1. The neutral decay vertex is typically at $(0, 0, 0)$, but the actual position is not well known because the liquid hydrogen target does not always sit in the exact same spot. Based on the asymmetry of the pull distributions (see the section on kinematic fitter) for the θ of the reconstructed γ's, the vertex position can move a few millimeters

[3] cbdata.base_feb14, 1997

forward or backward relative to the database values.

2. The absolute calibration coefficient for the energy of the γ's needs to be adjusted in most cases, in order to best satisfy the three constraints,
   (a) The $\pi^0 \rightarrow \gamma\gamma$ mass, 134.9764 MeV.
   (b) The $\eta \rightarrow \gamma\gamma$ mass, 547.45 MeV.
   (c) The $p\bar{p} \rightarrow 5\gamma$ total energy, 1876.543 MeV
3. The estimated 1σ errors of the γ parameters (E,ϕ,θ) are usually not quite right, and need to be adjusted in order for
   (a) the pull distributions of each of these parameters to be a unit Gaussian, and
   (b) the confidence level of the entire phase space fit to be flat.

In order to fix these 3 types of parameters, the following algorithm was used. The final values are given in table 15.2.

1. The θ pull distribution was fitted with a Gaussian, and the mean value gives a handle on the neutral vertex position. For a fixed point on the crystal surface, as the neutral vertex moves to positive z, the θ angle increases. It is found empirically that a $+0.15$ pull offset from zero needs roughly a $+1.0$ mm correction in the vertex z position. This process was iterated twice until all the means were within ± 0.015, the statistical error. The reason that the neutral vertex appears to change from run period to run period is because the z position is not well defined by the detector. The target is mounted to the LEAR beam pipe, while the rest of the detector is mounted on the floor. There

is no direct contact between the target and the detector, so the alignment between the two systems can vary a few millimeters if the detector is opened and closed in between run periods for service.

2. The total energy, $\gamma\gamma$ mass at the π^0 and the $\gamma\gamma$ mass at the η were fitted with a Gaussian plus linear background near the relative peak. Because the widths of the peaks differ, a scaling factor f was chosen that minimized the following function,

$$\chi^2 = \sum_i \left(\frac{x_0^i - f x^i}{\sigma_x^i} \right)^2$$

where the following values were used,

i	Value	x_0	σ_x
1	total Energy	1876.54 MeV	36 MeV
2	mass π^0	134.96 MeV/c^2	8.4 MeV/c^2
3	mass η	547.45 MeV/c^2	19 MeV/c^2

and x^i was measured for each run period by a Gaussian fit to the corresponding peak ($i = 1, 2, 3$). The values of f varied from run to run, but ranged from 0.994 to 1.013. See table 15.2 for a list.

3. The scalings of the errors is the hardest part and requires a certain art. The desired outcome is to have a flat confidence level (defined in section 15.4) and to have normal Gaussian pulls, i.e. with mean zero and width one. This is usually impossible to achieve in practice. The flatness of the confidence level is given first priority, and having equally wide pull distributions is second priority. With a few iterations, the confidence level can be made very flat above 0.2 and the Gaussian widths are typically 1.0 to 1.05 for the ϕ and $\sqrt{E}$ and 1.15 for the θ pull.

It is very difficult to modify the widths of certain pulls, rather than all three of them. However, in an attempt to compensate this, the θ errors were scaled higher (typically 10%) than the other errors.

The final tuning of the overage scaling was done by selecting true 5-gamma events, rather than all 5-gamma events which include background from 6-gamma events. Because the relative background is lowest along the ω bands in the corresponding Dalitz plots, we selected events from the ω bands (760 MeV $< m(\pi^0\gamma) <$ 800 MeV) for the $\eta\pi^0\gamma$ and $\pi^0\pi^0\gamma$ groups. The 4C confidence level of these selected events was histogrammed in 8 bins from CL=0.20 to 1.00, and fitted with a linear function $y = a + bx$. The total error scaling was modified until $b = 0$ (within 0.25 sigma), that is until the confidence level was flat from 20% to 100%. This was done for all ten data runs, and for the Monte-Carlo sets, $\eta\omega{\rightarrow}\eta\eta\gamma$, $\eta\omega{\rightarrow}\eta\pi^0\gamma$, $\pi^0\omega{\rightarrow}\pi^0\pi^0\gamma$, and $(\eta\rho^0{+}\eta\omega){\rightarrow}\eta\eta\gamma$. Note that the confidence levels histogrammed in 15.1 are of *all* events, and thus do not appear to be flat. This shows that the data does include background.

It is more important that the Monte Carlo match the data in the confidence level and pulls than to have absolutely perfect pulls in all cases, and hopefully the former has been accomplished.

The efficiency of the Kinematic Fit is shown in figure 15.2 as a function of run number. The efficiency is defined as the number of events accepted by the kinematic fit divided by the total events accepted by the first skim pass. The stability of the data is shown across 9 run periods from 1989 to 1994.

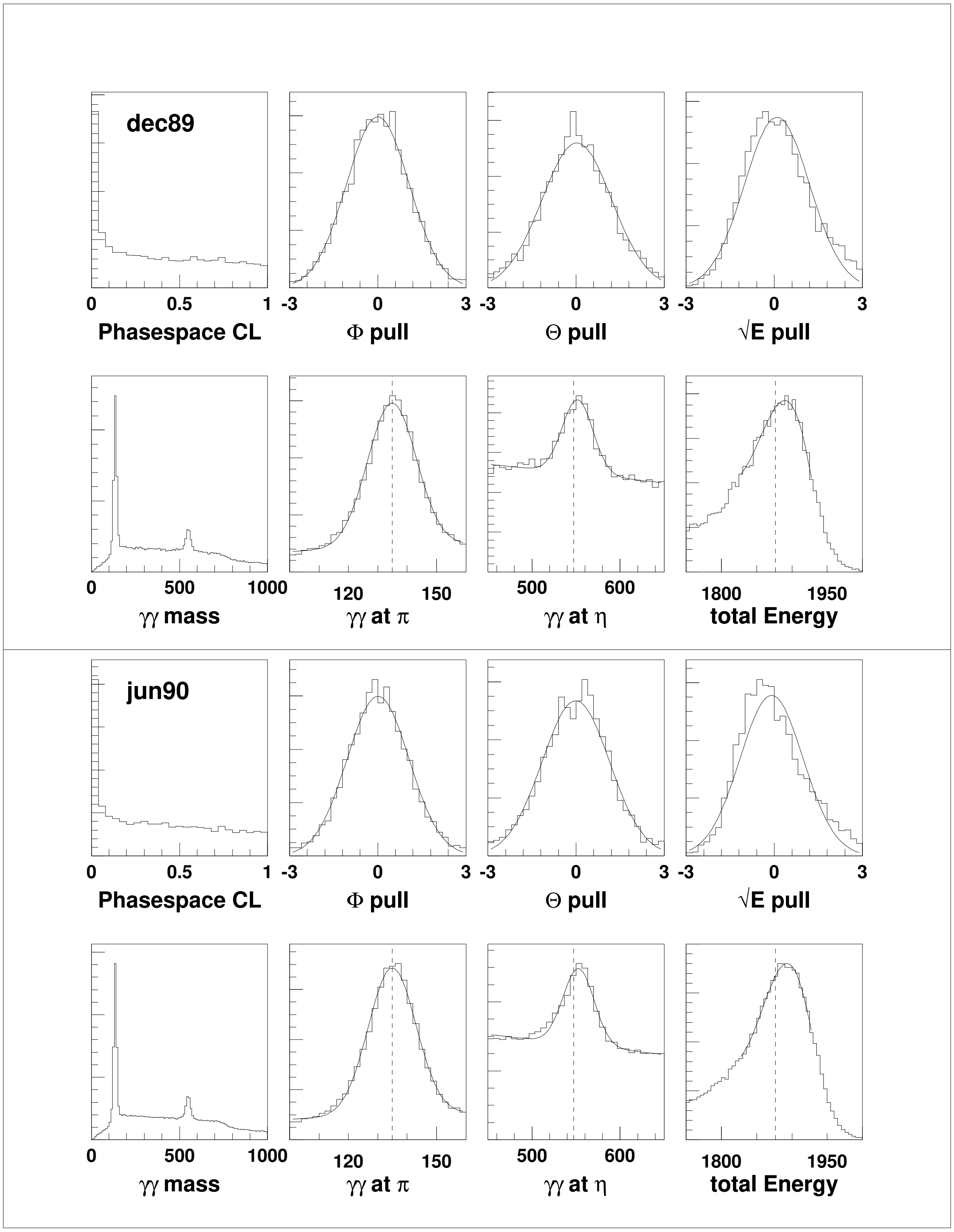

Figure 15.1: The pulls and calibration peaks for various run periods (this page and the following 5 pages).

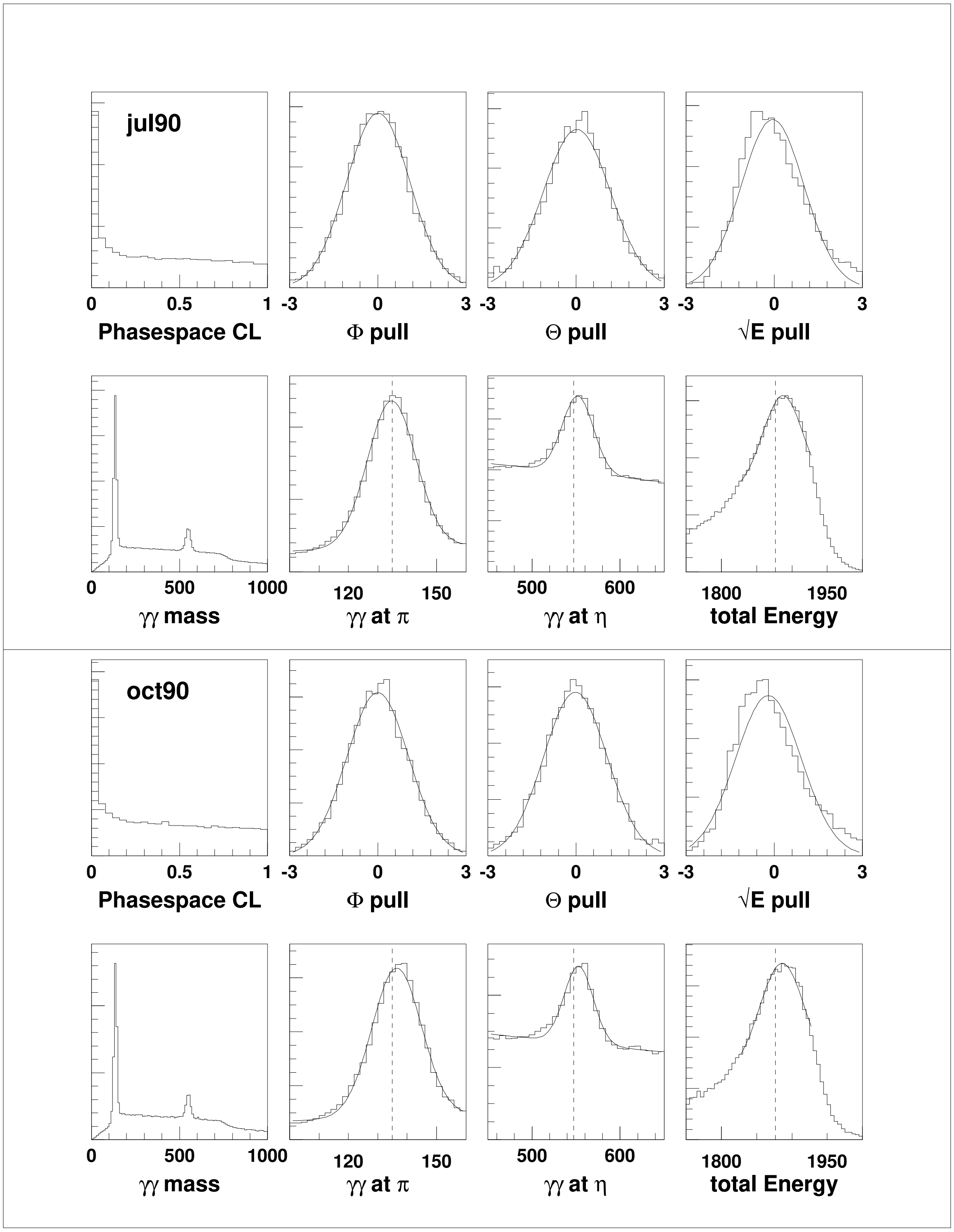

jul90
0
0.5
1
Phasespace CL
-3
0
3
Φ pull
-3
0
3
Θ pull
-3
0
3
√E pull
0
500
1000
γγ mass
120
150
γγ at π
500
600
γγ at η
1800
1950
total Energy
oct90
0
0.5
1
Phasespace CL
-3
0
3
Φ pull
-3
0
3
Θ pull
-3
0
3
√E pull
0
500
1000
γγ mass
120
150
γγ at π
500
600
γγ at η
1800
1950
total Energy

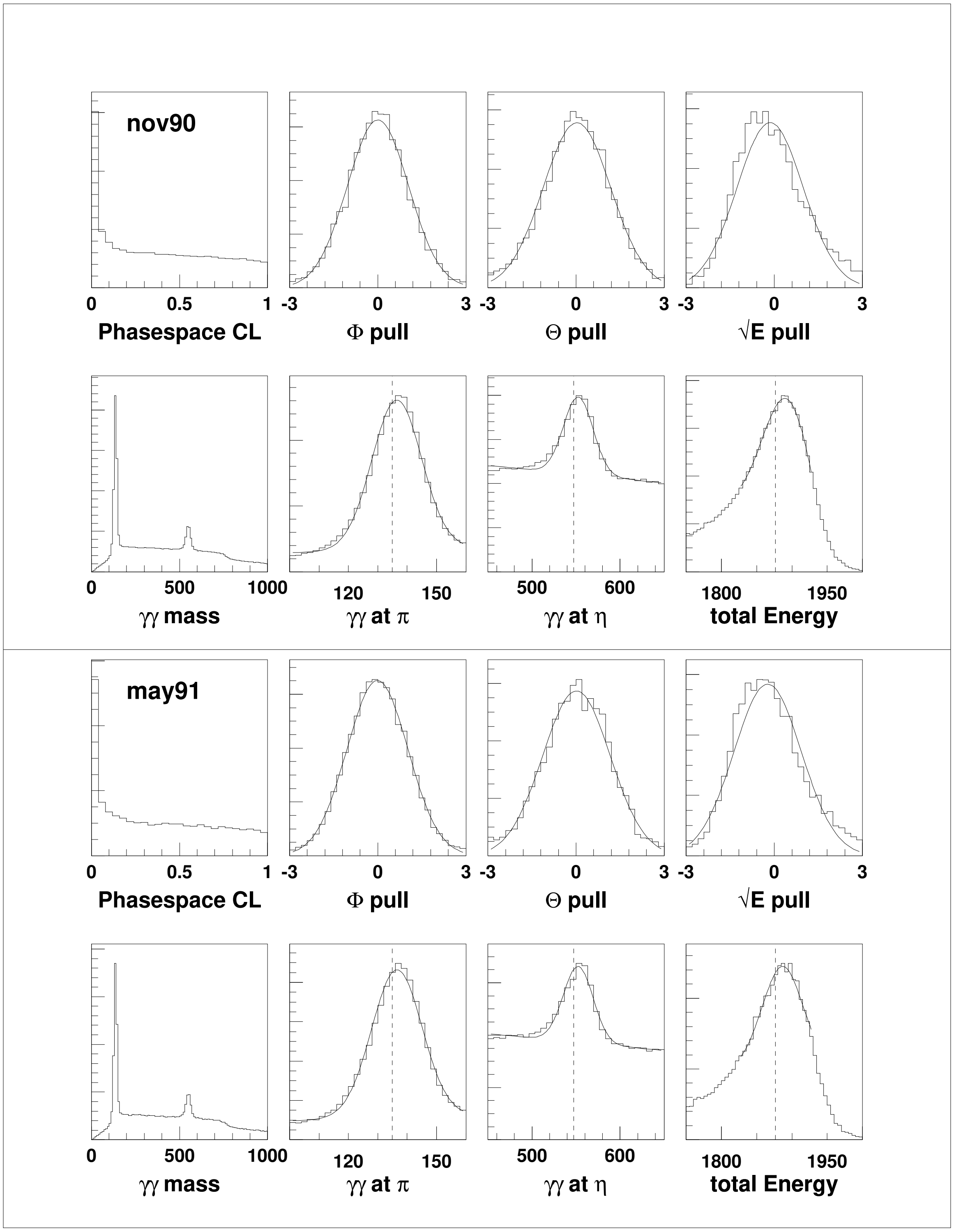
nov90
0
0.5
1
Phasespace CL
-3
0
3
Φ pull
-3
0
3
Θ pull
-3
0
3
√E pull
0
500
1000
γγ mass
120
150
γγ at π
500
600
γγ at η
1800
1950
total Energy
may91
0
0.5
1
Phasespace CL
-3
0
3
Φ pull
-3
0
3
Θ pull
-3
0
3
√E pull
0
500
1000
γγ mass
120
150
γγ at π
500
600
γγ at η
1800
1950
total Energy

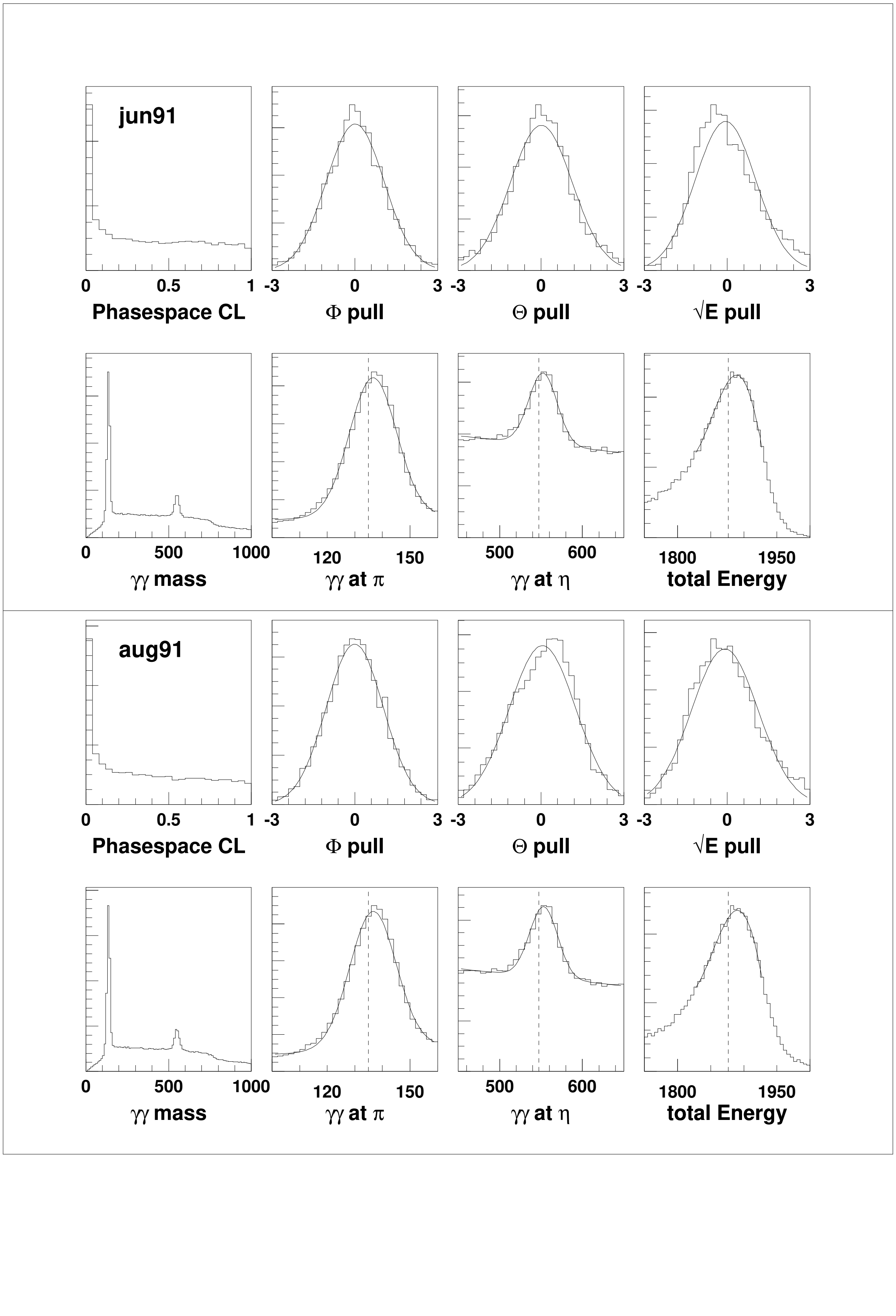
jun91
0
0.5
1
Phasespace CL
-3
0
3
Φ pull
-3
0
3
Θ pull
-3
0
3
√E pull
0
500
1000
γγ mass
120
150
γγ at π
500
600
γγ at η
1800
1950
total Energy
aug91
0
0.5
1
Phasespace CL
-3
0
3
Φ pull
-3
0
3
Θ pull
-3
0
3
√E pull
0
500
1000
γγ mass
120
150
γγ at π
500
600
γγ at η
1800
1950
total Energy

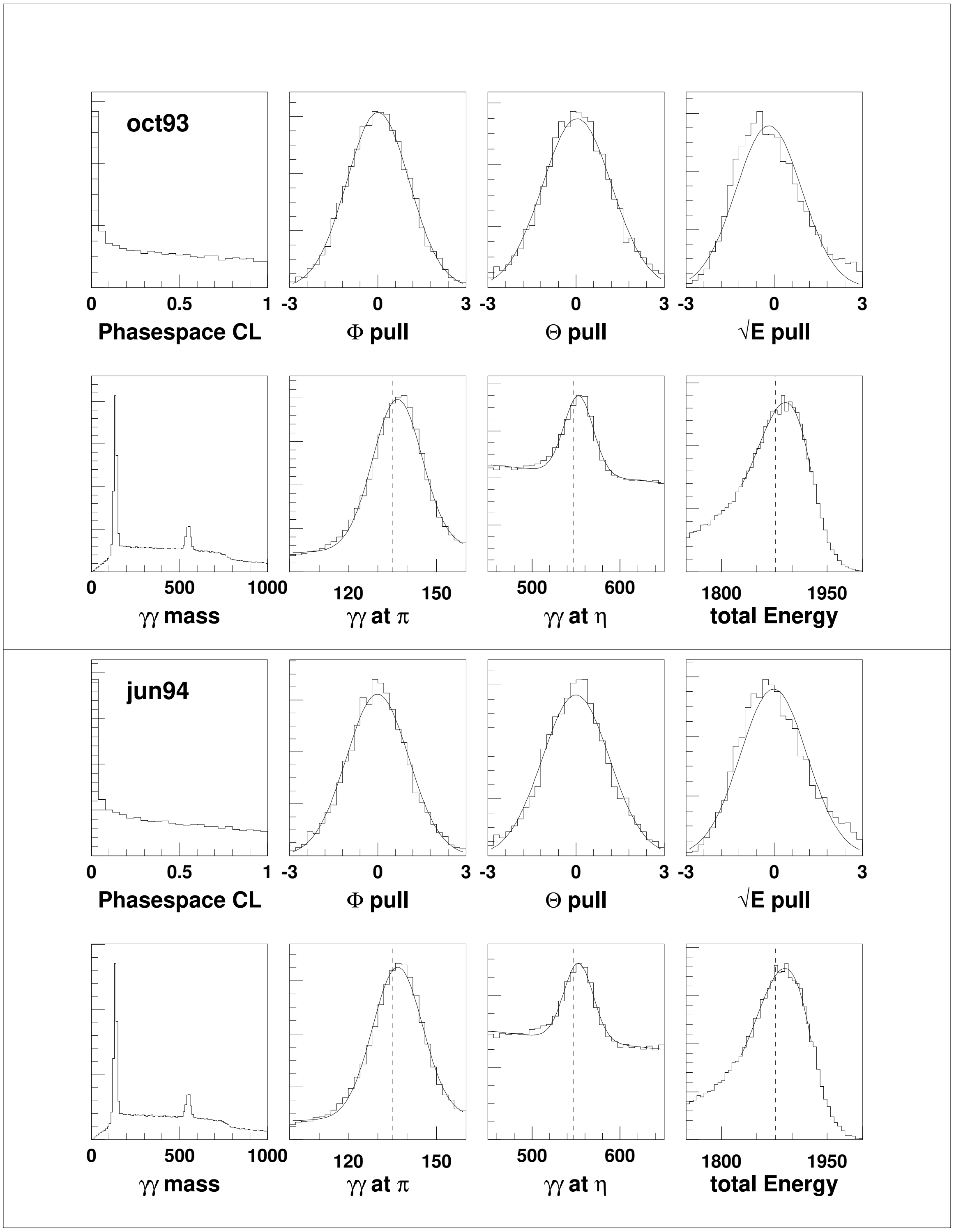
oct93
0 0.5 1
Phasespace CL
-3 0 3
Φ pull
-3 0 3
Θ pull
-3 0 3
√E pull
0 500 1000
γγ mass
120 150
γγ at π
500 600
γγ at η
1800 1950
total Energy
jun94
0 0.5 1
Phasespace CL
-3 0 3
Φ pull
-3 0 3
Θ pull
-3 0 3
√E pull
0 500 1000
γγ mass
120 150
γγ at π
500 600
γγ at η
1800 1950
total Energy

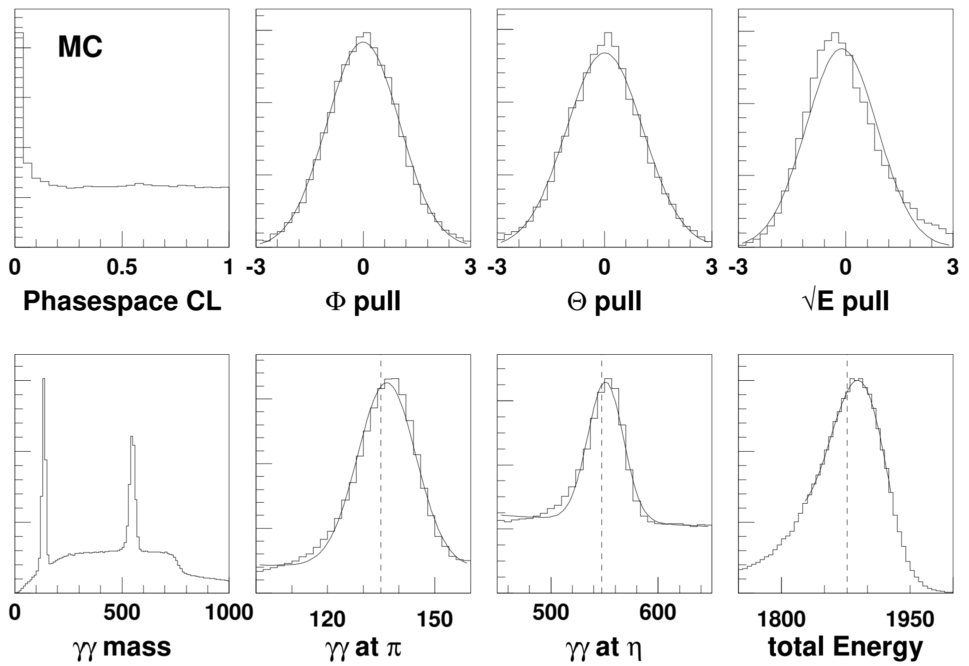

MC
0
0.5
1
Phasespace CL
-3
0
3
Φ pull
-3
0
3
Θ pull
-3
0
3
√E pull
0
500
1000
γγ mass
120
150
γγ at π
500
600
γγ at η
1800
1950
total Energy

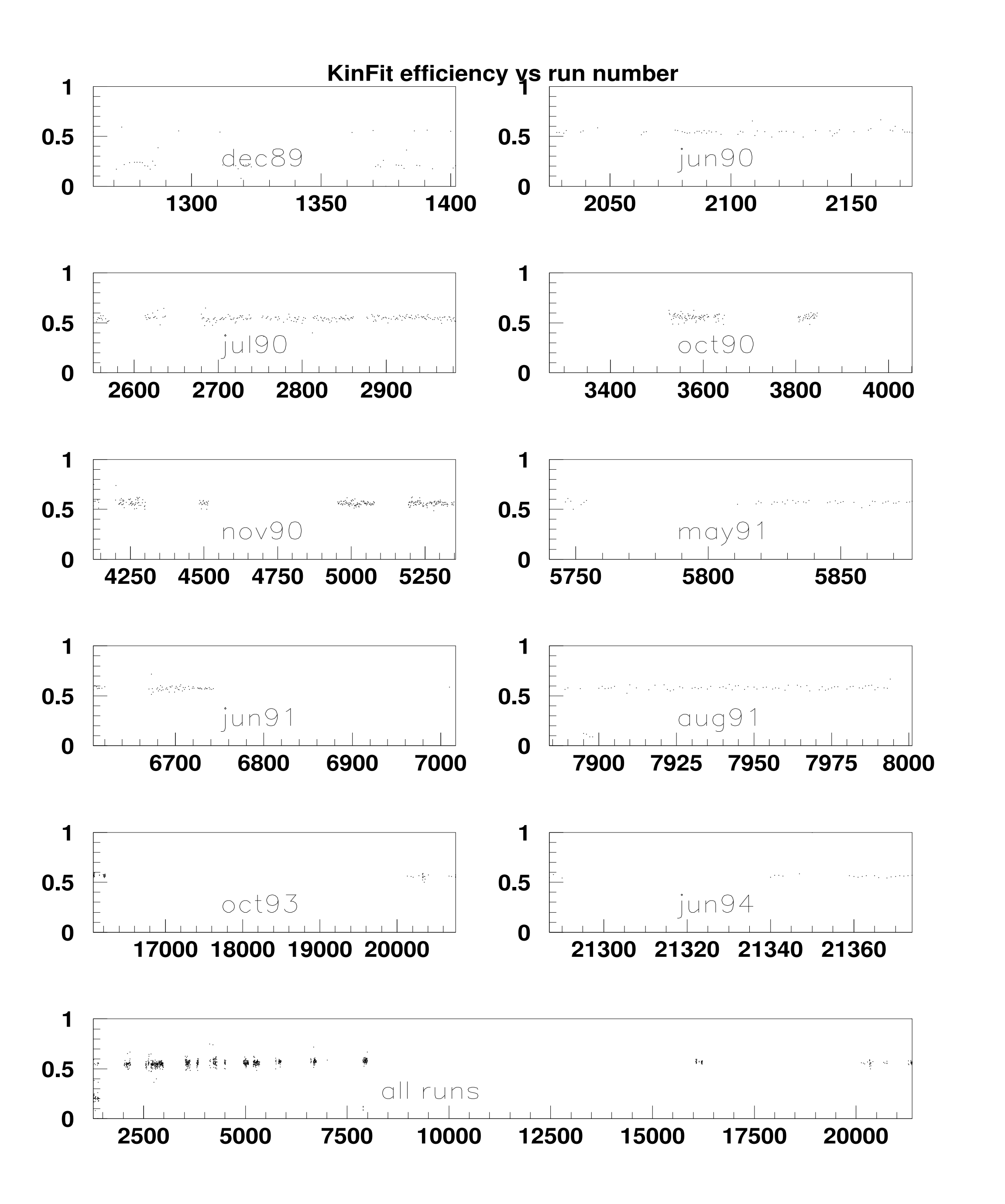

Figure 15.2: Efficiency of the KinFit as a function of run period. Efficiency is defined as the ratio of KinFit passing phase space events divided by the number of 5-γ events. Dec89 is discussed in the text.

Run Period	Energy Scale	Error Scalings			Neutral Vertex
	f	$\sigma(\phi)$	$\sigma(\theta)$	$\sigma(\sqrt{E})$	(cm)
M.C.	1.0080	1.05	1.05	1.05	(0.0,0.0,0.0)
dec89	1.0008	1.02	1.17	1.02	(0.0,0.0,-0.13)
jun90	0.9940	1.01	1.13	1.05	(0.0,0.0,0.050)
jul90	0.9962	0.95	1.20	1.07	(0.0,0.0,0.131)
oct90	1.0102	1.00	1.03	1.00	(0.0,-0.4,-0.21)
nov90	1.0102	0.96	1.06	1.01	(0.0,-0.4,-0.30)
may91	1.0102	0.98	1.18	1.03	(0.0,0.0,-0.79)
jun91	1.0112	0.86	0.91	0.86	(0.0,0.0,0.29)
aug91	1.0122	0.94	1.78	0.98	(0.0,0.0,-0.77)
oct93	1.0120	1.02	1.09	1.02	(0.0,0.0,0.18)
jun94	1.0128	1.01	1.10	1.00	(0.0,0.0,0.20)

Table 15.2: The scalings used for the different run periods and Monte Carlo data sets.

15.3 Erratum

We have discovered two small problems in our final data set after the analysis was completed. Neither problem has a significant impact on the final value. The problems appear to be a result of changing the PED reconstruction thresholds, since neither problem existed before. These problems were not discovered until this technical report was written and new figures produced. Because the problems are minor, it was decided that a reanalysis was not necessary.

The first problem is that the Dec89 run period has drop-outs in the kinematic fit efficiency, where the average acceptance drops from roughly 60% to 20% for several runs (see figure 15.2). The total number of events in these low efficiency runs is 38178 out 1127570, or 3.4%. Because the final answer is expressed as a ratio of rare branching ratio to reference branching ratio, this small effect is cancelled out, resulting in no change to the final answer.

The second problem is that all of the calibration peaks have shifted slightly upward on the order of 1-2% (see figure 15.1). Before the change in thresholds, all of the peaks were well centered on the desired π^0 mass, η mass and $p\overline{p}$ mass. However again, this problem is doubly cancelled in the final result. First, the energy shift appears equally in both the data and the Monte Carlo, so it is cancelled out by the efficiency calculation. Second, the final answer is a ratio of two measurements, so it is cancelled out again.

Because the final measurement is quoted with 40% errors, these problems are not significant.

15.4 Confidence level of KinFit to $\eta\eta\gamma$ Hypothesis

The confidence level is calculated as the probability that the kinematic fit could be "better" by having a smaller χ^2, or

$$\begin{aligned} \mathrm{CL}(\chi^2) &= \int_{\chi^2}^{\infty} f(z;n)dz \\ f(z;n) &= \frac{z^{n/2-1}e^{-z/2}}{2^{n/2}\Gamma(n/2)} \end{aligned} \tag{15.1}$$

where $f(z;n)$ is a probability density function for a χ^2 distribution for n degrees of freedom. For events that are distributed around the hypothetical perfect value in a normal distribution (real signal events), the confidence level is flat from 0 to 100%. For events whose χ^2 values are not distributed as a χ^2 (i.e. eq. 15.1) because just randomly satisfy the fit hypothesis, the confidence level will not be flat, and will be bunched up near 0.

We require all three groups to have a confidence level above the 10 th percentile. By definition, this should only discard 10% of the signal, but a much larger fraction of the background. Note that this assumption depends on the confidence level being flat. If it is not flat because of some wrong assumptions about error estimates, a cut at the 10 th percentile will not leave one with exactly 90%, but a substantially different amount.

In figure 15.3 are the confidence levels for the important channels (data and MC) for the three groups, $\eta\eta\gamma$, $\eta\pi^0\gamma$ and $\pi^0\pi^0\gamma$. The signal channels are reasonably flat, while the backgrounds fall quickly with increasing confidence level.

15.5 Removal of latent π^0's

In all three groups, there is a probability that the kinematic fit selects the wrong assignment of γ's to intermediate particles because the best fit was from an incorrect assignment with an accidentally lower χ^2. This can happen within a particular group's assignment, or between two groups. For instance, the $\pi^0\omega\rightarrow\pi^0\pi^0\gamma$ decay could be assigned to the $\pi^0\pi^0\gamma$ group, but the individual assignments of the γ's to the π^0's could be wrong. This case is not particularly troublesome. However, the $\eta\omega\rightarrow\eta\pi^0\gamma$ decay could be assigned to the $\eta\eta\gamma$ group with disastrous results, if it fails the $\pi^0\eta\gamma$ fit and it contains an accidental fake η within the $\omega\rightarrow 3\gamma$. The reason this is a problem is because the $\eta\omega\rightarrow\eta\pi^0\gamma$ channel is two orders of magnitude more intense than the $\eta\omega\rightarrow\eta\eta\gamma$ channel, and the fake η appears to come from an ω decay, thus faking the desired signal, unlike other non-resonant backgrounds.

To remove this second type of accidental assignment, it is critical to check pairwise combinations of particles after the kinematic fit. The most likely wrongly assigned γ is the unpaired "radiated" γ. Thus we pair the radiated γ with each of the other four γ's, and take the pair whose invariant mass is closest to 135 MeV. This pair is called a "latent π^0". Normally, the measured invariant mass of a π^0 does not vary more than 10 MeV from 135

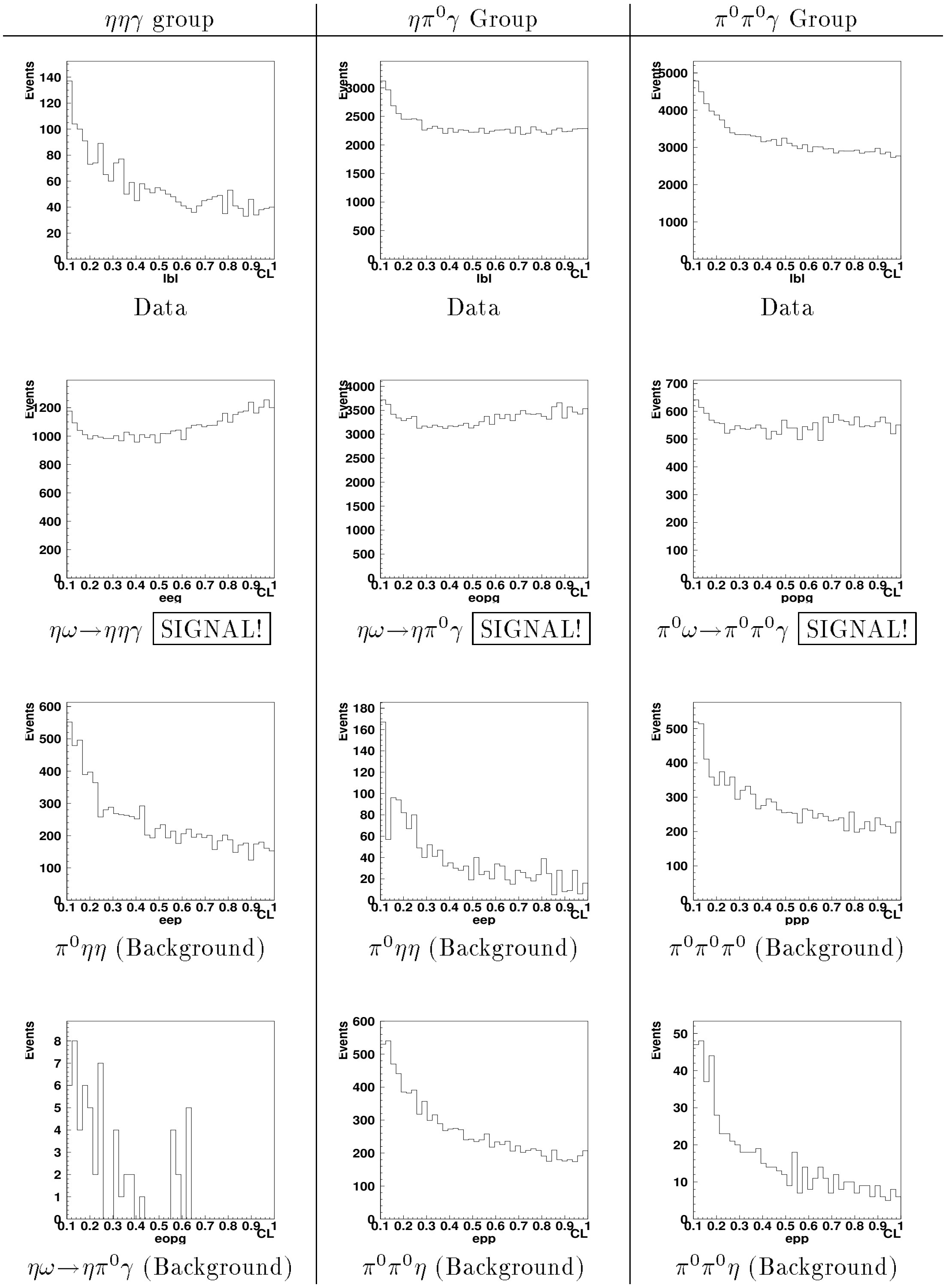

Figure 15.3: Confidence levels for data and selected Monte Carlo sets, for each of the three groups, $\eta\eta\gamma$ (Left column), $\eta\pi^0\gamma$(center column) and $\pi^0\pi^0\gamma$(right column).

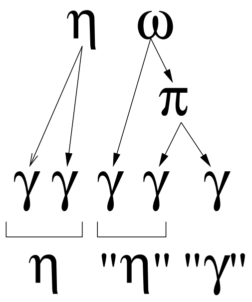

Figure 15.4: One way that the $\eta\omega \rightarrow \eta\pi^0\gamma$ channel can slip into the $\eta\eta\gamma$ group. Note that the fake "η" and fake "γ" form a real ω, so this channel is particularly important to remove completely, lest it contribute to the desired signal's peak. This background can be removed with the latent π^0 cut.

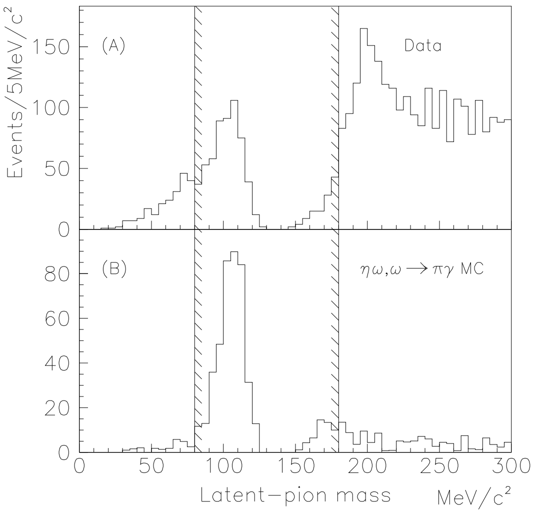

Figure 15.5: The latent π^0 distribution for data (left) and $\eta\omega \rightarrow \eta\pi^0\gamma$ MC (right). Events within the hatched region are discarded.

MeV. However, the tails of the mass distribution can extend to 50 MeV and beyond because of detector systematics. Such a poorly measured π^0 will fail a kinematic fit, and thus not be identified as a π^0. To remove this type of event, we cut all events with an latent π^0 mass between 85 and 185 MeV. See figure 15.5.

$$85 < m(\gamma\gamma)_{\mathrm{latent}} < 185 \text{ MeV}.$$

15.6 Unused cuts

We experimented with other cut variables. As mentioned before, one technique looked at subthreshold γ's as potential real γ's and calculated an invariant mass between each soft γ and the radiated γ. This technique showed promise, but unfortunately was too dependent on the low energy details of the Monte Carlo to be reliable for calculating correct efficiencies. Also, the slight SNR gain from this cut was essentially balanced by slight decrease in signal statistics, resulting in no net gain in overall precision.

Another technique was used to look for "merged" γ's, that is two γ's from two different mesons merging because they accidentally hit the same cluster of crystals in the calorimeter. Given three "γ's", we hypothesis that one is a merged γ, and break it into two pieces, with fractional energy x and $1 - x$. We then solve for x such that the four γ's came from $\pi^0 \rightarrow \gamma\gamma$ and $\pi^0 \rightarrow \gamma\gamma$. It was expected that there would be some identifying signature in a distribution of x or xE_γ, but no clear structure was observed.

15.7 Generating the histograms

The histograms used for the fits were two dimensional Dalitz plots, where the axes are the squared invariant masses of pairwise combinations of the final particles. For example, in the $\eta\eta\gamma$ group, the axes are $m^2(\eta_2\gamma)$ vs $m^2(\eta_1\gamma)$. η_1 is defined to be the $\gamma\gamma$ pair with momentum closest to 660 MeV/c, the proper momentum for recoil against an ω. This of course is equivalent to picking $\eta_2\gamma$ as the best ω candidate. The $\pi^0\pi^0\gamma$ group has the equivalent assignment. The $\eta\pi^0\gamma$ group, because of distinguishable particles, is plotted as $m^2(\pi^0\gamma)$ vs $m^2(\eta\gamma)$, and the whole Dalitz plot is fitted. In all histograms, the ω should appear as a horizontal band at $y = 0.6$ GeV$^2/c^4$. The histograms for the $\eta\eta\gamma$, $\eta\pi^0\gamma$ and $\pi^0\pi^0\gamma$ groups are shown in figures 15.6, 15.7 and 15.8, respectively.

To save unnecessary computation and to keep the events per bin high, the binning size was chosen to be large in regions were only background was expected. In regions where an ω signal is expected the binning is much smaller.

Real data events are entered into the histograms with a weight of 1. Monte Carlo channels flat in phase space are also weighted with 1, including $\eta\eta$, $\pi^0\pi^0$ $\eta\eta\gamma$, $\eta\pi^0\gamma$ and $\eta\pi^0\gamma$. For the remaining channels, the events were weighted according to the correct dynamics, as discussed in chapter 13.

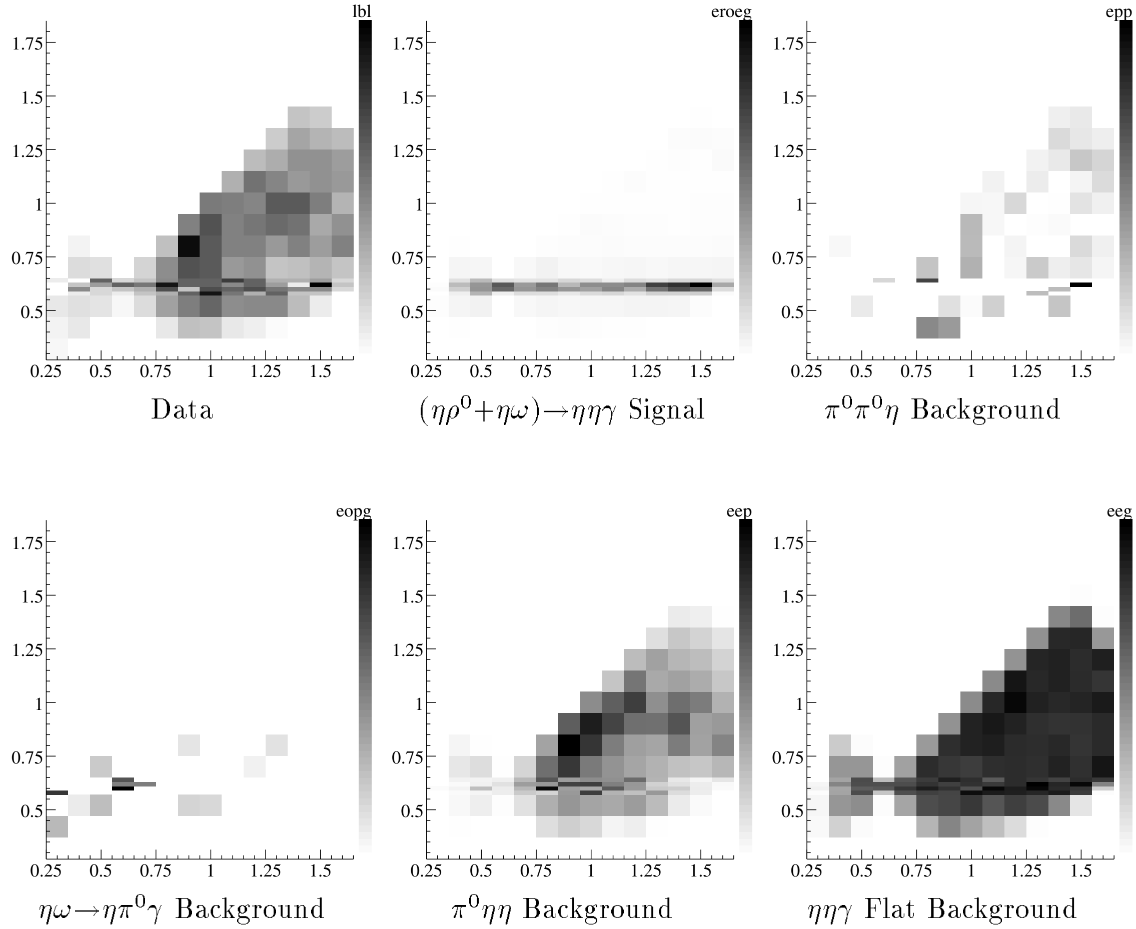

Figure 15.6: The components of the $\eta\eta\gamma$ group. The relative intensities of each Dalitz plot is arbitrary

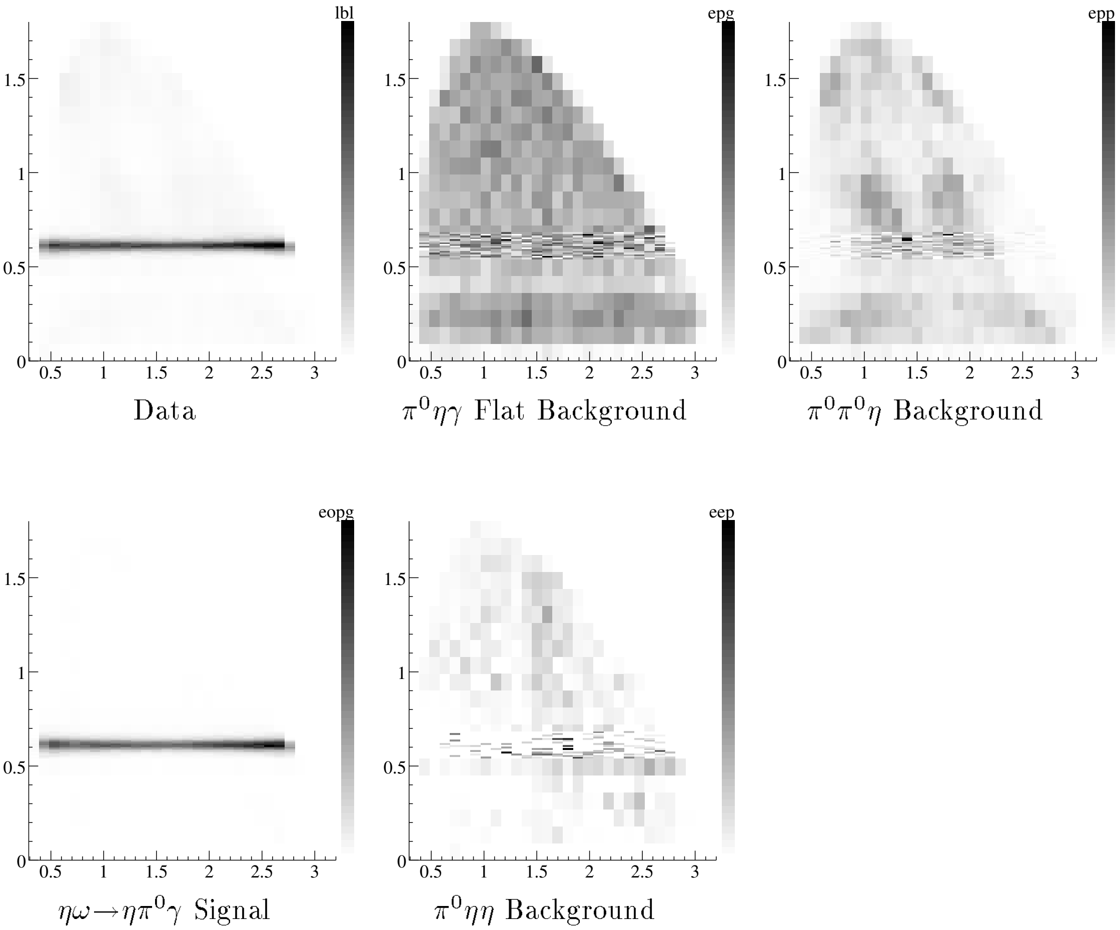

Figure 15.7: The components of the $\eta\pi^0\gamma$ group. The relative intensities of each Dalitz plot is arbitrary

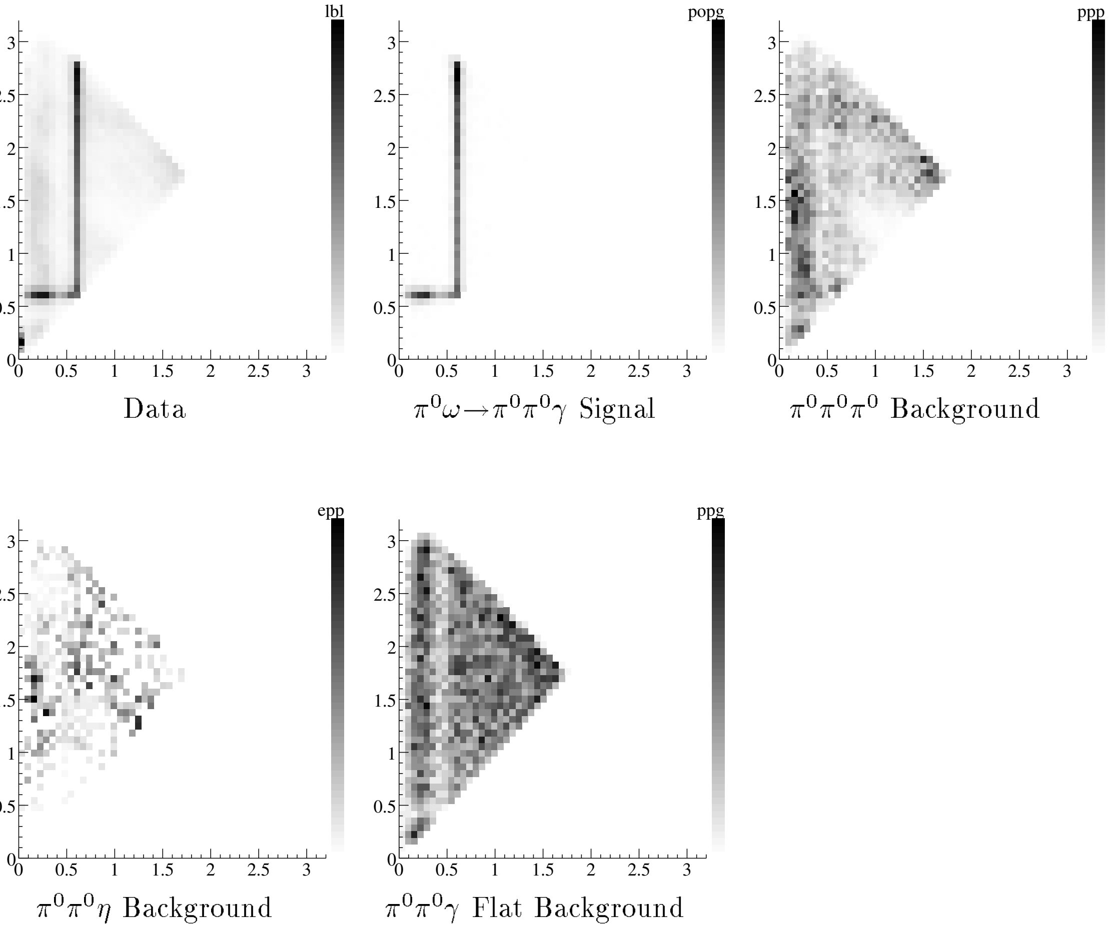

Figure 15.8: The components of the $\pi^0\pi^0\gamma$ group. The relative intensities of each Dalitz plot is arbitrary

Chapter 16

Fits

16.1 Introduction

Because of the low statistics and high backgrounds involved, the details of fitting procedure is critical to the success of this measurement. Because available histogramming and fitting packages were not suitable for this task (e.g Paw), a custom histogramming package and a custom likelihood function were employed. Details of these packages are given in the appendix.

As well as depending on the fitting procedure, the results also depend on which backgrounds are included in the fit. All known backgrounds were included in the fits; however, there is evidence for other previously unmeasured backgrounds. Without further study, we fit the data with and without these additional unknown backgrounds and combine the two results. We also present the results of the fits with the unknown backgrounds as first measurements of these channels.

We use the term "χ^2" rather loosely throughout this chapter, when it would be more exact to say “twice the minus log-likelihood”. The values given are twice the negative log-likelihood, which is equivalent to χ^2 for error estimation.

16.2 Fits

The events in the three samples, $\eta\eta\gamma$, $\eta\pi^0\gamma$ and $\pi^0\pi^0\gamma$, were plotted in variable-bin-width two-dimensional Dalitz-plot histograms, and fitted to a linear sum of distributions derived from Monte Carlo simulation of the signal and background channels. Because of limited statistics in both data and Monte Carlo, the following log-likelihood function was used[80],

$$-2\ln(L) = 2\sum_j \left[n_j \ln \lambda_j - \lambda_j + \sum_i (m_{ij} \ln f_{ij} - f_{ij}) \right], \tag{16.1}$$

where j runs over the bins of the Dalitz plot, i runs over the MC event samples which represent the constituent parts of the data, n is the number of data events, m is the number of unweighted, reconstructed MC events, f is the *expected* number of unweighted, reconstructed MC events, and λ is the expected number of reconstructed data events, defined as

$$\lambda_j = \sum_i a_i w_{ij} f_{ij} \tag{16.2}$$

where a_i is the strength of the i'th channel and $w_i j$ is the additional weight factor (such as angular distribution or dynamical form), normalized to average 1 summed over all j. The method for finding the unknown f_{ij}'s involves a minimization problem for each bin, and the algorithm is given in [80]. The initial values of the a_i are

$$a_{i0} = \frac{b_{\text{trigger}} N_{\text{trigger}}}{M_i} BR(p\overline{p}\rightarrow i) \tag{16.3}$$

where N_{trigger} is the number of triggered data events, b_{trigger} is the all–neutral trigger enhancement $((3.9\%)^{-1})$ [81] and M_i is the number of generated events in the i^{th} Monte Carlo set.

The fitting of each channel's contribution a_i is performed by minimizing the negative log-likelihood with MINUIT [37]. The fit error estimates were done using the MINOS algorithm, or in the case of BR($\omega\rightarrow\eta\gamma$) by inspecting the $\delta(-2\ln(L)) = 1$ contours.

We now discuss how the experimental resolution is folded into the histograms. Each Monte Carlo event has two sets of particle momenta, the initial generated momenta and the final reconstructed momenta. The reconstructed momenta are equal to the generated momenta plus smearing due to the detector resolution. Each event is weighted by a dynamic intensity as a function of the initial generated momenta. Since the reconstructed momenta were used in the fits, the reference histograms contain the physical line shapes convoluted with the detector resolution.

The list of statistically significant components of the fits is given in table 16.1. The first fits were done without the flat backgrounds, $\eta\eta\gamma$, $\eta\pi^0\gamma$, or $\pi^0\pi^0\gamma$, in each respective group. The results are shown in the first column of table 16.1. Results are quoted in terms of units of the literature values in table 13.2, for easy comparison to previous work. Ideally, all well known fit contributions should be indicated as unity in the table, demonstrating consistency with previously published measurements. However, while most contributions do agree with unity, the fit contribution of $\pi^0\pi^0\eta$ was 50% higher than expected; the contributions from $\pi^0\pi^0\pi^0$ and $\pi^0\eta\eta$ were higher too. This is evidence that there is an additional background contribution to each channel.

The result for the branching ratio of $\omega\to\eta\gamma$ with $C = 0$ (no $\eta\eta\gamma$) is $\mathrm{BR}(\omega\to\eta\gamma) = (1.7 \pm 0.6) \times 10^{-4}$. This value is clearly much smaller than previous measurements, which average 6.5 ± 10^{-4} [38].

Next, the fits were repeated with inclusion of these flat backgrounds, and in all cases the log-likelihood improved significantly. Indeed, when this new background is introduced into the fit, the contribution from $\pi^0\pi^0\eta$ drops to a more expected value. Similar results are seen in the $\eta\eta\gamma$ and $\pi^0\pi^0\gamma$ channels. (NB: The $\eta\pi^0\gamma$ and $\pi^0\pi^0\gamma$ backgrounds are treated incoherently.)

In the fit to the $\eta\eta\gamma$ group, there are four real parameters describing the coherent contributions to the ω peak: $\mathrm{BR}(\omega\to\eta\gamma)$, $\mathrm{BR}(\rho^0\to\eta\gamma)$ and the magnitude and phase of the complex constant C for the $\eta\eta\gamma$ background. Because the fit is not very sensitive to $\mathrm{BR}(\rho^0\to\eta\gamma)$, we must fix it to the value from table 13.2. The remaining values are iteratively scanned in pairs over a suitable range. The log-likelihood plots of the three scans are shown in figure 16.2.

The projections of the best fits to the three Dalitz plots is shown in figure 16.1. The strong ω peaks in the lower two plots are well fit, and indeed the fitted values for the $\mathrm{BR}(p\overline{p}\to\eta\omega\to\eta\pi^0\gamma)$ and $\mathrm{BR}(p\overline{p}\to\pi^0\omega\to\pi^0\pi^0\gamma)$ agree with each other and to the tabulated values. The top projection shows that the fit to the rare ω peak in the reaction $p\overline{p}\to\eta\omega$, $\omega\to\eta\gamma$ is satisfactory. The apparent mass shift of the ω peak by a half bin is not deemed statistically significant.

Group	channel		BR relative to literature	
			without bkgd	with new bkgd
$\eta\eta\gamma$	$p\overline{p}\rightarrow\omega\eta,\omega\rightarrow\eta\gamma$	$\bullet$	0.20 ± 0.07	$0.65^{+0.20}_{-0.28}$
	$p\overline{p}\rightarrow\rho^0\eta,\rho^0\rightarrow\eta\gamma$	$\bullet$	1.5 ± 1.5	1 (fixed)
	$p\overline{p}\rightarrow\pi^0\eta\eta$	$\circ$	1.22 ± 0.04	0.90 ± 0.04
	$p\overline{p}\rightarrow\eta\eta$	$\circ$	$1.2^{+0.2}_{-0.5}$	1.0 ± 0.7
	$p\overline{p}\rightarrow\eta\eta\gamma$	$\circ$	-	$(3.5 \pm 1.3) \times 10^{-5}$†
	$\eta\eta\gamma$ phase	$\circ$	-	140° †
	$-2\ln(L)$		165	129
	N_{df}		133	133
$\eta\pi^0\gamma$	$p\overline{p}\rightarrow\omega\eta,\omega\rightarrow\pi^0\gamma$	$\bullet$	1.01 ± 0.01	1.04 ± 0.01
	$p\overline{p}\rightarrow\pi^0\pi^0\eta$	$\circ$	1.50 ± 0.02	$0.87^{+0.4}_{-0.01}$
	$p\overline{p}\rightarrow\eta\pi^0\gamma$	$\circ$	-	2.5×10^{-4}†
	$-2\ln(L)$		2704	2592
	N_{df}		801	801
$\pi^0\pi^0\gamma$	$p\overline{p}\rightarrow\omega\pi^0,\omega\rightarrow\pi^0\gamma$	$\bullet$	1.00 ± 0.01	1.01 ± 0.01
	$p\overline{p}\rightarrow\pi^0\pi^0\pi^0$	$\circ$	1.13 ± 0.02	0.98 ± 0.02
	$p\overline{p}\rightarrow\pi^0\pi^0\gamma$	$\circ$	-	8.8×10^{-5}‡
	$-2\ln(L)$		1181	1054
	N_{df}		424	424

Table 16.1: The final fit values with uncorrected statistical errors in units of the tabulated literature values of table 13.2, except those marked with a † or ‡ which are absolute branching ratios, because there is no tabulated reference. ‡ is discussed in the text. $\bullet$ = signal, $\circ$ = background.

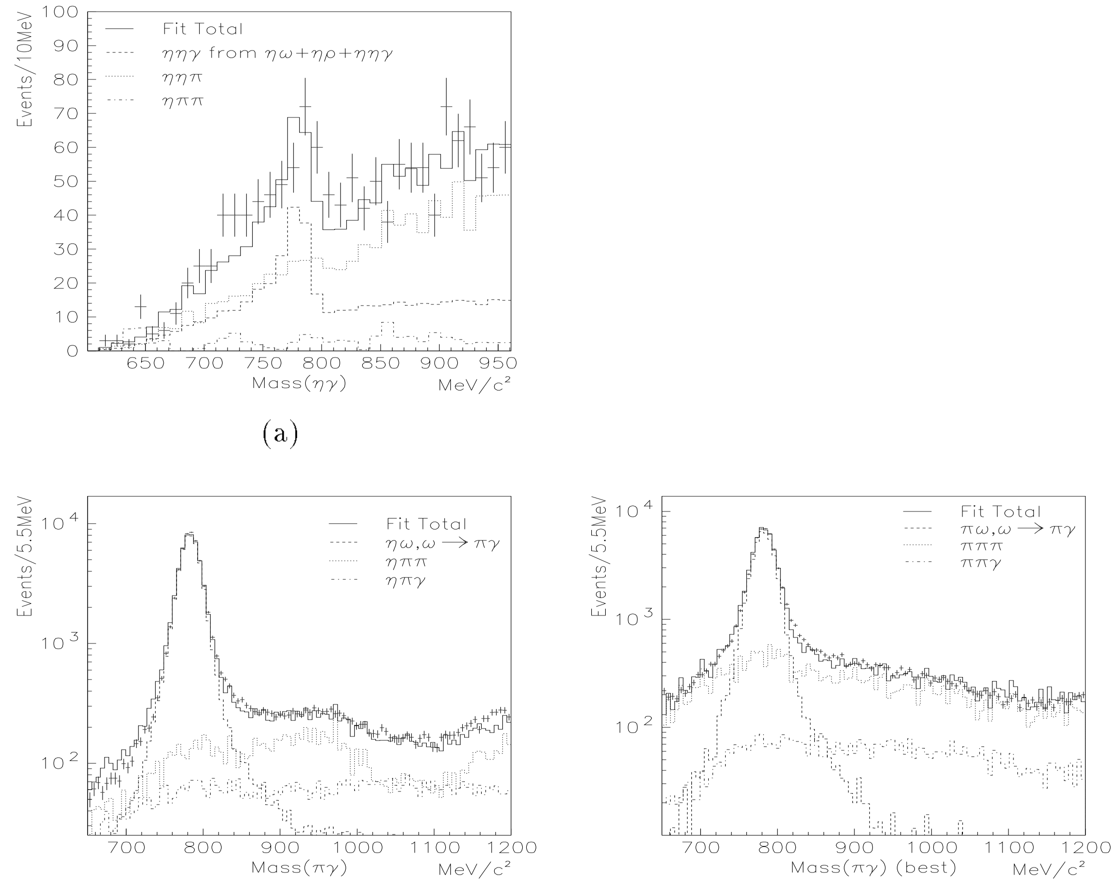

Figure 16.1: One-dimensional projections of the two-dimensional fits. (a) The $m(\eta\gamma)$ projection of the $\eta\eta\gamma$ channel fit, (b) The $m(\pi^0\gamma)$ projection of the $\eta\pi^0\gamma$ channel fit. (c) the $m(\pi^0\gamma)$ projection of the $\pi^0\pi^0\gamma$ channel fit. Figures (a) and (c) show only the "best" combination of $\eta\gamma$ or $\pi^0\gamma$ that is closest to the ω mass.

We have determined the branching ratio of the $p\overline{p}\rightarrow\eta\eta\gamma$ direct channel to be

$$BR(p\overline{p}\rightarrow\eta\eta\gamma) = (3.5 \pm 0.5(\text{stat}) \pm 1.2(\text{sys})) \times 10^{-5}.$$

This quantity is correlated to the amount of the $\pi^0\eta\eta$ background, because both backgrounds are relatively broad. The systematic error on this quantity was determined by the variation incurred by either fixing (to the tabulated values in table 13.2) or releasing the intensity of $\pi^0\eta\eta$ in the fit. The fit favors a phase of C of $(130^{+30}_{-10})^\circ$, as seen in figure 16.2. Finally, the branching ratio of $\omega\rightarrow\eta\gamma$ is determined to be

$$\text{BR}(\omega\rightarrow\eta\gamma) = 4.2^{+1.3}_{-1.8} \times 10^{-4} \tag{16.4}$$

from the 1σ contour in figure 16.2.

In the fits to the $\eta\pi^0\gamma$ and $\pi^0\pi^0\gamma$ groups, we find that the data is described by the branching ratios given in the literature, when the flat backgrounds $\eta\pi^0\gamma$ and $\pi^0\pi^0\gamma$ are added to the fits. In particular, the branching ratio of $\text{BR}(p\overline{p}\rightarrow\pi^0\pi^0\eta)$ is about 1.56 ± 0.01 times greater than predicted based on values from the literature when the $\eta\pi^0\gamma$ flat background is omitted. When the flat background $\eta\pi^0\gamma$ is added to the fit, the ratio of $\text{BR}(p\overline{p}\rightarrow\pi^0\pi^0\eta)$ to predicted becomes a much better value of $0.87^{+0.4}_{-0.01}$ and the χ^2 drops by -112 for 799 degrees of freedom. The same effect is seen in the $\pi^0\pi^0\gamma$ group, substituting $\pi^0\pi^0\pi^0$ for $\pi^0\pi^0\eta$ and $\pi^0\pi^0\gamma$ for $\eta\pi^0\gamma$ flat backgrounds. The χ^2 falls -137 for 423 degrees of freedom when the $\pi^0\pi^0\gamma$ background is included. These results are summarized in table 16.2.

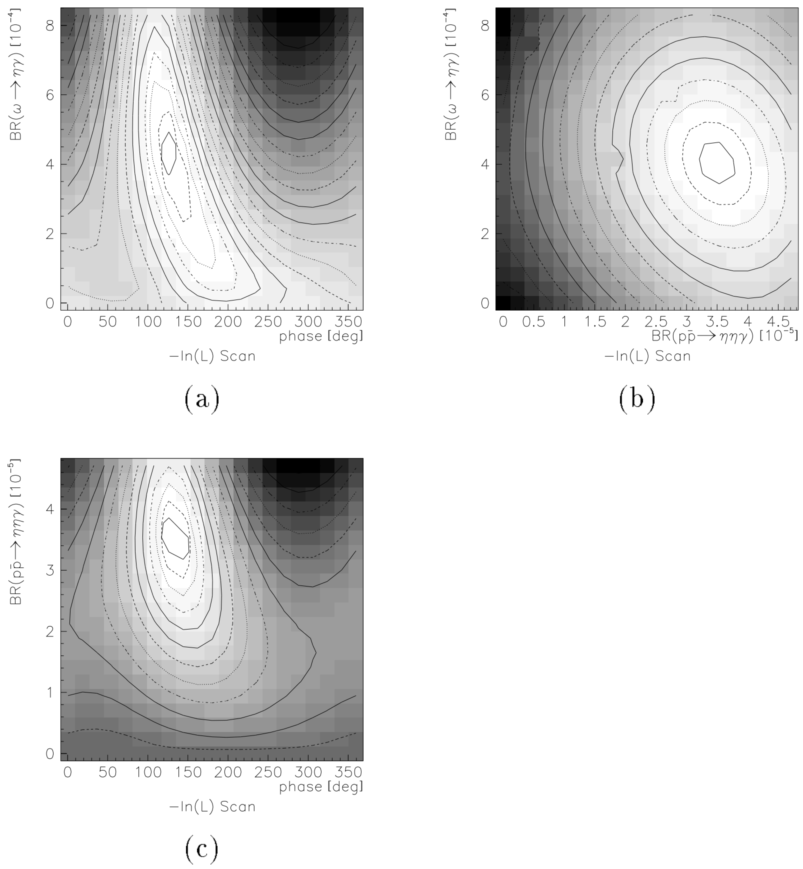

Figure 16.2: The contours of $-2\ln(L)$ over a scan of ω parameters. (a) BR($\omega\rightarrow\eta\gamma$) vs phase of $\eta\eta\gamma$(b) BR($\omega\rightarrow\eta\gamma$) vs BR($\eta\eta\gamma$) (c) BR($\eta\eta\gamma$) vs phase of $\eta\eta\gamma$. Contour lines are drawn at $-2\ln(L) = -2\ln(L)_{\mathrm{min}} + (i/2)^2$ where i is a positive integer. The second contour line is equivalent to $\Delta\chi^2 = 1$.

New Channel	BR($p\overline{p}\rightarrow$)	— without — – new bkgd –		——— with new bkgd ———				NDF
				PS bkgd fixed		PS bkgd free		
		PS scale	χ^2	PS scale	χ^2	PS scale	χ^2	
$\eta\eta\gamma$	$(3.5\pm1.3)\times10^{-5}$	1.27 ± 0.03	165	1.0000	134	$0.83^{+0.04}_{-0.09}$	129	133
$\eta\pi^0\gamma$	$(2.5^{+0.5}_{-2.5})\times10^{-4}$	1.56 ± 0.01	2704	1.0000	2601	$0.87^{+0.04}_{-0.01}$	2592	799
$\pi^0\pi^0\gamma$	$(8.8^{+6.2}_{-8.8})\times10^{-5}$	1.17 ± 0.02	1181	1.0000	1055	0.98 ± 0.02	1054	423

Table 16.2: New direct three body annihilation channels. Errors are approximate. The scaling of the pseudoscalar backgrounds (PS) are given for the cases with and without the new flat backgrounds. In the case "with", the pseudoscalar background scaling is set to 1.0000 to show the dependence on χ^2.

16.3 Systematics and Consistency checks

16.3.1 Stability versus Confidence Level cut

For the $\eta\eta\gamma$ group, we sliced the data into 3 sets based on confidence level: 0-33%, 33%-67% and 67% to 100%. For simplicity, we used a fixed ω/ρ^0 dynamical function, using the branching ratio found in the best fit. The fit result of the rare decay for either third of the full data set was consistent with the full data set: in ratio to the final answer, the three fit results for the BR($\omega\to\eta\gamma$) were 0.88 ± 0.88, 0.77 ± 0.44 and 1.53 ± 0.52, respectively for the three confidence intervals. When the confidence level cut was omitted (but still accepting only $\chi^2 < 5$), the relative fit result for BR($\omega\to\eta\gamma$) was 1.04 ± 0.41. When the latent π^0 cut was omitted, the fit results was 0.85 ± 0.78. When both cuts were omitted, the result was 1.12 ± 0.41. So the result is stable within (generous) errors, regardless of the cuts.

For the $\eta\pi^0\gamma$ and $\pi^0\pi^0\gamma$ groups, we sliced the data into five sets based on confidence level. The fit results for BR($\eta\omega\to\eta\pi^0\gamma$) and BR($\pi^0\omega\to\pi^0\pi^0\gamma$) as a function of confidence level (0-20%, 20-40%, 40-60%, 60-80%, 80-100%) are shown in figure 16.3.

If the backgrounds $p\overline{p}\to\eta\eta\gamma$, $p\overline{p}\to\eta\pi^0\gamma$ and $p\overline{p}\to\pi^0\pi^0\gamma$ are omitted, the fit values of the backgrounds from $\pi^0\eta\eta$, $\pi^0\pi^0\eta$, and $\pi^0\pi^0\pi^0$ increase with increasing confidence level, when they should be fixed constants for any cut. This indicates a problem in the characterization of the background. This problem can be eliminated by two methods. The first is to include the flat backgrounds ($\eta\eta\gamma$, $\eta\pi^0\gamma$ and $\pi^0\pi^0\gamma$). With this inclusion, the fit values of the 3-pseudoscalar backgrounds remain constant regardless of confidence level cut. The other alternative is to artificially increase the errors input into the kinematic fit

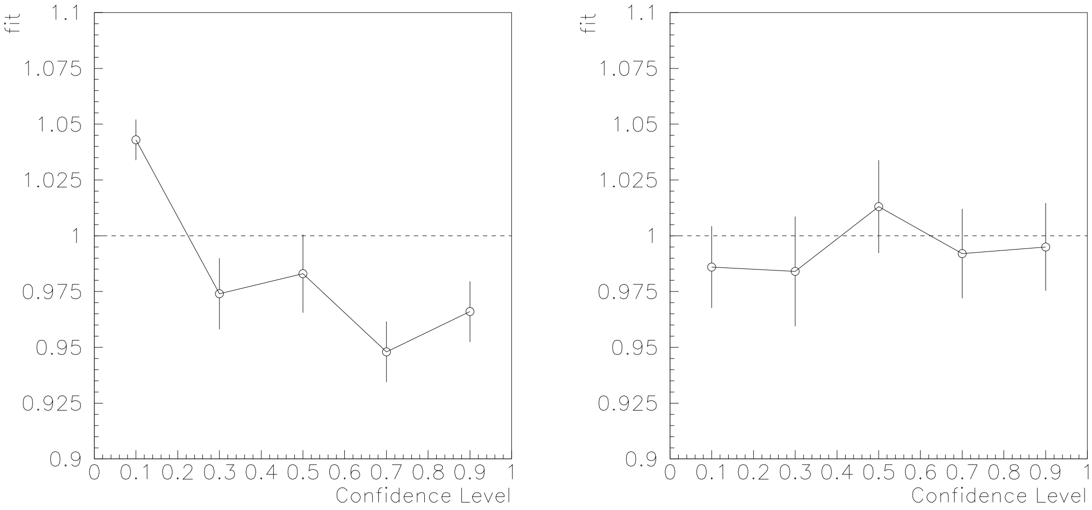

BR($p\overline{p}\to\eta\omega\to\eta\pi^0\gamma$) in $\eta\pi^0\gamma$ group

BR($p\overline{p}\to\pi^0\omega\to\pi^0\pi^0\gamma$) in $\pi^0\pi^0\gamma$ group

Figure 16.3: The stability of fit results versus confidence level

by 5-10% for the 3-pseudoscalar channels while keeping the other channels the same. This achieves a similar satisfactory result. Nevertheless, because this untenable problem only appears to affect the backgrounds, we attribute no additional systematic error to the signal measurements.

The only resonant background that can appear under the $\omega\to\eta\gamma$ peak is leak-through from $\eta\omega\to\eta\pi^0\gamma$, where the π^0 is not identified because of noise (a so-called latent-pion, described in section 15.5)), and a fake η is formed from a different permutation of the photons of the ω decay. The three photons from the ω decay still reconstruct to the ω mass. It is crucial to thoroughly remove this background channel from the data. To verify that the $\eta\omega\to\eta\pi^0\gamma$ background was sufficiently suppressed, the width of the latent-pion anticut interval was varied from 10 MeV/c^2 to 170 MeV/c^2. The expected number of leak-through events drops to 0 at an interval width of 90 MeV/c^2, and the final result is constant for all

Reference	Reaction	BR($\omega\to\eta\gamma$) [$\times 10^{-4}$]
[82]	6.7-10 γCu	$3.0^{+2.5}_{-1.8}$
[72]	$e^+e^-\to\omega$	$6.4^{+7.0}_{-4.7}$
[73]	$\pi^- p\to\omega n$	8.3 ± 2.1
[83]	$e^+e^-\to\omega$	$6.6^{+2.4}_{-2.6}$
This work[a]	$p\overline{p}\to\omega\eta$	1.7 ± 0.6
This work[b]	$p\overline{p}\to\omega\eta$	$4.2^{+1.3}_{-1.8}$

[a] Assuming incoherent background only

[b] With $\eta\eta\gamma$ coherent background

Table 16.3: Previous measurements of BR($\omega\to\eta\gamma$) in comparison to this work

widths above 90 MeV/c^2.

The entire analysis was redone with lower γ-thresholds (3 MeV cluster threshold, 3 MeV secondary maximum threshold, 20 MeV γ threshold). These low thresholds were chosen to minimize the background from 6 photon channels, but unfortunately reduced the signal by a large amount, too. There were larger fluctuations in the consistency checks and a larger disagreement with previously published values for the backgrounds. We attribute this to the inaccuracy of the Monte Carlo in simulating very soft photon interactions with the barrel. However, the measurement of the $\omega\to\eta\gamma$ signal was not affected.

To verify that the fit handles bins with low statistics well, the projections of the Dalitz plots where fitted as well. The resultant values were all consistent with the two dimensional fits within typically 0.5 sigma or less. The statistical errors, however, dominate the final result, so no extra systematic error is added.

16.3.2 The dependence on backgrounds

The 3 pseudoscalar backgrounds ($\pi^0\eta\eta$ and $\pi^0\pi^0\eta$) are known to exist, and their contributions can be fitted to the data. However, the fitted contributions are significantly larger than expected, from 20 to 50% larger.

Annihilation of $p\overline{p}$ usually proceeds through a two meson intermediate state. However, it can happen that the annihilation proceeds directly to a three particle final state, with two mesons and one photon. The fits to all three channels, $\eta\eta\gamma$, $\eta\pi^0\gamma$ and $\pi^0\pi^0\gamma$, improve if we assume that there exists a flat background channel that does not proceed through any intermediate resonances.

The evidence for these channels is three-fold. First, the χ^2 of the fits is greatly lower and a visual inspection of the fit quality greatly favors these new channels. Secondly, the fit values for the backgrounds channels $\pi^0\eta\eta$, $\pi^0\pi^0\eta$, and $\pi^0\pi^0\pi^0$ are too high without these new channels; in the case of $\pi^0\pi^0\eta$, the fit value is 50% too high.

Thirdly, the fitted values of these known background channels is not flat with respect to confidence level. The fit values increase significantly when the confidence level cut is increased. This indicates the existence of a background which does not drop off in confidence level as quickly as the 3 pseudoscalar backgrounds do. Remember that the 3 pseudoscalar backgrounds have “lost” a photon and therefore should not have a flat confidence level. However, these new channels are exactly the kinematic fit hypothesis and will have a flat confidence level distribution.

We believe that these three pieces of evidence favor the existence of these new channels. The branching ratios for these channels is given in table 16.2. The errors are estimated by taking the absolute limits of all of the fits tried. We set the lower error bar to include zero, because there is still the possibility that these channels could be faked by subtle inaccuracies in the Monte Carlo and may not exist at all. If the Monte Carlo is wildly inaccurate, then it is prudent to include these fake channels to make up for it.

If we average the six fits using just $\pi^0\eta\eta$(background type A) and the average the six fits using both $\pi^0\eta\eta$ and $\eta\eta\gamma$(background type B), we see that the two disagree by 20%. We assign this variation to the systematic error.

16.4 Conclusion

We have measured the branching ratio of $\omega\rightarrow\eta\gamma$, under the two hypotheses that this channel incoherently or coherently interferes with a flat background from $p\overline{p}\rightarrow\eta\eta\gamma$. Under the assumption that the interference in incoherent, the branching ratio for $\omega\rightarrow\eta\gamma$ is much smaller than any previously determined value in the literature. Under the assumption that the interference is coherent, the value is in agreement with the results from e^+e^- data.

The flat backgrounds (meaning not occuring through ω or ρ^0 intermediates) of $p\overline{p}\rightarrow\eta\eta\gamma$, $p\overline{p}\rightarrow\eta\pi^0\gamma$ and $p\overline{p}\rightarrow\pi^0\pi^0\gamma$ appear to be important in the fits by significant improvements in log-likelihood, and without the $p\overline{p}\rightarrow\eta\eta\gamma$ channel, the BR($\omega\rightarrow\eta\gamma$) would be much smaller than previously thought.

Bibliography

[1] Claude Amsler. Proton-antiproton annihilation and meson spectroscopy with the Crystal Barrel. hep-ex/9708025, 1997.

[2] E. Aker et al. The Crystal Barrel detector at LEAR. *Nuclear Instruments and Methods*, A321:69, 1992. CERN-PPE/92-126.

[3] C. Regenfus. The Crystal Barrel Si-vertex detector. *Nuclear Instruments and Methods*, A412:70–79, 1998.

[4] G.S. Bali et al. a comprehensive lattice study of SU(3) glueballs. *Physics Letters*, B309:378, 1993.

[5] J.C. Sexton et al. numerical evidence for the observation of a scalar glueball. *Physics Review Letters*, 75:4563, 1995.

[6] Stefan Spanier. Crystal barrel results on two body decays of the scalar glueball. In S. Narison, editor, *QCD96, Proceedings of the Conference*, volume 54A, page 362, France, 1997. Nucl. Phys B. Proc. Suppl.

[7] C. Amsler and F. Close. Is $f_0(1500)$ a scalar glueball? *Physics Review*, D53:295, 1996.

[8] E. Klempt. The scalar meson nonet and the glueball ground state. *Nuclear Physics*, A629:131–140, 1998.

[9] A. Abele et al. Observation of $f_0(1500)$ decay into $K_L K_L$. *Physics Letters*, B385:425, 1996.

[10] R.N. Cahn and P.V. Landshoff. Mystery of the $\delta(980)$ [ed: now called $a_0(980)$]. *Nuclear Physics*, B266:451–467, 1986.

[11] T. DeGrand et al. Masses and other parameters of the light hadrons. *Physics Review*, D12:2060, 1975.

[12] Frank Close. *An Introduction to Quarks and Partons*. Academic, New York, 1979.

[13] N. Isgur and G. Karl. P wave baryons in the quark model. *Physics Review*, D18:4187, 1978.

[14] N. Isgur and G. Karl. Positive parity excited baryons in a quark model with hyperfine interactions. *Physics Review*, D19:2653, 1979.

[15] C. Amsler and F. Myhrer. Low energy antiproton physics. *Annu. Rev. Nucl. Part. Sci.*, 41:219–267, 1991.

[16] C. J. Batty. S- and P-state annihilation in anti-p p interactions at rest. *Nuclear Physics*, A601:425–444, 1996.

[17] J.D. Hansen et al. Formalism and assumptions involved in partial wave analysis of three - meson systems. *Nuclear Physics*, B81:403, 1974.

[18] G. Ascoli et al. Partial-wave analysiso fthe deck amplitude for $\pi N \rightarrow \pi\pi\pi N^*$. *Physics Review*, D8:3894, 1973.

[19] B. Conforto and other. Experimental results on the ($K\bar{K}$) and (Kp) systems as observed in the annihilations $p\overline{p} \rightarrow K\bar{K}pi$ at rest. *Nuclear Physics*, B3:469–503, 1967.

[20] R. Armenteros et al. Experimental results on the annihilation $p\overline{p} \rightarrow K\bar{K}\pi$ at rest; K^* production. *Physics Letters*, 17:170, 1965.

[21] A. Abele et al. Antiproton-proton annihilation at rest into $K_L K^{\pm}\pi^{\mp}$. *Physics Review*, D57:3860, 1998.

[22] Aston et al. A study of $K^-\pi^{++}$ scattering in the reaction $K^-p \rightarrow K^-\pi^+n$ at 11 GeV/c. *Nuclear Physics*, B296:493–526, 1988.

[23] C. Amsler et al. Observation of a new I^G J^{PC} =1$^-$ 0^{++} resonance at 1450 MeV. *Physics Letters*, B333:277, 1994.

[24] S.M. Flatteé. Coupled-channel analysis of the $\pi\eta$ and $K\overline{K}$ systems near $K\overline{K}$ threshold. *Physics Letters*, B63:224, 1976.

[25] A.M. Badalyan et al. Resonances in coupled channels in nuclear and particle physics. *Physics Reports*, 82(2):31–177, 1982.

[26] Boutemeur. unknown. In Suk urk Chung, editor, *Glueballs, Hybrids, and Exotic Hadrons: Proceedings*, page 185. American Institute of Physics, Aug 29 - Sep 1 1989. QCD161:B58:1988.

[27] C. Amsler et al. Coupled channel analysis of antiproton proton annihilation into $\pi^0\pi^0\pi^0$, $\pi^0\eta\eta$ and $\pi^0\pi^0\eta$. *Physics Letters*, B355:425, 1995.

[28] A. Abele et al. Further analysis of $\overline{p}p \rightarrow 3\pi^0, \eta\eta\pi^0$ and $\eta\pi^0\pi^0$ at rest. *Nuclear Physics*, A609:562–584, 1996.

[29] G. Usai. Study of the isovector scalar mesons in the channel $p\overline{p}{\rightarrow}K^{\pm}K_S\pi^{\mp}$ at three hydrogren target densities. In Suh-Urk Chung and Hans J. Willutzki, editors, *Hadron Spectroscopy, 7th International Conference*, page 108. OBELIX collaboration, American Institute of Physics, August 1997.

[30] A. Abele et al. Study of the $\pi^0\pi^0\eta^{'}$ final state in antiproton proton annihilations at rest. *Physics Letters*, B404:179, 1997.

[31] A. Abele et al. Exotic $\eta\pi$ state in antiproton-deuterium annihilation at rest into $\pi^-\pi^0\eta p_{\mathrm{spectator}}$. *Physics Letters*, B423:175, 1998.

[32] W. Cleland et al. Resonance production in the reaction $\pi^{\pm}p \rightarrow K_S K^{\pm}p$ at 30 GeV/c and 50 GeV/c. *Nuclear Physics*, B208:228, 1982.

[33] A. Donacchie and Clegg. The decays of the $\rho^{'}$ and $\omega^{'}$ mesons. *Zeitschrift für Physik*, C51:689, 1991.

[34] Mark Lakata. CBDISP The Crystal Barrel Display Program. Technical Report CBNote 260, Crystal Barrel Collaboration, 1994.

[35] John Ousterhout. *Tcl and the Tk Toolkit.* Addison-Wesley, 1994.

[36] Mark Lakata. A new multi-vertex fitter and updated vertex-locater information. Technical report, Crystal Barrel, 1995. CB Note 285.

[37] Fred James. Minuit function minimization and error analysis reference manual. Technical report, CERN Program Library, 1992. D506 V92.1.

[38] Particle Data Group. Review of particle physics. *European Physical Journal*, C3:1–794, 1998.

[39] A.J.Noble. The release of CBGEANT 5.00. Technical Report CBNote 264, Crystal Barrel Collaboration, 1994.

[40] Rene Brun, F. Bruyant, M. Maire, A.C. McPherson, and P. Zanarini. GEANT. Technical Report DD/EE/81-1, CERN Program Library, 1987.

[41] Barash. Antiproton annihilation in hydrogen at rest. I. reaction $p\overline{p} \to K\bar{K}\pi$. *Physics Review*, 139B:1659, 1965.

[42] Charles Zemach. Use of angular-momentum tensors. *Physics Review*, 140B:97– 109, 1965.

[43] V. Filippini et al. Covariant spin tensors in meson spectroscopy. *Physics Review*, D51:2247, 1995.

[44] Frank von Hippel and C. Quigg. Centrifugal-barrier effects in resoance partial decay widths, shape, and production amplitudes. *Physics Review*, D5:624–638, 1972.

[45] S.U Chung et al. Partial wave analysis in the K-matrix formalism. *Ann. Physik*, 4:404, 1995.

[46] E. Aker et al. Observation of a 2^{++} resonance at 1515 MeV in proton antiproton annihilations into $\pi^0\pi^0\pi^0$. *Physics Letters*, B260:249, 1991.

[47] C. Amsler et al. Proton–antiproton annihilations into $\eta\eta\pi^0$ - observation of a scaler resonance decaying into $\eta\eta$. *Physics Letters*, B291:347, 1992. CERN-PPE/92-114.

[48] A. Bertin et al. Study of the isovector scalar mesons in the channel $p\overline{p}\rightarrow K^{\pm}K_S\pi^{\mp}$ at rest with initial angular momentum state selection. *Physics Letters*, B434:180–188, 1998.

[49] A. Bettini et al. The annihilation at rest $\overline{n}n\rightarrow K\overline{K}\pi$. *Nuovo Cimento*, 63A:1199, 1969.

[50] C. Amsler et al. High statistics study of the $f_0(1500)$ decay into $\eta\eta$. *Physics Letters*, B353:571, 1995.

[51] S. Teige et al. Properties of the $a_0(980)$ meson. *hep-ex*, 960817:1, 1996.

[52] C. Amsler et al. A high-statistics study of $f_0(1500)$ decay into $\pi^0\pi^0$. *Physics Letters*, B342:433, 1995.

[53] P.J. O'Donnel. Radiative decays of mesons. *Rev. Mod. Phys*, 53:673, 1981.

[54] C. Amsler et al. Radiative protonium annihilation, antiproton-proton goes to gamma x with x=γ, π^0, η, ω and η'. *Physics Letters*, B311:371, 1993. CERN-PPE/93-103.

[55] C. Amsler et al. Antiproton–proton annihilation at rest into two–body final states. *Zeitschrift für Physik*, C58:175, 1993. CERN-PPE/93-11.

[56] C. Amsler et al. First observation of pontecorvo reactions with a recoiling neutron. *Zeitschrift für Physik*, A351:325, 1995.

[57] C. Amsler et al. Observation of a scalar resonance decaying to $\pi^+\pi^-\pi^0\pi^0$ in antiproton proton annihilation at rest. *Physics Letters*, B322:431, 1994.

[58] C. Amsler et al. Study of antiproton-proton annihilation at rest into $\omega\eta\pi^0$. *Physics Letters*, B327:425, 1994.

[59] A. Abele et al. $\rho-\omega$ interference in antiproton proton annihilation at rest into $\pi^+\pi^-\eta$. *Physics Letters*, B411:354, 1997.

[60] C. Amsler and F. Myhrer. Low energy antiproton physics. *Annu. Rev. Nucl. Part. Sci.*, 41:235, 1991.

[61] R. Bizzari et al. Experimental results on the $\omega\pi$ and $\pi\pi$ systems as observed in the $p\overline{p}$ annihilations at rest: $p\overline{p}\rightarrow\omega\pi^+\pi^-$. *Nuclear Physics*, B14:169–194, 1969.

[62] R.M. Barnett et al. Review of particle physics. *Physics Review*, D54:1, 1996.

[63] N. Barik and P.C. Dash. Radiative decay of mesons in an independent-quark potential model. *Physics Review*, D46:3856, 1992.

[64] M. Gell-Mann. Decay rates of neutral mesons. *Physics Review Letters*, page 261, 1962.

[65] J.W. Durso. Vector dominance and radiative meson decays. *Physics Letters*, B184, 1987.

[66] L. Montanet M. Benayoun, Ph. Leruste and J.-L. Narjoux. Meson radiative decays and anomaly physics, a test of qcd. *LPC-94-31*, June 30 1994.

[67] Francis Halzen and Alan Martin. *Quarks & leptons: an introductory course in modern particle physics.* John Wiley & Sons, 1984.

[68] G.A. Miller P. Singer. $B^* \rightarrow B$ gamma decays in a bag model for heavy - light quark states. *Physics Review*, D39:825, 1989.

[69] A.W. Thomas Y.S. Zhong, T.S. Cheng. The m1 radiative decay of low-lying mesons in the cloudy bag model with centre-of-mass correction. *Nuclear Physics*, A559:579, 1993.

[70] P.C. Dash N. Barik. Radiative decay of light and heavy mesons. *Physics Review*, D49:299, 1994.

[71] A. Grau A. Bramon and G. Pancheri. Radiative vector-meson decays in su(3) broken effective chiral lagrangians. *Physics Letters*, B344:240, 1995.

[72] S. Dolinsky et al. Radiative decays of ρ^0 and ω mesons. *Zeitschrift für Physik*, C42:511, 1989.

[73] D. Alde et al. Model independent measurement of omega $\rightarrow$ eta gamma decay branching ratio. *Zeitschrift für Physik*, C61:35, 1994.

[74] A. Abele et al. Measurement of the $\omega \rightarrow \eta\gamma$ decay branching ratio. *Physics Letters*, B411:361, 1997.

[75] P. Weidenauer et al. $N\bar{N}$ annihilation at rest into five pions. *Zeitschrift für Physik*, C59:387, 1993.

[76] A.W. Thomas H.B. O Connell, B.C. Pearce and A.G. Williams. Rho-omega mixing, vector meson dominance and the pion form-factor. hep-ph/9501251, 1995.

[77] N.N. Achasov and G.N. Shestakov. Effects of $\rho^0 - \omega$ mixing and dynamics of vector meson production. *Sov. J. Part. Nucl*, 9:19, 1978.

[78] A.W. Thomas H.B. O Connell, B.C. Pearce and A.G. Williams. Rho-omega mixing and the pion electromagnetic form-factor. *Physics Letters*, B354:14–19, 1995.

[79] M. Lakata. A comparison of the berkeley and zurich $\omega \rightarrow \eta\gamma$ analyses. Technical Report CB Note 321, Crystal Barrel, 1998.

[80] D. Lambert P. Eberhard, G. Lynch. Fits of monte carlo distributions to data. *Nuclear Instruments and Methods*, A326:574–580, 1993.

[81] C. Amsler et al. Antiproton–proton annihilation at rest into $\omega\pi^0\pi^0$. *Physics Letters*, B311:362, 1993. CERN-PPE/93-74.

[82] D. Andrews et al. $\eta\gamma$ decays of ρ^0, ω, and *phi* mesons. *Physics Review Letters*, 38:198, 1977.

[83] M. Benayoun et al. A search for anomalous contribution in $e^+e^- \rightarrow \pi^0/\eta\gamma$ annihilations. *Zeitschrift für Physik*, C72:221, 1996.

Appendix A

Appendix

A.1 Kinematic Fitting

A.1.1 Introduction

A new kinematic fitter was written for the hypothesis, $p\overline{p} \rightarrow K^{\pm}\pi^{\mp}K_S$, because the standard Crystal Barrel software (CBKFIT) does not support this hypothesis. Because it worked very well and is easier to use than CBKFIT, we used it also on this analysis. The software is object-oriented, making it easy to add new constraints. Currently, the constraints are three-momentum conservation and mass conservation at the decay vertices. Any event with 6 or less final state particles can be fitted. (This restraint is imposed by CLHEP, but could be easier expanded if necessary).

There are many new C++ classes.

1. **KinFit** - This is the master class container of the hypotheses. It contains a list of hypotheses.

2. **KinFitHypothesis** - This contains the hypothesis and is a container for the permutations. The fit generates a list of good permutations for each hypothesis for each event. This list is sorted in order of χ^2.

3. **KinFitPermutation** - This contains the permutation of particles. After the fit is done, only valid permutations with valid χ^2 are kept.

4. **KinFitParticle** - A subclass of Particle, contain information about the pulls and also some mechanism for locking the particles when making combinations. These are made in KinFitHypothesis for use in KinFitPermutation. The final answer is in terms of these.

A.1.2 KinFitHypothesis

The Hypothesis class generates the permutations. The problem is to assign the n measured tracks/PEDs to the n final state particles in the predefined hypothesis.

The user initializes the hypothesis with a KinFitParticle, which is a description of the initial state and the immediate daughter particles. Each daughter particle can have further daughters, forming a hierarchy. For instance, the initial state is a $p\overline{p}$ pseudo-particle, with $K^{\pm}$, $\pi^{\mp}$, and K_S as the daughters. The K_S is defined with π^+,π^- as its two daughters.

First the given measured tracks/PEDs are assigned to 3 lists: charged "+", charged "-" and neutral. The final state particles in the hypothesis are symbolically linked to the corresponding lists. The next higher resonances are created using existing resonances; the new resonances are then added to the database to be used for the next iteration of resonance building. Resonances can require certain things about their daughters. For instance, a K_S

can require that the two daughter pions came from the same vertex.

When all resonances are built (ending with the $p\overline{p}$ root particle), each instance in the root particle list is copied to a KinFitPermutation. Each permutation is then fitted, and those permutations that fail the fit are deleted. At the end, the remaining permutations are sorted in increasing χ^2.

A.1.3 KinFitPermutation, description of fitting algorithm

The user submits a selected hypothesis, and the software returns a list of possible permutations that minimally satisfy it. If the list is zero, then no permutation worked. The minimum condition of satisfaction is that the total $\chi^2/N < 5.0$. The list is ordered, so the user typically only examines the first element of the list. The user can then extract the new fitted values of 4-momenta and the pulls from the permutation.

There are three momentum constraints ($\vec{p}_{\mathrm{tot}} = 0$) and m mass constraints, which are explicitly

$$f_i^{\mathrm{momentum}} = \sum_{j=1}^{n} P_i^j \{i = x, y, z\} \tag{A.1}$$

$$f_k^{\mathrm{mass}} = \frac{(m(\mathrm{theory})_k^2 - m(\exp)_k^2)}{m(\mathrm{theory})} \{k = 1..m\} \tag{A.2}$$

This gives a total of

$$c = 3 + m$$

constraints. The nominal phase space fit contains only one resonance (one mass constraint), the initial state ($p\overline{p}$), so has $3 + 1 = 4$ constraints as expected.

The measured values of momenta are written as a vector

$$\eta = (p_x^1, p_y^1, p_z^1, p_x^2, p_y^2, p_z^2, \ldots, p_z^n)$$

And the $3n$ by $3n$ block-diagonal symmetric error matrix is written as,

$$\mathbf{G}_\eta^{-1} = \begin{pmatrix} S_1 & & & \\ & S_2 & & \\ & & \ddots & \\ & & & S_n \end{pmatrix}$$

where the individual tracks have error matrices,

$$S_i = \begin{pmatrix} \sigma_{xx} & \sigma_{xy} & \sigma_{xz} \\ \sigma_{yx} & \sigma_{yy} & \sigma_{yz} \\ \sigma_{zx} & \sigma_{zy} & \sigma_{zz} \end{pmatrix}.$$

We then calculate the derivative matrix,

$$\mathbf{B} = \begin{pmatrix} \frac{\partial f_1}{\partial \eta_1} & \cdots & \frac{\partial f_1}{\partial \eta_{3n}} \\ \vdots & \ddots & \vdots \\ \frac{\partial f_c}{\partial \eta_1} & \cdots & \frac{\partial f_c}{\partial \eta_{3n}} \end{pmatrix}.$$

In this case,

$$\mathbf{B} = \begin{pmatrix} \begin{pmatrix} 1 & 0 & 0 \\ 0 & 1 & 0 \\ 0 & 0 & 1 \end{pmatrix} & \begin{pmatrix} 1 & 0 & 0 \\ 0 & 1 & 0 \\ 0 & 0 & 1 \end{pmatrix} & \cdots & \begin{pmatrix} 1 & 0 & 0 \\ 0 & 1 & 0 \\ 0 & 0 & 1 \end{pmatrix} \\ (\vec{F}_1^1)^T & (\vec{F}_1^2)^T & \cdots & (\vec{F}_1^n)^T \\ (\vec{F}_2^1)^T & (\vec{F}_2^2)^T & \cdots & (\vec{F}_2^n)^T \\ \vdots & & & \\ (\vec{F}_m^1)^T & (\vec{F}_m^2)^T & \cdots & (\vec{F}_m^n)^T \end{pmatrix}$$

where

$$\vec{F}^i_j = \frac{E_j \cdot \vec{\beta}^i - \vec{p}_j}{m(\text{theory})_j}$$

where E_j,$\vec{p}_j$,m_j is the energy/momentum/mass of the j^{th} resonances, and $\vec{\beta}^i$ is the velocity of the i^{th} track/PED.

We calculate the covariance matrix, in the constraint basis,

$$\mathbf{G_B} = (\mathbf{B}\mathbf{G}_\eta^{-1}\mathbf{B}^T)^{-1}$$

and then the improvements to the measured values,

$$\delta\eta = \mathbf{G}_\eta^{-1}\mathbf{B}^T\mathbf{G_B}\mathbf{f}$$

where are iteratively subtracted from the measured values

$$\eta := \eta - \delta\eta$$

The fit desires to make $\mathbf{f} = \mathbf{0}$, so on each calculation,

$$d^2 = \mathbf{f}^T\mathbf{G_B}\mathbf{f}$$

is calculated, and the iterations stop if any of the following conditions is met:

1. The value of d^2 is sufficiently close to zero, which is a successful fit.

2. The value of d^2 is higher than an allowed maximum, and the fit fails.

3. The number of iterations is too high, so the fit fails.

4. An internal error happens, such as inversion of a singular matrix, where the fit of course fails.

At the end of the fit, the χ^2 of the change in the measurements ($\epsilon = \eta - \eta_0$) is calculated,

$$\chi^2 = (\mathbf{B}\epsilon)^T \mathbf{G_B} (\mathbf{B}\epsilon)$$

where the degrees of freedom of the fit are simply the number of constraints, since there are no free parameters,

$$N_{\text{dof}} = 3 + m$$

The reduced χ^2 value is required to be

$$\frac{\chi^2}{N_{\text{dof}}} < 5.0$$

or else the permutation is deleted from the hypothesis.

A.1.4 Final Errors and pulls

In this notation, η = estimates of best values, $\mathbf{y}$ = original data values, $\mathbf{x}$ = parameters of fit. The normal kinematic fit has no free parameters, so $\mathbf{x}$ is not used.

The final errors are calculated using this formula

$$\mathbf{G}_\eta^{-1} = \mathbf{G}_\mathbf{y}^{-1} - \mathbf{G}_\mathbf{y}^{-1} B^T \mathbf{G}_B B \mathbf{G}_\mathbf{y}^{-1} + \mathbf{G}_\mathbf{y}^{-1} B^T \mathbf{G}_B A (A^T \mathbf{G}_B A)^{-1} A^T \mathbf{G}_B B \mathbf{G}_\mathbf{y}^{-1}$$

Note again, that if there are no free parameters, then $A = 0$ as well as $\mathbf{x} = 0$. If a special fit is added, for example the neutral decay position of the $K_S \rightarrow \pi^0 \pi^0$ then this will need to be used.

A pull is a measure of the displacement of the measured values to the fitted values. They are constructed so that a valid distribution of pulls will form a normal distribution with width 1 and mean 0. A pull of the observable λ is defined as

$$P = \frac{\lambda_f - \lambda_i}{\sqrt{\sigma(\lambda_i)^2 - \sigma(\lambda_f)^2}},$$

where i denotes value before fitting and f denotes value after fitting. The $\sigma(\lambda_f)$ comes from $\mathbf{G}_\eta^{-1}$, while the $\sigma(\lambda_i)$ are estimates supplied to the software. Note that the denominator really contains a subtraction and not an addition as might naively be thought. This is because the denominator describes just the statistical uncertainty of the measurement, which can be thought of the difference between the total measured uncertainty and the systematically fitted uncertainty. This also implies that the fitted errors must be always smaller (usually much smaller) than the original errors.

The pulls are a very sensitive measure of the goodness of the fit. If the mean of the pull distribution is not zero, then the data is biased for some reason. This bias could be background, or it could be a detector bias. For example the z-position of the neutral vertex shifts the distribution of the pull of θ_{PED}. If the width is not one, then usually the initial errors are not as good as they could have been. It is usual practice to globally scale the measured initial errors by a factor of order unity in order to force the pull distributions to have a width of one.

A.1.5 Conversion of Rectangular to Helix Parameters

Because the internal calculations are done in rectangular coordinate, the measured parameters of the tracks must be converted from helical coordinates. The conversion of the error matrices is a little more work. To calculate the pulls in the original basis, the internal values need to be converted back too.

$$
\begin{aligned}
P_\perp &= 1/\alpha && \text{(A.3)} \\
\vec{P} &= P_\perp(\cos\psi, \sin\psi, \tan\lambda)
\end{aligned}
$$

$$
\begin{aligned}
P_\perp &= \sqrt{P_x^2 + P_y^2} && \text{(A.4)} \\
\alpha &= 1/P_\perp && \text{(A.5)} \\
\psi &= \mathtt{ATAN2}(P_y, P_x) && \text{(A.6)} \\
\tan\lambda &= P_z/P_\perp && \text{(A.7)}
\end{aligned}
$$

$$
\begin{aligned}
\frac{\partial\vec{P}}{\partial\alpha} &= P_\perp^2(-\cos\psi, -\sin\psi, \tan\lambda) && \text{(A.8)} \\
\frac{\partial\vec{P}}{\partial\tan\lambda} &= (0, 0, P_\perp) && \text{(A.9)} \\
\frac{\partial\vec{P}}{\partial\psi} &= P_\perp(-\sin\psi, \cos\psi, 0) && \text{(A.10)}
\end{aligned}
$$

$$
\begin{aligned}
\frac{\partial\alpha}{\partial\vec{P}} &= \frac{1}{P_\perp^3}(-P_x, -P_y, 0) && \text{(A.11)} \\
\frac{\partial\tan\lambda}{\partial\vec{P}} &= \frac{1}{P_\perp^3}(-P_xP_z, -P_yP_z, P_\perp^2) && \text{(A.12)} \\
\frac{\partial\psi}{\partial\vec{P}} &= \frac{1}{P_\perp^2}(-P_y, P_x, 0) && \text{(A.13)}
\end{aligned}
$$

A.1.6 PED parameters to Rectangular

Because the internal calculations are done in rectangular coordinate, the measured parameters of the PEDs must be converted from spherical coordinates. The conversion of the error matrices is a little more work. To calculate the pulls in the original basis, the internal values need to be converted back too.

$$\vec{P} = (\sqrt{E})^2(\cos\phi\ \sin\theta, \sin\phi\ \sin\theta, \cos\theta) \quad (A.14)$$

$$P_\perp = \sqrt{P_x^2 + P_y^2} \quad (A.15)$$

$$P = \sqrt{P_x^2 + P_y^2 + P_z^2} \quad (A.16)$$

$$\phi = \mathtt{ATAN2}(P_y, P_x) \quad (A.17)$$

$$\theta = \arccos(P_z/P) \quad (A.18)$$

$$\sqrt{E} = \sqrt{P}$$

$$\frac{\partial\vec{P}}{\partial\phi} = (\sqrt{E})^2\,(-\sin\phi\ \sin\theta, \cos\phi\ \sin\theta, 0) \quad (A.19)$$

$$\frac{\partial\vec{P}}{\partial\theta} = (\sqrt{E})^2\,(\cos\phi\ \cos\theta, \sin\phi\ \cos\theta, -\sin\theta) \quad (A.20)$$

$$\frac{\partial\vec{P}}{\partial\sqrt{e}} = 2(\sqrt{E})\,(\cos\phi\ \sin\theta, \sin\phi\ \sin\theta, \cos\theta)$$

$$\frac{\partial \phi}{\partial \vec{P}} = \frac{1}{P_\perp^2}(-P_y, P_x, 0) \tag{A.21}$$

$$\frac{\partial \theta}{\partial \vec{P}} = \frac{1}{P^2}(\frac{P_x P_z}{P_\perp}, \frac{P_y P_z}{P_\perp}, -P_\perp) \tag{A.22}$$

$$\frac{\partial \sqrt{E}}{\partial \vec{P}} = \frac{1}{2P^{3/2}}(P_x, P_y, P_z) \tag{A.23}$$

A.2 KinFit C++ Class

KinFit code omitted to save paper

A.3 Fitting Algorithm

The problem of fitting many Monte Carlo distributions (with limited statistics) to the data (again with limited statistics) is difficult to solve. The standard log-likelihood method for Poisson data is to minimize the function

$$\chi^2 = \sum_i \left[2(N_i^{th} - N_i^{\text{observed}}) + 2N_i^{\text{observed}} \ln(N_i^{\text{observed}}/N_i^{\text{theory}}) \right]$$

If N_i^{observed}=0, then the second term is dropped. (PDG 1996,p. 1276).

However, this method breaks down when N_i^{theory} is zero and $N_i^{\text{observed}} \neq 0$. This can happen if there are statistical errors in the theory, such as is the case for Monte Carlo simulations of the theory. The obvious solution is to generate enough Monte Carlo so that every bin has at least a few events. However, this is nearly impossible for weak feed through channels.

Simply ignoring problem bins is not valid. Consider a two bin problem, with the true $N_i^{\text{theory}} = 0.5$, but with ${N_i^{\text{theory}}}_1 = 0$ and ${N_i^{\text{theory}}}_2 = 1$ as calculated by Monte Carlo. If we ignore the first bin, the average of remaining bins is now 1.0, rather than 0.5, which is clearly wrong and the result of a fit will be biased. The old fits of the ω decay problem were biased in this way, where the 2-D fit (with low statistics in the bins) differed from the 1-D fit (with high statistics) by 50%.

The key to the problem is that the true theoretical value is unknown, and this value should be another parameter in the fit, constrained by the data and the Monte Carlo.

The problem has been addressed by Eberhard *et al.* [80]. In their algorithm, they attempt to maximize the log-likelihood,

$$L = \sum_j \left[n_j \ln \lambda_j - \lambda_j + \sum_i (m_{ij} \ln f_{ij} - f_{ij}) \right],$$

where the j's run over bins, the i's run over the MC data sets, n is the number of data events, m is the number of MC events, f is the *expected* number of *MC* events, and λ is the expected number of data events, defined as

$$\lambda_j = \sum_i a_i f_{ij}$$

where a_i is the strength of the i'th MC channel.

Because all of the α_i and f_{ij} are unknowns, this problem becomes intractable as a direct minimization of too many free parameters. However, the next best thing to do solve for the f_{ij} first, and then maximize with respect to α. The method for solving for the f_{ij} is detailed in reference [80]. The algorithm was strictly followed, with the value of $\epsilon = 0.0002$ used as the convergence criterion when iteratively solving for the f, which is

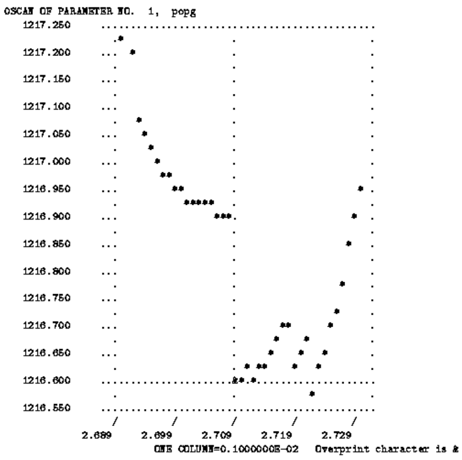

(A)

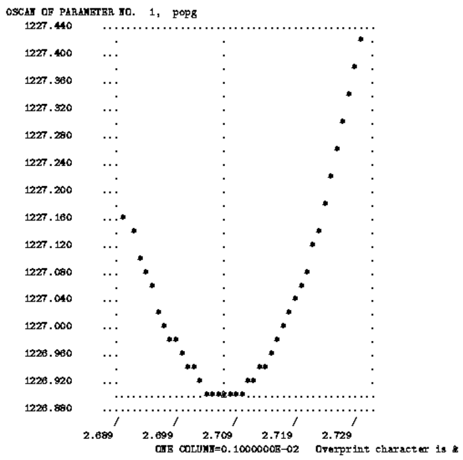

(B)

Figure A.1: The dependence of the negative log-likelihood ($\sim \chi^2$) on a fit parameter around the fit minimum for different convergence thresholds. (A) $\epsilon = 0.1$. Note the severe discontinuities which fool the minimization routine into local minima. (B) $\epsilon = 0.002$

roughly the precision to which the f's are solved. It was found that the value of $\epsilon = 0.1$ is too coarse, and causes aliasing in the total likelihood function, which subsequently causes severe problems in MINUIT because the aliasing causes micro-sized local minima. Values of $\epsilon = 0.01, 0.002$ greatly improve the simple gradient descent fit, but still cause problems with the MINOS calculation of the errors. The chosen value allows a sufficiently smooth likelihood function such that MINOS does not fail.

In some special cases with low statistics, Minuit would sometimes move into unphysical regions of the fit space. In this case, all parameters were then forced to be positive and the fit was repeated. Bounded fits in situations that did not require them show that the systematic problems normally associated with bounded fits were minimal.

Another improvement for the fitting was to introduce variable sized bins, which were smaller near the ω peak and larger in the background region. This increases the events per bin, and also cuts down on CPU time because there are fewer bins.

A.4 DLT

The DLT 0-prong summary tapes were copied from the raw data. Each tape contains nearly one hundred files, where each file is the contents of one IBM tape cartridge (named GHxxxx).

A full list of the contents is available from the author.

```
Listed by LB tape number

label  files Mbyte runs(nfiles:firstGH-lastGH)
-----------------------------------------------
LB0010  135  19293 may91(39:2998-3042)
                   jun91(47:3408-3606)
                   aug91(49:3906-3956)
LB0011  108  17093 aug91( 9:3957-3996)
                   oct93(45:7021-7607)
                   sep90(54:1730-1916)
LB0012  106  16322 sep90(53:1917-2190)
                   jun94(24:7738-7806)
                   dec89(29:0786-0846)
LB0013  106  16155 jun90(51:1101-1160)
                   nov90(55:2201-2605)
LB0014   83  16112 nov90(83:2606-2774)
LB0015  103  15595 nov90(33:2775-2816)
                   jul90(70:1371-1491)
LB0017  106  15115 jul90(99:1492-1613)
                   dec89( 7:0848-0858)
```

```
Listed by Run

run   Mevts  files tape(firstfile:lastfile) ...
-----------------------------------------
dec89  1.0    36   LB0012(77:105) LB0017(99:105)
jun90  1.5    51   LB0013(0:50)
jul90  5.0   169   LB0015(33:102) LB0017(0:98)
```

```
sep90  1.3   107   LB0011(54:107) LB0012(0:52)
nov90  5.0   171   LB0013(51:105) LB0014(0:82) LB0015(0:32)
may91  1.6    39   LB0010(0:38)
jun91  1.6    47   LB0010(39:85)
aug91  1.8    58   LB0010(86:134) LB0011(0:8)
oct93  1.9    45   LB0011(9:53)
jun94  1.1    24   LB0012(53:76)
---------------------------------
total 21.8   747   7 DLT's
```

A.5 Normalization for BW applied to Dalitz plot

The normalized Breit-Wigner,

$$BW(m) = \frac{1}{2\pi} \frac{\Gamma}{(m - m_\omega)^2 + \Gamma^2/4}$$

satisfies the normalization condition

$$\int_{-\infty}^{\infty} BW(m) dm = 1.$$

Branching ratio measurements are defined for "ideal" mass mesons, meaning that it only holds true for mesons with mass equal to the tabulated mean mass. Using this definition, the width of the ideal meson can be taken to be 0 and the BW resonance curve can be replaced by a delta function.

$$BW(m) \rightarrow \delta(m - m_\omega)$$

However, the delta function is only normalized when integrated in one dimension. We demand that our resonance function be normalized to unity on the Dalitz plot, so that each flat generated Monte Carlo event can be weighted properly. The normalization of the dalitz plot depends on the resonance mass and the mass of the recoiling particle. For example, because there is more phase space in the $\pi^0\rho^0$ dalitz plot than in the $\eta\rho^0$, the bare delta function would not have the same integral over the Dalitz space.

We shall find X such that

$$\frac{1}{X}\int\int_{\text{dalitz}} dm_{12}^2 dm_{13}^2 BW(\sqrt{m_{12}^2}) = 1$$

The value of X will have units of MeV^3. Let

$$BW(\sqrt{m_{12}^2}) \rightarrow \delta(\sqrt{(m_{12}^2)} - m_\omega)$$

then

$$X = \int\int_{\text{dalitz}} dm_{12}^2 dm_{13}^2 BW(\sqrt{m_{12}^2}) \tag{A.24}$$

$$= \int dm_{12}^2 \delta(\sqrt{(m_{12}^2)} - m_\omega) \int_{min}^{max} dm_{13}^2 \tag{A.25}$$

$$= \int dm_{12}^2 \delta(\sqrt{(m_{12}^2)} - m_\omega) 4\sqrt{(E_1^2 - m_1^2)(E_3^2 - m_3^2)} \tag{A.26}$$

$$= \int dm_{12}^2 \delta(\sqrt{(m_{12}^2)} - m_\omega) 4\sqrt{(E_1^2 - m_1^2)(E_3^2 - m_3^2)} \tag{A.27}$$

$$X = (2m_\omega) 4\sqrt{(E_1^2 - m_1^2)(E_3^2 - m_3^2)} \tag{A.28}$$

$$E_1 = (m_\omega^2 - m_2^2 + m_1^2)/2m_\omega \tag{A.29}$$

$$E_3 = (M^2 - m_\omega^2 + m_2^2)/2m_\omega \tag{A.30}$$

To do a statistical integration that equals the analytic integration, you need to multiply each sample by a weight α, which is the differential area divided by the X normalization

$$\alpha = \frac{dA}{X} = \frac{DalitzArea}{XN}$$

That's it. The numerical values of α (which have units on MeV) for each dalitz plot are given in table 13.2.

A.6 Contents of CDROM

A recordable Compact Disc is enclosed. The data format is the standard ISO-9660 format, which is readable on every popular computer of 1998. Hopefully this standard will be around for the next hundred years. The lifetime of recordable CDs is estimated to be at least 100 years based on accelerated aging tests. The CDROM contains the following data. Consult the `README.TXT` file for the latest information.

1. The thesis in postscript format
2. The thesis LaTeX and `.eps` source files.
3. Source code for AWP.
4. Compiled version for Solaris 2.5.
5. Example steering files.
6. Histograms, in 30x30 binning and 60x60 binning.
   (a) All Data
   (b) $K_S K^+ \pi^-$ Data
   (c) $K_S K^- \pi^+$ Data
   (d) All Monte Carlo Data
   (e) $K_S K^+ \pi^-$ Monte Carlo
   (f) $K_S K^- \pi^+$ Monte Carlo

7. All Data, event by event, with the following format (ASCII text). Each event is written as 25 numeric fields, each separated by one character of white space (0x20) and followed by the newline character (0x0A) at the end. Integer fields are formed from the digits '0' (0x30) to '9' (0x39) and an optional minus sign '-' (0x2d). Real fields are formed from the digits '0' (0x30) to '9' (0x39), a period '.' (0x2e), signs '+' (0x2b) or '-' (x02d) and an optional 'e' (0x65) for floating point notation. Examples of floating point are

```
 1.1e+06
 9.16515
-1.3e-12
```

Field	Real/Integer	Description
0	I	Run Number
1	I	Event Number
2	R	χ^2 of Kinematic Fit to $K_S K^\pm \pi^\pm$
3	R	$m^2(K_S\pi^\pm)$
4	R	$m^2(\pi^\mp K^\pm)$
5	R	$m^2(K^\pm K_S)$
6	R	x position of V0
7	R	y position of V0
8	R	z position of V0
9	R	x position of V1
10	R	y position of V1
11	R	z position of V1
12	R	p_x of kaon at V0
13	R	p_y of kaon at V0
14	R	p_z of kaon at V0
15	R	p_x of pion at V0
16	R	p_y of pion at V0
17	R	p_z of pion at V0
18	R	p_x of pion at V1 (+ charge)
19	R	p_y of pion at V1 (+ charge)
20	R	p_z of pion at V1 (+ charge)
21	R	p_x of pion at V1 (- charge)
22	R	p_y of pion at V1 (- charge)
23	R	p_z of pion at V1 (- charge)
24	I	Charge of kaon

```
WRIT 4
FZIN 'XT'
FZOU 'XT'
CHAM 'TRAK' 'RAWS' 'GPWC' 'PATT' 'CIRC' 'HELX'
XTAL 'TRAK' 'DECF' 'DECL' 'ALCE' 'CLST' 'PEDS' 'PDRG'
GLOB 'TRAK' 'MTCH'
BANK 'GLOB'
```

Table A.1: First pass reconstruction steering cards for CBOFF, Fortran Unit 99

```
WRIT 4
FZIN 'XT'
FZOU 'XT'
CHAM 'NONE'
XTAL 'NONE'
GLOB 'NONE'
BANK 'GLOB'
```

Table A.2: Second pass steering cards for energy and momentum selection for CBOFF, Fortran Unit 99

A.7 Software details of both Analysis

The cards used to drive the CBOFF analysis software are given in this chapter. The steerings cards for the $K_S K^{\pm}\pi^{\pm}$ analysis are given in tables A.1, A.2, A.3 and A.4. The information for the $\omega \rightarrow \eta\gamma$ analysis are given in tables A.5,A.6, A.7 and A.8.

```
WRIT 4
FZIN 'XT'
CHAM 'TRAK' 'RTRK' 'RAWS' 'GVTX' 'PATT' 'CIRC' 'HELX' 'VERT'
XTAL 'TRAK' 'RTRK' 'DECF' 'DECL' 'ALCE' 'CLST' 'PEDS' 'PDRG'
GLOB 'TRAK' 'RTRK' 'MTCH'

VERT 3
VFIT 2
VHER 0.8
```

Table A.3: Third pass steering cards for vertex fitting, with CBOFF unit 99 at top and Locater unit 81 at bottom

```
WRIT 4
FZIN 'XT'
CHAM 'NONE'
XTAL 'NONE'
GLOB 'NONE'
```

Table A.4: Fourth pass steering cards for kinematic fitting for CBOFF unit 99

Package	Version	Package	Version
cboff:	1.30/10	locater:	2.01/11
bctrak:	2.04/03	gtrack:	1.37/01
ccdbcb:	2.05/01	cbkfit:	3.09/00
cbdrop:	1.11/03	cbgeant:	5.05/04

Table A.5: CBOFF software versions used in the $\omega \rightarrow \eta\gamma$ analysis.

```
cboff steering cards:
CHAM 'TRAK' 'RAWS' 'GPWC' 'PATT' 'CIRC' 'HELX'
XTAL 'TRAK' 'DECF' 'DECL' 'ALCE' 'CLST' 'PEDS' 'PDRG'
GLOB 'TRAK' 'MTCH'
BANK 'GLOB'
DSTP 0
```

Table A.6: The steering cards used for CBOFF unit 99, $\omega \rightarrow \eta\gamma$ analysis.

5809	GH3012	LB0010	4231	2H6	1-May-91	BJ-PST-	IA
5810	GH3012	LB0010	6016	2H6	1-May-91	BJ-PST-	IA
7015	GH3605	LB0010	2041	2H9	12-Jun-91	B--PST-	4+Lprng
7996	GH3963	LB0011	20391	2H6	12-Aug-91	BJ-PST-	minbias
8001	GH3966	LB0011	269	2H6	12-Aug-91	BJ-PST-	minbias
16084	-???32	LB0011	-1	----	---------	-------	unknown
16146	-???43	LB0011	1217	----	---------	-------	unknown
16172	-???44	LB0011	-1	----	---------	-------	unknown
16173	-???44	LB0011	-1	----	---------	-------	unknown
16177	-???44	LB0011	-1	----	---------	-------	unknown
20352	GH7546	LB0011	1735	2xx	30-Oct-93	BJ-PST-	minbias;nigelflag
20353	GH7546	LB0011	11503	2xx	30-Oct-93	BJ-PST-	minbias;default
20358	GH7---	LB0011	-1	2Hx	x-Oct-93	-------	noinfo
3636	GH1938	LB0012	9304	2H6	9-Oct-90	-------	unknown
3848	GH2060	LB0012	6143	2H9	12-Oct-90	BJ-PS--	minbias
4049	GH2190	LB0012	-1	2E6	15-Oct-90	BJ-PS--	0prng
4050	GH2190	LB0012	2607	2E6	15-Oct-90	BJ-PS--	0prng
1272	GH0795	LB0012	5795	2H9	16-Dec-89	B------	pedestal
1277	GH0799	LB0012	6017	2H9	16-Dec-89	B------	pedestal
1288	GH0804	LB0012	4812	2H0	17-Dec-89	BJ--S--	0prng
1288	GH0804	LB0012	4812	2H0	17-Dec-89	BJ--S--	0prng
1289	GH0804	LB0012	4374	2H0	17-Dec-89	BJ--S--	0prng
1365	GH0836	LB0012	0	2H9	19-Dec-89	B------	pedestal
1384	GH0844	LB0012	5822	2H9	19-Dec-89	B------	pedestal
1411	GH1992	LB0012	16775	2H0	20-Dec-89	B------	pedestal
1411	GH1992	LB0012	16775	2H0	20-Dec-89	B------	pedestal
4199	GH2221	LB0013	366	2H6	9-Nov-90	BJ-PS--	minbias
5252	GH2756	LB0014	1	2H6	25-Nov-90	BJ-PS--	minbias
1399	GH0854	LB0017	7346	2H9	20-Dec-89	BJ--S--	genericdata

Table A.7: Wrong runs in $\omega \to \eta\gamma$ analysis

Description	FORTRAN cut
Momentum/Energy Conservation eff.	`en200/event.lt.0.4`
5 Gamma efficiency	`gamma5/event.lt.0.02`
Average gamma multiplicity	`ngamma.lt.6.or.ngamma.gt.10`
Average track multiplicity	`ntracks.lt.0.0001.or.ntracks.gt.0.5`
Average PED θ position	`abs(pedtheta).gt.0.1.and.pedtheta<20.0`

2079	2100	2131	2132	2160	2161	2165	2169	2170	2898
2932	2974	3271	3272	3273	3274	3275	3276	3277	3278
3279	3280	3281	3285	3286	3290	3299	3300	3301	3523
3524	3529	3531	3543	3614	3615	3618	3620	3624	3821
3848	4050	4133	4134	4136	4137	4199	4516	4523	4526
4988	5228	5241	5350	5351	5354	5355	6618	6672	16143
16147	16195	16197	20209	20352	20353	21344	21345	21348	21349
21351	21354	21355	21356						

Table A.8: The cuts at the top of the table were used to identify the bad runs which are listed at the bottom of the table.